THE UNIVERSITY *of* EDINBURGH

Active interfaces, a universal approach

Francesco Cagnetta

Doctor of Philosophy
The University of Edinburgh
February 2020

Abstract

This thesis proposes and characterises a stochastic model of an active interface within the framework of statistical mechanics. Statistical methods have indeed proven successful in probing the dynamics of kinetically roughened interfaces, producing results which fill a wide, 40 year long literature. The principle of universality, according to which large scales and long times screen a system intimate details, provides a mean to systematise such knowledge: many growing interfaces, for instance, are described by the same equation—the Kardar-Parisi-Zhang (KPZ) equation.

To what extent living interfaces fit into the picture is still an open question, a question this thesis attempts to answer by drawing inspiration from the membrane of moving cells. Here, the aforementioned universality principle can be used as a road roller to pave our way into the crowded and highly dynamic environment of the cell membrane. The hope is that of smoothening all—and only—the *irrelevant* asperities, minor attributes whose account does yield an insight nowhere near the effort they require.

The result of our crude approximation, that is the model presented in the thesis, can be thoroughly analysed with numerical and analytical methods: its main features turn out to match qualitatively those of actual membranes. In addition, the model allows for a rigorous derivation of the field equations which govern its large scales and long times properties. Scaling arguments then show that these equations include all the *relevant* ingredients, so as to corroborate the crude approximations made at the beginning. The model presented can thus be concluded to be a reasonable candidate for the universal description of active interfaces and reveal the signature features that can be looked for in experiments.

Lay Summary

Certain physical systems comprise a gigantic number of simple subunits. It might be convenient, in their study, to abandon the desperate task of computing the evolution of each subunit in favor of an approach based on the distribution of subunits over a set of conceivable configurations. Such studies were called by Maxwell *statistical*, as Gibbs reminds us in its book "Elementary Principles in Statistical Mechanics". Statistical mechanics itself is the epitome of a successful statistical approach, as it explains the emergence of thermodynamics from Newtonian mechanics when the number of particles in the system tends to the Avogadro constant. In the same book we are also reminded that "although, as a matter of history, statistical mechanics owes its origin to investigations in thermodynamics, it seems eminently worthy of an independent development". Today, indeed, we use the broader phrase *statistical physics*, to collect studies where the laws of probability replace deterministic evolution. In fact, we might adopt an even broader term, in that modern applications of statistical physics extend beyond physics and chemistry, towards biology and social sciences such as linguistics.

Unfortunately, not every statistical theory is afforded the status of a complete theory, as it is the case for statistical mechanics. The reason lies in the property of *thermodynamic equilibrium*, read the absence of macroscopic flows of matter and/or energy within the system: on the one hand, this property guarantees the possibility of representing the system with a probability distribution; on the other hand, it causes the probability distribution to depend solely on conserved quantities (volume, number of particles, etc.). Outside of thermodynamic equilibrium, where the conserved quantities might flow across the system, no general theory exists. Therefore, the study of each system constitutes a problem in itself; yet, concepts borrowed from statistical mechanics can provide deep, general insights. One of these concepts, largely used in this thesis, is *Universality*.

Introduced by Kadanoff in the 60s, the concept of universality entails the idea that, for certain systems, some properties—the *universal* properties—are insensitive to the microscopic details. Many systems, then, though seemingly unrelated, might display similar universal properties—it is said that they belong to the same *universality class*. The perfect example of universality is found close to the *critical point* of second order phase transitions, such as the ferromagnetic transition: because of correlations extending to the whole system, the closer the temperature to the critical point, the less sensitive the dependence of the magnetisation on the microscopic details. The idea is easily extended to dynamical problems, for instance Brownian motion. The price of financial assets, the orientation of a binary star's orbital plane, the position of the pollen grains observed by the botanist Robert Brown: all these variables experience fluctuations which grow as the square root of the time elapsed since the last measurement, despite the manifest difference in the details of the system.

If the classical physical system studied in statistical mechanics need to be close to a critical point in order to display universal properties, it is a common belief that several biological system achieve such state by themselves. In simple terms, this means there is no need to tune a temperature-like parameter on the critical value. It is said, in this repsect, that such systems are "poised at criticality". The idea behind the model presented in this thesis is that of exploiting universality to attempt a description of the cell membrane based on a minimal number of ingredients. In practice, I will present a lattice model of the membrane of motile cells based on the following assumptions: the membrane moves and its motion is directed by signalling proteins living on the membrane itself. Other details, notably the coupling between the proteins and the membrane curvature, are assumed to be irrelevant. The obvious advantage of such an approach is simplicity; the price to pay is that only universal properties are accessible. These include the exponents describing the distribution of proteins over the membrane, the membrane spatial fluctuations and their dynamics for very long times: all features which can be detected in experiments. Once a qualitative agreement with the dynamics of real membrane is established, I will proceed with the derivation of equations for the conserved quantities of the problem: protein density and membrane slope. The equations can be compared with other, more detailed descriptions of fluid membranes, where each additional detail corresponds to a new term, thus a new parameter, in the equations. Finally, I will apply Renormalisation group techniques to provide a unifying perspective on the problem and classify the details/parameters into relevant and irrelevant.

Declaration

I declare that this thesis was composed by myself, that the work contained herein is my own except where explicitly stated otherwise in the text, and that this work has not been submitted for any other degree or professional qualification except as specified.

Parts of this work have been published in [1–4].

Additional work not contributing to this thesis has been published in [5, 6].

(*Francesco Cagnetta, February 2020*)

Acknowledgements

I would like to express my deepest thanks to my principal supervisor, Martin Evans, for his guidance and support throughout the work presented here; and my second supervisor, Davide Marenduzzo, for the constant input and many insightful discussions.

I would also like to extend my gratitude to:

- Those I have had the lucky chance to work with: Davide Michieletto; Emil Mallmin; Viktor Škultéty, to whom I also owe the ability to write the majority of chapter 4;

- My long-term flatmates, Koko and Paul, for giving me a place where to happily come back after a working day;

- Heather, for her support as a friend and as a partner;

- My coffee-break friends at university, Fernando, James, Alessandro, Renato, Marco, Andrea, Giada; and all my friends in Edinburgh.

Voglio anche ringraziare gli amici "da casa", che porto con me dovunque vada; e, per la terza volta in una tesi, la mia famiglia. I miei genitori, in particolare, sono i veri responsabili del documento che vi si para davanti. Grazie.

Contents

Abstract i

Lay Summary iii

Declaration v

Acknowledgements vii

Contents ix

List of Figures xiii

1 Introduction 1

1.1 Fluctuating interfaces in and out of equilibrium 3

1.2 The call for an active description 6

1.2.1 A few more facts from cell biology 9

1.3 Structure of the thesis 11

2 Building a toy active interface 13

2.1 From facts to the lattice description 15

2.1.1 The discrete interface 15

2.1.2 Sliding activators 18

2.1.3 The active interface model 20

2.2 Dynamics of a "test" activator: numerical results 23

2.2.1 Observables and scaling 25

2.2.2 Fluctuating metadynamics at $r \leq 1$ 27

2.2.3 The surfing regime 33

2.3 Scaling of the discrete active interface: numerical results 38

2.3.1 Width and diffusion at finite density 39

2.3.2 Arrested path coalescence and waves 41

2.3.3 Concluding remarks 45

3 The active interface equations 47

3.1 The hydrodynamic limit 49

3.1.1 Factorised steady-state measure 50

3.1.2 Deterministic equations 52

3.1.3 Stochastic corrections 57

3.2 Solution of the inviscid limit 59

3.2.1 Riemann problem for the linear active interface equations ... 60

3.2.2 Nonlinear equations: shock waves 62

3.2.3 Nonlinear equations: rarefaction fans 66

3.3 Dynamics of the active interface: analytical results 72

3.3.1 Steady-state oscillations 72

3.3.2 The surfing regime, pt. 2 76

3.3.3 Concluding remarks 79

4 Large-scale dynamics of active interfaces 81

4.1 Dynamic equations and action functional 83

4.1.1 Symmetries of the active interface equations 85

4.1.2 Path probability and action functionals 89

4.1.3 A short introduction to perturbation theory 92

4.2 Mean field theory 95

4.2.1 Naive dimensional analysis 96

4.2.2 Oscillating dynamics at the Euler scale 99

4.2.3 Two novel critical lines 102

4.3 One-loop corrections at the KPZ fixed point 105

4.3.1 Renormalisation 108

4.3.2 Renormalisation Group flow 112

4.3.3 Concluding remarks 114

5 Conclusions 115

A Fourier transform conventions 123

B Method of characteristics for conservation laws 127

C Connected correlation and Vertex functions 133

D One-loop corrections to $\Gamma^{\tilde{\phi}\phi}$ 137

E One-loop corrections to $\Gamma^{\tilde{\phi}\tilde{\phi}}$ 141

Bibliography 147

List of Figures

(1.1) Simulated Eden cluster, grown from a seed with the following algorithm: choose an existing element with equal probability, then choose one of its free edges with equal probability and add a new element on that edge. 2

(1.2) Pictorial representation of the dendritic-nucleation model for lamellipodial protrusion of the leading edge. 8

(2.1) Details of the single-step model: the height variables equal the distance of the interface from the reference horizontal axis. The dynamics comprises wedge-to-trough and trough-to-wedge transitions. 16

(2.2) Schematic representation of the discrete active interface: the corner-flip rates depend on the local number of activators. 17

(2.3) Details of the activators motion. A) Normal diffusion is obtained by symmetric hopping on the lattice. B) The shape of the activators gives them a spontaneous curvature, thus coupling them with the curvature of the interface. C) Once activators are coupled with the curvature, the hopping rates depend on the local interface shape. 19

(2.4) Slope coupling arising from normal growth. Panel A displays a curved interface, being driven by an infinitesimal force in the direction of the local normal. As growth occurs along the local normal, the vertical displacement of the interface is effectively larger. Panel B shows the same scenario for an active interface being driven by a single activator: the normal force causes also a horizontal displacement of the activator in the x direction. Panel C shows how the slope coupling is included in the model: the hopping rate for sliding down a slope is higher (or simply different, in general) than that of the reversed transition. 21

(2.5) Scaling of the averaged width for $r = 1$, $\gamma = \lambda = 1$, with system size L as in the key. The best collapse is achieved by setting the exponents to the EW class values. A power law x^{α/z_1} is shown as a guide to the eye (black dashed line). The interface width has been averaged over 10^3 realisations of the stochastic dynamics. The number of realisations used for averages is the same in all the figures of this section unless otherwise stated. 28

(2.6) Scaling of the activator MSD for $r = 1$, $\gamma = \lambda = 1$, L as in the key. The data are collapsed by setting $\chi = 1/2$ and $z_2 = 3/2$, consistent with the second class particle scaling. The black dashed line is a guide to the eye suggesting $\langle X_t^2 \rangle \sim t^{4/3}$. The MSD, as in the following figures, is computed at steady state, meaning that the displacement X_t is measured since saturation of the interface width. 29

(2.7) Correlations $C_s(j,t)$ spreading from a fixed activator which catalyses growth in the interface. The slope correlation function is measured at different times (see key) and plotted against $j/t^{1/2}$ on the top panel and $j/t^{2/3}$ on the bottom panel. The overlap of the functions is much better in the latter case, suggesting that correlations spread around the activator as t^{1/z_2} where $z_2 = 3/2$. Averages here are performed over 10^5 realisations of the interface dynamics. 30

(2.8) Width (top) and MSD(bottom) vs rt, for $L = 2^{13}$, $\gamma = \lambda = 1$ and r as in the key. The width of a passive, EW interface is also shown for comparison. While rescaling time by r renders the interface dynamics independent of this parameter, the activator displays an early-time, subdiffusive regime, the extent of which scales as $1/r$, as pointed out in the text. 31

(2.9) Scaling plot of the activator MSD for $r = 10^{-2}$, $\gamma = \lambda = 1$. The black solid line is a guide to the eye for the superdiffusive law $\langle X_t \rangle \sim t^{4/3}$. 32

(2.10) Surfing regime snapshots. The interface profiles are ordered in time according to their color, from lighter to darker, while the activator is represented by a yellow dot of a significantly larger size, to ease the understanding of the picture. The earliest snapshot (light blue), depicts the initial growth, whose dynamics is analogous to that of the $r \to \infty$ limit (cf. subsubsection 2.2.3.1). The second (azure), is taken some moments after the activator has started moving: the wave is broken together with the left-right symmetry of the system. The last (dark blue) is the latest, and it shows that the activator keeps moving while 'ironing out' the interface: this is, in fact, the regime with the smallest roughness exponent. Notice how, due to the system finite size, the activator will soon reach the back of the wave: at this point it could stochastically revert his motion, so that the long-time dynamics is still diffusive (see discussion in the text). 33

(2.11) MSD scaling at $r = 100$. If one excludes the $L = 1000$ curve, which does not reach a full ballistic regime, the scaling exponents agree with the proposed values $\chi = z_2 = 1$. 34

(2.12) Width scaling at $r = 100$, $\gamma = \lambda = 1$. The oscillating widths collapse on a single curve for $\alpha = 0.175$ and $z_1 = 1$. 35

(2.13) Main: width scaling in the $r \to \infty$, L as in the key. $\alpha = 1$, $z_1 = 2$ causes overlap of the rightmost portion of the curves. The black solid lines are guides for the power laws $w \sim t^{1/4}$ and $w \sim t^{1/2}$ (see text). Inset: tent shape generated by a static activator. 37

(2.14) Average width of the active interface with $\lambda = 1$ and $\gamma = 0.5$ (points) and an EW interface (solid lines), scaled with the EW scaling exponents $\alpha = 0.5$ and $z_1 = 2$. The $w(L, t)$ curves of the EW interfaces collapse onto the same curve $\sim t^{1/4}$ ($\alpha/z = 1/4$), highlighted by the black dashed line. By contrast, the active interface width displays sustained oscillations superposed to the $t^{1/4}$ law. In this and the other scaling plots of this chapter averages are performed over 100 independent realisations of the stochastic dynamics. 40

(2.15) Average width of the active interface, $\lambda = 1$, $\gamma = 0.5$ and lattice size in the key. Here $z_1 = 1$, so as to highlight the oscillating component of the width. 41

(2.16) Scaling of the steady state MSD (measured after saturation of the interface width) for the active interface, with $\lambda = 1$, $\gamma = 0.5$ and L as in the key. As the interface width, the activators' MSD saturates after a time scaling linearly with the system size, i.e. $z_2 = 1$. The inset shows a zoom of the MSD scaling plots close to saturation, in order to highlight oscillations of the scaled MSD. 42

(2.17) Density fluctuations $\delta\rho^2(L,t)$ for several system sizes, $\gamma = 0.5$ and λ as in the key. The initial power-law growth, indicating coarsening, is followed by saturation. If the saturation value increases with L, as for $\lambda = 0$, the activators will ultimately coalesce in a single macroscopic aggregate. If the saturation value is independent of the system size, clusters grow only up to a finite size, as for $\lambda > 0$. 43

(2.18) Top: snapshots of an active interface with $L = 20000$, with $\gamma = 0.5$ and $\lambda = 1$. The interface is coloured according to the local number of activators n_i, from blue (no activators) to red (many acivators). The first snapshot is taken at $t = 0$, when the interface is flat and the distribution of activators uniform. In the other two snapshots, taken at later times, the activators have gathered at the bottom of interface valleys. Bottom: "kymograph" of the density profile, where each line represent the density profile (colour) at different times. The kymograph displays only a portion of the interface, and is taken in steady-state. The diagonal red lines represent the travelling nanosclusters discussed in the text. 45

(3.1) SEP/single-step mapping. The mapping relates the configurations of a single-step interface on the lattice and those of an asymmetric exclusion process on the half-lattice by associating particles with negative slopes and holes with positive slopes. The transitions through-to-wedge and wedge-to-trough correspond to particle-hole exchange transitions. The blue, dashed vertical lines delimit a cluster of holes/positive slopes while the red, dashed lines delimit a cluster of particles/negative slopes. 51

(3.2) Solution of the giant trough Riemann problem for the linearised, inviscid active interface equations. As time progresses, activators accumulate at the bottom of the wedge and make it grow. 62

(3.3) Shock curves of the active interface equations for several left states. Both the first and the second shock curves are represented. The grey dashed lines mark the portion of the curves discarded due to not satisfying the Lax entropy condition. The arrows represent the right eigenvectors of the current's Jacobian matrix and point towards the direction of increasing eigenvalue. 64

(3.4) The giant trough initial condition in the height variable (left panel) becomes a step in the slope variable (right panel). 65

(3.5) Schematic representation of the giant trough Riemann problem in the variables plane. The relevant part of the shock curves are shown as solid lines. The intermediate state must be reached via the first shock curve, as shown in the right panel, so that the two waves which form the full solution do not collide. 65

(3.6) Evolution of the giant trough initial condition in the height variable. The density profile is a top hat function which extends with the shock speeds. The increased density signals an accumulation of activators at the center of the valley, which, consequently, is flattened. 66

(3.7) Rarefaction curves of the active interface equations for several left states. Both the first and the second rarefaction curves are represented. The grey dashed lines mark the portion of the curves discarded due to the increasing eigenvalue constraint. The arrows represent the right eigenvectors of the current's Jacobian matrix, and point towards the direction of increasing eigenvalue. 67

(3.8) Giant peak initial condition in the slope and height variable (left) and corresponding construction of the solution in the variables plane (right). The solution of the giant peak Riemann problem is a double rarefaction fan, with an intermediate density lower than the initial density ρ_0. 69

(3.9) Schematic construction of the vanishing-density solution. On the vanishing-density line the system becomes linearly degenerate. As a result, the shock curve collapse onto a horizontal, straight line and can be extended towards lower slopes (see discussion in the text). This horizontal line, shown in red in the figure, can be used to move along the vanishing-slope axis, down to that point that can be connected directly to the right state via a rarefaction curve. 70

(3.10) Solution of the giant peak Riemann problem in the height-density variables (dashed lines represent the initial condition). The density is higher than the critical value in the left panel. In the right panel the density is lower than the critical value, i.e. so low that the advection due to the slope completely depletes the peak, whose smoothening freezes. 71

(3.11) Interface and density profiles at the time of the first waves collision. The initial condition is also shown with dashed lines. Two vertical, gray, dot-dashed lines mark the initial position of the discontinuities, while two red lines highlight the location of the discontinuities at the time of the collision. 73

(3.12) Snapshot of the density and height profiles at several times, all greater than or equal to the time of the first collision. A) At the collision, the profiles are the same as in Fig. 3.11. B) At a larger time the shock waves have passed through the front of the rarefaction fans: the density bump stretches and a new peak starts to form. C) After meeting the tails of the rarefaction fans, the shocks fill the low density region, while the rarefaction fans form a new height peak. D) Once the waves have travelled the whole system length, the density is again uniform, but positions of the initial peak and trough are interchanged. 74

(4.1) A) An interface (black solid line) h(x) (x and $y = h$ axis shown in black at the bottom left corner) is driven by a force λ in the direction of the local normal $\hat{n}$, thus $\delta h > \lambda \delta t$ (local normal/local tangent reference frame shown in grey on the bottom left corner). B) An active interface is driven by activators (red disk). The normal force causes also a horizontal displacement δx of the activator. 83

(4.2) Illustration of the Monge gauge for a 1-dimensional interface in the 2-dimensional space. The $\boldsymbol{x}$-axis is chosen so as to be parallel to the interface and the interface height measured along the orthogonal direction. This description is valid as long as $\nabla h \ll 1$. 88

(4.3) Mean-field phase diagram of the active interface equations. For any non-zero a_h and a_ϕ, such that $a_h a_\phi > 0$, scale transformations push the model towards the $z = 1$ fixed points, located at the top-right and bottom-left corners of the figure. The same is actually true for $a_h a_\phi < 0$, but the Gaussian model is unstable in this region. The 'unstable' and 'stable' phases, coinciding with the quadrants of the (a_h, a_ϕ) plane, are separated by two critical lines $a_h = 0$ and $a_\phi = 0$, with a bicritical point lying at their intersection. 105

(5.1) Comparison of a sketch of the leading edge (left, credits to *APS/Alan Stonebraker*) with the lattice active interface (right). Slope exchange causes vertical fluctuations of the interface. 115

(5.2) Pictorial representation of he two phases of the active interface model: for $a_h a_\phi < 0$, all the activators in the system are gathered on a single, macroscopic peak; for $a_h a_\phi < 0$ aggregates of finite size roam the interface by riding interface ripples. 120

(B.1) Two examples of shock wave in the Burgers' equation. The initial profile is shown on the bottom, while characteristic lines lines are displayed on the top of the figure. In the left panel, a decreasing velocity profile evolves into a shock which is physical, as it satisfies the Lax entropy condition (see discussion in the text). The right panel depicts an unphysical shock: it satisfies the Rankine-Hugoniot equation but not Lax condition. 129

(B.2) A limiting procedure shows how to fill the cone within the red dashed lines in the right panel with a rarefaction fan. Start with a piecewise linear function consisting of two horizontal segments joined by a slope-1 segment (left panel, bottom). The solution of this problem is obtained with the standard method of characteristics (left panel, top). The solution for the original initial datum (right panel) emerges in the limit where the size of the slope-1 segment vanishes. 131

Chapter 1

Introduction

Imagine the plasma membrane bounding a living cell; a crowded environment made up of complex individuals, locus to a wide variety of mechanical, chemical and thermal processes through which the cell communicates with its environment. Apply then the reductionist lens of statistical mechanics: what remains is an interface—the membrane—separating two regions—the interior and exterior of the cell—with very different physical properties; two *phases*, in the language of physics. From this point of view, the plasma membrane is comparable to a domain wall in a ferromagnetic material, but also to a flame front or the edge of a coffee stain. All these problems can, when looked at from sufficiently far away, be described with surprisingly similar equations. Is there an analogous description for plasma membranes? This is the main question addressed in the thesis.

This introductory chapter provides an extended description of the problem, by presenting scaling concepts and tools on which the later discussion builds, while also outlining the motivations behind the addressed question. Specifically, section 1.1 contains a brief introduction to the statistical mechanics of fluctuating interfaces, with reference to both in- and out-of-equilibrium aspects of the problem. Section 1.2 motivates the necessity for what is referred to as an *active* description (whence the term active interface), which goes beyond the models presented in section 1.1: here is where the goal of the thesis is made precise. A subsection, subsection 1.2.1, collects the biological information required to understand the model of chapter 2 and defines the scope of the latter model and of the general considerations that follow. Finally, section 1.3 consists of an extended table of contents where each of the following chapters is outlined.

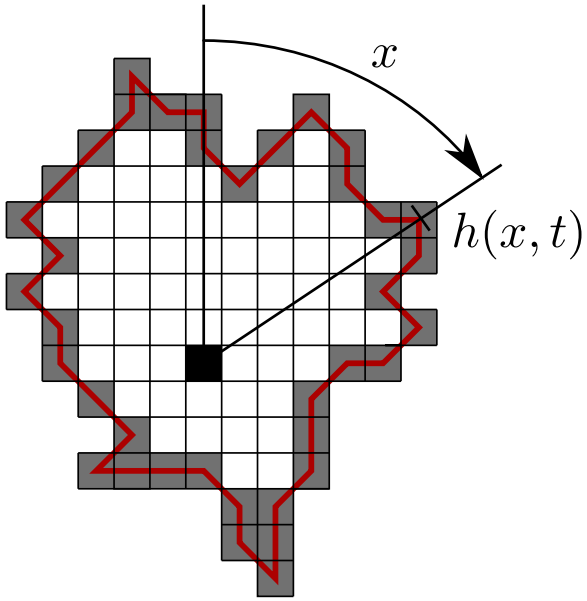

Figure 1.1 *Simulated Eden cluster with $N = 100$ units (squares in the figure). The cluster was grown from a seed element (black square in the figure) according to the following algorithm: choose an existing element with equal probability, then choose one of its free edges with equal probability and add a new element on that edge. Notice how the process by which the cluster is grown is both local and stochastic. At each time t (measured by the number of elements of the cluster) one can draw an interface (red solid line) by joining the centres of the boundary elements (gray in the figure). One can also define an "height" function $h(x,t)$ which measures the local radius of the cluster a function of the angle x from the zenith.*

1.1 Fluctuating interfaces in and out of equilibrium

At the beginning of the chapter, I have defined an interface as the object separating two phases in a material. This definition immediately sets the framework to be that of statistical mechanics. Moreover, it hints at two critical features of a fluctuating interfaces: the dynamics is *local* (as are the exchanges of matter between the two phases which displace the interface) and *stochastic* (as everything concerning a piece of matter at finite temperature should be). As useful as it is, however, the two-phases picture is fairly different from the one which motivated M. Eden to introduce the eponymous model of cluster growth [9]. The interface, as in Fig. 1.1, is now the boundary of an expanding colony of bacteria—a picture much closer to biology than statistical physics.

Broadly speaking, the Eden model mimics the formation of a large cluster (the colony) due to the consecutive random aggregation of many small elements (the individual cells). So does polymerisation, crystal growth, tumor growth, and, again, the nucleation of a new phase in a phase transition. As a consequence of the variety of subjects involved, the decades which followed the introduction of the Eden model have seen an expansion of the popularity of the topic, to such an extent that people with different backgrounds found themselves working effectively at the same problem [10–12]. Among the most attractive properties of the aforementioned clusters, there was the emergence of power laws relating various physical features of the cluster to the size of the cluster itself. The relevant mathematics was thus realised to be that of fractal objects [13], and, at least in the early stages, research in the field was mostly involved in finding all the cluster's properties which, by growing with a certain power of the cluster size, were found to exhibit fractal behaviour.

For the sake of concreteness, consider the Eden cluster shown in Fig. 1.1. As in the figure, one can define an interface by joining the outermost elements of the cluster, and describe it with a function $h(x,t)$ of the angle x and the number of cluster elements t (cf. Figure). The integral of h over x yields the cluster mean radius. The latter, as the cluster grows, diverges quite generally as a power of time/number of elements, thus defining a first fractal dimension. A second, more subtle, diverging length, is given by the *width* of the cluster edge, that is the typical difference in radius between different points of the cluster's edge. If the mean radius relates to the average of h, the width measures fluctuations—it is, in fact, computed by integrating h^2 over x. From the cluster perspective, a

diverging width implies that not only the cluster grows in size, but also its edge gets rougher, whence the name "kinetic roughening" to refer to the Eden model and related problems—see [14], chapter 3, or [12] for an extended introduction.

Another exponent can then be defined from the width divergence with time. A third exponent can be extracted by measuring, time fixed, how the width of a portion of the cluster edge grows with the portion size. As noted by H. E. Stanley in [15], the proliferation of exponents instills a feeling of déjà vu. In fact, not even twenty years had passed since Widom and Kadanoff, with their scaling hypotheses, brought order to the zoo of critical exponents found at second order phase transitions. The scaling hypothesis of kinetic roughening was proposed by F. Family and T. Vicsek in [16]: consider an interface growing from a flat initial condition over a substrate of size L. The interface width $w(L,t)$ displays a saturation profile obeying

$$w(L,t) = L^{\alpha} f(t/L^{z}), \tag{1.1}$$

where $f(x)$ behaves as $x^{\alpha/z}$ for small x and saturates for large arguments. α/z, also called β, determines the initial increase of the width with time. α controls how the saturated width scales with the substrate size L, and its called *roughness* exponent as $\alpha > 0$ causes the interface to appear rough.

With the Family-Vicsek scaling, interfaces generated by different processes are compared according to their scaling exponents. Following the analogy with equilibrium phase transitions, interfaces can be sorted into *universality classes*: groups of interfaces belonging to different problems but characterised by the same set of scaling exponents. The latter exponents should then be insensitive to the microscopic details of the interface genesis, but depend only on general aspects such as the symmetries of the process. The independence on the details is extremely powerful, as it allows to attempt the computation of the exponents in ultrasimplified models, as it is done, in the context of phase transitions, with the Ising model of ferromagnets. Such simple models can be formulated as discrete algorithms, like the Eden model, or, as the locality and stochasticity of growth processes suggests, stochastic partial differential equations—the variable would be, of course, the interface height $h(x,t)$.

Consider again the picture of an interface separating two phases in a piece of matter, assumed for simplicity to be two-dimensional. The interface equation inherits all the symmetries of the underlying system—translations in time and

space, rotations about the axis perpendicular to the interface. If, in addition, the two phases are equally stable (system at equilibrium), the equation must also be symmetric under $h \to -h$. The simplest equation satisfying all these symmetries has been introduced by S. F. Edwards and D. R. Wilkinson (EW) in [17]. It reads

$$\frac{\partial h}{\partial t} = \frac{\partial^2 h}{\partial x^2} + \eta, \tag{1.2}$$

where η is a stochastic force, and predicts Gaussian fluctuation for h with $\alpha = 1/2$ and $z = 2$—the EW class. When, instead, one phase is more stable and is invading the other (system out of equilibrium), M. Kardar, G. Parisi and Y.-C. Zhang (KPZ) have shown the relevant equation to be [18]

$$\frac{\partial h}{\partial t} = \left(\frac{\partial h}{\partial x}\right)^2 + \frac{\partial^2 h}{\partial x^2} + \eta. \tag{1.3}$$

Due to the added non-linear term, fluctuations are not Gaussian and the exponent z changes to $3/2$—the KPZ class. Many more equations can be written, to take into account processes where the mass of the two phases is conserved, or those driven by spatial inhomogeneities [14]. However, for the purpose of this thesis, that of kinetic roughening is—for now—a tale of two models: the Edwards-Wilkinson equation, for equilibrium conditions; the Kardar-Parisi-Zhang equation, for out-of-equilibrium conditions.

The KPZ class, in particular, turned out to include much more than moving interfaces and is now a cornerstone in the physics of *driven* systems [19, 20]. A driven system is taken to be held out of equilibrium due to some external driving force. Many far-from-equilibrium systems, however, especially those inspired by biological problems, are of a different nature, in that they are kept from relaxing by the continuous energy input at the microscales. They are generically referred to as *active* systems, and they have taken centre stage of statistical mechanics in the last few years. Whether an active analogue of KPZ exists or not is still an open question. This thesis proposes an answer within the context of active interfaces—peculiar active systems which, as kinetic roughening phenomena, can be described with a fluctuating interface. A more precise definition will be given in the next section, where I will present the paradigmatic active interface: the plasma membrane of a living cell. The model of the latter, subject of this thesis, will be presented in chapter 2.

1.2 The call for an active description

The theory of kinetic roughening does not refer to inanimate, or *passive*, objects only. The Eden model itself, for instance, was introduced as an oversimplified representation of a bacterial colony. However, while some biological interfaces are simply understood in terms of the scaling ideas of the previous section, the features of some others have proven far more challenging to fathom: the low-frequency fluctuations in the shape of red blood cells are a good example of the issue. Known since the end of the 19th century [21], the so-called flickering of red blood cells has left the community divided for several decades. The first satisfactory measure of the membrane fluctuations spectrum came in the mid-seventies with F. Brochard and J. Lennon [22], whose interpretation was anyhow debatable. The debate, as explained in [22] concerned the nature of fluctuations: are they due to active biological processes or just the result of thermal agitation?

The flickering of membranes, as other fluctuation-related phenomena, can be quantified experimentally by the average amplitude of fluctuations with a given wavenumber k—the so-called *structure factor* $S(k)$, related to the Fourier transform in space of the height function (for conventions and more detailed definitions, see [14] or Appendix A). The structure factor of a piece of matter describes how the latter scatters incident radiation. For a membrane subject to thermal undulations (temperature of the medium T), for instance, it is given by

$$S(k) = \frac{k_B T}{\nu k^2 + \kappa k^4} \tag{1.4}$$

where $k_B \simeq 1.38 \times 10^{-23}\ JK^{-1}$ is Boltzmann's constant, ν is the surface tension (energy increase due to an increase in the surface size) and κ the bending rigidity (energy increase due to an increase in surface curvature). For a one-dimensional interface described by the height function h, the surface energy is proportional to $(\partial h/\partial x)^2$ and the curvature energy to $(\partial^2 h/\partial x^2)^2$—counting the derivatives in each energy term yields the power of k in the corresponding term of the structure factor. According to the result above, a structure factor which diverges as k^{-4} for small k can be ascribed to thermal (i.e. equilibrium) fluctuations, provided a vanishingly small surface tension ν. This is, essentially, the conclusion of [22].

However, in the early nineties, the amplitude of membrane fluctuations in red blood cell was found to depend significantly on the concentration of adenosine triphosphate (ATP) [23]. ATP is the fuel of the active biological processes

executed by all the proteins which populate the cell membrane. By consuming ATP, these proteins operate far from thermodynamic equilibrium. Even from a purely theoretical point of view, as pointed out in [24], the k^{-4} dependence does not rule out the possibility of an athermal origin of membrane fluctuations. In fact, the addition of an *active* term proportional to k^{-4}, whose origin can be easily credited to a wealth of proteic activities, would not only enhance the amplitude of fluctuations in the tensionless $\nu = 0$ case, but also overshadow any non-vanishing surface tension, in the long wavelength limit $k \to 0$.

$$\frac{k_B T}{\nu k^2 + \kappa k^4} + \frac{A_{active}}{k^4} \xrightarrow{k \to 0} \frac{A_{active}}{k^4}. \tag{1.5}$$

Evidence in favour of the active nature of membrane fluctuations came only a few years later, with the experiment of J.-B. Manneville *et al.* on giant vescicles [25]. Specifically, the authors measured the coefficient of k^{-4} in the structure factor, and found it twice as large as the $k_B T/\kappa$ predicted by the equilibrium theory. For red blood cell flickering, instead, the smoking gun came as late as 2016 [26], with an experiment based on proving violations of the Fluctuation-Dissipation Theorem (FDT), the signature of equilibrium fluctuations.

The other most representative instance of active interface is the *leading edge*, to which the model studied in this thesis is inspired. The phrase "leading edge" is used in the literature to refer to the advancing front of an eukaryotic cell when crawling on a two-dimensional substrate. The first attempt towards a theoretical understanding of cell motility dates back to 1993, when C. Peskin *et al.* published their seminal paper [27]. The authors proposed a mechanism—they called it Brownian Ratchet—for protrusive forces generation by actin polymerisation. Cytoskeletal actin had already been confirmed to be one of the main actors in the play of cell dynamics, and Peskin & coworkers showed how intercalation of actin monomers between a rigid filament and a fluctuating membrane rectifies the membrane fluctuations. The Brownian Ratchet concept was further developed, mainly by A. Mogilner and G. Oster [28, 29], in subsequent years, in order to match the increasingly accurate experimental observations. In the ensuing picture, actin filaments impinge on the membrane at an angle, so that their bending energy provides an additional fluctuating mode to be ratcheted by polymerisation. Details removed, the dynamics of the leading edge does not seem to be profoundly different from that of a stable phase (the actin filaments network) invading a medium, which in turn is described by the KPZ equation.

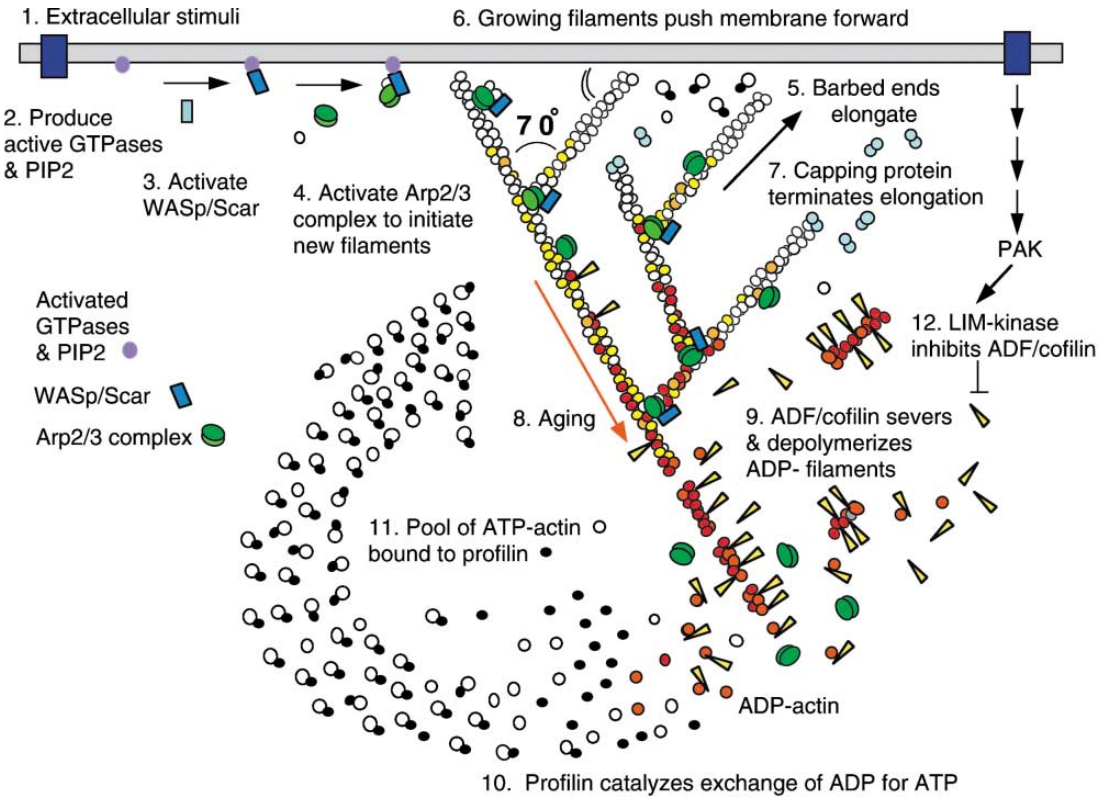

Figure 1.2 *Pictorial representation of the dendritic-nucleation model for lamellipodial protrusion of the leading edge, from [7].*

While the ratchet mechanism allows for conversion of polarisation affinity into protrusion of the leading edge, additional proteins are needed *in vivo* to achieve various practical tasks. Building the cytoskeletal network, so that filaments do not buckle under the membrane's load; promoting filament disassembly at the rear, so as to replenish the pool of monomers needed for polymerisation; focusing polymerisation on a few selected filaments, so as to avoid a rapid depletion of the monomers pool—these are all valid examples of tasks to be accomplished, and are all included in the dendritic-nucleation model [7, 30] sketched in Fig. 1.2. Signalling molecules living at the membrane conduct the orchestra of cell locomotion: most likely, this complex machinery is responsible for the high responsivity of the cell to variations in the pattern of external stimuli. Furthermore, as the tight regulation is achieved through complex feedback loops, the leading edge dynamics generates spatiotemporal patterns which the simple picture of the stable phase invading a medium fails to capture.

To sum up, the example of flickering shows that the difference between passive (as opposed to active) and active interfaces is *quantitative*, in that their properties can be predicted by similar models with different numbers. The example of the

leading edge shows that the difference is also *qualitative*: new features emerge which cannot be predicted by augmenting old models with new parameters. Based upon this very observation, several authors followed [24] in developing a theory of active membranes [31–33] by including "active stresses" into the hydrodynamic theory of fluid membranes [34, 35]. From a theoretical perspective, the difference between active stresses and external driving forces lies in the impossibility of deriving the former by coupling the system with some external, possibly unbounded potential—a reflection of the fact that active forces arise from the system's constituents. While the goal of this thesis is similar to that of the general active membranes literature, the approach is different. Namely, I will start from the simple models typical of the theory of kinetic roughening, and add one more ingredient to the description: an active interface moves due to the action of "activators" akin to the signalling molecules operating at the leading edge, rather than being driven by a uniform external fields as in the KPZ model. Such an approach explores the possibility that the complex scenario of active interface stems from the activated (and regulated) nature of their motion. The following subsection comprises all the notions upon which the active interface model is built.

1.2.1 A few more facts from cell biology

This section is aimed at *i)* introducing the "activators" mentioned in the last paragraph; *ii)* understanding their coupling with the membrane dynamics; *iii)* looking at some of the results of such a coupling. The content of the section is basic Biology, and can be found in every Biology degree website or classic books such as [36]. The regulatory pathways which link activators and membrane dynamics are reviewed in [37–39].

Any discussion about cell dynamics must include the cytoskeleton: the physical scaffolding which, by sustaining the membrane, gives the cell its shape. The cytoskeleton principal components are microtubules and actin filaments: the former maintain the structure and are involved intracellular transport, while the latter are responsible for movement. Crawling, for instance, as mentioned in section 1.2, is driven by actin polymerisation just below the leading edge. It is worth noticing that additional steps are required for the displacement of the whole cell, such as adhesion to the substrate and retraction of the back, but these are not as critical as actin polymerisation for the dynamics of the leading edge.

Actin is found in filaments about $7nm$ in diameter and up to $1\mu m$ long. The polymerisation rate at one end of the filament (+ end, or barbed end) exceeds that at the other end (- end, or pointed end), so that each filament is polar. As a result, under the right concentration, free actin monomers will be constantly removed from the - end and added to the + end—this is the phenomenon of actin treadmilling. As filaments are oriented with the + ends towards the membrane, treadmilling pushes the leading edge forward by ratcheting the membrane and the filaments fluctuations. The Brownian ratchet alone, however, cannot account for the speed measured *in vivo* [7]: additional proteins are required to accelerate the process.

Some proteins, such as Profilin and Cofilin, accelerate treadmilling of single filaments: they do so by favouring polymerisation at the front and severing filaments at the rear, respectively (cf. Fig. 1.2, steps 9 to 11). Together with capping proteins that stop some filaments from growing (step 7 of the figure), their action maintains the concentration of free monomer at the level required, thus controlling the speed of polymerisation. Other proteins, instead, enhance treadmilling by organising filaments in larger structures, such as the *lamellipodium* shown in Fig. 1.2. The lamellipodium is initiated by a complex of seven proteins called Arp2/3 (Actin-Related-Proteins). Arp2/3 binds to the side of an existing filaments and nucleates a branch at $\sim$ 70 degrees (step 4 of the figure), thus forming an orthogonal mesh. The latter mesh is stabilised by a cross-linking protein called Filamin. The actin network found in lamellipodia prevents filaments from buckling, so that they can sustain a protrusion for longer than when parallel.

If Arp2/3 and Filamin organise the filaments in a stable, orthogonal network, Fascin and Formin bind filaments in parallel bundles called *filopodia*. Filopodia sense the external environment while the lamellipodium propels the cell across a substrate. The "decision" on the structure to form occurs via complex pathways aimed at transducing extracellular stimuli into the activation of nucleation-promoting factors such as Arp2/3 and Formin (cf. Fig. 1.2, steps 1 to 4). The directors of such processes are small signalling proteins which, when active, are bound to the plasma membrane. As they regulate the actin dynamics depending on the cell requirements, these membrane proteins have been all collected in a single family called Rho. Rho proteins are thus the "activators" which steer the membrane dynamics: Rac, for instance, is responsible for lamellipodial protrusion, whereas Cdc42 initiates most of filopodia.

Importantly, the coupling is bidirectional: due to the BAR-domain (a banana-shaped dimer which is found to either bind to or recruit members of the Rho family) Rho proteins acquire an intrinsic curvature which interact with the membrane's one [40, 41]. The bidirectional coupling embodies the membrane with feedback loops which, in turn, generate patterns in the membrane profile and protein density. Such patterns, which include travelling nanoclusters and ripple waves, have attracted the interest of experimentalists and theoreticians alike [42–45]. These patterns are indeed measurable characteristics which can be both looked for in experiments and predicted by theoretical descriptions of the leading edge. One of the main features of the model of chapter 2 is the interpretation of such patterns in terms of active growth and the ensuing relation of the patterns' features to other measurable quantities such as the speed of the leading edge and the total density of activators.

1.3 Structure of the thesis

This section serves as an extended table of contents for the chapters to come. The aim of all these is that of establishing a description of active interface within the framework of kinetic roughening. Specifically, I will start from an idealised stochastic model which is similar, in spirit, to the Eden model of section 1.1 (Fig. 1.1); then extract field equations which, as the KPZ equation does for growing interfaces, capture the "universal" features of active interfaces.

Chapter 2, titled "Building a toy active interface", introduces the lattice model. In simple terms, the model is based on the assumption that the motion of the leasing edge is controlled by the density of activators, i.e. steps 1 and 6 of the dendritic-nucleation model of Fig. 1.2. The resulting process extends the asymmetric exclusion process (a lattice gas which can also represent a moving interface belonging to the KPZ universality class) by coupling it to a system of activators inspired by the signalling molecules of subsection 1.2.1. The model is defined in detail in section 2.1. A special attention is devoted to two particular parameters: one describing the bias of the interface dynamics due to the activators' action, the other the effect of the interface shape on the activators' displacement. The model is tested in section 2.2, which considers a single activator coupled to the interface. The main purpose of the test is that of defining the relevant observables for the particles and interface dynamics and starting to familiarise with the active interface physics. Finally, in section 2.3,

I will discuss the dynamics of an interface coupled with a macroscopic number of activators. The emphasis is placed on the phenomena which resemble those seen in experimental studies of biological interfaces. The scaling laws obeyed by the active interface model are also discussed in this section. Most of the results shown in chapter 2 are published in [1, 2].

Chapter 3, "The active interface equations", deals with the hydrodynamic limit of the lattice model defined in the previous chapter. The actual limit is performed in section 3.1, which begins with some exact results on the steady-state probability measure reached by the stochastic active interface. These results, obtained for special values of the model parameters, are required in order to derive an exact, large-scale and long-time description of the lattice model in terms of field equations. Section 3.2 outlines the solution of a particular limit of the field equations—the *inviscid* limit. This limit is, potentially, the most relevant for the description of the leading edge dynamics and will be considered again in chapter 4. In section 3.3, the solution of section 3.2 is used to provide analytical foundations to the results on the active interface steady state shown in section 2.3. In addition, a slightly modified version of the equations derived in section 3.1 can explain some of the features of the test-particle problem of section 2.2. Except for this last aspect, all the results derived in this chapter are published in [3].

Finally, in chapter 4 "Large-scale dynamics of active interfaces", the stochastic field equations of chapter 3 are genreralised and studied with the tools of the renormalisation group. The generalisation is discussed in section 4.1, where field equations similar to those of the previous chapter a derived in general spatial dimension. The derivation combines heuristic considerations with symmetry arguments. This section also introduces the formulation of the model in terms of an action functional—the *Janssen-DeDominicis* action—which is required in the following sections, and the generalities of perturbation theory. Section 4.2 consists of a detailed account of the linearised, or *Gaussian*, active interface model, which is obtained from an harmonic approximation of the aforementioned action. In particular, this section provides the mean-field phase diagram of the model: the latter comprises a phase which describes the leading edge of motile cells (discussed in section 2.3 from the lattice model perspective), a phase corresponding to activators running up interfacial slopes (not discussed in this thesis) and two critical lines. The two critical lines meet at a bi-critical point, representing a model where an ensemble of passive particles is advected by the slopes of a KPZ interface. Renormalisation of this model is carried in section 4.3.

Chapter 2

Building a toy active interface

This chapter introduces the lattice model of an active interface, consisting of a fluctuating interface coupled to a number of activators which stimulate its growth. As biological systems operate generically around room temperature[1], active interfaces are naturally studied with the tools of soft matter physics. The work of Cai and Lubensky on (passive) fluid membranes ([34, 35]) provides a prototype of the recipe to follow: first identify the conserved quantities of the problem; then infer dynamical equations by applying the rules of mechanics—Newtonian, Stokesian, even quantum or relativistic if required. The generalisation to active membranes does not pose any conceptual difficulty, as it suffices to include the thermodynamic forces generated by energy-consuming reactions in the conservation laws [33].

Nevertheless, the active generalisation adds an additional layer of complexity to hydrodynamic equations which are already too complex to be solved: a systematic approximation scheme is required. The authors of [34, 35], for instance, resort to a renormalisation procedure, whereby the high-wavenumber and high-frequency modes of the interface fluctuations are integrated out of the equations of motion. The integration produces effective equations for the remaining modes, i.e. those which vary slowly in space and time, with the eliminated modes appearing only as corrections to the original parameters. Nonlinear terms, especially, by coupling modes with different wavenumbers, produce nontrivial corrections. To sum up, a complex model has been re-written as a simplified model with renormalised

[1] The known upper and lower limits are $-20°C$ and $122°C$, both achieved by the nucleus-less prokaryotes *archaea*. The interval is halved for eukaryotes, which are not able to complete their life cycle for temperatures higher than $60°C$ or lower than $-2°C$ [46].

coefficients.

The simplified description comes at the price of having lost spatial and temporal resolution, as the modes which have been integrated out are no longer accessible by the theory. In other words, the renormalised theory probes the large-scale and long-time properties of the system at hand. As scales stretch and times lengthen, all the irrelevant details disappear from the theory and a few scaling laws, such as the structure factor divergence at small wavenumbers of section 1.2 and the (equivalent) Family-Vicsek scaling of section 1.1, identify the system's physics. This emerging universality brings the original, complex theory into question, as one wonders whether the aforementioned irrelevant details could have been neglected from the very beginning.

The answer is yes for a remarkably large number of systems, as confirmed by the success of idealised lattice models in statistical mechanics. Our understanding of phase transitions, for instance, would be far more primitive if it were based on a detailed theory of ferromagnetic materials rather than the Ising model [47]. In addition, the methods developed for studying order phenomena in simple systems, such as the Ising model, can be generalised to more complex forms of matter: so significant an observation that it granted de Gennes the Nobel prize in 1991. Lattice models, in particular, are adopted in various contexts—some of them reproduce the real system so faithfully that they are used in place of the full equations even for engineering applications [48].

The programme of this chapter is that of defining a lattice model inspired by the facts listed in subsection 1.2.1. The interface, in this chapter, is a line moving in a two-dimensional space—a so-called (1+1)-dimensional model—but generalisation to higher dimensions is straightforward. There are several advantages of a discrete description: first, above all, the dynamics of a (stochastic) lattice model can be easily and rapidly simulated with Monte Carlo techniques; secondly (and equally importantly) it might provide analytical insight on the full problem via exact results; thirdly, coarse-graining methods allow one to infer field equations for the conserved low-frequency/wavenumber modes of the model. The equations can then be compared to those derived from first principles [33] for an *a posteriori* validation of the assumptions made at the lattice scale. This last point will be explored in greater detail in chapter 3 and chapter 4. The model is defined in the following section, section 2.1. Section 2.2 and section 2.3, instead, illustrate the dynamics of our toy active interface with one activator or many, respectively.

2.1 From facts to the lattice description

The lattice active interface consists of three elements: the interface, the particles and the interactions between the two. Recalling the discussion of chapter 1, the interface represents the plasma membrane. The latter is actually a bilayer, but its thickness (a few nm) is much smaller than the cell size (tens of μm for eukaryotes). Regarding many of its properties, the membrane can then be considered as a single sheet. The particles are membrane proteins, in particular those which are responsible for the regulation of cell locomotion, such as the members of the Rho family introduced in subsection 1.2.1. As in the previous chapter, I will call them *activators*. The interactions are built to take into account the activated nature of growth: referring to Fig. 1.2, the goal of the model is to reproduce steps 1 to 6 while keeping the level of detail minimal. Let us begin with the interface model, then follow with the activators. The full active interface dynamics is reviewed at the end of the section.

2.1.1 The discrete interface

Our discrete interface, as in Fig. 2.1, is a system of L microscopic slopes, either positive ($/$) or negative ($\backslash$). By joining consecutive slopes one obtains the interface profile, which can be defined with a set of heights $\{h_i\}_{i=0,\dots,L}$ above the nodes of a 1D lattice. As periodic boundary conditions (PBC) are enforced, the 1D lattice is in fact a ring lattice with the L-th site coinciding with the 0-th site, i.e. $h_0 = h_L$. By construction, the interface satisfies the condition $|h_{i+1} - h_i| = 1$ $\forall i = 0, \dots, L$—the *single-step* condition [49, 50]—and it resembles the graph of a random walker. Moreover, the interface sites i can be split into slopes (either $h_{i-1} > h_i > h_{i+1}$ or $h_{i-1} < h_i < h_{i+1}$), *peaks* ($\wedge$, i.e. $h_i > h_{i-1}, h_{i+1}$) and *troughs* ($\vee$, i.e. $h_i < h_{i-1}, h_{i+1}$). Peaks and troughs can be generically referred to as *corners*.

This discretisation was introduced in [49, 50] as a candidate simple representation of both the EW and KPZ universality classes. The construction of the interface is sketched in Fig. 2.1. As in the figure, one starts with an arbitrary height h_0 above the 0-th lattice site, then add $+1$ or -1, according to whether the microscopic slope is positive or negative, respectively. In the figure's left-hand side, for instance, the first few slopes are all negative, hence $h_1 = h_0 - 1$ and

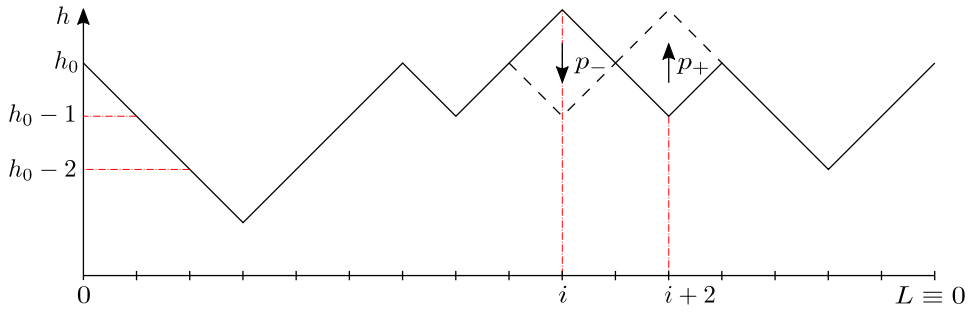

Figure 2.1 *Details of the single-step model: the height variables* $\{h_i\}_{i=0,\dots,L}$ *equal the distance of the interface (black broken line) from a reference horizontal axis (horizontal ticked line), as highlighted by the vertical dot-dashed lines on sites* i *and* $i+2$*; the dynamics comprises* $\wedge \to \vee$ *and* $\vee \to \wedge$ *transitions, with respective rates* p_- *and* p_+*. The two possible transitions on sites* i *and* $i+2$ *are shown as black dashed lines.*

$h_2 = h_1 - 1 = h_0 - 2$. On the opposite side of the figure, the dynamics which sets the interface in motion is depicted. The latter dynamics occurs at the interface corners [2]: when a given site is a trough (such as the $i+2$-th site in the figure), it can transform into a peak, i.e. $\vee \to \wedge$, with rate p_+. Consequently, the height of the site increases by 2 units. When the given site is a peak (such as the i-th site in the figure), it can transform into a trough, i.e. $\wedge \to \vee$, with rate p_-. The height, in this case, decreases by 2 units.

In the general case, the rates p_+ and p_- depend on the lattice coordinate. If they do not, the difference $p_+ - p_-$ can be perceived as an external force which drives the interface motion in a viscous environment. Tests of the Family-Vicsek scaling relations place this model in the KPZ universality class [49, 50] (cf. section 2.2). In particular, the continuum limit of the set of height variables $\{h_i\}_{i=0,\dots,L}$ can be shown to obey the one-dimensional KPZ equation [51] (reproduced here for clarity)

$$\frac{\partial h}{\partial t} = \lambda \left(\frac{\partial h}{\partial x} \right)^2 + \frac{\partial^2 h}{\partial x^2} + \eta, \tag{2.1}$$

where the coefficient of the nonlinear term λ is proportional to $-(p_+ - p_-)$—we will come back to this point int chapter 3. Notably, the model's scope includes the EW universality class as an equilibrium limit $p_+ = p_-$. This is the equilibrium limit because the external driving force $(p_+ - p_-)$ vanishes: on the formal side, for such a choice of rates the interface dynamics satisfies *detailed balance* with respect to the uniform measure, i.e. the measure which assigns the same probability to

[2] whence the name *corner-growth* by which the model is sometimes referred to.

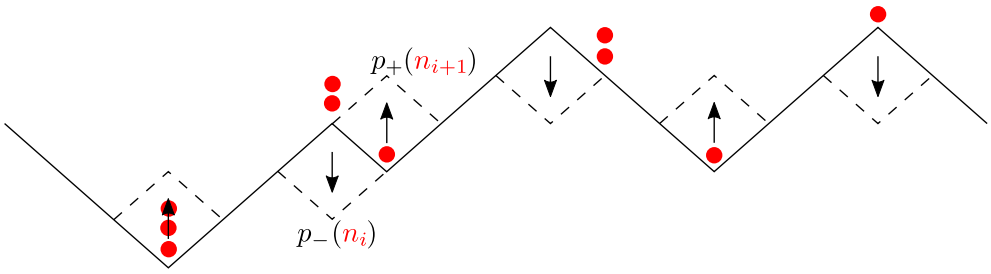

Figure 2.2 *Schematic representation of the discrete active interface: with respect to Fig. 2.1, the corner-flip rates depend on the local number of activators, represented here as red disks.*

each interface configuration which satisfies PBC. By calling $P(h_0, \ldots, h_{L-1})$ the probability of the interface configuration $(h_0, \ldots, h_{L-1})$, the condition of detailed balance can be written as

$$P(h_0, \ldots, h_i, \ldots, h_{L-1})p_+ = P(h_0, \ldots, h_i + 2, \ldots, h_{L-1})p_- \tag{2.2}$$

and is trivially satisfied by a uniform probability in the $p_+ = p_-$ limit.

In the active interface model introduced in [1], p_+ and p_- do depend on the lattice site and the difference $p_+ - p_-$ is proportional to the number of activators,

$$p_+(i) - p_-(i) = \lambda n_i, \tag{2.3}$$

where n_i denotes the number of activators at the i-th site, for $i = 0, \ldots, L$. The activators can be considered as additional particles living on the ring lattice, as is represented pictorially in Fig. 2.2. The parameter λ measures the local interface velocity due to a single activator: Eq. (2.3) assumes implicitly that the velocities caused by different activators sitting at the same site add linearly. Let us stress that for all those sites with no activators, i.e. i such that $n_i = 0$, the condition of detailed balance of Eq. (2.2) is restored. Thus, the activators are both setting the interface in motion and causing its departure from thermodynamic equilibrium. As the activators conduct the exertion of forces on the interface, the departure from equilibrium occurs at the microscales, hence our interface can be considered an active system.

2.1.2 Sliding activators

As stated at the beginning of the chapter, our active interface model assumes the interface thickness to be of no relevance for its motion. However, the finite thickness of the plasma membrane is essential for the dynamics of membrane proteins: whether they are partially or completely embedded in the interface, the fluid environment within the bilayer will cause the membrane proteins (and, among them, our activators) to diffuse laterally. The lateral diffusion of membrane proteins is, in fact, still an open problem, reviewed in [52]. It is widely accepted that thermal fluctuations of the membrane fluid alone cannot account for the diffusion coefficients measured by experiments, as several other factors such as geometrical and mechanical couplings of various sorts contribute to the protein's diffusion.

What matters for the present discussion is that membrane proteins do diffuse, and so do the activators considered in the active interface model. The simplest way of incorporating diffusion in the lattice model consists in letting the activators hop independently between the sites of the lattice, as a one-dimensional discrete *random walk*. Consider, for concreteness, an activator sitting on the i-th site of the lattice as in panel A of Fig. 2.3. The activator hops to the neighbouring site $i+1$ at some rate q, or to the other neighbouring site $i-1$ at the same rate. Once it has moved to a new site, the activator can hop again to the left or to the right with the same rate. Let us define the displacement d as $d = a$ for right hops, $d = -a$ for left hops, with a the lattice spacing. At each step, the squared displacement d^2 equals a^2. As movement happens at rate q, the diffusion coefficient (average square displacement per unit time) equals qa^2.

The diffusive hopping motion can be easily adapted to include the coupling with the interface curvature discussed in subsection 1.2.1. The coupling is summarised pictorially in panel B of Fig. 2.3. By binding to a specific curved domain, activators acquire an intrinsic curvature—they resemble the lampshade-like objects of Fig. 2.3. Curved activators have an affinity for interface sites with a matching curvature, which can be modelled by resorting to the principle of detailed balance (as in Eq. (2.2)). Specifically, the activators hopping rates are built so as to satisfy detailed balance with respect to a Gibbs measure $p(i) \propto e^{-\beta E(i)}$, with an energy $E(i)$ proportional to the interface curvature, i.e.

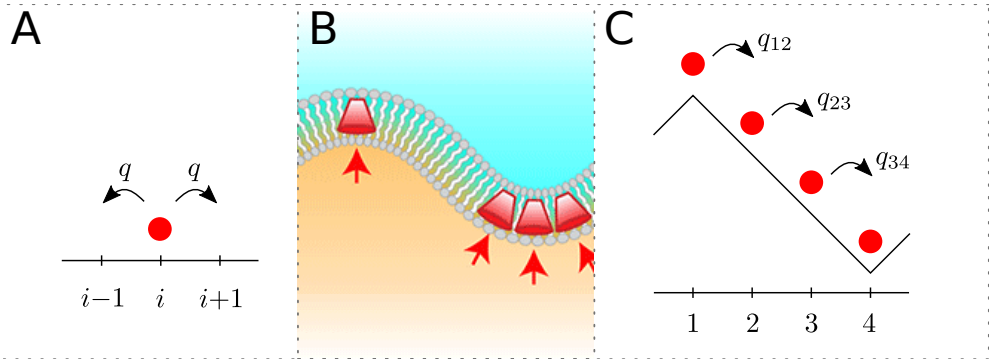

Figure 2.3 *Details of the activators motion. A) Normal diffusion is obtained by symmetric hopping on the lattice with rate q. B) The shape of the activators gives them a spontaneous curvature, thus coupling them with the curvature of the interface (from [8], credits to* APS/Alan Stonebraker*). C) Once activators are coupled with the curvature, the hopping rates depend on the local interface shape. Site 1 is a peak (negative curvature) while site 2 is a trough (positive curvature): if the activators favour positive curvatures as in panel B, $q_{12} > q_{21}$ and $q_{34} > q_{43}$.*

$E(i) = \epsilon\,(h_{i+1} + h_{i-1} - 2h_i)$. Namely,

$$q\,(i \to i+1)\,e^{-\beta E(i)} = e^{-\beta E(i+1)} q\,(i+1 \to i)\,, \tag{2.4}$$

$q\,(i \to j)$ denoting the hopping rate from the i-th to the j-th site. In minimising the curvature-energy $E(i)$, each activator will be attracted by sites with positive (negative) curvature for $\epsilon = -1$ ($\epsilon = +1$).

The curvature coupling is summarised pictorially in Fig. 2.3, panel C. It is worth remarking that the curvature energy should affect the interface dynamics too. In fact, by Newton's third law, each activator should cause a change in the interface curvature tantamount to the change in the activator position caused by the interface curvature. However, a coupling of this kind, which increases the likelihood of a site with high number of activators being a trough, is opposite to the active growth mechanism, which increases the rate of the $\vee \to \wedge$ transition by λ for each activator sitting on the site (cf. Eq. (2.3)). By assuming the active growth to be the dominant process, I will momentarily neglect the possibility that activators impose a given curvature on the interface. Nevertheless, a curvature-coupling term will appear in the field equations discussed in chapter 4, though as an irrelevant coupling for most of the parameters choices. Crucially, the active growth mechanism generates a kinematic coupling between the activators motion and interface slopes, whose effects shade the interaction with the curvature

implied by Eq. (2.4). This kinematic coupling arises for passive fluid membranes too, as explained in [34, 35].

The coupling with the slope can be rationalised with the following geometric argument. Consider, for simplicity, a one-dimensional interface described by an height function $h(x)$ as in Fig. 2.4. Any growth force that sets the interface in motion is exerted along the normal direction: this is true for both passive and active interfaces and widely regarded as the source of the nonlinear term in the KPZ equation. Think, for instance, of the picture of a stable phase invading a medium: the phase boundary will propagate along the local normal to the boundary (cf. Fig. 2.4, panel A). Consider now the activator shown in Fig. 2.4, panel B, sitting at the point $(x, y = h(x))$ of a certain reference frame. At x, in correspondence with the activator, there is an applied growth force whose direction is that of the local normal: the $\hat{y}$ component, $\hat{y}$ representing the vertical direction, will cause a shift in the interface height, while the $\hat{x}$ component, with $\hat{x}$ the horizontal direction, effectively pushes the fluid inside the membrane down the slope together with the activator. Therefore, particles residing on a moving interface are effectively advected by the slopes of the interface, with the sign of the advection depending on the average direction of motion of the interface. The activators' hop rates can be defined so as to mimic this effect, i.e.

$$q\left(i \to i \pm 1\right) = \begin{cases} q_+, & \text{if } h_{i\pm1} < h_i, \\ q_-, & \text{if } h_{i\pm1} > h_i. \end{cases} \tag{2.5}$$

That is, a different rate according to whether the destination site is at a lower or greater height than the departure site, as in panel C of Fig. 2.4. In analogy with Eq. (2.3), the hopping rates q_+ and q_- of the active interface model [1] are set so as to satisfy

$$q_+ - q_- = \gamma \left|h_i - h_{i+1}\right| = \gamma, \tag{2.6}$$

with γ the activators displacement per unit slope. Due to the nature of the slope-coupling, γ should have the same sign as the interface velocity $p_+ - p_-$.

2.1.3 The active interface model

Let us summarise the model described in the previous two subsections. It consists of a discrete interface, made of L unit-slope segments, and a collection of N activators. Both the interface and the activators live on the 1D lattice, with

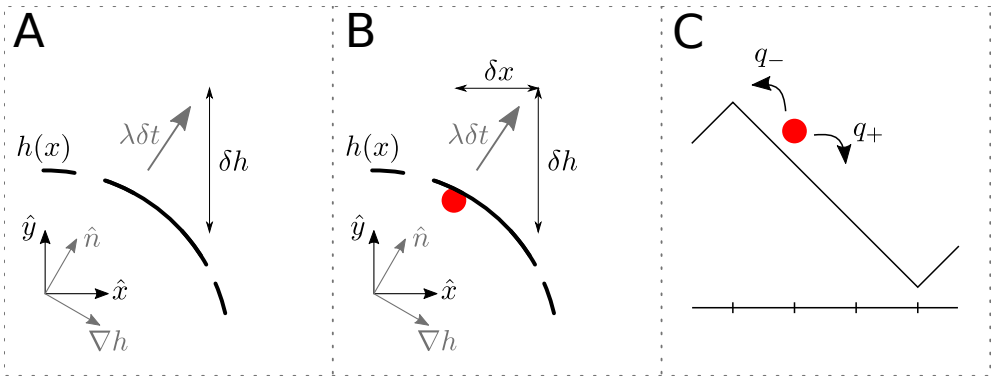

Figure 2.4 *Slope coupling arising from normal growth. Panel A displays a curved interface (black solid line) h(x), with the x and y axis of the frame of reference shown in black at the bottom left corner of the panel. The interface is being driven by an infinitesimal force λδt in the direction of the local normal, with the local normal/local tangent reference frame shown in grey in the bottom left corner. As growth occurs along the local normal, the interface displacement is δh along the y axis. Panel B shows the same scenario for an active interface being driven by a single activator (red disk). The normal force causes also a displacement δx of the activator in the x direction. Panel C shows how the slope coupling is included in the model: the hopping rate for sliding down a slope is higher (or simply different, in general) than that of the reversed transition.*

PBC enforcing the ring topology. The lattice spacing is set to $a = l/L$, so that the ring circumference equals l. Being made of unitary slopes, the interface can be described with a set of height variables $\{h_i\}$ over the lattice points $i = 0, \ldots, L$ which obey the single-step condition $|h_{i+1} - h_i| = 1$. Each activator is represented by a discrete random walk hopping between neighbouring lattice sites. The activators dynamics is thus specified by two (site-dependent) hopping rates $q\,(i \to i \pm 1)$, which are defined as

$$q\,(i \to i \pm 1) = \begin{cases} q_+, & \text{if } h_{i\pm1} < h_i, \\ q_-, & \text{if } h_{i\pm1} > h_i, \end{cases} \qquad q_+ - q_- = \gamma. \tag{2.7}$$

According to Eq. (2.7), activators slide down negative slopes at rate q_+ and climb up positive slopes at rate q_-—the difference γ measures the rate of advection per unit slope. In addition, the left and right hopping rates coincide at $\gamma = 0$. One can thus define a (inverse) timescale q for the activators motion as

$$q \equiv q_+|_{\gamma=0} = q_-|_{\gamma=0}. \tag{2.8}$$

The interface, in turn, evolves according to the following, local dynamics. Due to the single-step condition, each site can be a peak ($\wedge$), a trough ($\vee$) or a slope ($\diagdown$ or $\diagup$). Troughs can grow and become peaks at rate p_+ whereas peaks become troughs at rate p_-, so that the single-step condition is preserved at all times. In order to account for the growth-stimulating action of the activators, the interface rates $p_\pm$ depend on the local number of activators n_i, such that

$$p_+(i) - p_-(i) = \lambda n_i. \tag{2.9}$$

According to Eq. (2.9), each activator increases the growth rate of the interface by λ. As no exlusion interaction is assumed, $n_i = 0, \ldots, N$. As in Eq. (2.8), a timescale p for the interface motion can be defined as

$$p \equiv p_+(i)|_{\lambda=0} = p_-(i)|_{\lambda=0}, \tag{2.10}$$

and is independent of the lattice site.

The stochastic dynamical rules prescribed by Eq. (2.7) and Eq. (2.9) can be simulated with a Monte Carlo algorithm. Both the interface transitions and the hops of the activators are Poisson processes, meaning that the number of transitions K occuring in a time interval Δt follows the Poisson distribution

$$\text{Prob.}\left\{K(\Delta t) = k\right\} = \frac{(w\Delta t)^k}{k!} e^{-w\Delta t} \tag{2.11}$$

w being the rate of the corresponding transition. The time t between two consecutive transitions, instead, is an exponential random variable with probability density function

$$p(t) = we^{-wt}. \tag{2.12}$$

Therefore, in order to simulate a Poisson process, one would have to draw a time from the exponential distribution above and perform the transition at that time.

There is, however, an approximate shortcut which is particularly useful when dealing with large systems where many transitions can happen simultaneously. Such a shortcut builds on the fact that a Poisson process describes events which are independent from one another and occur continuously in time. Upon discretising time with timestep δt small enough that at most one event can occur within it, the Poissonian probability of Eq. (2.11) becomes binomial,

$$P\left\{K(\delta t) = 1\right\} = w\delta t + O(\delta t^2), \quad P\left\{K(\delta t) = k\right\} \simeq 0 \quad \forall k > 1, \tag{2.13}$$

and the number of events occurring at different timesteps are independent from one another. As a result, after N trials such that $N\delta t = \Delta t$,

$$P\left\{K(\Delta t) = k\right\} = \binom{\Delta t/\delta t}{k} (w\delta t)^k \left(1 - w\delta t\right)^{\frac{\Delta t}{\delta t} - k}. \tag{2.14}$$

The accuracy of the approximation is controlled by the Poisson limit theorem, stating the convergence in distribution of the sequence of N binomial trials with probability $w\delta t$ to a Poisson process with parameter w in Δt, as $\delta t \to 0$ and $N \to \infty$ with $N\delta t = \Delta t$ finite.

Coming back to our Monte Carlo simulation, the system can be updated by performing, at every timestep, each of the allowed transitions with probability $w\delta t$, w being the rate of the corresponding transition, with δt much smaller that $1/w$. Alternatively, one can pick one of the possible transitions at random and perform it with probability w rather than $w\delta t$—this updating scheme is called *random-sequential*. Loosely speaking, the small factor δt is replaced by the probability $1/R$ of choosing a given transition among a pool of R with R large. For an active interface on a lattice of L sites with N activators, each step comprises (on average) N activator updates and rL interface updates, with r some positive factor, so that the total number of transitions R equals $N + rL$. In each of the $N+rL$ substeps, the updating routine picks an activator with probability N/R or an interface site with probability rL/R. If an activator is chosen, with is current location i, one of the neighbouring sites is chosen with equal probabilities (the $i+1$-th or the $i-1$-th) and the activator displaced with probability $q\left(i \to i \pm 1\right)$ from Eq. (2.7). If an interface site is chosen, the transition depends on its local curvature $C_i = h_{i+1} + h_{i-1} - 2h_i$: if $C_i > 0$, meaning i is a trough, the chosen site becomes a peak with probability $p_+(i)$; if $C_i < 0$, meaning i is a peak, the site becomes a trough with probability $p_-(i)$; nothing happens if the local curvature vanishes. A particular value of the ratio p/q can be selected by tuning r.

2.2 Dynamics of a "test" activator: numerical results

This section describes the dynamics of a single activator on the interface [2]. I refer to it, with a light abuse of notation, as a *test* activator: the purpose is that of testing the active interface model but, unlike the usual test particles

considered in problems of gravitation or electrostatics, this test particle influences the interface dynamics by enhancing the growth rate p_+. In a true test particle setting the activator would only slide over the interface profile without affecting the interface, i.e. $\gamma \neq 0$ and $\lambda = 0$. The resulting dynamics can be thought of as an idealised representation of the problem of passive scalar advection, where one or more passive tracers are coupled to a generally far-from-equilibrium medium. Such a system is realised, for instance, when fluorescent dyes are used to highlight turbulent flow in a fluid [53], with passive particles sliding down a fluctuating potential landscape [54–56], or with a so-called second class particle, whose dynamics is designed to locate shocks in driven diffusive systems [57]. The particles of all these problems can be considered *passive*, in the sense that they do not affect the dynamics of the medium they are moving in.

By contrast, our test particle is *active* and does affect the dynamics of the medium, namely the interface. The resulting phenomenology depends on the relative timescales of interface and activator motion. In a first regime, realised when the activator diffusion is faster with respect to the interface relaxation, the process resembles *metadynamics*, a method of computational physics aimed at easing the sampling of complex free energy landscapes [58]. If the interface is faster than the activator, instead, an intriguing *surfing* regime emerges whereby the interface bump created by the activator travels ballistically and pushes the activator itself forward. Lastly, for an infinitely fast interface dynamics, the activator is unable to perform its sliding motion and the problem reduces to that of a passive interface with a defect.

The presentation follows that of [1]: it begins with definitions of the observables of interest and a discussion their expected behaviour, and progresses with the analysis of the three dynamical regimes. The rates, throughout this section, are set to the following values:

$$q_\pm = q\left(1 \pm \gamma\right), \gamma = 1; \quad p_\pm = p\left(1 \pm \lambda n_i\right), \lambda = 1. \tag{2.15}$$

This is the maximal choice of λ and γ compatible with the requirement that all the probabilities of the Monte Carlo algorithm lie in $[0, 1]$: it will allow us to avoid extended crossovers from the passive limits $\lambda = 0$ and $\gamma = 0$ and to explore the effect of varying $r = p/q$.

2.2.1 Observables and scaling

As the system at hand is made of two components (activator and interface), each pushing the other far from equilibrium, it is natural to characterise the dynamical and statistical properties of each component.

Most of the global statistical properties of the interface, as in the theory of kinetic roughening, can be discerned from its first two moments [59], the mean height $\overline{h} = L^{-1}\sum_{i=1}^{L} h_i$ and the squared width $W^2 = L^{-1}\sum_{i=1}^{L}\left(h_i - \overline{h}\right)^2$. Notice that both $\overline{h}$ and W^2 are stochastic variables, as are the h_i's. In a typical numerical experiment, an initially flat interface, i.e. $h_i = 0$ for even i's and $h_i = 1$ for odd i's, is allowed to evolve according to the prescribed stochastic dynamics. Repeating the experiment with different random numbers generates a different *realisation* of the dynamics and the interface properties can be averaged over many realisations. I denote the ensemble-averaged width by lower case w, i.e.

$$w(L,t) = \sqrt{\langle W^2 \rangle} = \sqrt{\frac{1}{L}\left\langle \sum_{i=1}^{L}\left(h_i - \overline{h}\right)^2 \right\rangle} \tag{2.16}$$

As was mentioned in the introduction, $w(L,t)$ is expected to follow the Family-Vicsek scaling hypothesis [16],

$$w(L,t) = L^{\alpha} f(t/L^{z_1}), \tag{2.17}$$

where α and z_1 are the roughness and dynamic exponent of the interface, respectively, whereas the scaling function f behaves as a power law for small arguments and a constant for large ones. The width grows in time as a power law $\sim t^{\beta}$ until, at a time $t \sim L^{z_1}$, it saturates due to the finite size of the interface. According to Eq. (2.17), the saturation value scales with the size as L^{α}, while, in order to cancel any system size dependence at short times $t \ll L^{z_1}$, $f(y)$ must behave as y^{α/z_1} for small y, which implies that the initial growth exponent obeys $\beta = \alpha/z_1$.

Following this line of thought, the activator dynamics can be analysed by looking at the first two moments of the displacement X_t. As, in this section, there is only one activator, averages will be performed over several realisations of the stochastic dynamics. In section 2.3, instead, the activator properties will be averaged over all the activators in the system as well. Contrary to the height first moment, the

average displacement of the activator is identically zero, as nothing breaks the left-right symmetry of averages (we will see though that such symmetry is broken at the level of individual trajectories). The mean squared displacement, however, obeys a scaling form akin to that of Eq. (2.17),

$$\left\langle X_t^2 \right\rangle = tL^{\chi} g(t/L^{z_2}), \tag{2.18}$$

where z_2 is a dynamic exponent relating the time it takes for the activator to reach its steady-state behaviour to the system size. The form of Eq. (2.18) can be understood from the requirement that on large timescales, on a finite system ($t \gg L^{z_2}$), the motion of the activator becomes diffusive $\langle X_t^2 \rangle \sim t$. Thus, the scaling function g must be constant for large arguments, with χ specifying the system-size-dependence of the effective, long-time diffusion coefficient. On the other hand, the early-time behaviour should not depend on the system size, and the small argument behaviour of g is fixed by requiring the L's in Eq. (2.18) to cancel each other for $t \ll L^{z_2}$. With $g(y) \sim y^{\chi/z_2}$, one obtains the early times law

$$\left\langle X_t^2 \right\rangle \sim tL^{\chi} \left(\frac{t^{\chi/z_2}}{L^{\chi}} \right) \sim t^{\eta}, \tag{2.19}$$

where $\eta = 1 + \chi/z_2$. The scaling hypothesis Eq. (2.18) was proposed in [57] for a 'second class particle' which exhibits superdiffusive behaviour and was later used in related problems of Brownian particles passively coupled to time-dependent random environments [60–62].

Now, the theory of transport in random environment [63] states that the spatial correlations of a stochastic medium may give rise to anomalous diffusion of the particles living there. Then, one may write (for a system of infinite spatial extent)

$$\left\langle X_t^2 \right\rangle \sim t^{2/z_P} \tag{2.20}$$

where z_p is yet another dynamical exponent. z_p characterises the anomalous diffusion as follows: after time t the particle will have explored a distance $\langle X_t^2 \rangle^{1/2} \sim t^{1/z_P}$. Thus the particle should explore a finite system size L after time $t \sim L^{z_p}$. The value of z_p is not necessarily equal to that of z_2: demanding that the two dynamical exponents z_2 and z_p are indeed equal implies the scaling relation

$$\chi + z_2 = 2 \, . \tag{2.21}$$

Such a special condition can be perceived as the signature that no other

lengthscale than the system size affects the particle motion [60]. In fact, $\chi+z_2 = 2$ holds in the several "passive" versions of our model considered in the literature, such as the second class particle problem and that of a passive slider on a self-affine interface [57, 60, 64]. It appears, in addition, that also z_1 and z_2 can be identified with each other, at least in most of the problems mentioned in this section [3]. Consequently, one single dynamic exponent suffices to characterise all dynamical features of the system. This is not always the case in our active model, as will be clarified in the forthcoming section.

2.2.2 Fluctuating metadynamics at $r \leq 1$

Let us begin by setting $r = 1$, i.e. considering the case where activator and interface have the same bare mobility. On the $2\gamma = \lambda$ line of the phase diagram, that the steady-state interface is described exactly by Edwards-Wilkinson statistics (as will be seen in chapter 3). The numerics of Fig. 2.5 show indeed that $\alpha = 1/2$ and $z_1 = 2$—the roughness and dynamic exponents of the EW class [17]. With regard to the activator MSD, the numerics agree with the scaling form in Eq. (2.18), as is shown in Fig. 2.6. The exponents, $\chi = 1/2$ and $z_2 = 3/2$, appear to be the same as in the second class particle problem [57]. The second class problem describes a particle coupled to a driven diffusive system: due to the well-known mapping between the totally asymmetric simple exclusion process and a discrete interface model in the KPZ class (cf. chapter 3), this model can be obtained by setting $p^{\pm} = p(1 \pm \lambda)$ uniformly over the interface instead of on the activator's site only. The exponent $z_2 = 3/2$ of [57] mirrors the dynamic exponent of the (passive) interface and the value $\chi = 1/2$ is compatible with $z_P = z_2 = 3/2$, so that the scaling relation Eq. (2.21) is obeyed.

In our model, conversely, there is a mismatch between z_1 and z_2, i.e. the interface and activator dynamic exponents are not the same. A possible explanation for such a difference is the following. The exponent z_1 refers to the saturation of a global interfacial variable such as the width: it is reasonable to expect a single activator not to dramatically alter its properties. The interface dynamics is thus dominated by the up/down-symmetric growth events away from the activator, resulting in $z_1 = 2$. The value of z_2, on the other hand, is related to the early-time superdiffusive behaviour of the activator (Eq. (2.19)). Such behaviour is triggered

[3] The only exception seems to be the "KPZ anti-advection" case, as hinted in [56] and suggested by the numerics in [65].

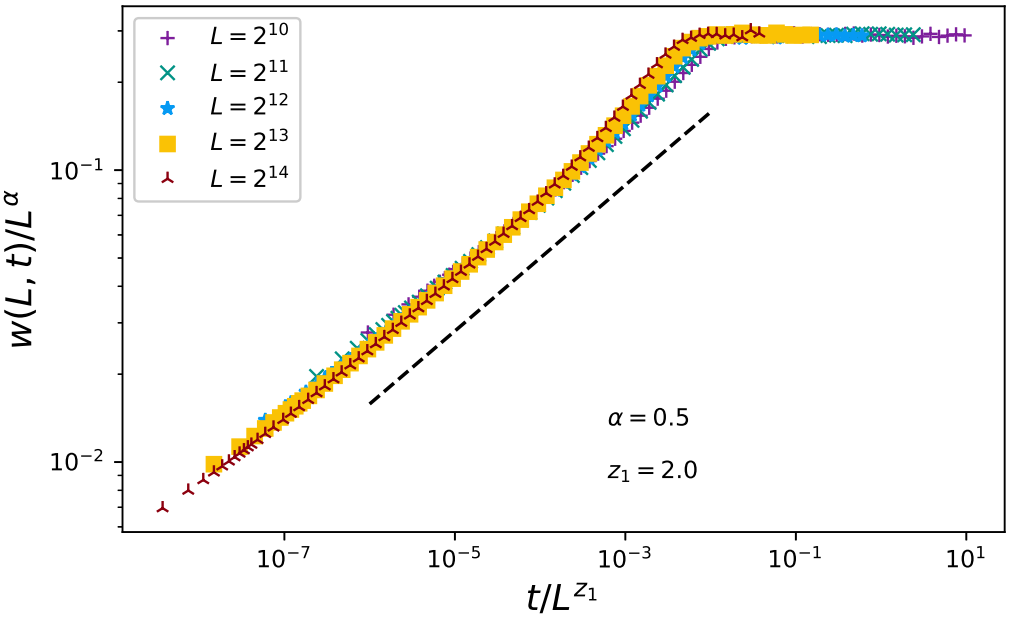

Figure 2.5 *Scaling of the averaged width for $r = 1$, $\gamma = \lambda = 1$, with system size L as in the key. The best collapse is achieved by setting the exponents to the EW class values. A power law x^{α/z_1} is shown as a guide to the eye (black dashed line). The interface width has been averaged over 10^3 realisations of the stochastic dynamics. The number of realisations used for averages is the same in all the figures of this section unless otherwise stated.*

by the local environment around the activator rather than the instantaneous global structure. Here, owing to the activator itself, the up/down symmetry of fluctuations is broken and the dynamic exponent 3/2 is plausible.

In order to corroborate the idea that the activator experiences a different dynamic exponent to that of the interface as a whole, Fig. 2.7 shows the spatial spreading of correlations from the activator's site. Imagine pinning the activator on a site k by setting $q_+ = q_- = 0$ while still allowing it to catalyse the interface growth, then let the interface evolve and measure the slope correlation function

$$C_s(j,t) = \langle (h_{k+1}(t) - h_k(t))\,(h_{k+j+1}(t) - h_{k+j}(t)) \rangle$$

at different times. Due to the left-right symmetry, measurements are limited to the half of the interface on the activator's right-hand side. The data collapse of Fig. 2.7 provides evidence that around the activator the correlation length grows, at least for relatively short times, as t^{1/z_2} with $z_2 = 3/2$. This is consistent with

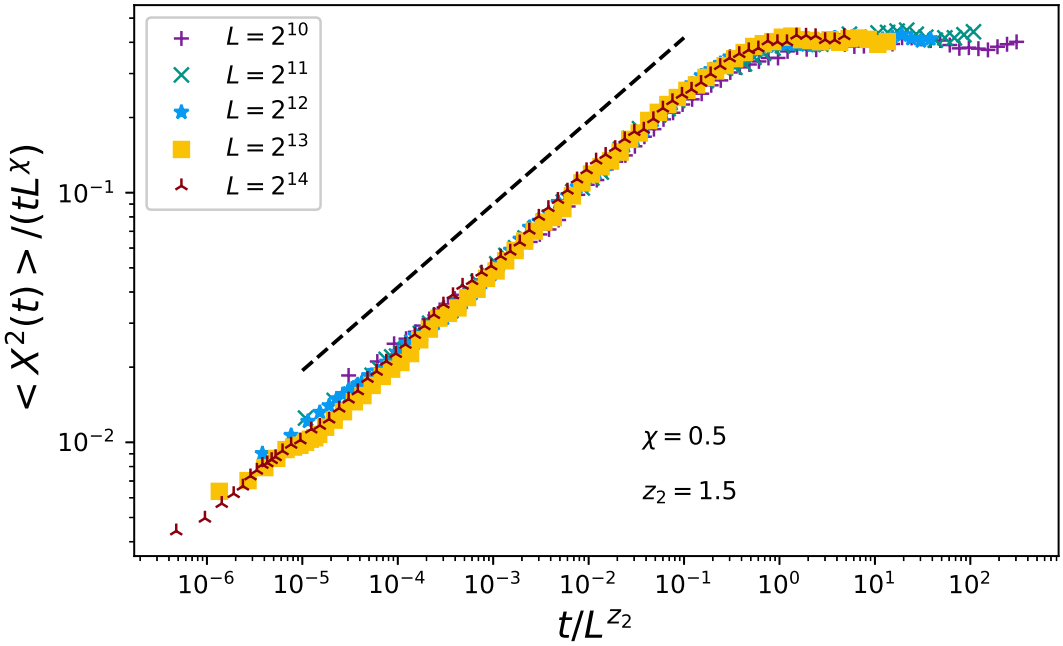

Figure 2.6 *Scaling of the activator MSD for $r = 1$, $\gamma = \lambda = 1$, L as in the key. The data are collapsed by setting $\chi = 1/2$ and $z_2 = 3/2$, consistent with the second class particle scaling. The black dashed line is a guide to the eye suggesting $\langle X_t^2 \rangle \sim t^{4/3}$. The MSD, as in the following figures, is computed at steady state, meaning that the displacement X_t is measured since saturation of the interface width.*

the dynamical exponent of the KPZ universality class.

To summarise the dynamics in the $r = 1$ case, the interface behaves as an EW one. The activator, in turn, behaves as if it were passively sliding on a KPZ interface, displaying an initial superdiffusive regime $\langle X_t^2 \rangle \sim t^{4/3}$, followed by normal diffusion $\langle X_t^2 \rangle \sim D_{\text{eff}} t$ with $D_{\text{eff}} \sim L^{1/2}$. The crossover, caused by the system finite size, occurs at a time $t \sim L^{3/2}$. The picture just described holds for $r < 1$ as well, at least asymptotically. Therefore,

$$r \leq 1 : \quad \begin{aligned} &\alpha = 1/2, \quad z_1 = 2; \\ &\chi = 1/2, \quad z_2 = 3/2. \end{aligned} \tag{2.22}$$

The coincidence of the exponents in the whole $r \leq 1$ region of the parameters' space is manifest in the width dynamics: if one plots, as in the upper panel of Fig. 2.8, the width of systems with different r's, a trivial rescaling of time by r will cause an almost perfect overlap of all the curves.

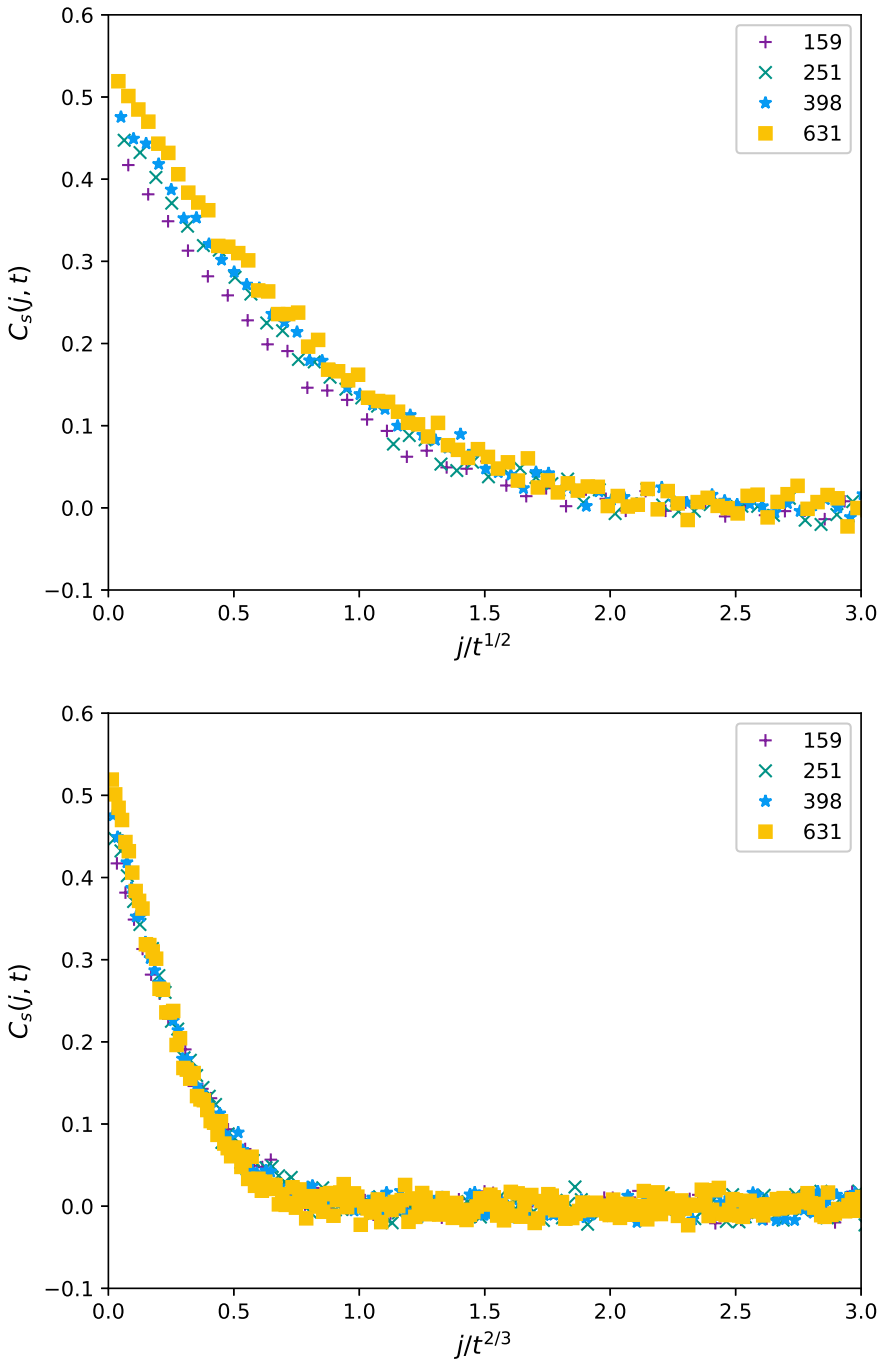

Figure 2.7 *Correlations $C_s(j,t)$ spreading from a fixed activator which catalyses growth in the interface. The slope correlation function is measured at different times (see key) and plotted against $j/t^{1/2}$ on the top panel and $j/t^{2/3}$ on the bottom panel. The overlap of the functions is much better in the latter case, suggesting that correlations spread around the activator as t^{1/z_2} where $z_2 = 3/2$. Averages here are performed over 10^5 realisations of the interface dynamics.*

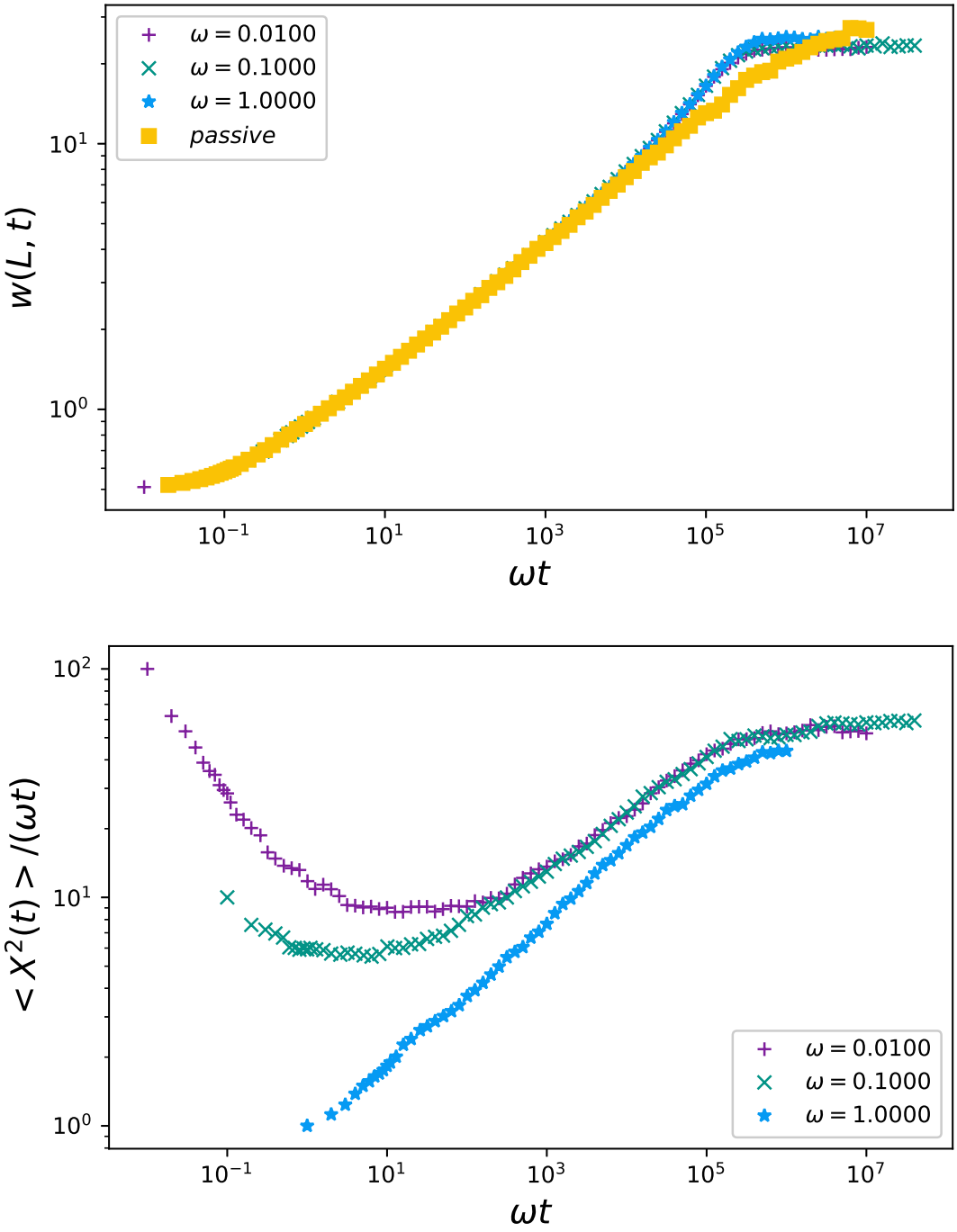

Figure 2.8 *Width (top) and MSD(bottom) vs rt, for $L = 2^{13}$, $\gamma = \lambda = 1$ and r as in the key. The width of a passive, EW interface is also shown for comparison. While rescaling time by r renders the interface dynamics independent of this parameter, the activator displays an early-time, subdiffusive regime, the extent of which scales as $1/r$, as pointed out in the text.*

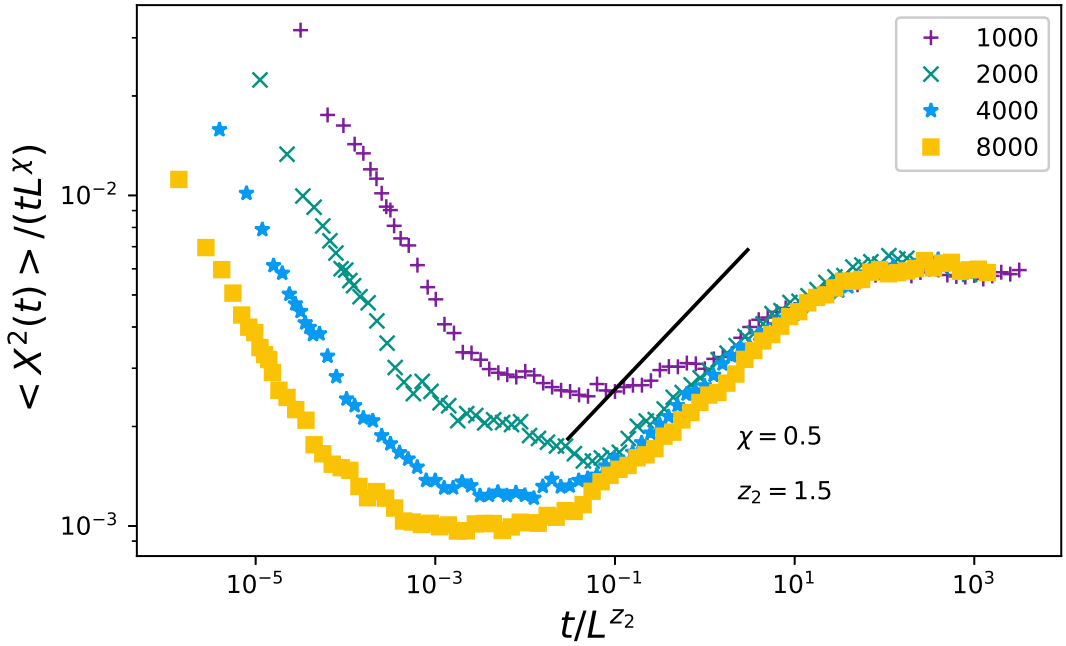

Figure 2.9 *Scaling plot of the activator MSD for $r = 10^{-2}$, $\gamma = \lambda = 1$. The black solid line is a guide to the eye for the superdiffusive law $\langle X_t \rangle \sim t^{4/3}$.*

The MSD, conversely, shows an initial subdiffusive regime, reminiscent of the typical behaviour displayed by random walkers in random environments. Subdiffusive behaviour appears in Fig. 2.8, lower panel, as a decreasing curve when $\langle X_t^2 \rangle / (rt)$ is plotted as a function of rt. In a completely static random environment (such as a quenched random potential) the subdiffusive behaviour due to trapping can be as slow as $\langle X_t^2 \rangle \sim (\log t)^4$ [66]. In Fig. 2.8 however, after a time $\sim r^{-1}$, subdiffusion is replaced by superdiffusion, which eventually crosses over to normal diffusion ($\langle X_t^2 \rangle / (rt) \to const.$) due to the finiteness of the medium. As a result, the scaled MSD at $r < 1$ tends to the $r = 1$ curve for sufficiently large scaled times, as in the lower panel of Fig. 2.8.

In fact, r^{-1} is the average time at which the interface site under the activator undergoes its first update. Hence, this is the time at which the interface activity steps in, together with the mechanisms responsible for the physics of the system at $r = 1$. This clarifies the late emergence of the same exponents which describe the $r = 1$ case. Let us close the section by showing the MSD scaling at fixed r, with L in the range 2^{10}—2^{13}, so as to support the hypothesis $\chi = 1/2$, $z_2 = z_p = 3/2$ in the whole $r \leq 1$ of the parameter space (Fig. 2.9). The late-time collapse of the superdiffusive and diffusive regimes is fully compatible with the proposed

exponents [4], whereas the early-time MSD obeys the trivial collapse $\chi = z_2 = 0$.

2.2.3 The surfing regime

While a uniform scaling unifies the $r \in (0, 1]$ section of the parameter space, novel properties emerge when $r > 1$. The ensuing regime—I call it the surfing regime—occurs for r large, but still smaller than a diffusive problem saturation time, which is $O(L^2)$. The reason for the given name, as anticipated in the section's introduction, comes from the behaviour of the activator, which is peculiar to this system and a specific range of parameters and is summarised in Fig. 2.10.

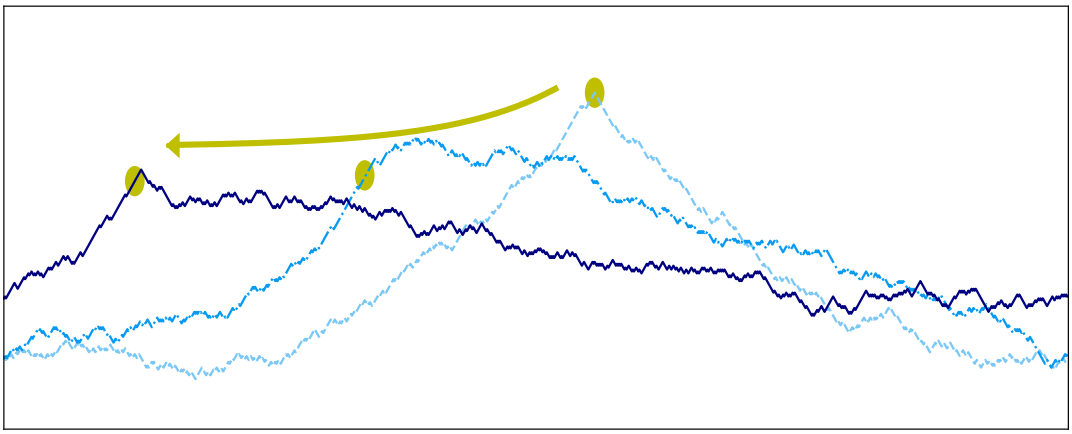

Figure 2.10 *Surfing regime snapshots. The interface profiles are ordered in time according to their color, from lighter to darker, while the activator is represented by a yellow dot of a significantly larger size, to ease the understanding of the picture. The earliest snapshot (light blue), depicts the initial growth, whose dynamics is analogous to that of the $r \to \infty$ limit (cf. subsubsection 2.2.3.1). The second (azure), is taken some moments after the activator has started moving: the wave is broken together with the left-right symmetry of the system. The last (dark blue) is the latest, and it shows that the activator keeps moving while 'ironing out' the interface: this is, in fact, the regime with the smallest roughness exponent. Notice how, due to the system finite size, the activator will soon reach the back of the wave: at this point it could stochastically revert his motion, so that the long-time dynamics is still diffusive (see discussion in the text).*

At first, the activator pulls the interface as a static defect, thus creating a tent-like

[4] A cleaner scaling requires the sub- and superdiffusive regimes to be well separated in time. Such a separation, in turn, would require system sizes much bigger than those used throughout this section, hence significantly longer simulations—as we are dealing with a single particle on a fluctuating interface, for each realisation one needs to simulate the whole interface dynamics.

shape which will be discussed in detail later on. The tent width increases so as to match, in a time $O(L^2)$, the system size L. However, as r is finite, the activator will move before. Pictorially (see Fig. 2.10), the activator randomly chooses one side of the tent as the direction to move away, then the tent breaks like a sea wave towards the activator's direction of motion. As the interface keeps following the activator by shifting the tent top towards its position, the activator will keep finding itself on a downslope and being pushed forward—it appears to surf the interface. The first, immediate consequence of this peculiar dynamics is that the activator is able to use the protrusive force it exerts on the membrane to propel itself. A qualitatively similar mechanism gives rise to waves in the finite density case, which will be discussed in section 2.3: first the activator creates a bump in the interface profile, then it is advected away from it.

With respect to the MSD, one would expect a ballistic regime $\langle X_t^2 \rangle \sim t^2$, which develops after an initial transient (before the activator "chooses" a side) and eventually crosses over to normal diffusion (due to the system finite size). As

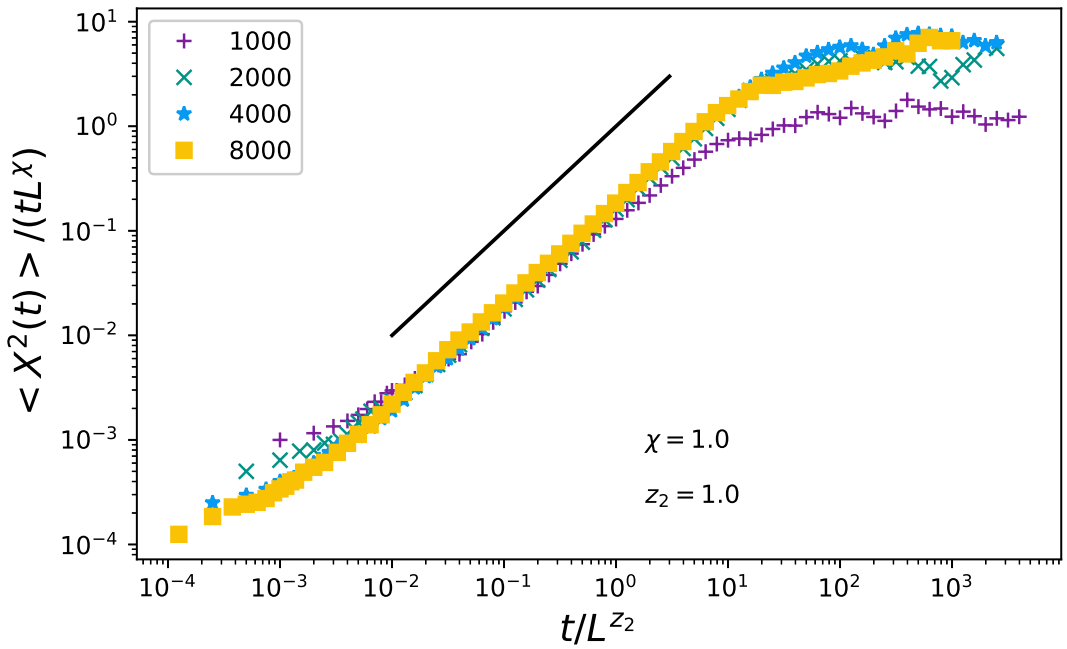

Figure 2.11 *MSD scaling at $r = 100$. If one excludes the $L = 1000$ curve, which does not reach a full ballistic regime, the scaling exponents agree with the proposed values $\chi = z_2 = 1$.*

shown in Fig. 2.11, the MSD obeys the scaling law Eq. (2.18) with $\chi = z_2 = 1$. The value of z_2, together with $\chi + z_2 = 2$, is consistent with the ballistic regime

expected to occur before saturation. What is the meaning of $\chi = 1$? It implies that the long-time effective diffusion coefficient D_{eff} is directly proportional to the system size L. The coupling of this observation with the kinetic interpretation of the diffusion coefficient D = (mean free path) $\times$ (speed) suggests that the activator surfs the interface for its whole length before reverting its motion. This is indeed what emerges by inspecting snapshots of the system as those collected in Fig. 2.10: after travelling about a system length, the activator meets the tail of the wave it is surfing, hence it will have to stop and create a new wave to surf, possibly in the opposite direction. The resulting motion is that of a persistent random walk, with the interface size as persistence length.

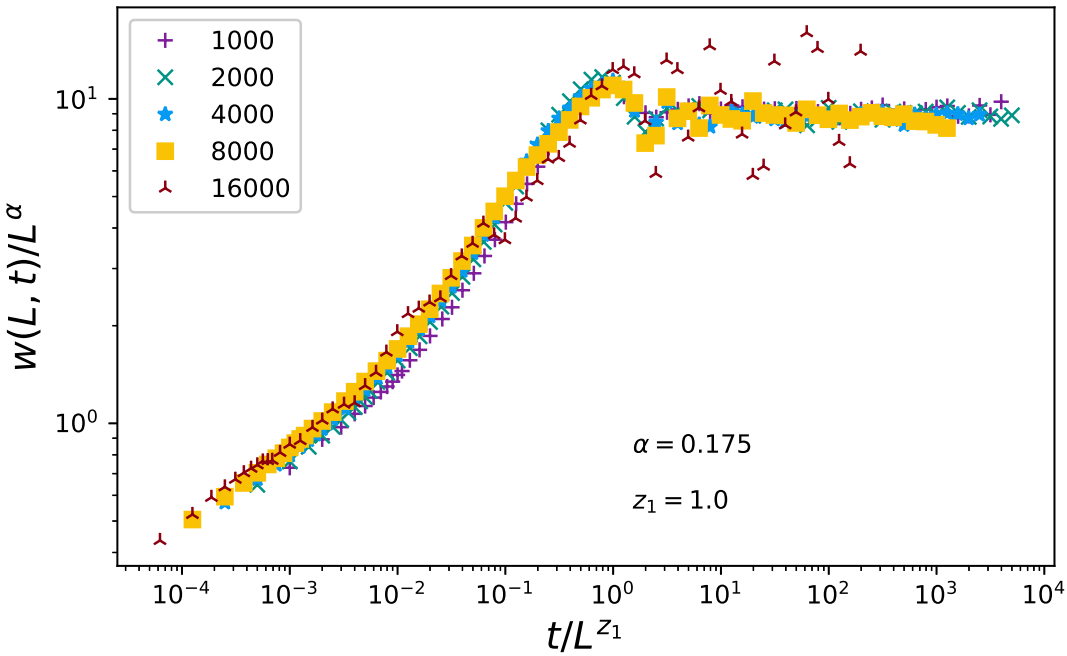

Figure 2.12 *Width scaling at $r = 100$, $\gamma = \lambda = 1$. The oscillating widths collapse on a single curve for $\alpha = 0.175$ and $z_1 = 1$.*

As a byproduct of the peculiar dynamics of the activator, the width scaling appears to differ from the previous sections or indeed any of the known universality classes. First, the dynamics is dominated by oscillations (as in the finite density case, cf. subsection 2.3.1 and subsection 2.3.2): the interface roughens when the activator creates the tent, then smoothens as it surfs the membrane wave. Once the activator has stopped running, due to the finiteness of the interface size, the width increases again and the cycle repeats. The period of the oscillations, being controlled by the running time of the activator, scales as the system size, hence $z_1 = 1$, as can be observed in Fig. 2.12. Notice

that this is the only case where $z_1 = z_2 = z_P$, as in passive scalar advection problems. Furthermore, due to the "ironing" action performed by the surfing activator, the interface appears significantly smoother than in the other phases. A reasonable width collapse in Fig. 2.12 is achieved for $\alpha = 0.175$ (about 1/6), but the possibility that the roughness will vanish upon increasing the system size even further cannot be ruled out, thus implying the active interface to be flat on large scales. The observed exponent could also be ascribed to multiplicative logarithmic corrections. While numerical tests remain inconclusive, further evidence for a flat active interface will be discussed in chapter 4 with scaling arguments. To conclude,

$$1 < r \ll L^2 : \qquad \begin{array}{ll} \alpha \lesssim 0.175, & z_1 = 1; \\ \chi = 1, & z_2 = 1. \end{array} \tag{2.23}$$

2.2.3.1 The $r \to \infty$ limit

In the $r \to \infty$ limit the interface reaches a stationary state before the activator can even move. Most of the system features, including the various exponents considered in this section, depend on the stationary shape the interface reaches between subsequent jumps of the activator, as such a shape will determine the jump rates in the following step. In order to gain insight into this stationary shape, it is useful to consider the related problem of a stochastic interface with a defect site. Forcing the activator to stay put on a single site means that the interface is being pulled from this specific site, whilst there are only up/down-symmetric fluctuations elsewhere on the ring. One can readily infer the nature of the system steady state, especially with the parameter choice Eq. (2.15), by considering the interface as a gas of $\pm$ slopes. Then the transitions $\vee \to \wedge$ and $\wedge \to \vee$) corresponds to a slope-exchange dynamics with hard-core repulsion. Normally, slopes do not have a preferred direction of motion, except at the activator site: the latter acts as a semi-permeable membrane which allows negative slopes to move only right and positive slopes to move only left. All the negative slopes starting on the activator's left will eventually cross it and lie on its right, while there will be only positive slopes on the left. As a result, the steady-state interface will look like a "tent" - a macroscopic convex wedge as in the inset of Fig. 2.13.

According to the width scaling shown in Fig. 2.13, main, noise dominates the roughening dynamics at early times, with $w(t) \sim t^{1/4}$ as for EW interfaces (recall

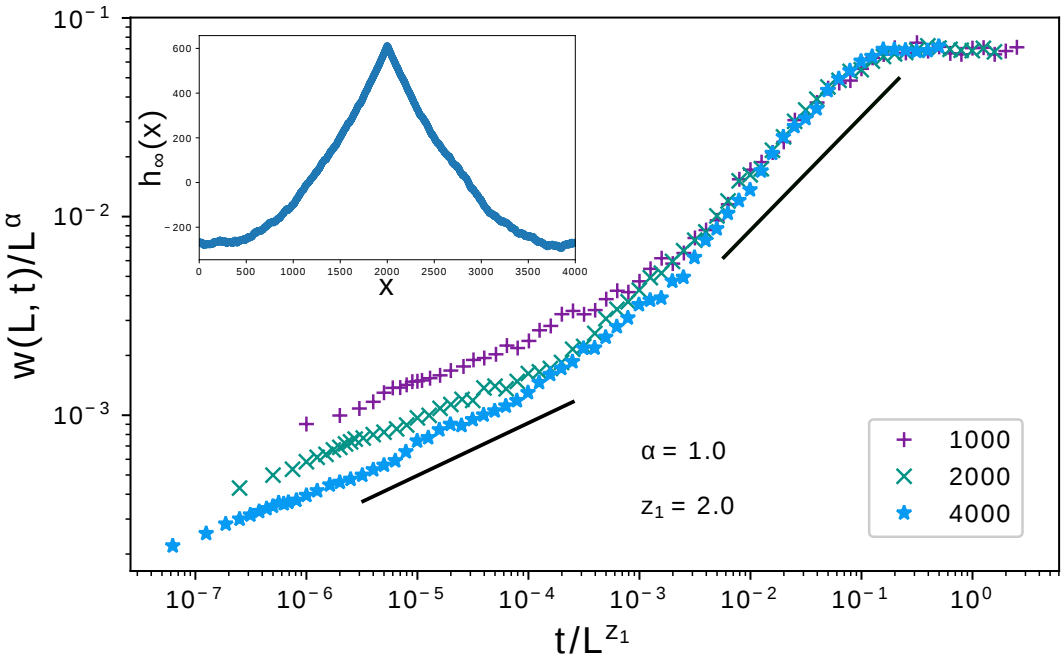

Figure 2.13 *Main: width scaling in the $r \to \infty$, L as in the key. $\alpha = 1$, $z_1 = 2$ causes overlap of the rightmost portion of the curves. The black solid lines are guides for the power laws $w \sim t^{1/4}$ and $w \sim t^{1/2}$ (see text). Inset: tent shape generated by a static activator.*

the early growth $w(t) \sim t^{\beta}$ with $\beta = \alpha/z$). As the interface grows, the weight of the deterministic contribution of the defect site increases, until it overcomes that of the noise and β approaches 1/2. Although slope correlations spread around the defect site as in Fig. 2.7 at early times, diffusive behaviour is recovered at longer times, hence $z = 2$. The dynamic exponent can be inferred by observing that, once the tent profile has formed, growth is limited by slope diffusion: the interface must be concave ($\vee$) at the defect site for the tent to grow again, so that a $+1$-slope segment has to diffuse across the -1-slope region on the right of the defect while a -1-slope segment has to diffuse across the $+1$-slope region on the left of the defect. $z_1 = 2$ is confirmed by the numerics (Fig. 2.13) and, together with $\alpha = 1$ implied by the tent-like shape which spans the whole lattice, it produces the $\beta = 1/2$ seen at long times in Fig. 2.13.

The activator dynamics is also easily understood, as the latter will always be sitting on the top of the tent before moving. Then, from Eq. (2.7), the left and right jump rates coincide with each other and are equal to q_+, so that the particle undergoes normal diffusion at all times and the exponents χ and z_2 are

trivially zero. To sum up, for infinite r the system settles on a steady-state profile with a tent-shaped interface and the activator sitting on top of the tent. Both the activator and the tent hop symmetrically at rate q_+. The various scaling exponents are given by

$$r \gtrsim L^2 : \qquad \begin{array}{ll} \alpha = 1, & z_1 = 2; \\ \chi = 0, & z_2 = 0. \end{array} \tag{2.24}$$

where $r \gtrsim L^2$ mean r larger than the static defect problem saturation time.

2.3 Scaling of the discrete active interface: numerical results

Finally, let us discuss the properties of the active interface model with a macroscopic number N of activators. A 'macroscopic' number is intended as a finite fraction of the system size L, so as to have a certain density $\phi = N/L$ which is specifically set to 1. Let us stress that the overall density does not affect the results to be presented, unless pushed to exceedingly small (or large) values. The dilute limit $\phi \to 0$ was considered already in section 2.2. In the opposite limit $\phi \to \infty$ density dishomogeneities appear negligible on the overall density scale, hence the active interface approaches a passive KPZ interface with uniform rate difference $p_+ - p_- \simeq \lambda\phi$ (cf. Eq. (2.3)), although fluctuations might still yield a non-trivial contribution. This possibility will be considered in chapter 4 from a renormalisation group perspective.

The timescale ratio r is fixed together with the density of activators, so as to focus on the λ-γ plane of the parameter space, specifically the physical sector where λ and γ have the same sign. The transition rates of the model are set to

$$q_\pm = q \pm \frac{\gamma}{2}, \quad p_- = p, \quad p_+ = p + \frac{\lambda}{2} n_i, \quad p = q = 1/2, \tag{2.25}$$

in this section. It is particularly convenient to keep γ fixed while changing λ, so as to maintain a continuous connection with the models of passive scalar advection mentioned in section 2.2. This connection is explicitly realised as a $\lambda \to 0$ limit. Models of passive scalar advection with a macroscopic number of passive particles are used to study the interactions which emerge when particles are advected by the same fluctuating medium. The latter problem was pioneered

by Deutsch, in [67], who studied the aggregation of Brownian particles subject to the same spatiotemporal noise. The specific problem of advection by the slopes of a fluctuating interface was considered later in [64], with a lattice description following after a decade [54, 60].

This section begins with a presentation of the scaling of interface width and activators mean square displacement for the active interface model, as was done in each of the subsections of section 2.2. A new observable is then introduced, in order to characterise the aggregation of activators in the model and compare it with the clustering of passive sliders. The section ends with a short summary of the main properties of the active interface model introduced and studied numerically in this chapter.

2.3.1 Width and diffusion at finite density

As in the test-activator case of section 2.2, the properties of our active interface can be inferred by measuring the interface width and the activators MSD. All measurements are obtained, as in section 2.2, by *i)* preparing a flat interface of L sites with $N = L$ activators distributed uniformly over the sites; *ii)* simulating the system dynamics according to the stochastic update rules of section 2.1; *iii)* comparing systems of different sizes according to the scaling relations 2.17 and 2.18. Let us begin with the interface width.

The scaled width $w(L,t)/L^{\alpha}$ is plotted in Fig. 2.14 for active interfaces of various sizes and compared to the scaled width of Edwards-Wilkinson interfaces of the same size. The EW width (solid lines in the figure) grows in time as $t^{1/4}$ before reaching a saturation value which scales as $L^{1/2}$. The width of the active interface (points of the figure) appears to grow faster than EW, but, after reaching the EW saturation value, begins oscillating. With oscillations removed (e.g., by averaging over the period of oscillation) the EW scaling with roughness exponent $\alpha = 1/2$ and dynamic exponent $z_1 = 2$ is restored. As $\lambda = 2\gamma$ in Fig. 2.14, the observed $\alpha = 0.5$ is compatible with the steady-state probability discussed in chapter 3, and it extends to the whole $\lambda, \gamma > 0$ sector of the parameter space. The oscillations, instead, require a different scaling. Notably, collapse of the oscillating component of the width is obtained with $z_1 = 1$, as in the surfing regime of the test activator problem (cf. Fig. 2.12 and Fig. 2.15). However, unlike in the surfing regime, there is no numerical evidence for a reduction of the roughness exponent. Although the numerics remain inconclusive, we will discuss again the possibility of a flat

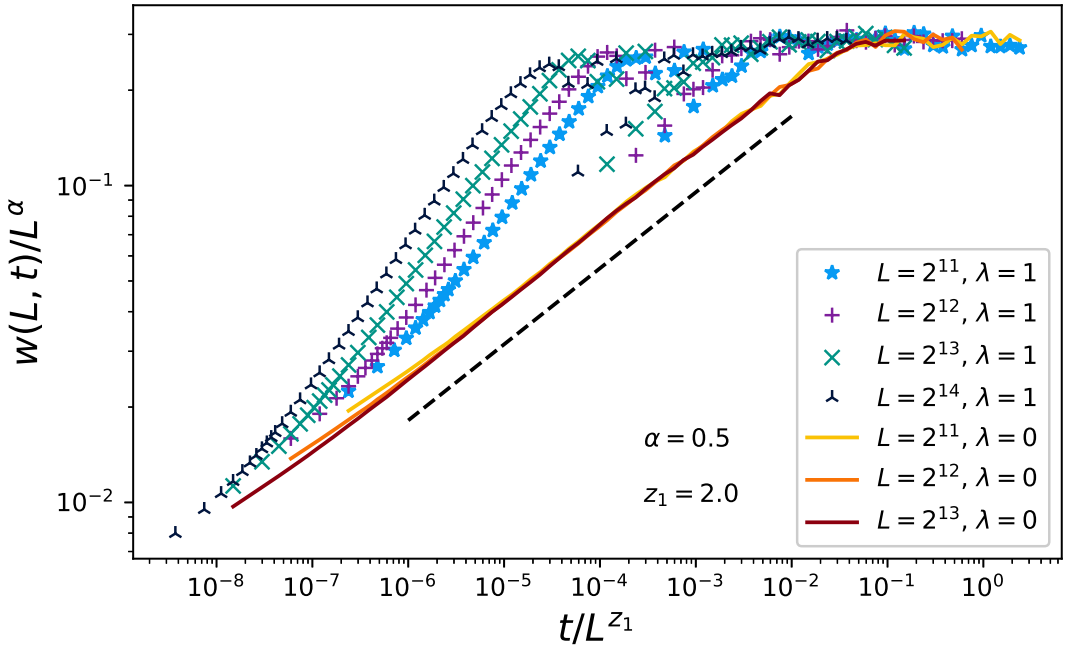

Figure 2.14 *Average width of the active interface with* $\lambda = 1$ *and* $\gamma = 0.5$ *(points) and an EW interface (solid lines), scaled with the EW scaling exponents* $\alpha = 0.5$ *and* $z_1 = 2$*. The* $w(L,t)$ *curves of the EW interfaces collapse onto the same curve* $\sim t^{1/4}$ *(*$\alpha/z = 1/4$*), highlighted by the black dashed line. By contrast, the active interface width displays sustained oscillations superposed to the* $t^{1/4}$ *law. In this and the other scaling plots of this chapter averages are performed over* 100 *independent realisations of the stochastic dynamics.*

interface in chapter 4, from a renormalisation group perspective.

Let us now turn to the MSD, which we measure in steady state after the width saturation time $\sim L^2$. As usual, we scale the MSD with time so that a horizontal curve corresponds to normal diffusion, while descending and ascending branches to sub- and superdiffusion, respectively. As shown in Fig. 2.16, the scaled MSD rapidly increases and plateaus again on an higher value, indicating normal diffusion albeit with an enhanced diffusion coefficient. After a time which scales linearly with the system size, the scaled MSD jumps to yet another plateau, which sits between the previous plateau and the original bare diffusion coefficient.

Unlike for the test activator, the long-time diffusion coefficient of the finite-density system does not depend on the system size, thus $\chi = 0$. The saturation time, instead, scales linearly with L, hence $z_2 = z_1 = 1$. Thus, at finite activator

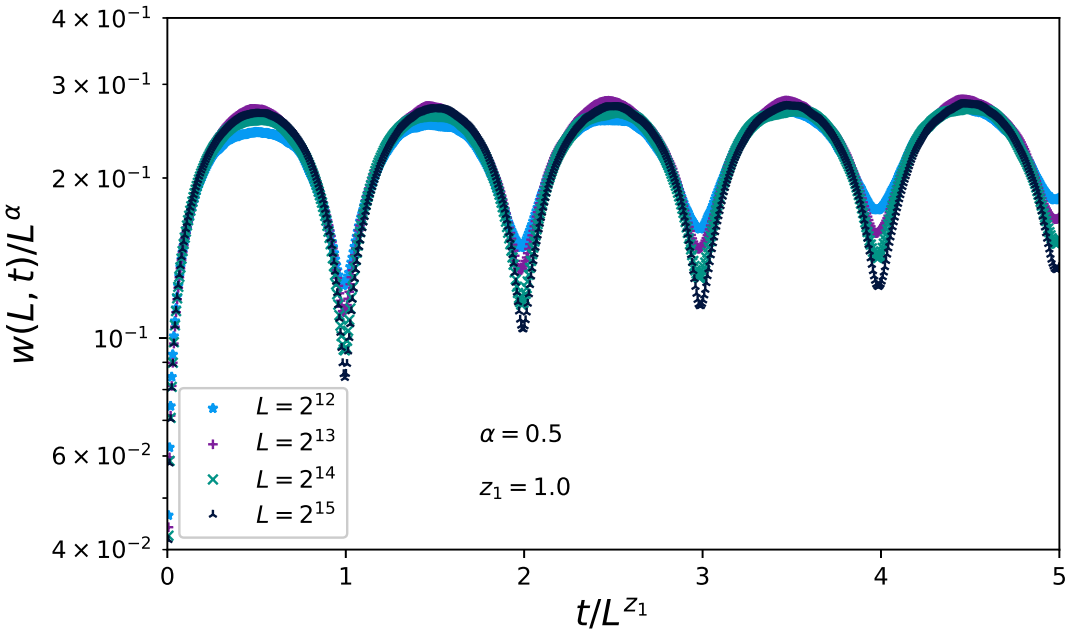

Figure 2.15 *Average width of the active interface, $\lambda = 1$, $\gamma = 0.5$ and lattice size in the key. Here $z_1 = 1$, so as to highlight the oscillating component of the width.*

densities, the coincidence of z_1 and z_2 extends from the large-r regime towards smaller timescale ratios. A zoom of the scaled MSD close to saturation reveals an oscillatory pattern analogous to the one observed for the width, suggesting that the initial increase-plateau-decrease of the scaled MSD might just be the first period of the oscillation. In summary, the active interface scaling is characterised by the following exponents,

$$\text{finite } \phi: \quad \begin{aligned} \alpha &= 0.5, \qquad & z_1 &= 1; \\ \chi &= 0, \qquad & z_2 &= 1. \end{aligned} \tag{2.26}$$

It is worth remarking that the same exponents are found for all $\gamma, \lambda > 0$, timescale ratio r, and density ϕ, although scaling might be plagued by slow crossovers when any of these parameters is pushed to extremely small or extremely large values.

2.3.2 Arrested path coalescence and waves

This section is devoted to the aggregation properties of activators in the active interface model. Clustering, in general, can be understood via the growth of

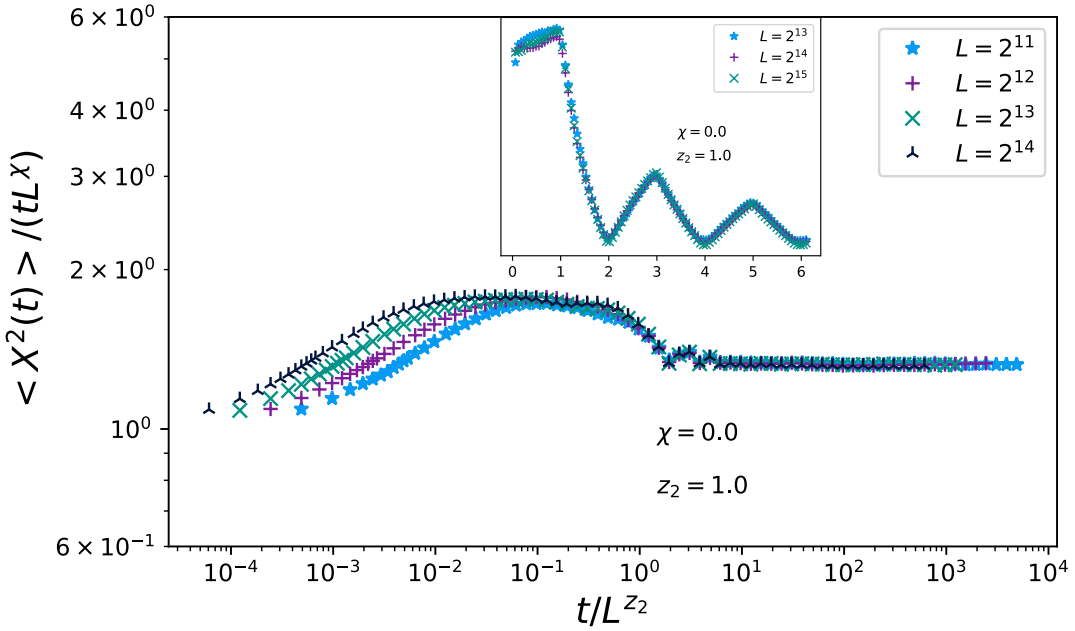

Figure 2.16 *Scaling of the steady state MSD (measured after saturation of the interface width) for the active interface, with $\lambda = 1$, $\gamma = 0.5$ and L as in the key. As the interface width, the activators' MSD saturates after a time scaling linearly with the system size, i.e. $z_2 = 1$. The inset shows a zoom of the MSD scaling plots close to saturation, in order to highlight oscillations of the scaled MSD.*

a certain lengthscale $\mathcal{L}(t) \sim t^{1/z_c}$, where z_c is a dynamic exponent describing coarsening [68]. Particles advected by a fluctuating medium, in particular, show a tendency to aggregate known as *path coalescence* [67]. The fluctuating medium generates a stochastic force field in which particles move. The association of random forces with points in space does not influence the single particle dynamics, which can still be explained by a simple time-dependent stochastic force. Nevertheless, adjacent particles subject to the same spatiotemporal noise will experience similar random kicks, thus stick together rather than increasing their average distance as predicted by standard diffusion. Such an aggregation can be understood in terms of a growing lengthscale $\mathcal{L}(t)$ too, specifically the linear size of the cluster's basin of attraction or, alternatively, the typical size between distinct clusters. For passive random walkers advected by a discrete KPZ interface, z_c coincides with the interface dynamic exponent, while it is slightly different for an EW interface [65] (although the difference might be ascribed to logarithmic corrections).

In this section, instead, we characterise aggregation with a width-like observable, defined as the variance of the occupation numbers n_i over the ring lattice, i.e

$$\delta\rho^2(L,t) = \frac{1}{L}\sum_{i=1}^{L}\left(n_i - \frac{1}{L}\sum_{j=1}^{L} n_j\right)^2 . \tag{2.27}$$

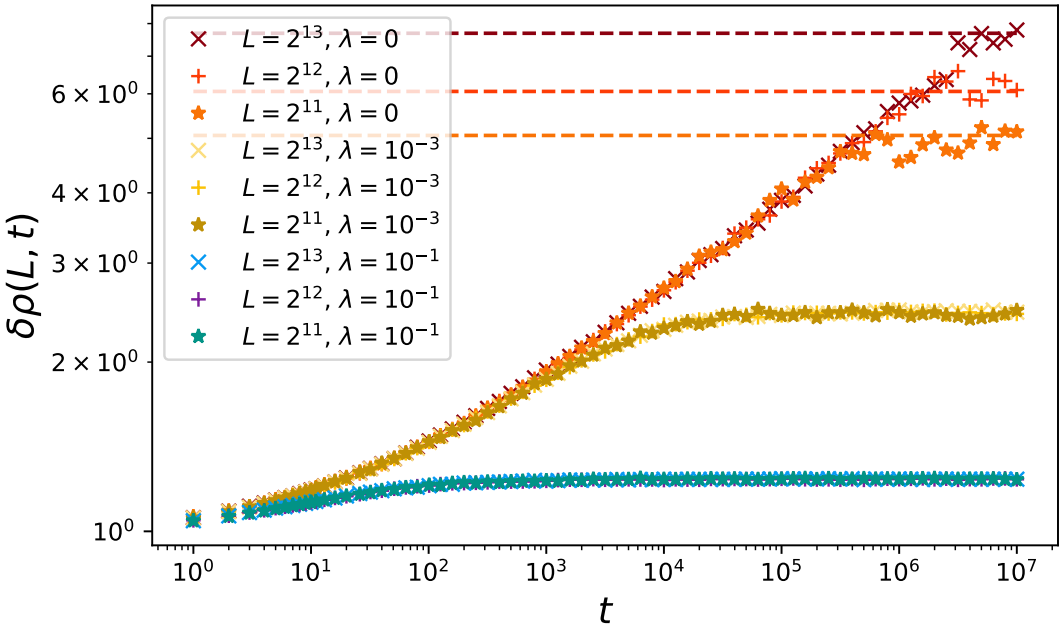

Figure 2.17 *Density fluctuations $\delta\rho^2(L,t)$ for several system sizes, $\gamma = 0.5$ and λ as in the key. The initial power-law growth, indicating coarsening, is followed by saturation. If the saturation value increases with L, as for $\lambda = 0$, the activators will ultimately coalesce in a single macroscopic aggregate. If the saturation value is independent of the system size, clusters grow only up to a finite size, as for $\lambda > 0$.*

The above quantity is analogous to a *participation ratio*, whose inverse is used to study localisation phenomena in quantum disordered systems. If macroscopic clustering takes place, i.e. a finite number of sites hosts a finite fraction of the available particles, then a few n_i's scale as $N = \phi L$, while all the others are close to zero. After squaring, summing and dividing by L, $\delta\rho^2$ will scale as L. For an homogeneous distribution, in contrast, each n_i is of order 1 so $\delta\rho^2$ does not depend on the system size. The scaling of $\delta\rho^2(L,t)$ with the system size L is shown in Fig. 2.17 for several values of λ, together with the $\lambda = 0$ limit. The latter limit

corresponds to passive particles advected by an EW interface: here, the density fluctuations $\delta\rho^2$ increase with the size of the system, albeit sublinearly. As soon as $\lambda > 0$, $\delta\rho^2$ saturates to a size-independent value which decreases by increasing λ. If every site hosts exactly 1 particle, $\delta\rho^2 = 0$. If every l sites there is 1 with l particles and $l-1$ empty ones, then $\delta\rho^2 = [(l-1)^2 + (l-1)]/l$, so that the finite value of $\delta\rho^2$ can be taken as a measure on the size l of nanoclusters in the system. Hence, we conclude that the size of activator nanoclusters decreases with increasing λ.

An instance of path coalescence in the active interface is shown in the top panel of Fig. 2.18, where the profile of an active interface of size $L = 2^{10}$ is shown at various times. The colour of the interface represents the local density of activators, from blue (empty sites) to red (many activators). The first snapshot (top) shows the initial condition, i.e. a flat interface with a uniform distribution of activators. The second snapshot shows the same interface at a later time: as the profile becomes rougher, the activators, driven by the slopes, accumulate at the bottom of interfacial troughs. Once enough activators have accumulated, the active component of interface growth dominates, so that the troughs collecting most of the particles become peaks and stop attracting additional activators. The higher λ is, the sooner we expect the cluster to stop growing and the smaller their size, in agreement with the λ-dependence of the long-time density fluctuations of Fig. 2.17.

Because of the advective bias γ, nanoclusters will tend to drift away from the bumps they have generated and slide down the slopes on the bump's side until they reach a new trough. Once clusters have reached new troughs, the cycle starts again: this is the origin of the width and diffusion oscillations shown in Fig. 2.15 and Fig. 2.16. Notably, when moving from a peak to a trough, clusters slide ballistically down the interface slopes. These travelling waves, accompanied by waves of interface protrusion, are manifest in the kymograph shown in the bottom panel of Fig. 2.18. As the colour code is the same as in the top panel, travelling nanoclusters appear in the kymograph as diagonal red lines on an overall blue field. These lines have a finite length but all display a similar slope, either positive or negative. We will explore the significance of these waves further at the end of chapter 3. The ballistic runs explain the initial increase in the scaled MSD, which then plateaus again because runs are short and occur in both directions.

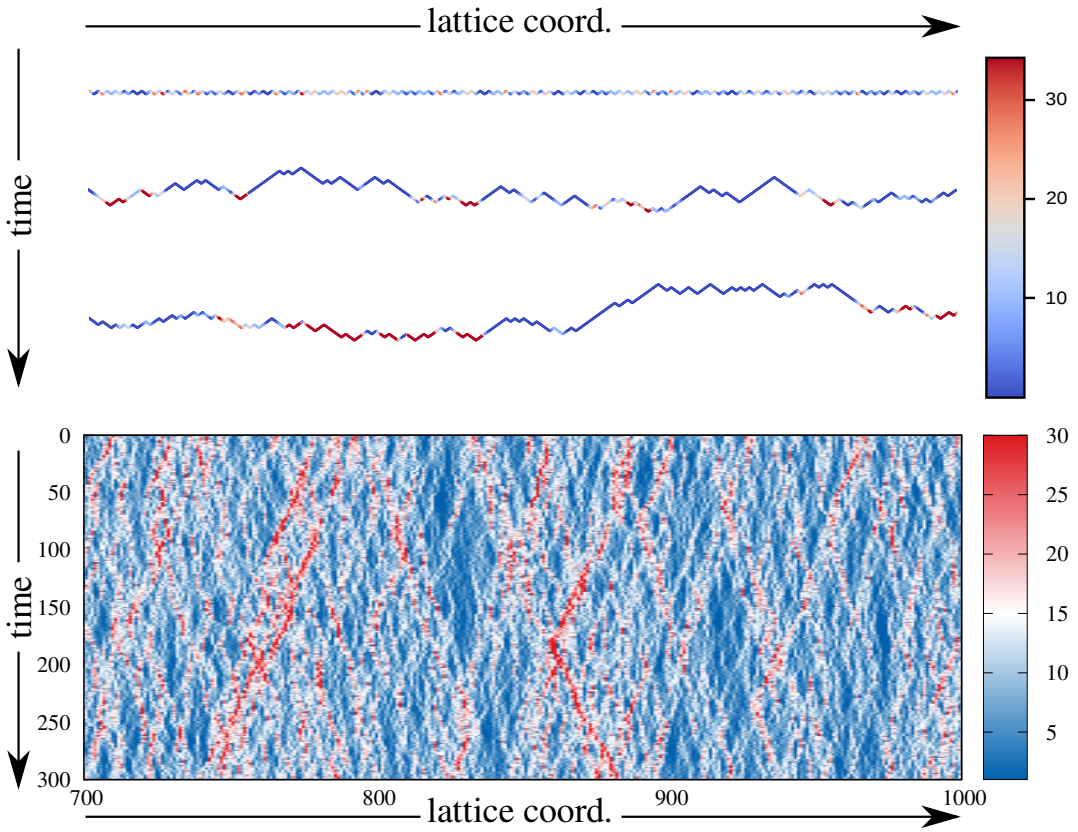

Figure 2.18 *Top: snapshots of an active interface with $L = 20000$, with $\gamma = 0.5$ and $\lambda = 1$. The interface is coloured according to the local number of activators n_i, from blue (no activators) to red (many acivators). The first snapshot is taken at $t = 0$, when the interface is flat and the distribution of activators uniform. In the other two snapshots, taken at later times, the activators have gathered at the bottom of interface valleys. Bottom: "kymograph" of the density profile, where each line represent the density profile (colour) at different times. The kymograph displays only a portion of the interface, and is taken in steady-state. The diagonal red lines represent the travelling nanosclusters discussed in the text.*

2.3.3 Concluding remarks

These concluding paragraphs sum up the most relevant properties of the active interface model introduced at the beginning of the chapter. The model consists of a fluctuating interface and a number of activators which stimulate the interface growth and are advected by the interface slopes. This coupling harbours a negative feedback loop, in that the activators cause the interface height to increase on their location, but then are advected towards portions of the interface at lower

height. This is the origin of the patterns typical of the system steady state, such as the travelling nanoclusters of Fig. 2.18 and the interface ripples on which nanoclusters surf. It is worthwhile to stress the resemblance of these patterns with those detected in experiments of living membranes, which were mentioned back in subsection 1.2.1 [43–45].

Even with only one activator on the interface, the competition between the negative feedback loop and the relaxational timescales of the individual components result in a rich range of dynamical behaviours. When the interface relaxation is much slower than the activator diffusion, for instance, the interface dynamics bears the signatures of the Edwards-Wilkinson, equilibrium dynamics, whereas the activator behaves as if it was moving on a driven interface. In the opposite limit, where the interface relaxation is much faster than the activator diffusion, the motion of the former depends entirely on the active pull exerted by the latter, while the latter is insensitive to fluctuations of the former. Between the two limiting regimes, the active (vertical) pull of the activator is converted into (horizontal) sliding motion through the coupling with the interface slope.

In addition, this complex phenomenology implies a non-trivial scaling of the interface, both with a single activator and a finite density thereof. In the finite density case, particularly, the roughness exponent equals $1/2$ as for both EW and KPZ interfaces, while the dynamic exponent $z = 1$ differs from the diffusive $z = 2$ of EW and $z = 3/2$ typical of the KPZ universality class (cf. Eq. (2.26)). Different exponents can be found in the regimes of the test-particle problem (Eq. (2.22) and Eq. (2.24)), but also in different models of active kinetic roughening [4].

The next chapter is aimed at proving that the active interface model admits a large-scale and long-time descriptions in terms of partial differential equations, as both the EW and KPZ models do. In contrast with these passive models, the equation describing fluctuations in the height of our active interface is coupled to an equation for the activator density. The equations derived will also be used to understand the steady-state dynamics described in section 2.3.

Chapter 3

The active interface equations

This chapter is dedicated to the *hydrodynamic limit* of the stochastic lattice model defined in section 2.1. The goal is that of establishing partial differential equations (PDEs) which describe the evolution of the system variables on a coarse-grained scale. The problem, in its general form, is as old as the kinetic theories of Maxwell and Boltzmann. The word "hydrodynamic" stems from the original aim, i.e. deriving the continuum equations of fluid mechanics from the microscopic dynamics of the molecules forming the fluid. Since the introduction of the theory of statistical mechanics, this problem has been critical for the foundations of the theory [1]. The two most important aspects of the issue are *i)* the seemingly random motion of the system constituents at the microscopic scale, where the fully reversible laws of mechanics should hold, and *ii)* the deterministic flow observed at the macroscopic scale, given the randomness of the microscopic motion.

While a complete and satisfactory treatment of the first aspect is still lacking, a considerable progress has been made in the understanding of the second [69]. In fact, the statement that microscopic stochasticity translates, under certain condition, to macroscopic determinism, can be proven with the desired level of rigour. The common intuition is that conservation laws, which are not immediately visible at the microscales, place firmer constraints on the larger scales—we will later see a direct example of this intuition. However, all these proofs require the insertion by hand of some sort of microscopic randomness, either on the initial condition of the deterministic microscopic dynamics or on

[1] It has even made it in the famous Hilbert's list, as part of the 6th problem (together with the axiomatic definition of probability)

the latter dynamics itself—think about the *Stosszahlansatz*, or molecular chaos hypothesis of the kinetic theory of gases [70].

Fortunately, we will not need such an assumption, as the "microscopic" dynamics we are starting from is rather "mesoscopic", with a significant stochastic component. Let us recall the active interface model components: a portion of the cell membrane, driven by a number of activators, and the activators themselves, partially or completely embedded in the membrane. The exertion of protrusive forces on the membrane is controlled by the activators via complex signalling pathways (some of which have been outlined in subsection 1.2.1). Therefore, membrane motion is better represented with a set of transition rates. For activators, instead, stochasticity comes from the medium, i.e. the plasma membrane. The latter is made of lipid molecules whose positions fluctuate at finite temperature, thus giving random, thermal kicks to membrane proteins.

Once a stochastic lattice model is available, the hydrodynamic limit is performed as follows. While the circumference of the ring lattice is fixed (to 1, for convenience), the number of lattice points L is increased, so that the discrete sets of lattice variables approach continuous functions. The deterministic partial differential equations for such functions emerge as a $L \to \infty$ limit of the average variation of the lattice variables due to the stochastic dynamics. Small fluctuations around the average give stochastic corrections to the deterministic equations. The convergence of the lattice variables to the corresponding continuous function is controlled by a law of large numbers, where the large number is the number of lattice points L.

The chapter consists of three sections. The actual hydrodynamic limit is performed in section 3.1: if a certain relation between the system parameters is satisfied, deterministic equations for interface height and activator density can be derived exactly. The techniques used in this section are those developed to study the hydrodynamic limit of interacting particle systems [71, 72]. In the second section, section 3.2, the exact active interface equations are postulated to extend to the whole parameter space. In a particular limit, namely the inviscid limit, the equations can be cast as a hyperbolic set of conservation laws, then solved for a particular set of initial conditions. Finally, in section 3.3, I present analytical evidence for some of the results discussed in chapter 2. Specifically, the solution of the inviscid limit provides a description of the peculiar steady-state dynamics discussed in subsection 2.3.2, whereas the complete equations of section 3.1 explain some of the features of the test-particle problem.

3.1 The hydrodynamic limit

This section contains the derivation of the active interface equations for the coarse-grained density of activators $\rho(x,t)$ and interface slope $u(x,t)$ on the ring $x \in [0,1]$. In order to obtain the continuous fields from the lattice variables $n_i(t)$ and $h_i(t)$, first define the staircase functions

$$\rho_L(x,t) = \sum_{i=1}^{L} \langle n_i(t) \rangle \, \chi_{\left[\frac{i}{L}, \frac{i+1}{L}\right)}(x), \quad u_L(x,t) = \sum_{i=1}^{L} \langle h_{i+1}(t) - h_i(t) \rangle \, \chi_{\left[\frac{i}{L}, \frac{i+1}{L}\right)}(x), \tag{3.1}$$

where $\chi_{[a,b)}$ is the indicator function of the semi-open interval $[a,b)$, then perform a $L \to \infty$ limit. As periodic boundary conditions are enforced, $L+1 \equiv 1$. Recall that, unlike in chapter 2, L denotes the number of lattice points rather than the system size. The averages in Eq. (3.1) run over realisations of the stochastic dynamics described in section 2.1, which I will now recall for completeness. For each site $i = 1, \ldots, L$,

$$\begin{aligned} &h_i \to h_i + 2, \text{ at rate } p_+(i) = p + \lambda n_i \text{ iff } h_{i+1} - h_i = h_{i-1} - h_i = 1, \\ &h_i \to h_i - 2, \text{ at rate } p_-(i) = p \text{ iff } h_{i+1} - h_i = h_{i-1} - h_i = -1, \end{aligned} \tag{3.2}$$

and, for each pair of adjacent sites i, j

$$n_i, n_j \to n_i - 1, n_j + 1 \text{ at rate } q_\pm = q \pm \gamma/2 \text{ if } h_i - h_j = \pm 1. \tag{3.3}$$

The coarse-grained fields ρ and u are the $L \to \infty$ limits of ρ_L and u_L, respectively. As it will be shown in the following, ρ and u obey

$$\partial_t \rho = \Lambda \partial_x (\rho u) + D \partial_{xx}^2 \rho, \tag{3.4a}$$

$$\partial_t u = \Lambda \partial_x \left[\rho \left(1 - u^2 \right) \right] + \nu \partial_{xx}^2 u, \tag{3.4b}$$

where

$$D = \lim_{L \to \infty} \frac{q}{L^2}, \quad \nu = p/q, \quad \Lambda = \lim_{L \to \infty} \frac{\lambda}{2L} = \lim_{L \to \infty} \frac{\gamma}{L}. \tag{3.5}$$

The remainder of the section is structured as follows. First, in subsection 3.1.1, the model of chapter 2 is shown to admit a factorised steady-state measure for $\gamma = \lambda/2$ (as in Eq. (3.5)). The steady-state measure is then used in subsection 3.1.2 for the derivation of the deterministic active interface equations Eq. (3.4), and in subsection 3.1.3 to derive stochastic corrections to the deterministic equations.

3.1.1 Factorised steady-state measure

In this section it is shown that, under a particular condition on the model rates $q_\pm$ and $p_\pm$, the factorised probability measure

$$P_{ss}(\{h_i\},\{n_i\}) = Z_{L,N}^{-1}\prod_{j=1}^{L} f(n_j), \quad f(n) = \frac{(q_+ + q_-)^{-n}}{n!}, \tag{3.6}$$

is invariant for the dynamics summarised by Eq. (3.2) and Eq. (3.3). In simple terms, Eq. (3.6) states that the stationary probability is independent of the interface configuration, $\{h_i\}$, and depends on the configuration of particles $\{n_i\}$ in a factorised way, which implies vanishing of correlations in the large system limit. In Eq. (3.6),

$$Z_{L,N} = {\sum_{\{h_i\}}}' \sum_{\{n_i\}} \prod_{j=1}^{L} f(n_j)\delta_{\sum_{j=1}^{L} n_j, N}\ , \tag{3.7}$$

where the $'$ on the h_i's sum represents the single-step condition $|h_{i+1}(t) - h_i(t)| = 1$, while the conservation of the total number of activators N appears explicitly as a Kronecker delta. Eq. (3.6), then, consists of a Bernoulli product measure for the interface slopes (each slope $h_{i+1} - h_i$ is either 1 or -1 with probability 1/2) multiplied by a Poisson product measure with intensity $(q_+ + q_-)^{-1}$ for the activator numbers. The proof, which is required for the derivations of subsection 3.1.2 and subsection 3.1.3, follows the lines of the calculation of the steady-state probability of zero-range processes (ZRP) [73].

In order to determine when Eq. (3.6) holds, let us write the master equation for $P_t(\{h_i\},\{n_i\})$ as

$$\partial_t P_t(\{h_i\},\{n_i\}) = \sum_{j=1}^{L} \partial_t^{(j)} P_t(\{h_i\},\{n_i\}), \tag{3.8}$$

where $\partial_t^{(j)}$ is a shorthand denoting the variations of $P_t(\{h_i\},\{n_i\})$ due to transition occurring at the j-th site, e.g. a change of h_j or an activator jumping in or out the j-th lattice site. $\partial_t^{(j)} P$ depends on the local conformation of the interface, according to the classification introduced in subsection 2.1.1: peaks ($\wedge$), troughs ($\vee$) and slopes ($\nearrow$ or $\searrow$). On positive slopes, such as the sites between the trough at k and the peak at l in Fig. 3.1 (blue dashed lines), there are no interface transitions allowed, while the activators hop to the right at rate q_- or

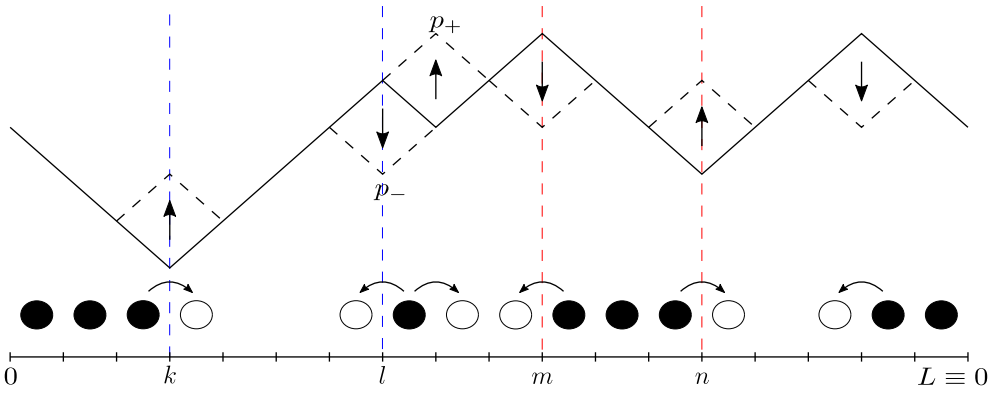

Figure 3.1 *SEP/single-step mapping. The mapping relates the configurations of a single-step interface on the lattice $i = 1, \ldots, L$ and those of an asymmetric exclusion process on the half-lattice $i+1/2$ by associating particles with negative slopes and holes with positive slopes. The transitions $\vee \to \wedge$ and $\wedge \to \vee$ correspond to particle-hole exchange transitions. The blue, dashed vertical lines delimit a cluster of holes/positive slopes between sites k and l while the red, dashed lines delimit a cluster of particles/negative slopes between sites m and n.*

to the left at rate q_+. Hence, for $k < j < l$,

$$\begin{aligned}\partial_t^{(j)} P_t(\{h_i\},\{n_i\}) =&(n_{j-1}+1)q_- P_t\left(\{h_i\},\ldots,n_{j-1}+1,n_j-1,\ldots\right)\\ &+(n_{j+1}+1)q_+ P_t\left(\{h_i\},\ldots,n_j-1,n_{j+1}+1,\ldots\right)\\ &-\left[n_j(q_++q_-)\right]P_t\left(\{h_i\},\ldots,n_{j-1},n_j,n_{j+1},\ldots\right),\end{aligned} \tag{3.9}$$

The first term in Eq. (3.9) stems from the transition $(n_{j-1}+1, n_j-1) \to (n_{j-1}, n_j)$ (total rate $(n_{j-1}+1)q_-$), the second from the transition $(n_j - 1, n_{j+1} + 1) \to (n_j, n_{j+1})$ (total rate $(n_{j+1}+1)q_+$) and the last from $(n_j, n_{j+1}) \to (n_j-1, n_{j+1}+1)$ and $(n_{j-1}, n_j) \to (n_{j-1}+1, n_j-1)$. As in simple asymmetric random walks [73], the right-hand side of Eq. (3.9) vanishes on P_{ss} given by Eq. (3.6), with

$$f(n) = \prod_{l=1}^{n} \frac{1}{l(q_+ + q_-)} = \frac{(q_+ + q_-)^{-n}}{n!}. \tag{3.10}$$

On negative slopes, such as the sites between the peak at m and the trough at n in Fig. 3.1 (red dashed lines), activators hop to the right at rate q_+ or to the left at rate q_-. Thus, the contribution to $\partial_t^{(j)} P$ with $m, j < n$ is obtained by swapping q_+ and q_- in Eq. (3.9) and vanishes for the same choice of $f(n)$ as Eq. (3.10).

On troughs and peaks also interface transition contribute to $\partial_t^{(j)} P$. On troughs such as the k-th and n-th site of Fig. 3.1, the positive contributions to $\partial_t^{(j)} P$

come from activators hopping from the neighbouring site at rate q_+ and a peak of height $h_k + 2$ becoming a trough (rate $p_-(n_k)$). The negative contributions include activators jumping out of the trough at rate q_- or the trough becoming a peak (rate $p_+(n_k)$). Therefore

$$\begin{aligned}\partial_t^{(k)} P_t(\{h_i\},\{n_i\}) =& p_-(n_k) P_t(\dots, h_k+2, \dots, \{n_i\}) \\ & -p_+(n_k) P_t(\dots, h_k, \dots, \{n_i\}) \\ & +(n_{k-1}+1) q_+ P_t(\{h_i\}, \dots, n_{k-1}+1, n_k-1, \dots) \\ & +(n_{k+1}+1) q_+ P_t(\{h_i\}, \dots, n_k-1, n_{k+1}+1, \dots) \\ & -2 n_k q_- P_t(\{h_i\}, \dots, n_{k-1}, n_k, n_{k+1}, \dots),\end{aligned} \tag{3.11}$$

Upon substituting P_t with P_{ss} from Eq. (3.6), the right-hand side of the above equation becomes

$$\left[p_-(n_j) - p_+(n_j)\right] Z_{L,N}^{-1} \left[\prod_{i=1}^{L} f(n_i)\right] + 2\left(q_+ - q_-\right) Z_{L,N}^{-1} \left[\prod_{i=1}^{L} f(n_i)\right], \tag{3.12}$$

which vanishes for all $n_k = 1, \dots, N$ if and only if

$$p_+(n_k) - p_-(n_k) = 2\left(q_+ - q_-\right) n_k. \tag{3.13}$$

Crucially, the condition expressed by Eq. (3.13) ensures that $\partial_t^{(j)} P$ vanishes also on peaks such as the l-th and m-th site of Fig. 3.1, whose contribution to the master equation can be obtained by substituting, in Eq. (3.11), q_+ with q_-, p_+ with p_- and h_k+2 with h_k-2. With our choice of rates $q_\pm = q \pm \gamma/2$, $p_- = p$, $p_+ = p + \lambda n_k$ Eq. (3.13) is satisfied if $\lambda = 2\gamma$. Notice that the measure Eq. (3.6), which assigns the same probability to each allowed interface configuration, is compatible with the roughness exponent $\alpha = 0.5$ found in Monte Carlo simulations of the model with $\lambda = 2\gamma$ (cf. subsection 2.3.1).

3.1.2 Deterministic equations

Following the programme outlined in the introduction, we here derive the deterministic active interface equations Eq. (3.4) for the coarse-grained interface slope $u(x,t)$ and activator density $\rho(x,t)$. The derivation follows that of the hydrodynamic limit of general interacting particle systems [72]. It is particularly fruitful, in this respect, to make use of the well-known mapping between single-

step interfaces and simple exclusion processes (SEP) [49]: the mapping, illustrated in Fig. 3.1, transforms the interface into a particle system on the half-lattice $i + 1/2$, $i = 1, \ldots, L$, such that a particle is associated to every negative slope and a hole to every positive slope. The exclusion process state is determined by the occupation numbers $\tau_{i+\frac{1}{2}}$, which are related to the interface heights,

$$1 - 2\tau_{i+\frac{1}{2}} = h_{i+1} - h_i. \tag{3.14}$$

The single-step condition causes $\tau_{i+\frac{1}{2}}$=0, 1, providing the exclusion interaction.

Central to the derivation is the net current of slopes/SEP particles from $i - 1/2$ to $i + 1/2$ between t and $t + dt$, called dJ_t^i. On the one hand, the difference in currents between neighbouring sites determines the variation of the occupation numbers as

$$d\tau_{i+\frac{1}{2}}(t) = -dJ_t^{i+1} + dJ_t^i \equiv -\Delta dJ_t^i, \tag{3.15}$$

where Δ is a shorthand for the (forward) lattice gradient. On the other hand, each dJ_t^i is the sum of two Poisson processes, one counting the hops from $i-1/2$ to $i+1/2$ (let us call it $dJ_t^{i,+}$) and the other counting the hops in the opposite direction ($dJ_t^{i,-}$). Hence, averages and variances of the dJ_t^i's can be simply expressed in terms of the (site-dependent) rates of the Poisson processes $dJ_t^{i,\pm}$. As sketched in Fig. 3.1, right hops across the i-th site occur at rate $p_+(i)$ while left hops occur at rate $p_-(i)$. To these bare rates one must add the exclusion interaction, which causes the effective rates of forbidden transitions to vanish. Specifically,

$$\begin{aligned} p_+(i) &\to p_+(i) \left[\tau_{i-\frac{1}{2}} \left(1 - \tau_{i+\frac{1}{2}}\right)\right], \\ p_-(i) &\to p_-(i) \left[\tau_{i+\frac{1}{2}} \left(1 - \tau_{i-\frac{1}{2}}\right)\right], \end{aligned} \tag{3.16}$$

meaning that each hop (e.g., the right hop with rate p_+) occurs *iff* the departure site is occupied ($\tau_{i-\frac{1}{2}} = 1$) and the arrival site is empty ($\tau_{i+\frac{1}{2}} = 0$). The effective hopping rates depend on the interface/SEP configuration through the exclusion factors in square brackets and on the activators distribution through the bare rates $p_\pm(i) = p_\pm(n_i)$. Thus, the computation of dJ_t^i's average is a two-step process, where the first average is performed at *fixed* configuration ($\{n_i\}, \left\{\tau_{i+\frac{1}{2}}\right\}$) while the second is an average *over* the configurations. As the hopping processes are Poisson, the first average yields the transition rates (times the time-interval width dt) of the present configuration. The second average, instead, is an average of

the transition rates over the system configurations, i.e.

$$\left\langle dJ_t^i \right\rangle = -\left\langle p_-(i)\left[\tau_{i+\frac{1}{2}}\left(1-\tau_{i-\frac{1}{2}}\right)\right]\right\rangle dt + \left\langle p_+(i)\left[\tau_{i-\frac{1}{2}}\left(1-\tau_{i+\frac{1}{2}}\right)\right]\right\rangle dt. \quad (3.17)$$

After a simple manipulation, $\langle dJ_t^i \rangle$ can be written in a more convenient form,

$$\begin{aligned}\left\langle dJ_t^i \right\rangle = &-\left\langle \frac{p_+(i)+p_-(i)}{2}\left(\tau_{i+\frac{1}{2}}-\tau_{i-\frac{1}{2}}\right)\right\rangle dt \\ &+\left\langle \frac{p_+(i)-p_-(i)}{2}\left(\tau_{i-\frac{1}{2}}+\tau_{i+\frac{1}{2}}-2\tau_{i-\frac{1}{2}}\tau_{i+\frac{1}{2}}\right)\right\rangle dt.\end{aligned} \quad (3.18)$$

Notice that, upon averaging over the Poisson hopping processes, the net current over dt becomes proportional to dt, hence infinitesimally small for $dt \to 0$.

In the next step of the derivation, the averages on Eq. (3.18)'s right-hand side are factorised by resorting to a *local equilibrium* assumption [69]. As shown in subsection 3.1.1, the invariant measure of the active interface system is a product measure with uniform density, meaning that the probabilities of the lattice variables do not depend on the lattice site. Although such a measure allows the factorisation of averages in the $L \to \infty$ limit, it also implies that $\langle n_i \rangle$ and $\langle h_i \rangle$ (together with $\langle \tau_{i+1/2} \rangle$) do not depend on i, so that the functions $u(x,t)$ and $\rho(x,t)$ are constant functions of x. The derivation of PDEs would then be meaningless, unless the invariance of a product measure with constant density is extended to product measures with a density which varies slowly in space. In fact, this extension is the content of the local equilibrium assumption. Consider, for instance, the activator distribution at time t to be a product measure with density $\rho(x)$, i.e.

$$\langle n_i(t) \rangle = \rho(x,t)|_{x=i/L}. \quad (3.19)$$

As ρ is continuous, the difference in the average occupation number between neighbouring sites can be made infinitesimally small in the large-L limit. In other words, the chosen measure becomes, as $L \to \infty$, a product measure with locally uniform density and, as such, justifies the factorisation of averages.

Therefore, by defining (in complete analogy with Eq. (3.1))

$$\tau_L(x,t) = \sum_{i=1}^{L} \left\langle \tau_{i+\frac{1}{2}}(t) \right\rangle \chi_{\left[\frac{i}{L},\frac{i+1}{L}\right)}(x), \quad (3.20)$$

then averaging Eq. (3.15) and substituting Eq. (3.18) for the right-hand side, we

get, for $x \in \left[\frac{i}{L}, \frac{i+1}{L}\right)$,

$$\begin{aligned}\frac{\partial}{\partial t}\tau_L(x,t) \simeq \Delta\left[\left(p+\frac{\lambda}{2}\rho_L(x,t)\right)\Delta\tau_L(x-1/L,t)\right] \\ -\frac{\lambda}{2}\Delta\left[\rho_L(x,t)\left(\tau_L(x,t)+\tau_L(x-1/L,t)-2\tau_L(x,t)\tau_L(x-1/L,t)\right)\right],\end{aligned} \tag{3.21}$$

where, in agreement with our choice of parameters, $(p_+(n_i)-p_-(n_i))/2$ has been substituted with $\lambda n_i/2$ and $(p_+(n_i)+p_-(n_i))/2$ with $p+\lambda n_i/2$ (see Eq. (3.13) and the lines that follow it). The approximation in the above equality stems from the small correlations neglected in factorising $\left\langle \tau_{i-\frac{1}{2}}\tau_{i+\frac{1}{2}}\right\rangle$. In fact, the measure of Eq. (3.6) implies a small correlation between the $\tau_{i+1/2}$'s: due to PBC on the height, $\sum_i \tau_{i+1/2} = L/2$, giving a small anticorrelation $\sim 1/L$ to pairs of $\tau_{i+1/2}$'s.

As L gets larger, this approximation becomes exact and τ_L and ρ_L can be replaced with their continuum limits $\tau(x,t)$ and $\rho(x,t)$ with negligible error. Furthermore, as τ and ρ are smooth, the lattice gradient Δ equals the scaled space-derivative $\partial_x \times 1/L$ plus contributions of order $1/L^2$. Therefore,

$$\begin{aligned}\partial_t\tau_L(x,t) = \frac{1}{L^2}\partial_x\left[\left(p+\frac{\lambda}{2}\rho_L(x,t)\right)\partial_x\tau_L(x,t)\right] \\ -\frac{1}{L}\lambda\partial_x\left[\rho_L(x,t)\left(\tau_L(x,t)-\tau_L^2(x,t)+\mathcal{O}(1/L)\right)\right]+\mathcal{O}(1/L^2).\end{aligned} \tag{3.22}$$

The right-hand side of the equation above vanishes as $L\to\infty$, consistently with the fact that the system's measure becomes locally uniform, hence invariant. However, if p/L^2 tends to some constant ν when $L\to\infty$, while $\lambda/2L \to \Lambda$, then Eq. (3.22) converges to a PDE for τ which, after the change of variable $1-2\tau = u$ (cf. Eq. (3.14)), becomes

$$\partial_t u = \Lambda\partial_x\left[\rho\left(1-u^2\right)\right]+\nu\partial_{xx}^2 u. \tag{3.23}$$

The different scaling of symmetric fluctuations ($p\sim L^2$) and the rates asymmetry ($(p_+-p_-)\propto\lambda\sim L$) is required to keep both diffusive and advective contributions in the equations. It should also be noted that, according to the discussion above, the hydrodynamic limit provides more than equations for averages. Specifically, if the system initial state is sampled from a product measure with slowly-varying density as in Eq. (3.19), the limit guarantees that, at later times, the state of the system can still be described with a product measure with slowly-varying density and provides an equation for such density.

The steps required to derive the density equation parallels those we have followed in deriving Eq. (3.23). The starting point is the analogue of Eq. (3.15), i.e.

$$dn_i(t) = -dJ_t^{i+\frac{1}{2}} + dJ_t^{i-\frac{1}{2}} \equiv -\Delta dJ_t^{i-\frac{1}{2}}, \tag{3.24}$$

where $dJ_t^{i-\frac{1}{2}}$ stands for the net current of activators between the $i-1$-th and the i-th site. This current includes a positive contribution counting the hops from $i-1$ to i and a negative contribution counting the opposite hops. As each activator hops independently, the effective jump rate is proportional to the number of activators at the departure site. In addition, the bare jump rate depends on the interface slope between the two sites:

$$\begin{aligned} q(i-1 \to i) &= q_+ \tau_{i-\frac{1}{2}} + q_- \left(1 - \tau_{i-\frac{1}{2}}\right), \\ q(i \to i-1) &= q_- \tau_{i-\frac{1}{2}} + q_+ \left(1 - \tau_{i-\frac{1}{2}}\right), \end{aligned} \tag{3.25}$$

so that, if $\tau_{i-1/2} = 1$ (negative slopes), activators hop right at rate q_+ and left at rate q_-, while, if $\tau_{i-1/2} = 0$ (positive slopes), activators hop left at rate q_+ and right at rate q_-.

Once again, the current must be averaged over the hopping process at fixed configuration first and then over configurations, i.e.

$$\begin{aligned} \left\langle dJ_t^{i-\frac{1}{2}} \right\rangle = &- \left\langle n_i \left(q_- \tau_{i-\frac{1}{2}} + q_+ \left(1 - \tau_{i-\frac{1}{2}}\right)\right)\right\rangle dt \\ &+ \left\langle n_{i-1} \left(q_+ \tau_{i-\frac{1}{2}} + q_- \left(1 - \tau_{i-\frac{1}{2}}\right)\right)\right\rangle dt, \end{aligned} \tag{3.26}$$

which can be written in the more convenient form,

$$\begin{aligned} \left\langle dJ_t^{i-\frac{1}{2}} \right\rangle = &- \left\langle \frac{q_+ + q_-}{2} \left(n_i - n_{i-1}\right) \right\rangle dt \\ &- \left\langle \frac{q_+ - q_-}{2} \left(n_i + n_{i-1}\right) \left(1 - 2\tau_{i-\frac{1}{2}}\right) \right\rangle dt. \end{aligned} \tag{3.27}$$

After substituting $(q_+ + q_-)/2$ with q, $(q_+ - q_-)/2$ with $\gamma/2$, rescaling time so that

$$q/L^2 \xrightarrow{L\to\infty} D, \quad \gamma/L = \lambda/2L \xrightarrow{L\to\infty} \Lambda, \tag{3.28}$$

and substituting $1 - 2\tau$ with u, the deterministic density equation reads

$$\partial_t \rho = \Lambda \partial_x \left(\rho u\right) + D \partial_{xx}^2 \rho. \tag{3.29}$$

3.1.3 Stochastic corrections

The deterministic equations emerge from the average of Eq. (3.15) and Eq. (3.24), which express the infinitesimal (on average) variation in the lattice variable as the discrete gradient of infinitesimal (on average) currents, e.g. (Eq. (3.24))

$$dn_i(t) = -\Delta dJ_t^{i-\frac{1}{2}} = -\Delta\left[\left\langle dJ_t^{i-\frac{1}{2}}\right\rangle + \text{stochastic contributions}\right], \tag{3.30}$$

where the stochastic corrections to the mean current $\left\langle dJ_t^{i-\frac{1}{2}}\right\rangle$ average to 0 by definition. When sufficiently close to the mean current, the stochastic contributions can be represented as Gaussian random variables whose variance matches the variance of $dJ_t^{i-\frac{1}{2}}$, i.e.

$$dn_i(t) \simeq -\Delta\left[\left\langle dJ_t^{i-\frac{1}{2}}\right\rangle + \sqrt{\left\langle (dJ_t^{i-\frac{1}{2}})^2\right\rangle - \left\langle dJ_t^{i-\frac{1}{2}}\right\rangle^2}\,\xi_i(t)\right], \tag{3.31}$$

where the ξ_i's are independent Gaussian random variables with zero mean and unit variance. This Gaussian approximation will not capture higher order cumulants of the lattice variables but provides a controlled route to the addition of stochastic contributions to the deterministic PDEs derived in the previous section.

As each current $dJ_t^{i-\frac{1}{2}}$ is the difference of two Poisson processes counting the number of hops in both directions, the variance is given by the sum of the rates of these Poisson processes (in contrast with the average, given by the difference as in Eq. (3.27)). For the activator number current, for instance,

$$\begin{aligned}\left\langle (dJ_t^{i-\frac{1}{2}})^2\right\rangle - \left\langle dJ_t^{i-\frac{1}{2}}\right\rangle^2 &= \left\langle n_i\left(q_-\tau_{i-\frac{1}{2}} + q_+\left(1-\tau_{i-\frac{1}{2}}\right)\right)\right\rangle dt \\ &\quad + \left\langle n_{i-1}\left(q_+\tau_{i-\frac{1}{2}} + q_-\left(1-\tau_{i-\frac{1}{2}}\right)\right)\right\rangle dt \\ &= q\left\langle (n_i + n_{i-1})\right\rangle dt + \frac{\gamma}{2}\left\langle (n_i - n_{i-1})\left(1-2\tau_{i-\frac{1}{2}}\right)\right\rangle dt.\end{aligned} \tag{3.32}$$

The second term on the above equation right-hand side contains the difference $n_i - n_{i-1}$: the latter vanishes as $1/L$ in the $L \to \infty$ limit, thus will be omitted in what follows. What is left, upon isolating the stochastic term of Eq. (3.31), is

$$\frac{dn_i(t)}{dt} + \Delta\left\langle dJ_t^{i-\frac{1}{2}}\right\rangle \simeq -\Delta\left[\sqrt{q\left\langle (n_i + n_{i-1})\right\rangle}\frac{\xi_i}{\sqrt{dt}}\right]. \tag{3.33}$$

In the continuum limit defined in subsection 3.1.2, q diverges as L^2. The factor $\sqrt{q}$ in Eq. (3.33) is then balanced by the L^{-1} factor coming from the substitution $\Delta \to \partial_x \times 1/L$. Therefore, in the limit described in Eq. (3.28), Eq. (3.31) converges to

$$\partial_t \rho = \Lambda \partial_x (\rho u) + D \partial_{xx}^2 \rho - \partial_x \left(\sqrt{\frac{2D\rho}{L}} \xi(x,t) \right), \tag{3.34}$$

where, in analogy with Eq. (3.1),

$$\xi(x,t) = \lim_{L\to\infty, dt\to 0} \sum_{i=1}^{L} -\frac{\xi_i(t)}{\sqrt{dt/L}} \chi_{\left[\frac{i}{L}, \frac{i+1}{L}\right)}(x). \tag{3.35}$$

Notice that, when the noise is defined as above, the stochastic term is only a $\mathcal{O}(L^{-1/2})$ correction to the leading, average behaviour of the conserved fields.

The $\sqrt{dt/L}$ factor which divides the Gaussian random variable ξ_i guarantees that the spatiotemporal correlations of the space-time noise $\xi(x,t)$ become the typical delta-correlations of a Gaussian white noise in the $dt \to 0, L \to \infty$ limit:

$$\left\langle \frac{\xi_i(t)}{\sqrt{dt/L}} \frac{\xi_j(t')}{\sqrt{dt/L}} \right\rangle = \frac{\delta_{t,t'}}{dt} \times L\delta_{i,j} \xrightarrow[i=\lfloor xL \rfloor, j=\lfloor yL \rfloor]{dt\to 0, L\to\infty} \delta(t-t')\delta(x-y), \tag{3.36}$$

which can be proved by checking that the correlation $\langle \xi(x,t)\xi(x',t') \rangle$ has all the defining properties of a Dirac delta function. Hence, we write

$$\langle \xi(x,t)\xi(x',t') \rangle = \delta(t-t')\delta(x-x'). \tag{3.37}$$

Similar arguments can be applied to the $\tau_{i+\frac{1}{2}}$ dynamics, yielding the stochastic PDE

$$\partial_t \tau = -2\Lambda \partial_x \left[\rho\tau (1-\tau) \right] + \nu \partial_{xx}^2 \tau - \partial_x \left(\sqrt{\frac{2\nu}{L} \tau(1-\tau)} \zeta(x,t) \right), \tag{3.38}$$

which, by setting $1 - 2\tau = u$, becomes

$$\partial_t u = \Lambda \partial_x \left[\rho \left(1 - u^2 \right) \right] + \nu \partial_{xx}^2 u + \partial_x \left(\sqrt{\frac{\nu}{2L} \left(1 - u^2 \right)} \zeta(x,t) \right). \tag{3.39}$$

The noise $\zeta(x,t)$ has the same definition and spatiotemporal correlations of—but is independent from—$\xi(x,t)$.

3.2 Solution of the inviscid limit

The deterministic active interface equations Eq. (3.4) can be solved in the limit where the activators bare diffusion coefficient D and the interface tension ν vanish—the *inviscid* limit. The solution, which is the subject of this section, builds on the structure of conservation laws of the active interface equations:

$$\partial_t \begin{pmatrix} \rho \\ u \end{pmatrix} + \partial_x \begin{pmatrix} -\Lambda\rho u \\ -\Lambda\rho(1-u^2) \end{pmatrix} = 0, \tag{3.40}$$

where the 'viscous' terms, proportional to the Laplacian of the fields, have already been neglected. The equations that we are going to solve are actually a modification of Eq. (3.40). First, we will replace the driving term $\Lambda\rho(1-u^2)$ in the u equation by $\Lambda\rho$, tantamount to neglecting the KPZ-like nonlinearity $(\nabla h)^2$ in the height equation ($\nabla h = u$). This approximation will be justified *a posteriori*, by noticing that the field u remains bounded in all the solutions that will be considered, and it can be made as small as required by rescaling parameters. Secondly, we will extend the active interface equations beyond the $\gamma = \lambda/2$ line of the parameter space of the model (cf. Eq. (3.13)), i.e.

$$\partial_t \begin{pmatrix} \rho \\ u \end{pmatrix} + \partial_x \begin{pmatrix} -\Gamma\rho u \\ -\Lambda\rho \end{pmatrix} = 0. \tag{3.41}$$

As factorisation of correlations between lattice variables of neighbouring sites is no longer guaranteed, the general equations can be considered as a mean-field approximation with respect to the exact limit $\Lambda = \Gamma$.

Given the elementary form of a one-dimensional conservation law for a field φ, i.e. $\partial_t\varphi + \partial_x J_\varphi = 0$, one can immediately define a slope current J_u and an activator current J_ρ from Eq. (3.41). Specifically, the activator current $J_\rho = -\Gamma\rho u$ is proportional to the negative slope and the slope current $J_u = -\Lambda\rho$ is proportional to the negative density of activators. The remainder of the section comprises three parts. Subsection 3.2.1 illustrates the solution strategy via the example of the linearised active interface equations, and also serves as an introduction to the *Riemann problem*: the class of initial conditions for Eq. (3.41) whose evolution in time can be computed. This class can be further split into two sub-classes, giving raise to different solutions. The two sub-classes, called *shock waves* and *rarefaction fans*, are treated in subsection 3.2.2 and subsection 3.2.3, respectively.

3.2.1 Riemann problem for the linear active interface equations

Let $\mathbf{v}$ be a vector having ρ and u as components, and $\mathbf{J}(\mathbf{v})$ the corresponding vectorial current. By defining a matrix $\mathbf{A}(\mathbf{v})$ such that $A_{i,j} = \partial_{v_j} J_i$, Eq. (3.41) can be written compactly as

$$\partial_t \mathbf{v} + \mathbf{A}(\mathbf{v}) \cdot \partial_x \mathbf{v} = \mathbf{0}. \tag{3.42}$$

When equipped with a discontinuous initial condition such as

$$\mathbf{v}(x,t)|_{t=0} = \begin{cases} \mathbf{v}_l, & x < 0, \\ \mathbf{v}_r, & x > 0, \end{cases} \tag{3.43}$$

Eq. (3.44) is called a *Riemann problem* [74]. In the course of this chapter we will refer to a Riemann problem with given initial datum as the $(\mathbf{v}_l, \mathbf{v}_r)$ Riemann problem, with the convention that the first element of the couple $(\mathbf{v}_l, \mathbf{v}_r)$ is the vector of initial data for $x < 0$ while the second element correspond to the $x > 0$ portion of the initial condition. The Riemann problem is useful because, on the one hand, it provides the basic building blocks for the solution of more general initial value problems and, on the other hand, it focuses on the most interesting phenomena which affect a certain class of conservation laws, namely the spontaneous formation and relaxation of discontinuities.

Let us consider, as an introductory example, a linearised Riemann problem, i.e. the solution of a linearisation of Eq. (3.42) with step-like initial condition. The linearised equation is obtained by calculating $\mathbf{A}(\mathbf{v})$ at a specific value $\bar{\mathbf{v}}$, which we choose to be the homogeneous profile compatible with periodic boundary conditions on the height, $\bar{\mathbf{v}} = (\rho_0, 0)$:

$$\partial_t \mathbf{v} + \bar{\mathbf{A}} \cdot \partial_x \mathbf{v} = \mathbf{0}, \quad \bar{\mathbf{A}} \equiv \mathbf{A}(\bar{\mathbf{v}}) = \begin{pmatrix} 0 & -\Gamma' \\ -\Lambda & 0 \end{pmatrix}, \tag{3.44}$$

where $\Gamma' = \Gamma \rho_0$. Eq. (3.44) becomes exact in the limit of high density, where variations in the latter with respect to the homogeneous profile ρ_0 are relatively small. Let $\bar{\lambda}_i$ denote the i-th eigenvalue of $\bar{\mathbf{A}}$ (solution of $\det(\bar{\mathbf{A}} - \bar{\lambda}\mathbf{I}) = 0$) and

$\bar{\mathbf{l}}_i$ the corresponding left eigenvector (such that $\bar{\mathbf{l}}_i \cdot \bar{\mathbf{A}} = \bar{\lambda}_i \bar{\mathbf{A}}$). Namely,

$$\bar{\lambda}_1 = -\sqrt{\Gamma' \Lambda}, \quad \bar{\lambda}_2 = \sqrt{\Gamma' \Lambda}, \quad \bar{\mathbf{l}}_1 = \begin{pmatrix} \sqrt{\Lambda} \\ \sqrt{\Gamma'} \end{pmatrix}, \quad \bar{\mathbf{l}}_2 = \begin{pmatrix} \sqrt{\Lambda} \\ -\sqrt{\Gamma'} \end{pmatrix}, \tag{3.45}$$

so that eigenmodes are labelled in the order of increasing eigenvalues.

By projecting Eq. (3.44) (and the discontinuous initial condition $(\mathbf{v}_l, \mathbf{v}_r)$) on the left eigenvectors, the two-dimensional system decomposes into two independent ones

$$\begin{cases} \partial_t e_i + \lambda_i \partial_x e_i = 0, \\ e_i(x, 0) = e_i^0(x), \end{cases} \tag{3.46}$$

where the e_i's are the system eigenmodes $\bar{\mathbf{l}}_i \cdot \mathbf{v}$ and $e_i^0(x)$ equals $\bar{\mathbf{l}}_i \cdot \mathbf{v}_l$ for $x < 0$ and $\bar{\mathbf{l}}_i \cdot \mathbf{v}_r$ for $x > 0$. The system of equations (3.46) has a trivial solution, $e_i(x, t) = e_i^0(x - \bar{\lambda}_i t)$, where the discontinuity at $x = 0$ travels with speed $\bar{\lambda}_i$. In other terms, the eigenvalues $\bar{\lambda}_i$ identify *characteristic lines* in the $x - t$ plane along which the projections $e_i = \bar{\mathbf{l}}_i \cdot \mathbf{v}$ are constant.

The solution in the $\mathbf{v}$ variables is finally obtained by resorting to the strict hyperbolicity of Eq. (3.44). A system of conservation laws such as the latter is said *strictly hyperbolic* when the eigenvalues of the matrix of coefficients $\bar{\mathbf{A}}$ are real and distinct. Strict hyperbolicty guarantees that left and right eigenvectors, if properly normalised, form a biorthogonal system, i.e.

$$\bar{\mathbf{l}}_i \cdot \bar{\mathbf{r}}_j = \delta_{ij}, \quad i, j = 1, 2. \tag{3.47}$$

In addition, the eigenvectors allow to decompose any vector $\mathbf{v}$ in the $\mathbf{v}$-space as

$$\mathbf{v} = \sum_{i=1,2} \left(\bar{\mathbf{l}}_i \cdot \mathbf{v} \right) \bar{\mathbf{r}}_i. \tag{3.48}$$

Therefore, the composition of the projections $e_i(x, t)$ with the right eigenvectors $\bar{\mathbf{r}}_i$ yields the solution $\mathbf{v}(x, t)$ of the linearised Riemann problem,

$$\mathbf{v}(x, t) = \begin{cases} \mathbf{v}_l, & x < \bar{\lambda}_1 t, \\ \mathbf{v}_l + \left[\bar{\mathbf{l}}_1 \cdot (\mathbf{v}_r - \mathbf{v}_l) \right] \bar{\mathbf{r}}_1, & \bar{\lambda}_1 t < x < \bar{\lambda}_2 t, \\ \mathbf{v}_l + \displaystyle\sum_{i=1,2} \left[\bar{\mathbf{l}}_i \cdot (\mathbf{v}_r - \mathbf{v}_l) \right] \bar{\mathbf{r}}_i \equiv \mathbf{v}_r, & \bar{\lambda}_2 t < x \ . \end{cases} \tag{3.49}$$

To sum up, the linearised Riemann problem is solved in three steps: *i)* project

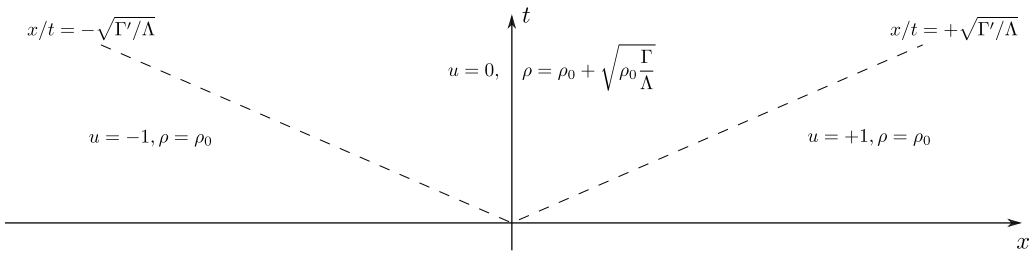

Figure 3.2 *Solution of the giant trough Riemann problem (uniform density $\rho_l = \rho_r = \rho_0$ with slopes $u_l = 1 = -u_r$) for the linearised, inviscid active interface equations. As time progresses, activators accumulate at the bottom of the wedge and make it grow.*

the initial datum, i.e. the step-like discontinuity onto the system left eigenvectors $\bar{\mathbf{l}}_i$; *ii)* transport the projections along characteristic lines $x = \bar{\lambda}_i t$; *iii)* glue the projection together with the right eigenvectors $\bar{\mathbf{r}}_i$, normalised so as to have $\bar{\mathbf{l}}_i \cdot \bar{\mathbf{r}}_j = \delta_{ij}$. Fig. 3.2 displays the solution of the Riemann problem with $\rho_l = \rho_r = \rho_0$ and $u_l = -u_r = -1$. We refer to this particular initial condition as the giant trough, because it represents an infinitely wide trough in the height variable, uniformly filled with activators (cf. Fig. 3.4). In the solution, activators accumulate at the bottom of the trough while flattening the trough itself (cf Fig. 3.6).

3.2.2 Nonlinear equations: shock waves

In the nonlinear problem the matrix $\mathbf{A}$ is a function of the variable $\mathbf{v}$ (cf. Eq. (3.42)) and reads

$$\mathbf{A}(\mathbf{v}) = \begin{pmatrix} -\Gamma u & -\Gamma\rho \\ -\Lambda & 0 \end{pmatrix}. \tag{3.50}$$

The eigenvalues, also functions of ρ and u, are (in increasing order)

$$\lambda_{1/2} = -\Gamma u/2 \mp \sqrt{\Gamma^2 u^2/4 + \Lambda\Gamma\rho}, \tag{3.51}$$

They are real for positive Γ and Λ and distinct as long as u and ρ do not vanish simultaneously. The matrix $\mathbf{A}(\mathbf{v})$ is thus *strictly hyperbolic* for $\rho > 0$. Hyperbolicity, as in the linear case of subsection 3.2.1, is a crucial property for the solution of the Riemann problem. In the nonlinear problem, however, due to the eigenvectors dependence on ρ and u, the eigenvector basis is only local, so that a generic initial discontinuity with arbitrarily far left and right states cannot be decomposed along the system eigenvectors. This apparent issue is solved via the definition of shock and rarefaction curves, which cover the whole

physical section of the ρ, u plane and have the right eigenvectors of $\mathbf{A}(\mathbf{v})$ as local tangents. The present subsection focuses on shock curves, which are derived and used to solve the giant trough Riemann problem for the nonlinear equations. Rarefaction curves are derived in the next subsection.

3.2.2.1 Shock curves and the giant trough

A shock wave is a propagating discontinuity. Due to the lack of derivative at the shock front, a shock wave cannot be a solution of Eq. (3.42) in the classical sense, but it can still be a solution in the weak sense (cf. Appendix B). As in the scalar conservation law case, discussed in the appendix, the speed σ of the propagating discontinuity—the shock speed—satisfies the Rankine-Hugoniot condition

$$\mathbf{J}(\mathbf{v}_r) - \mathbf{J}(\mathbf{v}_l) = \sigma\left(\mathbf{v}_r - \mathbf{v}_l\right), \tag{3.52}$$

where $\mathbf{J}$ is the current vector with components $J_\rho = -\Gamma\rho u$, $J_u = -\Lambda\rho$ and $\mathbf{v}_{l/r}$ denotes the value of the system variables on the left/right of the discontinuity.

For a fixed $\mathbf{v}_l$, Eq. (3.52) defines a curve in the $\mathbf{v}$-space, set of all the points (ρ, u) which satisfy

$$\begin{aligned} \sigma(\rho - \rho_l) &= -\Gamma(\rho u - \rho_l u_l), \\ \sigma(u - u_l) &= -\Lambda(\rho - \rho_l). \end{aligned} \tag{3.53}$$

Once σ is eliminated from the equations, there remains a quadratic equation for ρ as a function of u (or vice versa) and $\mathbf{u}_l$. The two solutions for ρ are

$$\begin{aligned} \rho_1(u;\mathbf{v}_l) &= \rho_l + \frac{u-u_l}{\Lambda}\left[\Gamma u/2 + \sqrt{\Gamma^2u^2/4 + \Gamma\Lambda\rho_l}\right], \\ \rho_2(u;\mathbf{v}_l) &= \rho_l + \frac{u-u_l}{\Lambda}\left[\Gamma u/2 - \sqrt{\Gamma^2u^2/4 + \Gamma\Lambda\rho_l}\right]. \end{aligned} \tag{3.54}$$

The graphs of $\rho_1(u)$ and $\rho_2(u)$, shown in Fig. 3.3, are the aforementioned *shock curves*. Let us call them $\mathbf{v}^s_{1/2}$ and parametrise them with u, e.g. $\mathbf{v}^s_1(u;\mathbf{v}_l)$ has components $(\rho_1(u;\mathbf{v}_l), u)$.

By definition of the shock curves, the $(\mathbf{v}_l, \mathbf{v}^s_i(u,\mathbf{v}_l))$ Riemann problem is solved by a shock wave with shock speed σ_i given by the Rankine-Hugoniot conditions. σ_i can also be written as a function of u and $\mathbf{v}_l$,

$$\begin{aligned} \sigma_1(u;\mathbf{v}_l) &= -\Gamma u/2 - \sqrt{\Gamma^2u^2/4 + \Lambda\Gamma\rho_l}, \\ \sigma_2(u;\mathbf{v}_l) &= -\Gamma u/2 + \sqrt{\Gamma^2u^2/4 + \Lambda\Gamma\rho_l}. \end{aligned} \tag{3.55}$$

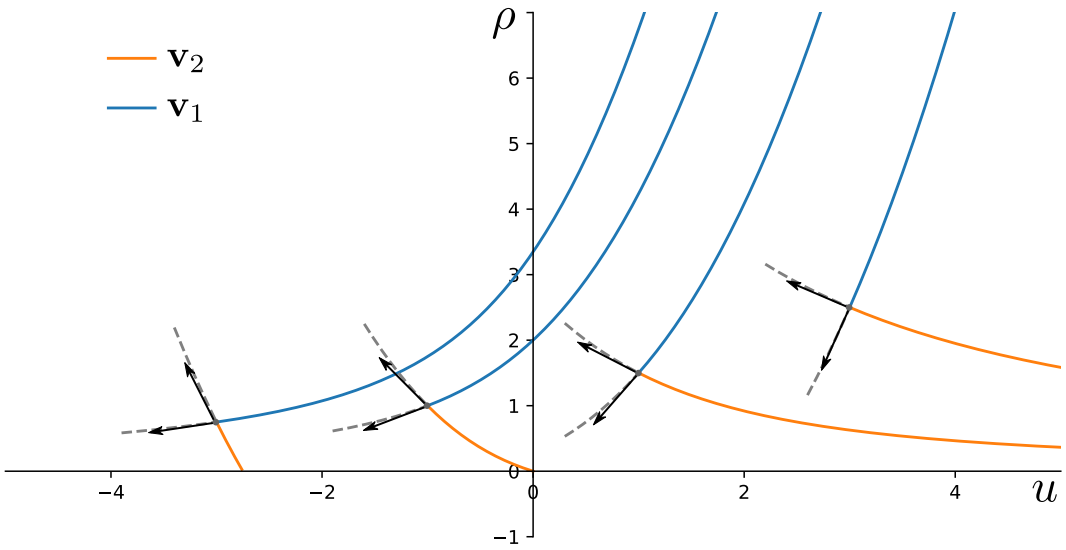

Figure 3.3 *Shock curves of the active interface equations for several left states* $\mathbf{v}_l$ *(see discussion in the text).* $\mathbf{v}_1^s$ *(*$\mathbf{v}_2^s$*) denotes the graph of the function* $\rho_1(u)$ *(*$\rho_2(u)$*), i.e the first (second) shock curve. The grey dashed lines mark the portion of the curves discarded due to not satisfying the Lax entropy condition. The arrows represent the right eigenvectors of* $\mathbf{A}(\mathbf{v})$*, and point towards the direction of increasing eigenvalue.*

By performing a $\rho, u \to \rho_l, u_l$ limit of Eq. (3.52–3.55), it can be shown that the i-th shock curve tangent tends to the i-th eigenvector of $\mathbf{A}(\mathbf{v}_l)$ (see Fig. 3.3), whereas σ_i tends to the corresponding eigenvalue. The eigenvalues, as for the linearised equations, define the slopes of characteristic lines in the $x - t$ plane. Hence, it is natural to extend the Lax condition Eq. (B.9) as [75]

$$\lambda_i(\mathbf{v}_l) \geq \sigma_i(u; \mathbf{v}_l) \geq \lambda_i(\mathbf{v}_i^s(u, \mathbf{v_l})), \tag{3.56}$$

so that characteristic lines can end on a shock front but never emanate from it. In order to meet these conditions, the portion of the shock curves with $u < u_l$ must be discarded. In the language of the active interface equations, a shock develops only if the interface slope is higher on the right than on the left.

We are now able to compute the evolution of the giant trough initial condition (see Fig. 3.4), which was already considered in the linearised case (subsection 3.2.1). The solution amounts to combining two shock waves travelling in opposite directions. The giant trough initial condition has $u_l = -1, \rho_l = \rho_0$ and $\rho_r = \rho_l = \rho_0$ but $u_r = +1$, so that $u_r > u_l$. As shown in Fig. 3.5 left panel, $\mathbf{v}_r$ is neither on $\mathbf{v}_1^s$ nor $\mathbf{v}_2^s$: we need to proceed, as in the linearised problem, by decomposing $\mathbf{v}_r - \mathbf{v}_l$ along the right eigenvectors of $\mathbf{A}(\mathbf{v})$. The only difference with

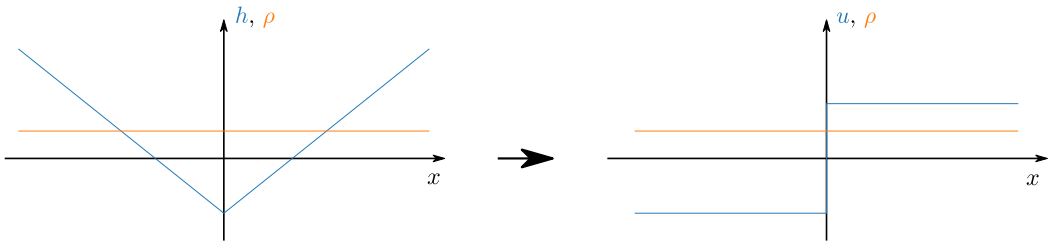

Figure 3.4 *The giant trough initial condition in the height variable (left panel) becomes a step in the slope variable (right panel).*

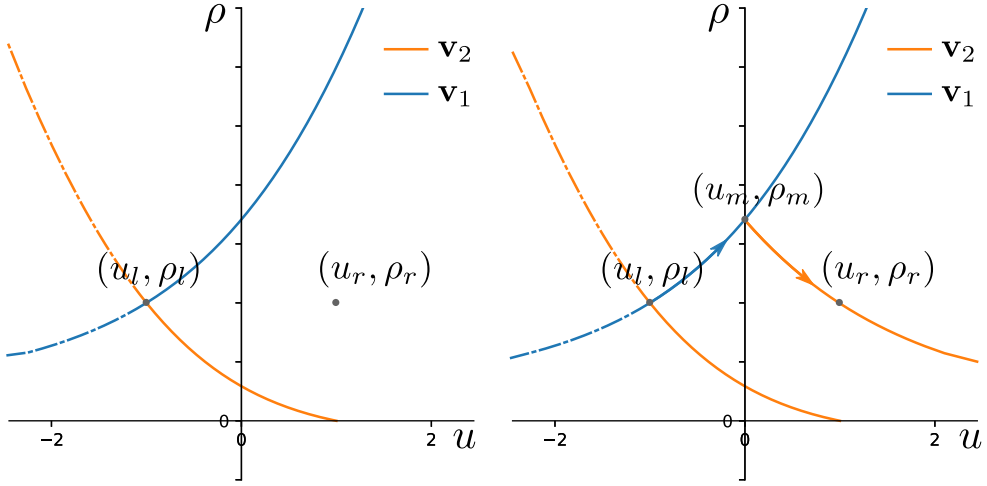

Figure 3.5 *Schematic representation of the giant trough Riemann problem in the* $\mathbf{v}$*-plane. The relevant part of the shock curves are shown as solid lines. The intermediate state must be reached via the curve* $\mathbf{v}_1^s$*, as shown in the right panel, so that the two waves which form the full solution do not collide.*

the linear case is that the eigenvectors depend on $\mathbf{v}$, thus we will not connect $\mathbf{v}_r$ to $\mathbf{v}_l$ with two straight lines but with two curves—the shock curves. Specifically, we will move along $\mathbf{v}_1^s(u;\mathbf{v_l})$, until we hit a point $\mathbf{v}_m = (\rho_1(u_m;\mathbf{v}_l), u_m)$, such that $\mathbf{v}_r$ lies on the second shock curve emanating from $\mathbf{v}_m$, i.e. $\mathbf{v}_2^s(u_r;\mathbf{v}_m) = \mathbf{v}_r$. The path from $\mathbf{v}_l$ to $\mathbf{v}_r$, through $\mathbf{v}_m$, is highlighted by the arrows in the right panel of Fig. 3.4. The equation for the intermediate state $\mathbf{v}_m$, is

$$\mathbf{v}_2^s(u_r;\mathbf{v}_1^s(u_m;\mathbf{v}_l)) = \mathbf{v}_r \Rightarrow \rho_2(u_r;\mathbf{v}_m) = \rho_r \tag{3.57}$$

and it is solved by

$$u_m = 0, \quad \rho_m = \rho_1(0;\mathbf{v}_l) = \rho_0 + \sqrt{\rho_0 \frac{\Gamma}{\Lambda}}. \tag{3.58}$$

The giant trough Riemann problem solution follows by gluing the two shock waves

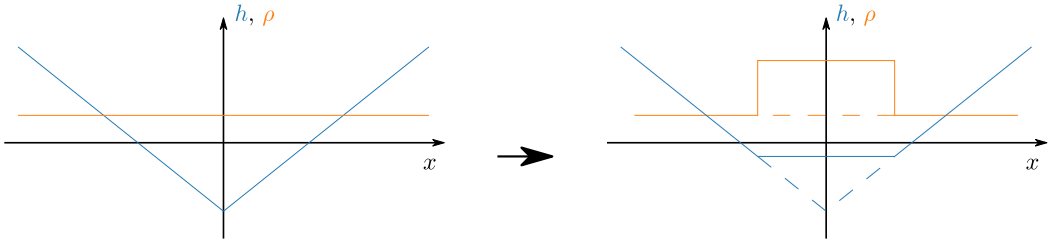

Figure 3.6 *Evolution of the giant trough initial condition in the height variable. The density profile is a top hat function which extends with the shock speeds. The increased density signals an accumulation of activators at the center of the valley, which, consequently, is flattened.*

together,

$$(\rho, u)(x,t) = \begin{cases} (\rho_0, -1), & x/t < -\sqrt{\Lambda\Gamma\rho_0}, \\ \left(\rho_0 + \sqrt{\dfrac{\Gamma}{\Lambda}}\rho_0, 0\right), & -\sqrt{\Lambda\Gamma\rho_0} < x/t < \sqrt{\Lambda\Gamma\rho_0}, \\ (\rho_0, +1), & \sqrt{\Lambda\Gamma\rho_0} < x/t, \end{cases} \tag{3.59}$$

where $-$ and $+\sqrt{\Lambda\Gamma\rho_0}$ come from $\sigma_1(u_m; \mathbf{v}_l)$ and $\sigma_2(u_r; \mathbf{v}_m)$, respectively. Following the shock curves in the order of increasing eigenvalue (first $\mathbf{v}_1^s$, then $\mathbf{v}_2^s$) ensures that $\sigma_1 < \sigma_2$, i.e. the two shock waves do not collide.

The solution of the giant trough problem is shown in the height variable in Fig. 3.6. The solution coincides with that of the linear problem: it entails two shock fronts emanating from the apex of the trough and leaving behind a region of increased density and height.

3.2.3 Nonlinear equations: rarefaction fans

When $u_r < u_l$ the Lax condition Eq. (3.56) is not satisfied. Intuition coming from the study of scalar conservation laws (cf. Appendix B) suggest that, in such a case, the step-like initial condition will smooth out as a rarefaction fan rather than propagating as a shock wave. The specific form of the rarefaction fan is found by plugging into Eq. (3.41) the generic functional form of a rarefaction fan $\mathbf{v}(x,t) = \mathbf{v}(x/t)$. The equation becomes

$$[\mathbf{A}(\mathbf{v}(\xi)) - \xi\mathbf{I}] \cdot \mathbf{v}'(\xi) = 0, \tag{3.60}$$

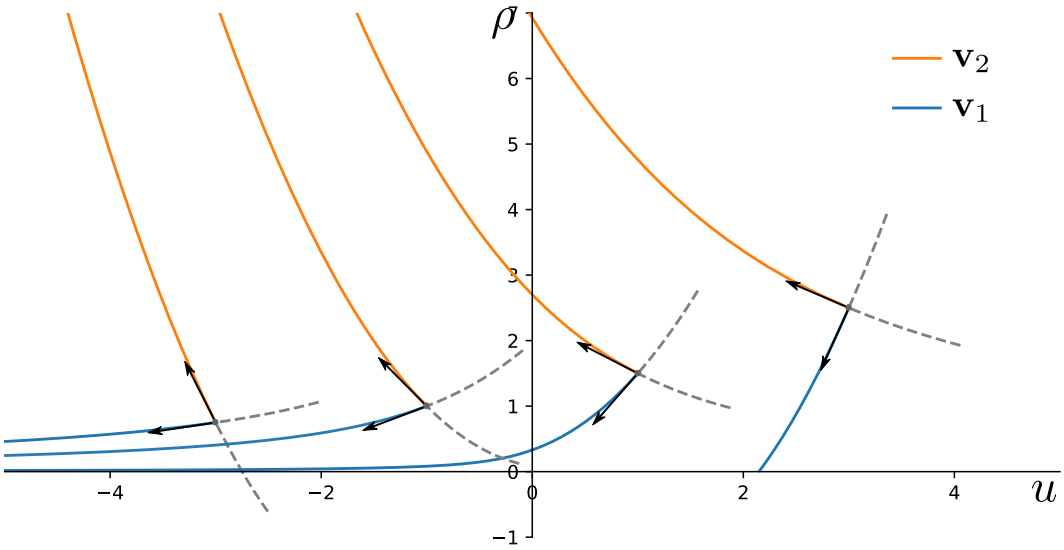

Figure 3.7 *Rarefaction curves of the active interface equations for several left states* $\mathbf{v}_l$ *(see discussion in the text).* $\mathbf{v}_1^r$ *(*$\mathbf{v}_2^r$*) denotes the first (second) rarefaction curve. The grey dashed lines mark the portion of the curves discarded due to the increasing eigenvalue constraint. The arrows represent the right eigenvectors of* $\mathbf{A}(\mathbf{v})$*, and point towards the direction of increasing eigenvalue.*

in the variable $\xi = x/t$, with the prime denoting derivative w.r.t. ξ. Eq. (3.60) is identically satisfied provided $\mathbf{v}'$ coincides with the right eigenvector of $\mathbf{A}(\mathbf{v})$ of eigenvalue ξ, or, compactly,

$$\begin{cases} \mathbf{v}'(\xi) = \mathbf{r}_i(\mathbf{v}(\xi)), \\ \lambda_i(\mathbf{v}(\xi)) = \xi. \end{cases} \tag{3.61}$$

$\lambda_i(\mathbf{v}(\xi)) = \xi$ is, in fact, only a condition on the normalisation of the i-th eigenvector. Differentiation of both sides w.r.t. ξ yields $(\nabla_{\mathbf{v}}\lambda_i) \cdot \mathbf{v}'(\xi) = (\nabla_{\mathbf{v}}\lambda_i) \cdot \mathbf{r}_i = 1$. The latter condition can be met by appropriately normalising the eigenvectors, provided

$$(\nabla_{\mathbf{v}}\lambda_i) \cdot \mathbf{r}_i \neq 0. \tag{3.62}$$

The above inequality is called the *genuine nonlinearity condition*, and it will be assumed to hold in subsubsection 3.2.3.1. Violations of Eq. (3.62) will be considered in subsubsection 3.2.3.2.

3.2.3.1 Rarefaction curves and the giant peak

The right eigenvectors of the matrix in Eq. (3.50), normalised so as to satisfy $(\nabla_{\mathbf{v}}\lambda_i)\cdot\mathbf{r}_i = 1$, are

$$\mathbf{r}_1 = \begin{pmatrix} -\frac{\sqrt{\Gamma^2u^2/4+\Lambda\Gamma\rho}}{\Lambda\Gamma} \\ \frac{\sqrt{\Gamma^2u^2/4+\Lambda\Gamma\rho}}{\Gamma\lambda_1} \end{pmatrix}, \quad \mathbf{r}_2 = \begin{pmatrix} \frac{\sqrt{\Gamma^2u^2/4+\Lambda\Gamma\rho}}{\Lambda\Gamma} \\ -\frac{\sqrt{\Gamma^2u^2/4+\Lambda\Gamma\rho}}{\Gamma\lambda_2} \end{pmatrix}. \tag{3.63}$$

Each will give rise to an equation such as Eq. (3.61). We resort to the same approach as in subsection 3.2.2: fix $\mathbf{v}_l$ (the left initial vector of the Riemann problem) and use Eq. (3.61) to find two more curves in the $\mathbf{v}$-plane. These two curves are *rarefaction curves*. As with the shock curves, these curves will connect $\mathbf{v}_l$ to all the points $\mathbf{v}(\xi)$ such that the $(\mathbf{v}_l,\mathbf{v}(\xi))$ Riemann problem is solved by a rarefaction fan. The appropriate initial condition for Eq. (3.61) is then $\mathbf{v}(\xi_0) = \mathbf{v}_l$, with $\xi_0 = \lambda_i(\mathbf{v}_l)$ determined by $\xi = \lambda_i(\mathbf{v}(\xi))$. The two solutions—let us call them $\mathbf{v}_1^r$ and $\mathbf{v}_2^r$—are

$$\begin{pmatrix} \rho_1^r(\xi;\mathbf{v}_l) \\ u_1^r(\xi;\mathbf{v}_l) \end{pmatrix} = \begin{pmatrix} \frac{\xi^2}{3\Gamma\Lambda} - \frac{\sqrt{\lambda_1(\mathbf{v}_l)\xi}}{\Lambda}\left[u_l + \frac{2\lambda_1(\mathbf{v}_l)}{3\Gamma}\right] \\ \sqrt{\frac{\lambda_1(\mathbf{v}_l)}{\xi}}\left[u_l + \frac{2\lambda_1(\mathbf{v}_l)}{3\Gamma}\right] - \frac{2\xi}{3\Gamma} \end{pmatrix}, \tag{3.64}$$

and

$$\begin{pmatrix} \rho_2^r(\xi;\mathbf{v}_l) \\ u_2^r(\xi;\mathbf{v}_l) \end{pmatrix} = \begin{pmatrix} \frac{\xi^2}{3\Gamma\Lambda} + \frac{\sqrt{\lambda_2(\mathbf{v}_l)\xi}}{\Lambda}\left[u_l + \frac{2\lambda_2(\mathbf{v}_l)}{3\Gamma}\right] \\ \sqrt{\frac{\lambda_2(\mathbf{v}_l)}{\xi}}\left[u_l + \frac{2\lambda_2(\mathbf{v}_l)}{3\Gamma}\right] - \frac{2\xi}{3\Gamma} \end{pmatrix}. \tag{3.65}$$

In agreement with $(\nabla_{\mathbf{v}}\lambda_i)\cdot\mathbf{r}_i = 1$, only the portion of rarefaction curve along which the corresponding eigenvalue increases shall be retained. As $\lambda_i(\mathbf{v}(\xi)) = \xi$, the eigenvalue increases in the direction of increasing ξ. In the $\mathbf{v}$-space this is the direction of decreasing u, i.e. $u_i^r \leq u_l$. In the language of the active interface, discontinuities consisting of a drop in the slope give rise to rarefaction fans.

The rarefaction curves of the inviscid active interface equations are shown in Fig. 3.7. By definition of $\mathbf{v}_i^r$, the $(\mathbf{v}_l, \mathbf{v}_i^r(\xi,\mathbf{v}_l))$ Riemann problem is solved by a rarefaction fan, whose shape also depends on $\mathbf{v}_i^r(\xi;\mathbf{v}_l)$:

$$\mathbf{v}(x,t) = \begin{cases} \mathbf{v}_l, & x/t < \lambda_i(\mathbf{u}_l) \\ \mathbf{v}_i^r(x/t), & x/t \in [\lambda_i(\mathbf{v}_l), \xi] \\ \mathbf{v}_i^r(\xi;\mathbf{v}_l), & x/t > \xi. \end{cases} \tag{3.66}$$

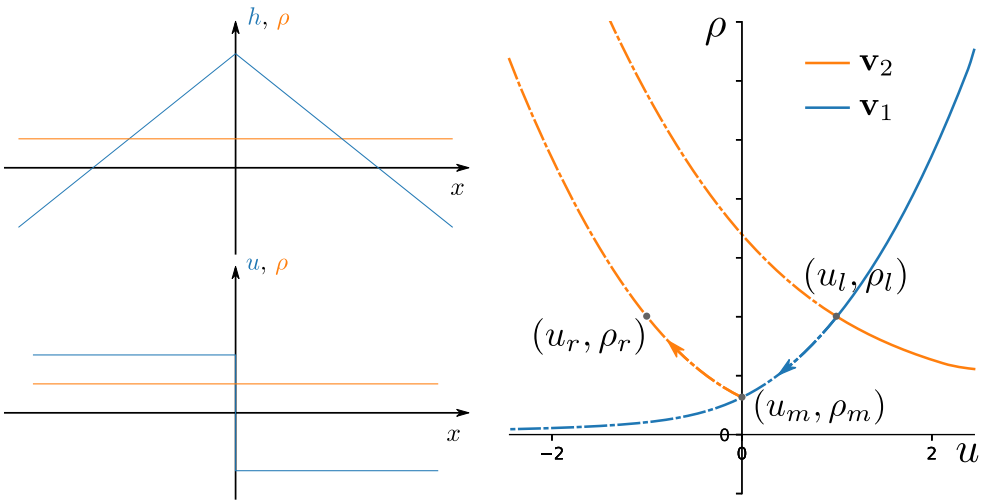

Figure 3.8 *Giant peak initial condition in the slope and height variable (left) and corresponding construction of the solution in the* $\mathbf{v}$*-plane (right). The solution of the giant peak Riemann problem is a double rarefaction fan, with an intermediate density* ρ_m *lower than the initial density* ρ_0*.*

We are now in a position to solve the giant peak Riemann problem $u_l = 1 = -u_r$, $\rho_r = \rho_l = \rho_0$, shown in the left panel of Fig. 3.8 in both the slope and the height variable. The solution amounts to combining two rarefaction waves travelling in opposite directions. The procedure is analogous to that used for shock waves, hence we will not explain it in detail. The solution reads

$$(\rho, u)\,(x,t) = \begin{cases} (\rho_0, +1)\,, & x/t < \lambda_1(\rho_0, +1), \\ (\rho_1^r(x/t), u_1^r(x/t))\,, & \lambda_1(\rho_0, +1) < x/t < \lambda_1(\rho_1(\bar{\xi}), 0), \\ \big(\rho_1(\bar{\xi}), 0\big)\,, & \lambda_1(\rho_1^r(\bar{\xi}), 0) < x/t < \lambda_2(\rho_1^r(\bar{\xi}), 0), \\ (\rho_2^r(x/t), u_2^r(x/t))\,, & \lambda_2(\rho_1^r(\bar{\xi}), 0) < x/t < \lambda_2(\rho_0, -1), \\ (\rho_0, -1)\,, & \lambda_2(\rho_0, -1) < x/t, \end{cases} \tag{3.67}$$

where $\bar{\xi}$ is such that $\mathbf{v}_1^r(\bar{\xi}) = \mathbf{v}_m$ and is found by solving

$$\mathbf{v}_r = \mathbf{v}_2^r(\lambda_2(\rho_r, u_r); \mathbf{v}_1^r(\bar{\xi}; \mathbf{v}_l)).$$

The solution for the giant peak initial condition is shown in Fig. 3.10, left panel: it consists, as anticipated, of two rarefaction waves emanating from the apex of the peak. In propagating, these rarefaction waves leave behind a region where the density is reduced and the height profile is smoothened (the flat solid line in the figure replaces the sharp, dashed wedge). There is, however, a complication arising when the inclusion density at the bottom of the trough is reduced to

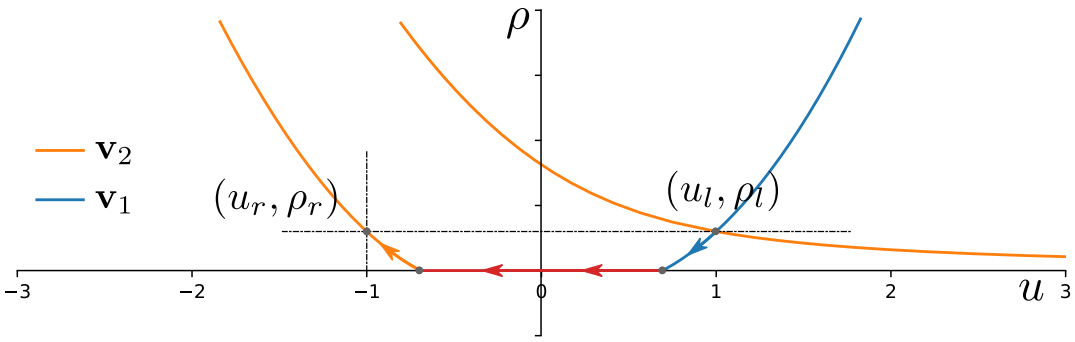

Figure 3.9 *Schematic construction of the solution shown in Eq. (3.69). On the $\rho = 0$ line the system becomes linearly degenerate. As a result, the shock curve collapse onto a horizontal, straight line and can be extended for u smaller than the starting point (see discussion in the text). This horizontal line, shown in red in the figure, can be used to move along the u-axis, down to that point that can be connected directly to $\mathbf{v}_r$ via a rarefaction curve.*

zero, as in the right panel of Fig. 3.10. The density must be physically greater than zero: mathematically, we require ρ_1^r to be positive to satisfy the genuine nonlinearity condition Eq. (3.62). Due to the functional form of $\rho_1^r(\xi; \mathbf{u}_l)$, the condition translates into

$$u_l + \frac{2\lambda_1(\rho_l, u_l)}{3\Gamma} < 0 \Leftrightarrow \rho_l > \rho_c \equiv \frac{3\Gamma}{4\Lambda} u_l^2. \tag{3.68}$$

As long as $\rho_l > \rho_c$ the giant peak Riemann problem is solved as above by Eq. (3.67). The case $\rho_l \leq \rho_c$, instead, requires the additional concept of *linear degeneracy*, considered in the next subsection.

3.2.3.2 Linear degeneracy at vanishing density

Consider the giant peak initial condition with $\rho_l < \rho_c$, as in the right panel of Fig. 3.10. In the $\mathbf{v}$-space, when leaving $\mathbf{v}_l$ along the first rarefaction curve, there is a $\tilde{\xi}$ such that $\rho_1^r(\tilde{\xi}; \mathbf{v}_l) = 0$ and $u_1^r(\tilde{\xi}; \mathbf{v}_l) = \tilde{u} > 0$ (cf. Fig. 3.9). As $\rho = 0$, both λ_2 and $(\nabla_{\mathbf{v}} \lambda_2) \cdot \mathbf{r}_2$ vanish. As a result, the genuine nonlinearity condition Eq. (3.62) ceases to hold and the corresponding rarefaction curve ($\mathbf{v}_2^r$ in this case) is not defined. The pair $\lambda_2, \mathbf{r}_2$ is then said to be *linearly degenerate* (as opposed to genuinely nonlinear). The name stems from the constancy of λ_2 along the direction of $\mathbf{r}_2$, so that, along $\mathbf{r}_2$, the conservation laws are effectively linear. The solution of the problem reduces indeed to a simple transport wave such as those of subsection 3.2.1.

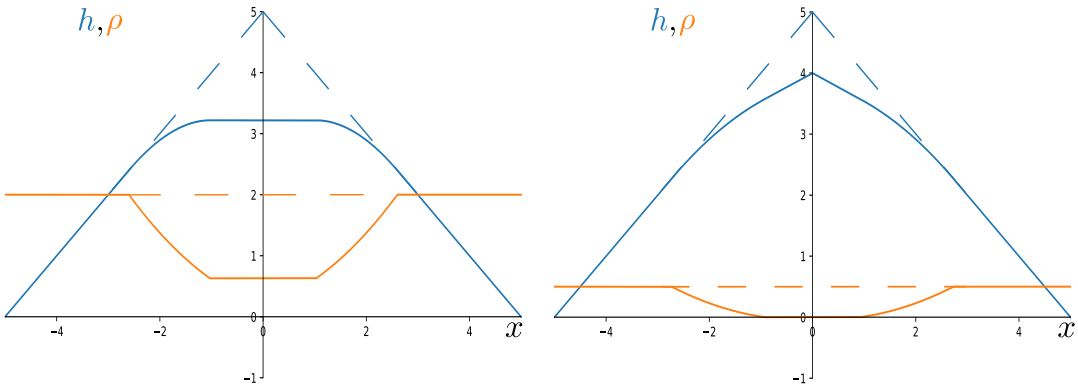

Figure 3.10 *Solution of the giant peak Riemann problem in the height-density variables (dashed lines represent the initial condition). $\rho_0 > \rho_c$ in the left panel (Eq. (3.67)). In the right panel, where $\rho_0 < \rho_c$ (Eq. (3.69)), the initial activator density is so low that the advection due to the slope completely depletes the peak, whose smoothening freezes.*

This can be shown by considering the second shock curve. When emanating from a point on the positive u axis this curve coincides with the horizontal line $\rho = 0$ (cf. $\rho_2(u; \mathbf{v}_l)|_{\rho_l=0}$ from Eq. (3.54)), and the shock speed $\sigma_2(u, \mathbf{v}_l)$ vanishes. As the second eigenvalue λ_2 vanishes too at $\rho = 0$, the Lax condition Eq. (3.56)) is identically satisfied. Thus, the transport wave with vanishing speed is the physical solution. For $u < 0$ the pair $\lambda_2, \mathbf{r}_2$ meets again the genuine nonlinearity condition, but the pair $\lambda_1, \mathbf{r}_1$ does not. By repeating the argument used for positive u, $u = 0$ can be connected with $u = -\tilde{u}$ via the first shock curve $\mathbf{v}_1$ emanating from the $\mathbf{v}$-plane origin (see again Fig. 3.9). As $\sigma_1(u; \mathbf{v}_l)$ vanishes on the half-line $\rho = 0, u < 0$, there is no inconsistency in moving first along the second shock curve and along the first shock curve later—they are both associated with a static discontinuity. A static discontinuity between $u = \tilde{u}, \rho = 0$ and $u = -\tilde{u}, \rho = 0$ is also physically reasonable, as $\partial_t h$ is proportional to ρ in the inviscid limit. Therefore, the solution of the giant peak problem with $\rho_0 < \rho_c$ is given by

$$(\rho, u)\,(x,t) = \begin{cases} (\rho_0, +1)\,, & x/t < \lambda_1(\rho_0, +1), \\ (\rho_1(x/t), u_1(x/t))\,, & \lambda_1(\rho_0, +1) < x/t < \lambda_1(0, u_1(\hat{\xi})), \\ \left(0, u_1(\hat{\xi})\right), & \lambda_1(0, u_1(\hat{\xi})) < x/t < 0, \\ \left(0, -u_1(\hat{\xi})\right), & 0 < x/t < \lambda_2(0, -u_1(\hat{\xi})), \\ (\rho_2(x/t), u_2(x/t))\,, & \lambda_2(0, -u_1(\hat{\xi})) < x/t < \lambda_2(\rho_0, -1), \\ (\rho_0, -1)\,, & \lambda_2(\rho_0, -1) < x/t. \end{cases} \tag{3.69}$$

3.3 Dynamics of the active interface: analytical results

This section collects some analytical results based on the study of the field equations derived in section 3.1 which support some of the numerical findings exposed in chapter 2. Here we focus primarily on the steady-state dynamics in the finite-density case (subsection 2.3.2) and the fast-interface/slow-particle sector of the test-particle problem (subsection 2.2.3).

First, we will use the solution of the inviscid limit to make sense of the oscillatory steady state described in subsection 2.3.2, where clusters of activators form, travel and break while the interface undergoes periodic modulations of the width. Secondly, we will introduce an alternative representation of the diffusive equations Eq. (3.4) which is particularly effective in tackling the test-particle problem. With such a representation, we will gain some understanding in the emergence of the surfing regime of subsection 2.2.3 and the crossover to the static defect problem in the limit where the interface is infinitely faster than the activator.

3.3.1 Steady-state oscillations

In the two Riemann problems considered in section 3.2 the system was assumed to extend indefinitely. If periodic boundary conditions are enforced, instead, peaks and troughs must appear in pairs: the initial condition we consider in this section is made of one of such pairs on a ring of size l, with uniform density ρ_0, as represented in Fig. 3.11 (dashed lines). The dynamics is most easily visualised by a numerical solution of the inviscid equations. The numerical solution, which can be obtained by a standard discretisation of time and space, is shown in Fig. 3.12 and we shall refer to this in the following discussion.

Let us denote with $x_s = l/4$ and $x_r = 3l/4$ the locations of the initial discontinuities (vertical gray, dot-dashed lines in Fig. 3.11). According to the calculations of subsection 3.2.2, the discontinuity at x_s generates two shocks. The shock fronts move away from x_s at speed $\pm\sqrt{\Gamma\Lambda\rho_0}$: their positions after time t are are $x_{s,1}(t) = l/4 + \sqrt{\Gamma\Lambda\rho_0}t$, $x_{s,2}(t) = l/4 - \sqrt{\Gamma\Lambda\rho_0}t$. As travelling, the shock fronts leave behind a region of increased density $\rho_+ > \rho_0$ (as in Fig. 3.11, between the vertical red lines). Meanwhile, the peak at x_r triggers two rarefaction waves,

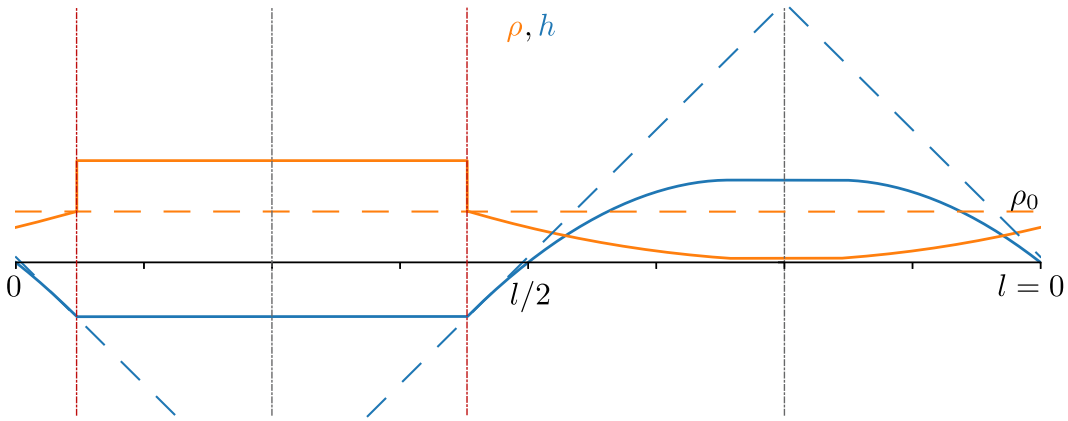

Figure 3.11 *Interface (blue) and density (orange) profiles at the time of the first waves collision T. The profiles come from Eq. (3.59) and Eq. (3.67). The initial condition is also shown with dashed lines. Two vertical, gray, dot-dashed lines mark the initial position of the discontinuities, while two red lines highlight the location of the discontinuities at time T.*

which travel at speed $\pm\left(\Gamma/2 + \sqrt{\Gamma^2/4 + \Lambda\Gamma\rho_0}\right)$ towards the shock fronts while leaving behind a reduced activator density $\rho_- < \rho_0$. This solution (a combination of (3.59) and (3.67-3.69)) holds until the meeting of rarefaction and shock fronts, which occurs at time

$$T = \frac{l}{2\left(\Gamma/2 + \sqrt{\Gamma^2/4 + \Lambda\Gamma\rho_0} + \sqrt{\Lambda\Gamma\rho_0}\right)}. \tag{3.70}$$

The system state at the meeting time is shown in Fig. 3.11 and also displayed in panel A of Fig. 3.12.

The two discontinuities at time T (highlighted in Fig. 3.11 by vertical red lines) do not constitute, strictly speaking, a Riemann problem, as the values of ρ and u on their sides are not constant; yet they can be considered as such and provide the system dynamics for $t > T$. Specifically, we will proceed as if we were solving two new Riemann problems with

$$\mathbf{v}_l = \mathbf{v}(x^-_{s,1}(T), T), \quad \mathbf{v}_r = \mathbf{v}(x^+_{s,1}(T), T),$$

and the same for the discontinuity at $x_{s,2}(T)$, whose left and right values are inverted. For the first discontinuity (the leftmost red line in Fig. 3.11) the values on the left are $u_l = -1$ and $\rho_l = \rho_0$, as in the giant trough of the last section. The shock and rarefaction curves emanating from such $\mathbf{v}_l$ are shown in Fig. 3.5. The values on the right are $u = 0, \rho = \rho_+$—nothing but the intermediate state

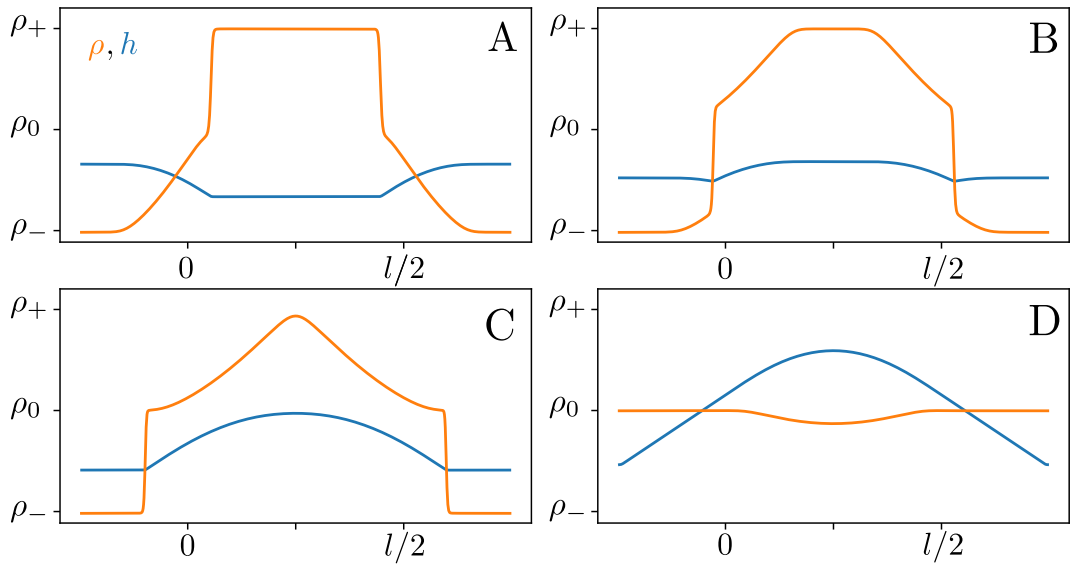

Figure 3.12 *Snapshot of the density (orange) and height (blue) profiles at several times, all greater than or equal to the time of the first collision T. A) At time T the profiles are the same as in Fig. 3.11. B) At $t > T$ the shock waves have passed through the front of the rarefaction fans: the density bump stretches and a new peak starts to form. C) After meeting the tails of the rarefaction fans, the shocks fill the low density region ρ_-, while the rarefaction fans form the new height peak. D) Once the waves have travelled the whole system length, the density is again uniform, but positions of the initial peak and trough are interchanged.*

$\mathbf{v}_m$ of Fig. 3.5, right panel. The shock is then initially preserved, as is preserved its speed $-\sqrt{\Gamma\Lambda\rho_0}$. As the shock progresses through the rarefaction fan, however, the left state changes, with ρ decreasing and u shifting towards zero, following the rarefaction fan profile. In the $\mathbf{v}$-space, the representative point $\mathbf{v}_l$ of the system state ahead of the shock front moves towards the origin of the axes, along the portion of the second rarefaction curve which connects $\mathbf{v}_m$ to $\mathbf{v}_r$ in Fig. 3.8. As soon as $\mathbf{v}_l$ moves down (it will eventually hit the $\mathbf{v}_m$ of Fig. 3.8), it cannot be connected to $u = 0, \rho = \rho_+$ with a single shock curve anymore, but another rarefaction curve can be used to bridge the gap. This rarefaction curve needs to be that associated with the second eigenspace, as the shock curve is that associated with the first, and it gives rise to a rarefaction fan connecting the shock front with the high density peak around $x = l/4$ (vertical grey line of Fig. 3.11). Putting the theory aside for a moment, it is as if the shock wave and the front of the rarefaction fan pass through each other. In doing so, the rarefaction fan acquires the discontinuity of the shock, while the shock lowers its speed due to the lower density found after the rarefaction fan (see panel B of Fig. 3.12).

The slower shocks keeps propagating through the rarefaction fans and decreasing

their speed, until they both meet the tails of the rarefaction fans, which travel at speed $\pm\sqrt{\Gamma\Lambda\rho_-}$ (cf. Eq. (3.67)). The snapshot shown in panel C is taken at the time when the shocks collides with the tails of the original rarefaction fans. Here the density cluster has stretched so much that the density on the back of the shock front is the same as the initial condition, and the interface is forming peak at $l/4$, where the initial condition had a trough. This collisions can be understood again in terms of two new Riemann problems: we focus on the on the one with $\mathbf{v}_l = (0, \rho_-)$ and $\mathbf{v}_r = (+1, \rho_0)$, located on the left-hand side of panel C, Fig. 3.12. The other Riemann problem can be solved by swapping left and right states and changing the sign of the wave speeds. The result is again a combination of a shock wave and a rarefaction fan, with the shock that will now fill the low-density region and form a new trough at $3l/4$, while the rarefaction wave will keep reducing the density and building the peak at $l/4$.

Thus, there are now two shocks travelling towards each other, as are the two rarefaction waves. The next two collisions will take place at $x = 3l/4$ and $l/4$, for shocks and rarefaction fans, respectively (see panel D of Fig. 3.12). The system now looks like a shifted version of the one we started with, with the density returning to a uniform value ρ_0, but the interface peak at $l/4$ and the trough at $3l/4$. Notice, however, the new peak is not as sharp as that of the initial condition and that ρ has not quite attained the value ρ_0 everywhere. For the numerical solution, the cause is the small viscous term (as small as the lattice spacing of the spatial discretisation) which was added to stabilise the solution. This small viscous term is a source of dissipation, so that at every iteration of the dynamics just described the interface is slightly flatter than before—it will, ultimately, be flat. In fact, this dissipation affects the analytical solutions too, where the vanishingly small viscous terms enter through the Lax condition [75].

To summarise, when put on a periodic system, the giant trough and giant peak Riemann problems produce an oscillatory behaviour. In the cycle, illustrated in Fig. 3.12, the peak and trough reform at diametrically opposite positions, via a pair of shock waves and rarefaction fans travelling around the system and passing through each other. Eventually, dissipation kicks in, the waves running through the system decay diffusively, so that the density becomes uniform and the interface flat. The addition of noise could prevent this trivial outcome: by creating random kinks in the interface and displacing the inclusions, it will generate small peaks and troughs and density inhomogeneities that give rise to new waves even after dissipation has completely smoothened the initial condition.

3.3.2 The surfing regime, pt. 2

Let us finally consider an application of Eq. (3.4) in the context of the test-particle problem. First of all we shall introduce a modified density equation which replaces Eq. (3.34) when the number of activators does not scale with the size of the interface. Let us then recall, for the sake of clarity, Eq. (3.34):

$$\partial_t \rho = \Lambda \partial_x (\rho u) + D\partial_{xx}^2 \rho - \partial_x \left(\sqrt{\frac{2D\rho}{L}} \xi(x,t) \right). \tag{3.71}$$

The density ρ, defined in Eq. (3.1), integrates to $\rho_0 = N/L$, N being the number of activators and L the number of lattice points. In the test particle problem, ρ_0 vanishes. Let us then define a new density via $\rho' = L\rho$, which integrates to the total number of activators N rather than the mean density. The equation for ρ' is

$$\partial_t \rho' = \Lambda \partial_x (\rho' u) + D\partial_{xx}^2 \rho' - \partial_x \left(\sqrt{2D\rho'} \xi(x,t) \right). \tag{3.72}$$

Though finite even if the number of activators is not macroscopically large, the density function ρ' is not the ideal descriptor for the trajectory of a single particle. The solution comes from the work of Dean [76], who showed how to derive equations such as Eq. (3.72) from the N Langevin equations for the particle coordinates X_t^μ,

$$\dot{X}_t^\mu = -\Lambda u(x,t)|_{X_t^\mu} + \sqrt{2D}\xi_\mu(t), \quad \mu = 1, \ldots, N, \tag{3.73}$$

with the $\xi_\mu(t)$'s being independent Gaussian white noises, provided the density is defined as $\rho(x,t) = \sum_{\mu=1}^{N} \delta(x - X_t^\mu)$. Here we apply the inverse relation, and claim that the description in terms of a density function, Eq. (3.72), is equivalent to the trajectory representation of Eq. (3.73), then set $N = 1$.

The ρ factor in the driving term of the slope equation shall also be replaced, for consistency, with ρ'/L, then $\delta(x - X_t)/L$, X_t being the position at time t of the only activator in the system. Thus, by further neglecting the u^2 terms as in section 3.2,

$$\partial_t u = \frac{\Lambda}{L} \partial_x \delta(x - X_t) + \nu \partial_{xx}^2 u + \partial_x \left(\sqrt{\frac{\nu}{2L}} \zeta(x,t) \right). \tag{3.74}$$

Eq. (3.74), linear, can be solved for u as a function of x, t and X_t. The result, once

plugged in Eq. (3.73), yields a closed equation for X_t. Before proceeding with the derivation of such an equation, it is worthwhile commenting on the order of magnitude of the various terms in Eq. (3.73). Due to the linearity of u's equation, the infinitesimal coefficient Λ/L which multiplies the δ-function source term for the field $u(x,t)$ controls also the magnitude of the u-dependent force in the X_t's equation, Eq. (3.73)

In order to render the force on X_t finite, we can resort again to an inviscid limit, i.e. a hydrodynamic limit different from that of Eq. (3.5). Instead of asking p/L^2 (and q/L^2) to tend to ν (and D) in the large-L limit, we ask p/L (and q/L) to tend to ν (and D). In other words, both the bare rates p and q and the 'interaction rates' λ and $\gamma = 2\lambda$ should diverge as L in the large-L limit. This amounts to substituting ν and D with ν/L and D/L, respectively, yielding

$$\dot{X}_t = -\Lambda u(x,t)|_{X_t} + \sqrt{2D/L}\xi(t), \tag{3.75a}$$

$$\partial_t u = \frac{\Lambda}{L}\partial_x \delta(x - X_t) + \frac{\nu}{L}\partial^2_{xx} u, \tag{3.75b}$$

plus terms of higher order in L^{-1}. Notice that Eq. (3.75) is not exact in the continuum limit, as all nonlinearities in u's equation have been neglected. Yet, as it is described below, it yields some insight into the peculiar dynamics of the test-particle problem discussed in section 2.2.

By resorting to the Fourier transform $u_k(t) = \int_{[0,l]} dx\, u(x,t)e^{-ikx}$, with l the interface length, and integrating Eq. (3.75b) from $t = 0$, with $u(x,t)|_{t=0} = 0$, one gets

$$u_k(t) = \int_0^t ds\, e^{-\nu k^2 (t-s)/L} \left[ik\Lambda e^{-ikX_s}\right]/L. \tag{3.76}$$

$u_k(t)$ can now be plugged in the Fourier decomposition of u in Eq. (3.75a) right-hand side, so as to obtain (recalling $u(x,t) = l^{-1}\sum_k u_k(t)e^{ikx}$, with the sum running over $k = 2\pi n/l$ with n integer)

$$\dot{X}_t = -\frac{\Lambda^2}{lL}\sum_k ik \int_0^t ds\, e^{-r\nu k^2 (t-s)/L} e^{ik(X_t - X_s)} + \sqrt{2D/L}\xi(t). \tag{3.77}$$

Eq. (3.77) is just a reformulation of Eq. (3.75) and cannot be solved. There are, however, a few conclusions to be drawn in the large-L limit. First, $\lim_{L\to\infty} \dot{X}_t$ vanishes at $t = 0$. $\dot{X}_t = 0$ is actually a solution at all times if the noise in Eq. (3.77) vanishes. By contrast, the numerics of subsection 2.2.3 display a test particle surfing the interface at later times.

Based on the numerics, we argued the surfing length to diverge in the $L \to \infty$ limit, implying the existence and finiteness of the limit

$$\lim_{L\to\infty} \lim_{t\to\infty} \dot{X}_t = v_s, \tag{3.78}$$

which can be thought as the definition of the surfing speed v_s. Rather than calculating v_s from the solution of Eq. (3.77), we can assume Eq. (3.78) to hold and find a self-consistent equation for v_s. First, let us regard the stochastic noise in Eq. (3.75a) as a higher order (in L^{-1}) contribution, thus neglect it. Secondly, let us notice that, due to the decaying exponential factor $e^{-\nu k^2 (t-s)/L}$ (the 0-th mode does not contribute because of the ik factor), the long-t limit of the s-integral on Eq. (3.77)'s right-hand side is insensitive to the value of the integrand at small s. For sufficiently large s, instead, due to Eq. (3.78), $X_t - X_s$ is approximated by $v_s(t-s)$. Therefore

$$\begin{aligned} v_s &= \lim_{t\to\infty} \left\{ -\frac{\Lambda^2}{lL} \sum_k ik \int_0^t ds\, e^{[ikv_s - \nu k^2](t-s)/L} \right\} \\ &= \frac{\Lambda^2}{lL} \sum_k \frac{ik}{ikv_s - \nu k^2/L} = \frac{\Lambda^2}{\nu l} \sum_{k>0} \frac{2Lv_s/\nu}{(Lv_s/\nu)^2 + k^2}. \end{aligned} \tag{3.79}$$

Notice that v_s above remains finite as L increases, thus justifying the neglect of translational noise in Eq. (3.75a).

In the limit of large interface length l, the above sum can be evaluated by replacing $l^{-1} \sum_k$ with $(2\pi)^{-1} \int dk$, where the constraint $k > 0$ fixes the lower limit of the integral to $2\pi/l$. Finally,

$$v_s \simeq \frac{\Lambda^2}{2\pi\nu} \int_{2\pi/l}^{\infty} dk\, \frac{2Lv_s/\nu}{(Lv_s/\nu)^2 + k^2} = \frac{\Lambda^2}{2\nu} \left[\mathrm{sign}(v_s) - \frac{2}{\pi} \tan^{-1}\left(\frac{2\pi r \nu}{lLv_s} \right) \right]. \tag{3.80}$$

Eq. (3.80) is the sought self-consistent equation. The inverse tangent vanishes as $L \to \infty$, leaving an equations with solutions $v_s = 0, \pm\Lambda^2/(2\nu)$, hence showing that Eq. (3.77) admits a surfing solution. How does the system transition from the $\dot{X}_t = 0$ solution to one of the two surfing ones? This question has proven much harder to answer, as a small-t expansion of Eq. (3.77) results in all the derivatives of X_t vanishing. The inspection of simulations of the test-particle problem suggests that the small translational noise causes the transition after some latency period where $\dot{X}_t = 0$, but a proof of such statement remains an open problem.

3.3.3 Concluding remarks

The principal result of this chapter is the derivation of partial differential equations, Eq. (3.4), which describe the one-dimensional lattice model of chapter 2 at the diffusive scale of Eq. (3.5). Furthermore, it was shown how to tweak this derivation in order to extract a continuum description of the test-particle problem, namely Eq. (3.75). The latter is actually an approximation of the exact equations, in that it neglects *all* contributions which are not linear in the interface slope. Nevertheless, accepting Eq. (3.75) a suitable description has allowed us to predict the emergence of 'surfing solutions', where the test particle travels at a finite speed.

In another limit—the inviscid limit—the one-dimensional partial differential equations can be solved for piecewise-constant initial conditions. The inviscid limit is somewhat complementary to the diffusive scale, as the focus is shifted from dissipative terms such as diffusion and viscosity to those representing interactions between interface and activator density. In particular, the combination of two specific piecewise-constant initial conditions (the giant trough of subsubsection 3.2.2.1 and the giant peak of subsubsection 3.2.3.1) results in an oscillatory state which matches quantitatively the steady-state dynamics of the lattice model [1]. Eventually, solutions of the deterministic equations decay towards the constant, homogeneous solution. Can stochastic fluctuations alter such a trivial outcome?

In fact, fluctuations due to the noise acting on interface and activators have been left out of the calculations of section 3.2 and section 3.3: it is legitimate to ask whether they can change the picture presented and, if they do, to what extent. A plausible answer will be given in chapter 4, where the stochastic equations are studied within a renormalisation group framework. It will also be shown that all the nonlinearities of the active interface equations are *irrelevant* in the inviscid limit. This is another justification for the neglect of nonlinear terms, although it only refers to universal properties such as the large-scale and long-time decay of correlations. Another possibility comes from the theory of nonlinear fluctuating hydrodynamics, whose results were recently extended to one-dimensional problems with two conserved fields [77, 78]. Although beyond the scope of this thesis, a comparison between the two approaches would be of interest in the general field of one-dimensional transport.

Another aspect left out of this chapter is the quantitative comparison of the hydrodynamic limit Eq. (3.4) with Monte Carlo simulations of the lattice model. This comparison can be attained with high precision by following a well-defined recipe. First, the initial state of the system should be drawn from a product measure with slowly-varying density, as in Eq. (3.19). Secondly, in order to match the timescales of the limit in Eq. (3.5), the time in the trajectory of the lattice model should be scaled with L^2. In other words, one unit of time of the PDEs corresponds to L^2 units of time of the lattice dynamics. As the rescaling of time effectively increases the model rates by a factor L^2, the first two conditions in Eq. (3.19) are reproduced by setting the bare rates q and p of the lattice model to the coefficients D and ν of the PDEs, respectively. The parameter $\lambda = 2\gamma$ is also multiplied by L^2, thus it must be set to $2\Lambda/L$ in order to satisfy the last condition in Eq. (3.19). The inviscid limit of the lattice model, for instance, could be obtained by setting q and p to some infinitesimally small value. However, from Eq. (3.22) and Eq. (3.27), the vanishing of q and p causes the emergence of next-to-leading order terms of a form different than $\partial_x^2\tau$ and $\partial_x^2\rho$, whereas the solution presented in section 3.2 assumes indirectly that next-to-leading order terms are exactly $\partial_x^2\tau$ and $\partial_x^2\rho$. This assumption is hidden in the application of the Lax condition. Therefore, a quantitative inviscid limit of the lattice model remains an open problem.

Chapter 4

Large-scale dynamics of active interfaces

All the results derived in chapter 3 are specific to the one-dimensional lattice model of chapter 2, when the lattice is made into a continuum by reducing the distance between adjacent lattice points while scaling the model rates with a certain power of such distance (cf. Eq. (3.5)). The purpose of the lattice model, quoting the introductory paragraphs of chapter 2, was that of minimising the *irrelevant* complexity of more detailed descriptions, in order to make room for the *universal* aspects of the problem. It is only natural, then, to conclude the thesis by checking whether this purpose is fulfilled or not, by resorting to the apparatus of the Renormalisation Group (RG) [79–81].

In general, the term RG accompanies studies which are based on unfolding the transformation laws which determine how the defining parameters of a problem change as the scale of observation is increased [80]. The expression 'scale of observation' may refer both to length- and time-scales, so that RG applies to static as well as dynamic phenomena. These transformation laws form, strictly speaking, a semi-group (rather than a group): the coarse-graining procedure which allows one to focus on larger and larger scales by neglecting the microscopic details is clearly irreversible. Therefore, the flow of these transformation laws, or *renormalisation group flow*, partitions the parameter space into basins of attraction of the transformation's fixed points. Each of these basins of attraction corresponds to a *phase*, whose physics is controlled by the relevant fixed point.

Deep in each phase, the system displays some sort of scale invariance, so that the

relevant observables obey scaling laws analogous to the Family-Vicsek hypothesis for the width of a fluctuating interface [82]. The exponents entering a scaling law are closely related with the properties of the corresponding fixed point. Of special interest are those fixed points which are saddle points in the parameter space, also called *critical fixed points*. They are normally located at the boundaries between the basin of attractions of attractive fixed points and, by studying the flow along the outwards directions of the saddle, one learns about the divergence of certain observables across a phase transition. Therefore, critical points are well suited for the description of the properties of systems close to a second-order phase transition.

In this chapter, RG methods are applied to the active interface equations. The main result is that the parameter sub-space spanned by the slope-advection coupling and active-growth coupling parameters partitions into four sections, related two by two by a change of variables. In each of these sections, the system dynamics is described by the inviscid limit of the active interface equations (cf. subsection 4.2.2). The two critical lines separating the sections describe systems where the active-growth coupling or the slope-advection coupling can be made to vanish: here other terms, such as the curvature coupling mentioned in chapter 2, emerge under the RG flow. The KPZ fixed point for passive interfaces appears at the intersection of the two critical lines.

In the first section of this chapter, section 4.1, I will provide an heuristic derivation of the active interface equations, valid, unlike Eq. (3.4), in general dimensions. All the parameters appearing in the equations will be considered as independent, unless related by a fundamental symmetry of the problem. This section also introduces the Janssen-DeDominicis formalism for dynamic problems and the perturbation theory that will be adopted later. Section 4.2 is devoted to mean field theory, i.e. the theory of the linearised interface equations. The latter allows us to take a first look at the phase diagram of the model, and turns out to exactly describe the system's physics when both the slope-advection and the active-growth coupling are non-zero. Section 4.3 focuses on the KPZ fixed point: this is a necessary starting point for the (perhaps more interesting) RG analysis of the full phase diagram. In section 4.3, available one-loop calculations on the KPZ equations [83] are extended to take into account the coupling with the density field, possibly shedding new light on the old problem of passive scalar advection.

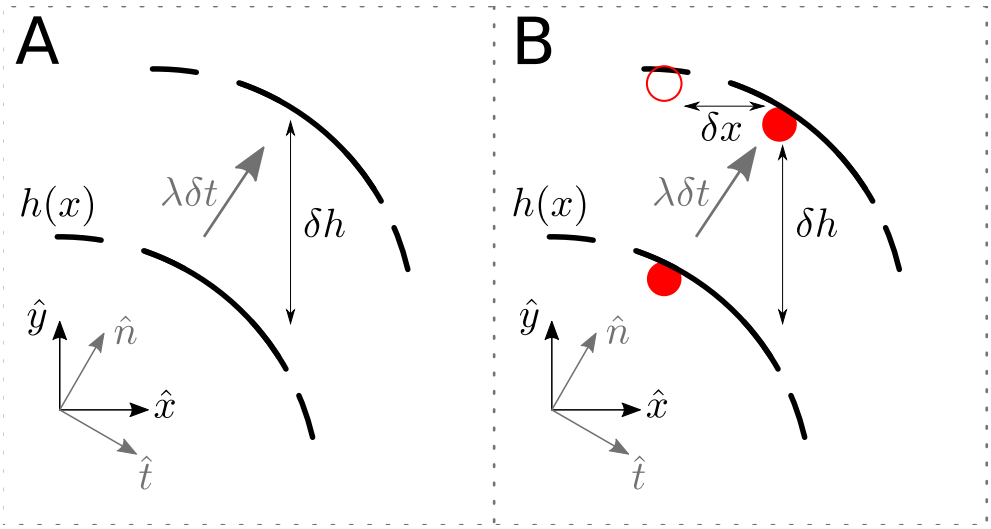

Figure 4.1 *A) An interface (black solid line) $h(x)$ (x and $y=h$ axis shown in black at the bottom left corner) is driven by a force λ in the direction of the local normal $\hat{n}$, thus $\delta h > \lambda\delta t$ (local normal/local tangent reference frame shown in grey on the bottom left corner). B) An active interface is driven by activators (red disk). The normal force causes also a horizontal displacement δx of the activator.*

4.1 Dynamic equations and action functional

The active interface equations, as derived in chapter 3, hold in one dimension, when the slope-advection rate is related to the active-growth rate as in Eq. (3.13). In order to extend the equations to the whole parameter space, and towards higher dimensions, we must resort to a heuristic approach. This approach is based on geometric considerations akin to those of subsection 2.1.2, which led to the introduction of a slope-advection rate in the lattice model (cf. Fig. 2.4).

Consider the picture displayed in Fig. 4.1 A. The interface, described by the function $h(\boldsymbol{x}, t)$, is subject to a force λ acting along the interface normal. As the interface is assumed to fluctuate in a viscous medium, the force translates into velocity, i.e. displacement δh over time δt. As the displacement is normal to the local tangent, $\delta h > \lambda\delta t$. In fact, to obtain the actual displacement, $\lambda\delta t$ shall be multiplied by the factor $\sqrt{1+(\boldsymbol{\nabla}h)^2}$—proved by applying the Pythagorean theorem to the triangle formed by the displacement δh, $\lambda\delta t$ and the local tangent. Hence, as $\delta t \to 0$,

$$\partial_t h(\boldsymbol{x}, t) = \lambda\sqrt{1+(\boldsymbol{\nabla}h)^2} \simeq \lambda + \frac{\lambda}{2}(\boldsymbol{\nabla}h)^2\,, \tag{4.1}$$

where the approximation is obtained by expanding the square root for small slopes $\boldsymbol{\nabla} h$. The derivation does not change if the force intensity depends on the local concentration of activators, i.e. $\lambda \to \lambda\rho(\boldsymbol{x}, t)$.

Analogous arguments allow one to obtain the effective force felt by the activators when the interface is moving. Let us consider the case of a constant driving force first. The activators do not move by themselves, as they are rigidly fixed to the interface—remember our interface is a bilayer and the activators live inside it. However, as the activator density is measured as a function of $\boldsymbol{x}$ rather than the position within the interface, they experience an effective displacement $\delta\boldsymbol{x}$ due to the interface motion, as illustrated by panel B of Fig. 4.1. The amplitude of the displacement is obtained by projecting the normal displacement $\lambda\delta t$ along the $\boldsymbol{x}$-axis, while the direction is that of the interface slope. That is,

$$\partial_t \rho(\boldsymbol{x}, t) = \boldsymbol{\nabla} \left(\frac{\lambda\rho\boldsymbol{\nabla} h}{\sqrt{1 + (\boldsymbol{\nabla} h)^2}} \right) \simeq \boldsymbol{\nabla} \left(\lambda\rho\boldsymbol{\nabla} h \right), \tag{4.2}$$

where the approximation is obtained by expanding again for small slopes. The derivation of the density equation can also be extended to a density-dependent force, $\lambda \to \lambda\rho(\boldsymbol{x}, t)$, provided the factor λ is not moved out of the gradient first.

A few comments are in order. The derivation of the height equation is the same as the one provided by Kardar, Parisi and Zhang in [18]: as in [18], the λ term on the right hand-side can be removed by a shift of the height, $h \to h + \lambda t$. This is not possible if the force is proportional to another field such as ρ. With respect to the density equation, an analogous driving term was introduced in [35] in the equation for the density of a fluid membrane (see [42] for a discussion in the context of active membranes), as it represents the effective displacement of fluid within the membrane due to displacement of the membrane itself. This point will be touched upon again in the following section, where the equations are augmented with stochastic and viscous terms. Unlike in chapter 3, the coefficients of the equations will all be independent from each other, unless related by one of the fundamental symmetries of the problem. The symmetries are listed in the first subsection. The second subsection introduces an alternative formulation of the field equations based on an action functional, whereas the third outlines the perturbative treatment of nonlinearities.

4.1.1 Symmetries of the active interface equations

Here the heuristic derivation of the active interface equations is completed—let us consider the interface height h first. In the absence of any activators, one might assume that the d-dimensional interface fluctuates in *equilibrium* with its $d+1$-dimensional medium. The dynamics would then be controlled by the surface energy $\mathcal{H} = \int d^d x \, \nu \left(\boldsymbol{\nabla} h\right)^2 /2$ and uncorrelated thermal kicks, i.e.

$$\partial_t h(\boldsymbol{x}, t) = -\Gamma \frac{\delta \mathcal{H}}{\delta h(\boldsymbol{x}, t)} + \sqrt{2\Gamma'}\eta(\boldsymbol{x}, t) = \Gamma\nu\nabla^2 h(\boldsymbol{x}, t) + \sqrt{2\Gamma'}\eta(\boldsymbol{x}, t), \tag{4.3}$$

where $\eta(\boldsymbol{x}, t)$ is a unit-variance spatiotemporal Gaussian noise. As the dynamics entailed in Eq. (4.3) is made of purely thermal fluctuations about the equilibrium state $h = const.$, the coefficients Γ and Γ' are fixed by imposing the Fluctuation-Dissipation Theorem [84] (FDT):

$$C(k, \omega) = \frac{2k_B T_e}{\omega} \mathrm{Im}\left[\chi(k, \omega)\right], \tag{4.4}$$

where k_B is Boltzmann's constant, T_e the temperature of the environment, while $C(k, \omega)$ and $\chi(k, \omega)$ denote the Fourier transform (conventions in Appendix A) of correlation and response function, respectively.

In real space, the (height) correlation function is defined as

$$C^{hh}(\boldsymbol{x}' - \boldsymbol{x}, t' - t) = \langle h(\boldsymbol{x}', t') h(\boldsymbol{x}, t) \rangle, \tag{4.5}$$

and, as in all the cases considered in this thesis, it depends on $\boldsymbol{x}' - \boldsymbol{x}, t' - t$ due to translational symmetry in time and space. The average is taken over all the realisations of the noise in Eq. (4.3). The (height) response function, instead, is defined as

$$\chi^{hh}(\boldsymbol{x}' - \boldsymbol{x}, t' - t) = \left. \frac{\delta \left\langle h(\boldsymbol{x}', t') \right\rangle_v}{\delta v(\boldsymbol{x}, t)} \right|_{v=0}, \tag{4.6}$$

where $\langle . \rangle_v$ means that the average is taken after the addition of a term $-\int d^d x \, vh$ to the energy $\mathcal{H}$, or, analogously, the addition of a term $\Gamma v(\boldsymbol{x}, t)$ to the right-hand side of Eq. (4.3). From the space-time Fourier transform of Eq. (4.3) (plus $\Gamma v(\boldsymbol{x}, t)$),

$$\left(-i\omega + \Gamma\nu k^2\right) h(\boldsymbol{k}, \omega) = \Gamma v(\boldsymbol{k}, \omega) + \sqrt{2\Gamma'}\eta(\boldsymbol{k}, \omega), \tag{4.7}$$

with the transformed noise having zero average and variance $\langle \eta(\boldsymbol{k}, \omega)\eta(\boldsymbol{k}', \omega') \rangle =$

$(2\pi)^{d+1}\delta(\boldsymbol{k}+\boldsymbol{k}')\delta(\omega+\omega')$ (cf. Eq. (A.8), Appendix A), one readily infers

$$\chi^{hh}(k,\omega)=\frac{\Gamma}{-i\omega+\Gamma\nu k^2};\quad C^{hh}(k,\omega)=\frac{2\Gamma'}{\omega^2+(\Gamma\nu k^2)^2}. \tag{4.8}$$

The FDT Eq. (4.4) is satisfied provided the relation $\Gamma'=\Gamma k_B T_e$, between noise intensity (Γ'), mobility (Γ) and temperature. Upon recalling the driving term due to active growth from Eq. (4.1) (with $\lambda\to\lambda\rho$), the full height equation reads

$$\partial_t h=\lambda\rho+\frac{\lambda\rho}{2}\left(\boldsymbol{\nabla}h\right)^2+\nu_h\nabla^2 h+\sqrt{2D_h}\eta, \tag{4.9}$$

where $\nu_h=\Gamma\nu$ and $D_h=\Gamma k_B T_e$.

The simplest derivation of the density equation follows again the approach of [76]: first write down Langevin equations for the $\boldsymbol{x}$-coordinates of the activators, $\{\boldsymbol{X}_i(t)\}$, then obtain an equation for the density $\rho(\boldsymbol{x},t)=\sum_i\delta(\boldsymbol{X}_i(t)-\boldsymbol{x})$. In the coordinate Langevin equations, the noise amplitude D can be set to the diffusion coefficient *within* the membrane, which is not necessarily related to the temperature of the environment *outside* the membrane. If no active growth occurs, the density equation entails only noise and diffusion $D=k_B T_m$, with T_m the membrane temperature and unitary mobility assumed. Like the height equation, such density equation can be written as a (conservative) equilibrium equation

$$\partial_t\rho=\boldsymbol{\nabla}\cdot\left(\rho\boldsymbol{\nabla}\frac{\delta\mathcal{H}}{\delta\rho(\boldsymbol{x},t)}\right)+\boldsymbol{\nabla}\cdot\left(\sqrt{2D\rho}\boldsymbol{\xi}\right), \tag{4.10}$$

with $\mathcal{H}=\int d^dx\, k_B T_m\rho\ln\rho$, i.e. the entropy of an ideal gas. It is worth, in preparation for the following sections of this chapter, to consider the excess density $\phi(\boldsymbol{x},t)=\rho(\boldsymbol{x},t)-\rho_0$ rather than $\rho(\boldsymbol{x},t)$, as the former's average vanishes while the latter's equals ρ_0. Furthermore, in setting $\rho=\rho_0+\phi$, we can also *i)* remove the constant term $\lambda\rho_0$ from Eq. (4.9) by a shift of the height; *ii)* neglect terms which contain a third power of the fields; *iii)* replace the multiplicative noise $\sqrt{2D\rho}\boldsymbol{\xi}$ with the additive one $\sqrt{2D\rho_0}\boldsymbol{\xi}$. All these approximations will be given justification in the following section, section 4.2, where all the terms neglected will be shown to be irrelevant in the RG sense. As $\mathcal{H}[\rho_0+\phi]\simeq\int d^dx\, D(\phi+\phi^2/2\rho_0)$ for small ϕ, the excess density equation reads

$$\partial_t\phi=\boldsymbol{\nabla}\cdot\left(\rho_0\boldsymbol{\nabla}\frac{\delta\mathcal{H}}{\delta\phi(\boldsymbol{x},t)}\right)+\boldsymbol{\nabla}\cdot\left(\sqrt{2D\rho_0}\boldsymbol{\xi}\right)=D\nabla^2\phi+\boldsymbol{\nabla}\cdot\left(\sqrt{2D\rho_0}\boldsymbol{\xi}\right). \tag{4.11}$$

When computing the response function for ϕ, one must recall that a perturbation

$-\int d^dx\, v\phi$ in $\mathcal{H}$ produces an additional term $-\rho_0\nabla^2 v$ in Eq. (4.11)'s right-hand side, so that, in Fourier space

$$\left(-i\omega + Dk^2\right)\phi(\boldsymbol{k},\omega) = \rho_0 k^2 v(\boldsymbol{k},\omega) + i\sqrt{2D\rho_0}\boldsymbol{k}\cdot\boldsymbol{\xi}(\boldsymbol{k},\omega). \tag{4.12}$$

Thus, given the usual noise correlation in Fourier space,

$$\chi^{\phi\phi}(k,\omega) = \frac{\rho_0 k^2}{-i\omega + Dk^2}, \quad C^{\phi\phi}(k,\omega) = \frac{2D\rho_0 k^2}{\omega^2 + (Dk^2)^2}, \tag{4.13}$$

so that the FDT Eq. (4.4) is satisfied with temperature $k_B T_m = D$. Notice that only the D in the noise amplitude needs to be set to $k_B T_m$ in order to satisfy the FDT, while the coefficient of $\nabla^2\phi$ can be set to an arbitrary value. Upon adding also the driving term $\boldsymbol{\nabla}\cdot(\rho^2\boldsymbol{\nabla}h)$, from Eq. (4.2) with $\lambda \to \lambda\rho$, one gets

$$\partial_t\phi = \lambda\rho_0^2\nabla^2 h + 2\lambda\rho_0\boldsymbol{\nabla}\cdot(\phi\boldsymbol{\nabla}h) + \nu_\phi\nabla^2\phi + \boldsymbol{\nabla}\left(\sqrt{2D_\phi}\boldsymbol{\xi}\right), \tag{4.14}$$

where the third-order term $\boldsymbol{\nabla}\cdot(\lambda\phi^2\boldsymbol{\nabla}h)$ has been neglected, D has been arbitrarily set to ν_ϕ and $D_\phi = D\rho_0$.

We have now two equations, Eq. (4.14) for ϕ and Eq. (4.9) for h, which satisfy the FDT for $\lambda = 0$, where no active growth occurs. The equations are also invariant for translations of time, space and interface height. They are symmetric for rotations of the substrate $\boldsymbol{x}$, but not for height inversion $h \leftrightarrow -h$, because of the driving terms. Moreover, Eq. (4.14) and (4.9) should be invariant for *infinitesimal tilts*, parametrised by the d-dimensional infinitesimal vector $\boldsymbol{\epsilon}$,

$$\begin{cases} \boldsymbol{x} \to \boldsymbol{x}' = \boldsymbol{x} - \boldsymbol{\epsilon}\lambda t, \\ h \to h' = h + \boldsymbol{\epsilon}\cdot\boldsymbol{x}. \end{cases} \tag{4.15}$$

The infinitesimal tilt symmetry is inherited from a larger symmetry of the most general description of a fluid membrane, where the latter is considered as a d-dimensional manifold in a $d+1$ dimensional space. This larger symmetry is general covariance, i.e. the covariance of the equations which describe the motion of the membrane/manifold with respect to smooth change of coordinates on the manifold and general coordinate transformations in the $d+1$-dimensional space [34]. The simplified description considered throughout this thesis corresponds to the *Monge gauge* (Fig. 4.2), suitable for the description of nearly-flat interfaces with no overhangs. In the Monge gauge, the reference frame is chosen so that the interface is parallel to the plane spanned by the first d of the

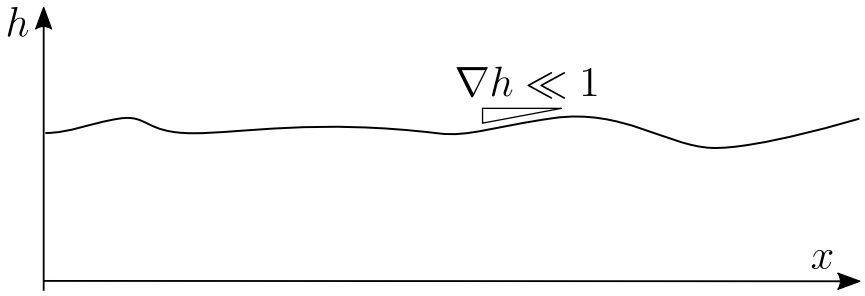

Figure 4.2 *Illustration of the Monge gauge for a* 1*-dimensional interface in the* 2*-dimensional space. The* $\boldsymbol{x}$*-axis is chosen so as to be parallel to the interface and the interface height measured along the orthogonal direction. This description is valid as long as* $\nabla h \ll 1$*.*

$d+1$ coordinates of the space. The membrane/manifold, then, is parametrised with the first d coordinates, $\boldsymbol{x} = (x_1, \ldots, x_d)$, while its position is specified by the relation $x_{d+1} = h(\boldsymbol{x}, t)$. Due to the gauge choice, the general covariant equations for the membrane/manifold reduce to a partial differential equation for the height function. General covariance itself reduces to a smaller symmetry which collects all coordinate transformations within the Monge gauge: rotations of the substrate $\boldsymbol{x}$, translation of $\boldsymbol{x}$ and h and infinitesimal tilts.

Infinitesimal tilts, from Eq. (4.15), affect only time-derivatives and the nonlinear terms $(\boldsymbol{\nabla} h)^2$ and $\boldsymbol{\nabla} \cdot (\phi \boldsymbol{\nabla} h)$. Specifically,

$$\begin{cases} \partial_t \to \partial_t + \lambda \boldsymbol{\epsilon} \cdot \boldsymbol{\nabla}, \\ (\boldsymbol{\nabla} h)^2 \to (\boldsymbol{\nabla} h)^2 + 2\boldsymbol{\epsilon} \cdot \boldsymbol{\nabla} h + \mathcal{O}(\epsilon^2), \\ \boldsymbol{\nabla} \cdot (\phi \boldsymbol{\nabla} h) \to \boldsymbol{\nabla} \cdot (\phi \boldsymbol{\nabla} h) + \boldsymbol{\epsilon} \cdot \boldsymbol{\nabla} \phi. \end{cases} \tag{4.16}$$

The density ρ, together with the excess density ϕ, is intended as number of activators per unit of interface area, thus it does not change under tilt. For the equations to be invariant under Eq. (4.16), the coefficient of $(\boldsymbol{\nabla} h)^2$ must be set to $\lambda/2$ and that of $\boldsymbol{\nabla} \cdot (\phi \boldsymbol{\nabla} h)$ to λ—this will be the choice of parameters from here on, regardless of the heuristic derivation. Notice that the linear interaction terms $\lambda\phi$ and $\lambda\rho_0^2 \nabla^2 h$, also originating from active growth, are not related by the symmetry for infinitesimal tilt, hence the respective coefficients will be left free to assume any value. In general, the equations we will study are

$$\partial_t h = a_h \phi + \frac{\lambda}{2} (\boldsymbol{\nabla} h)^2 + \nu_h \nabla^2 h + \sqrt{2D_h}\eta, \tag{4.17a}$$

$$\partial_t \phi = a_\phi \nabla^2 h + \lambda \boldsymbol{\nabla} \cdot (\phi \boldsymbol{\nabla} h) + \nu_\phi \nabla^2 \phi + \boldsymbol{\nabla} \cdot \left(\sqrt{2D_\phi} \boldsymbol{\xi} \right). \tag{4.17b}$$

4.1.2 Path probability and action functionals

The Langevin equations Eq. (4.17) are equivalent to a path probability

$$P[h,\phi] = \left\langle \delta\left(h(\boldsymbol{x},t) - h_{\eta,\boldsymbol{\xi}}\right)\delta\left(\phi(\boldsymbol{x},t) - \phi_{\eta,\boldsymbol{\xi}}\right)\right\rangle_{\eta,\boldsymbol{\xi}}, \tag{4.18}$$

for the solutions $h_{\eta,\boldsymbol{\xi}}$ and $\phi_{\eta,\boldsymbol{\xi}}$ of Eq. (4.17) to coincide with the *given* time-dependent fields $h(\boldsymbol{x},t)$ and $\phi(\boldsymbol{x},t)$. The symbols $h_{\eta,\boldsymbol{\xi}}$ and $\phi_{\eta,\boldsymbol{\xi}}$ highlight that the solutions of Eq. (4.17) depend on the spatiotemporal noises η and $\boldsymbol{\xi}$, and the average $\langle . \rangle_{\eta,\boldsymbol{\xi}}$ is over realisations of such noises. Both noises are Gaussian, thus their path-probabilities are known [85]. In particular, the path-probabilities of the stochastic terms $\zeta_h = \sqrt{2D_h}\eta$ and $\zeta_\phi = \boldsymbol{\nabla}\cdot\left(\sqrt{2D_\phi}\boldsymbol{\xi}\right)$, are given by

$$P\left[\zeta_h\right] = e^{-\frac{1}{4D_h}\int d^dx dt\, \zeta_h^2(\boldsymbol{x},t)}, \quad P\left[\zeta_\phi\right] = e^{+\frac{1}{4D_\phi}\int d^dx dt\, \zeta_\phi(\boldsymbol{x},t)\left(\nabla^2\right)^{-1}\zeta_\phi(\boldsymbol{x},t)}, \tag{4.19}$$

modulo some normalisation factor. The average in Eq. (4.18) can be written explicitly as a functional integral over the measure $\mathcal{D}[\zeta_h]\mathcal{D}[\zeta_\phi]P\left[\zeta_h\right]P\left[\zeta_\phi\right]$. The functional integrals are then performed with the aid of the delta functions, after changing their arguments from h,ϕ to ζ_h,ζ_ϕ. For the height h, from Eq. (4.17a),

$$\delta\left(h - h_{\eta,\boldsymbol{\xi}}\right) = \delta\left(\partial_t h - F_h[h,\phi] - \zeta_h\right)\left|\frac{\delta h(\boldsymbol{x},t)}{\delta\zeta_h(\boldsymbol{x}',t')}\right|^{-1}, \tag{4.20}$$

with $F_h[h,\phi] = a_h\phi + \lambda\left(\boldsymbol{\nabla}h\right)^2/2 + \nu_h\nabla^2 h$. If the solution of Eq. (4.17a) is perceived as a functional of the noise, $h[\zeta_h]$, then $|\delta h(\boldsymbol{x},t)/\delta\zeta_h(\boldsymbol{x}',t')|$ denotes the (functional) determinant of the Jacobian matrix of $h[\zeta_h]$. Analogously,

$$\delta\left(\phi - \phi_{\eta,\boldsymbol{\xi}}\right) = \delta\left(\partial_t\phi - F_\phi[h,\phi] - \zeta_\phi\right)\left|\frac{\delta\phi(\boldsymbol{x},t)}{\delta\zeta_\phi(\boldsymbol{x}',t')}\right|^{-1}, \tag{4.21}$$

with $F_\phi[h,\phi] = a_\phi\nabla^2 h + \lambda\boldsymbol{\nabla}\cdot(\phi\boldsymbol{\nabla}h) + \nu_\phi\nabla^2\phi$.

The actual functional form of both Jacobian determinants depends on the interpretation of stochastic integrals, as discussed extensively in the literature (see, for instance, [86] and [87]). In general, determinants of this kind can be expressed as a constant factor, which adds to the normalisation constant, and a field-dependent factor of the form

$$\exp\left\{-\theta(0)J[h,\phi]\right\}, \tag{4.22}$$

where $\theta(x)$ is the Heaviside function and J a functional of the fields. The θ-function value at zero ranges from 0 to 1 depending on the interpretation of stochastic integrals: in the Itô prescription, for instance, $\theta(0) = 0$, while $\theta(0) = 1/2$ in the Stratonovich convention. As the noise terms in Eq. (4.17) do not depend on the fields ϕ and h, the two conventions yield equivalent results [88]. Hence we can conveniently adopt the Itô convention and forget about Jacobian determinants. Moreover, it can be shown that Jacobian determinants do not affect the perturbation theory which will be defined later ([81], chapter 4.5).

With the Jacobian determinants set to 1, $P[h, \phi]$ is simply given by $P[\zeta_h]P[\zeta_\phi]$ computed, due to the delta functions, at $\zeta_h = \partial_t h - F_h$ and $\zeta_\phi = \partial_t \phi - F_\phi$. Namely,

$$\begin{aligned} P[h,\phi] = \exp\left\{-\frac{1}{4D_h}\int d^dx dt\ \left(\partial_t h - F_h[h,\phi]\right)^2\right\} \\ \times \exp\left\{\frac{1}{4D_\phi}\int d^dx dt\ \left(\partial_t \phi - F_\phi[h,\phi]\right)\left(\nabla^2\right)^{-1}\left(\partial_t \phi - F_\phi[h,\phi]\right)\right\}. \end{aligned} \tag{4.23}$$

The functional at the exponent is called the *Onsager-Machlup* functional. A representation such as Eq. (4.23), with the (path) probability of the relevant variables expressed as the exponential of an action functional, is analogous to the formulation of an equilibrium problem, where the (static) probability of the order parameter is written as the exponential of a free energy functional. Therefore, it is particularly advantageous from a field-theoretic perspective, in that it allows for a painless extension of all the tools developed for (static) equilibrium problems.

Actually, it is convenient to adopt a different representation, where the action functional is simplified at the price of the introduction of two auxiliary fields. The new action is called *Janssen-DeDominicis* (JD) functional and is obtained as follows. Working with the h field, first consider the delta-function representation

$$\delta\left(\partial_t h - F_h[h,\phi] - \zeta_h\right) = \int \mathcal{D}[i\tilde{h}] \exp\left\{-\int d^dx dt\, \tilde{h}\left(\partial_t h - F_h[h,\phi] - \zeta_h\right)\right\}. \tag{4.24}$$

Then perform the Gaussian integral in $\mathcal{D}[\zeta_h]$ inside the $\mathcal{D}[i\tilde{h}]$ integral, so that

$$\begin{aligned} &\int \mathcal{D}[\zeta_h]\delta\left(\partial_t h - F_h[h,\phi] - \zeta_h\right) P[\zeta_h] = \\ &\int \mathcal{D}[i\tilde{h}] \exp\left\{-\int d^dx dt\ \left[\tilde{h}\left(\partial_t h - F_h[h,\phi]\right) - D_h\tilde{h}^2\right]\right\}. \end{aligned} \tag{4.25}$$

Applying the same procedure for the ϕ field as well as h yields

$$P[h,\phi] = \int \mathcal{D}[i\tilde{h}]\mathcal{D}[i\tilde{\phi}]\, \exp\Big\{-\mathcal{A}_0[h,\tilde{h},\phi,\tilde{\phi}] - \mathcal{A}_{nl}[h,\tilde{h},\phi,\tilde{\phi}]\Big\}, \tag{4.26}$$

where the JD functional $\mathcal{A}$ has been split into a quadratic, Gaussian contribution (corresponding to the linearised Langevin equations)

$$\begin{aligned}\mathcal{A}_0[h,\tilde{h},\phi,\tilde{\phi}] = \int d^d\boldsymbol{x}dt\, \Big[&\tilde{h}\left(\partial_t - \nu_h\nabla^2\right)h - a_h\tilde{h}\phi - D_h\tilde{h}^2 \\ &+\tilde{\phi}\left(\partial_t - \nu_\phi\nabla^2\right)\phi - a_\phi\tilde{\phi}\nabla^2 h + D_\phi\tilde{\phi}\nabla^2\tilde{\phi}\Big],\end{aligned} \tag{4.27}$$

and an anharmonic contribution (containing all the nonlinearities)

$$\mathcal{A}_{nl}[h,\tilde{h},\phi,\tilde{\phi}] = \int d^d\boldsymbol{x}dt\, \left[-\frac{\lambda}{2}\tilde{h}\left(\nabla h\right)^2 - \lambda\tilde{\phi}\boldsymbol{\nabla}\cdot(\phi\boldsymbol{\nabla}h)\right]. \tag{4.28}$$

As in the theory of equilibrium critical phenomena, the separation of the action functional into harmonic and anharmonic contributions is the basis for setting up a perturbation expansion in the *coupling constant* λ, coefficient of the anharmonic action. In fact, all correlation (e.g. $\langle hh\rangle$) can be computed as (from Eq. (4.26))

$$\begin{aligned}\langle h(\boldsymbol{x},t)h(\boldsymbol{x}',t')\rangle &= \int \mathcal{D}[h,\phi,i\tilde{h},i\tilde{\phi}]h(\boldsymbol{x},t)h(\boldsymbol{x}',t')e^{-\mathcal{A}_0[h,\tilde{h},\phi,\tilde{\phi}]-\mathcal{A}_{nl}[h,\tilde{h},\phi,\tilde{\phi}]} \\ &= \frac{\left\langle h(\boldsymbol{x},t)h(\boldsymbol{x}',t')e^{-\mathcal{A}_{nl}[h,\tilde{h},\phi,\tilde{\phi}]}\right\rangle_0}{\left\langle e^{-\mathcal{A}_{nl}[h,\tilde{h},\phi,\tilde{\phi}]}\right\rangle_0},\end{aligned} \tag{4.29}$$

$\langle . \rangle_0$ denoting average w.r.t. the probability measure given by the exponential of the harmonic action. If the exponential of $\mathcal{A}_{nl}$ in Eq. (4.29) is expanded in powers of λ, one is left with Gaussian averages of products of fields h, ϕ, $\tilde{h}$ and $\tilde{\phi}$, which can be all factorised into two-point averages by virtue of the Wick theorem.

The aim of renormalisation (cf. subsection 4.3.1) is that of absorbing perturbative corrections in the coefficients of the action. Such corrections contain, in general, divergent factors: only when the number of divergent factors is finite, divergences can be regularised by introducing an arbitrary scale and absorbed in the action coefficient [79, 81]. The dependence of the renormalised coefficients on the arbitrary scale yields some flow equations: if these flow equations admit a stable fixed point for large scales, then the properties of the fixed point describe the scale-invariant features of correlation functions of the model at hand.

4.1.3 A short introduction to perturbation theory

It is worthwhile, before proceeding with the RG analysis of the active interface equations, outlining the generalities of dynamic perturbation theory [1] within the simpler example of the KPZ equation,

$$\partial_t h = \frac{\lambda}{2} \left(\boldsymbol{\nabla} h\right)^2 + \nu_h \nabla^2 h + \sqrt{2D_h}\eta. \tag{4.30}$$

The corresponding JD action is $\mathcal{A}_0 + \mathcal{A}_{nl}$, with

$$\mathcal{A}_0 = \int d^d x dt \, \left[\tilde{h}\left(\partial_t - \nu_h \nabla^2\right) h - D_h \tilde{h}^2\right], \mathcal{A}_{nl} = -\frac{\lambda}{2} \int d^d x dt \, \tilde{h} \left(\nabla h\right)^2. \tag{4.31}$$

In Fourier space (notation in Appendix A),

$$\mathcal{A}_0[h, \tilde{h}] = \int d\mathbb{k} \, \left[\tilde{h}(-\mathbb{k})\left(-i\omega + \nu_h k^2\right) h(\mathbb{k}) - D_h \tilde{h}(-\mathbb{k})\tilde{h}(\mathbb{k})\right], \tag{4.32}$$

where $\mathbb{k} = (\boldsymbol{k}, \omega)$ and $d\mathbb{k} = d^d k d\omega/(2\pi)^{d+1}$, which can be written compactly as

$$\mathcal{A}_0[h, \tilde{h}] = \frac{1}{2} \int d\mathbb{k} \, \begin{pmatrix} \tilde{h} & h \end{pmatrix} (-\mathbb{k}) \boldsymbol{A}_0(\mathbb{k}) \begin{pmatrix} \tilde{h} \\ h \end{pmatrix} (\mathbb{k}), \tag{4.33}$$

with the coupling matrix

$$\boldsymbol{A}_0(\mathbb{k}) = \begin{pmatrix} -2D_h & -i\omega + \nu_h k^2 \\ +i\omega + \nu_h k^2 & 0 \end{pmatrix}. \tag{4.34}$$

As, for $\lambda = 0$, $P[h, \tilde{h}] \sim e^{-\mathcal{A}_0}$, $\boldsymbol{A}_0(\mathbb{k})$ is, by definition of a multivariate Gaussian distribution, the inverse covariance matrix. That is,

$$\left\langle \begin{matrix} \tilde{h}(\mathbb{k})\tilde{h}(\mathbb{k}') & \tilde{h}(\mathbb{k})h(\mathbb{k}') \\ h(\mathbb{k})\tilde{h}(\mathbb{k}') & h(\mathbb{k})h(\mathbb{k}') \end{matrix} \right\rangle_0 = \boldsymbol{A}_0^{-1}(\mathbb{k}) \left(2\pi\right)^{d+1} \delta(\boldsymbol{k} + \boldsymbol{k'})\delta(\omega + \omega'). \tag{4.35}$$

Notice that the $\tilde{h}$-$\tilde{h}$ correlation vanishes, because the action is linear in h. The h-$\tilde{h}$ correlation, instead, coincides with the height response function $\chi^{hh}(k, \omega)$ via

$$\left\langle h(\mathbb{k})\tilde{h}(\mathbb{k}')\right\rangle = \chi^{hh}(k, \omega) \left(2\pi\right)^{d+1} \delta(\boldsymbol{k} + \boldsymbol{k'})\delta(\omega + \omega'), \tag{4.36}$$

whence the name *response field* for $\tilde{h}$. The 0-th order value of χ^{hh} is given by the

[1] This section is mostly based on [79] and [81]

corresponding element of $\boldsymbol{A}_0^{-1}$. Using

$$-\int d^dx dt\, \tilde{h}\,(\nabla h)^2 = \int d\mathbb{k}_1 d\mathbb{k}_2 d\mathbb{k}_3 (\boldsymbol{k}_2\cdot\boldsymbol{k}_3)\tilde{h}(\mathbb{k}_1)h(\mathbb{k}_2)(\mathbb{k}_3)\delta(\mathbb{k}_1+\mathbb{k}_2+\mathbb{k}_3), \quad (4.37)$$

with $\delta(\mathbb{k})$ a shorthand for $(2\pi)^{d+1}\delta(\boldsymbol{k})\delta(\omega)$, the first additional contribution is found at second order in λ,

$$\begin{aligned}&\left\langle h(\mathbb{k})\tilde{h}(\mathbb{k}')\right\rangle = \left\langle h(\mathbb{k})\tilde{h}(\mathbb{k}')\right\rangle_0 + \\ &\frac{\lambda^2}{4}\int d\mathbb{k}_1\ldots d\mathbb{k}_6(\boldsymbol{k}_2\cdot\boldsymbol{k}_3)(\boldsymbol{k}_5\cdot\boldsymbol{k}_6)\delta(\mathbb{k}_1+\mathbb{k}_2+\mathbb{k}_3)\delta(\mathbb{k}_4+\mathbb{k}_5+\mathbb{k}_6) \\ &\times\left\langle h(\mathbb{k})\tilde{h}(\mathbb{k}')\tilde{h}(\mathbb{k}_1)h(\mathbb{k}_2)(\mathbb{k}_3)\tilde{h}(\mathbb{k}_4)h(\mathbb{k}_5)(\mathbb{k}_6)\right\rangle_0.\end{aligned} \quad (4.38)$$

The decomposition of the 8-point correlation on the right-hand side using Wick's theorem generates several contributions, which are conveniently organised by resorting to a graphical representation in terms of Feynman diagrams. However, this procedure is known to generate some redundancies, as discussed in standard textbooks on field theory and the renormalisation group (see, e.g., chapter 5 of [79], or chapter 4.4 of [81]). For the purpose of this thesis it suffices to notice that all redundancies disappear when, instead of calculating perturbative corrections to correlation functions, one computes perturbative corrections to the path probability itself. This observation, which is nothing but a generalisation of Dyson's equation for the self-energy in quantum field theory, can be formalised by recalling that the action, read the logarithm of the path probability, is related to the generating function of the fields correlations by a Legendre-Fenchel transformation [89]. In Fourier space,

$$\begin{aligned}Z[J,\tilde{J}] &= \int \mathcal{D}[h,\tilde{h}]P[h,\tilde{h}]e^{\int d\mathbb{k}\left[\tilde{J}(\mathbb{k})\tilde{h}(-\mathbb{k})+J(\mathbb{k})h(-\mathbb{k})\right]} \\ &= \sum_{n_h,n_{\tilde{h}}=0}^{\infty}\int d\mathbb{k}_1\ldots d\mathbb{k}_{n_h+n_{\tilde{h}}}\left\langle\prod_{i=1}^{n_h}h(\mathbb{k}_i)\prod_{j=1}^{n_{\tilde{h}}}\tilde{h}(\mathbb{k}_{n_h+j})\right\rangle \\ &\times\frac{J(-\mathbb{k}_1)\ldots J(-\mathbb{k}_{n_h})}{n_h!}\frac{\tilde{J}(-\mathbb{k}_{n_h+1})\ldots\tilde{J}(-\mathbb{k}_{n_h+n_{\tilde{h}}})}{n_{\tilde{h}}!}\end{aligned} \quad (4.39)$$

is the generator of h and $\tilde{h}$ correlations. Its logarithm, $F[J,\tilde{J}]$, generates connected correlation functions, whereas the Legendre-Fenchel transform

$$\Gamma[h,\tilde{h}] = \sup_{J,\tilde{J}}\left\{\int d\mathbb{k}\,\left[\tilde{J}(\mathbb{k})\tilde{h}(-\mathbb{k})+J(\mathbb{k})h(-\mathbb{k})\right]-F[J,\tilde{J}]\right\} \quad (4.40)$$

generates vertex functions $\Gamma^{n_h,n_{\tilde{h}}}$:

$$\Gamma[h,\tilde{h}] = \sum_{n_h,n_{\tilde{h}}=0}^{\infty} \int d\mathbb{k}_1 \dots d\mathbb{k}_{n_h+n_{\tilde{h}}} \Gamma^{n_h,n_{\tilde{h}}}(\mathbb{k}_1,\dots,\mathbb{k}_{n_h+n_{\tilde{h}}}) \\ \times \frac{h(-\mathbb{k}_1)\dots h(-\mathbb{k}_{n_h})}{n_h!} \frac{\tilde{h}(-\mathbb{k}_{n_h+1})\dots \tilde{h}(-\mathbb{k}_{n_h+n_{\tilde{h}}})}{n_{\tilde{h}}!}. \tag{4.41}$$

In simpler terms, vertex functions are the coefficients of the powers of the fields appearing in the renormalised action. For a Gaussian action such as Eq. (4.33), for instance, the only non-vanishing vertex function are two-point vertex functions, coefficients of $\tilde{h}\tilde{h}$, $\tilde{h}h$, $h\tilde{h}$ and hh [2]:

$$\delta(\mathbb{k}+\mathbb{k}') \begin{pmatrix} -2D_h & -i\omega+\nu_h k^2 \\ +i\omega+\nu_h k^2 & 0 \end{pmatrix} = \begin{pmatrix} \Gamma_0^{\tilde{h}\tilde{h}}(\mathbb{k},\mathbb{k}') & \Gamma_0^{\tilde{h}h}(\mathbb{k},\mathbb{k}') \\ \Gamma_0^{h\tilde{h}}(\mathbb{k},\mathbb{k}') & \Gamma_0^{hh}(\mathbb{k},\mathbb{k}') \end{pmatrix}. \tag{4.42}$$

Luckily, because of the tilt symmetry and the particular structure of the active interface equations, two-point vertex functions are all we need to think about in the two following sections. Perturbative corrections to vertex functions are computed, as corrections to correlation functions, by resorting to diagrammatic techniques that will be introduced later in the chapter.

Once the corrections at a given order of λ are given, one can identify a *critical dimension* d_c such that, above d_c, the Fourier-space integrals appearing in the corrections are affected by *ultraviolet* (i.e. large-$\mathbb{k}$) divergences. For $d < d_c$, in general, these integrals are well-behaved, apart from some low-dimensional subspaces of the parameter space. In fact, it might happen that, when the model parameters are tuned to some specific values, corrections to correlations and vertex functions exhibit *infrared* (i.e. small-$\mathbb{k}$) divergences when the momenta of the fields entering the correlation/vertex functions are also vanishingly small. This is a general indication that, for the selected parameter values, the model is *critical* and displays scale-invariance at large lengthscales and long times ($\mathbb{k} \to 0$). Furthermore, infrared divergences imply that perturbative corrections will be important for the model's scaling behaviour (for $d < d_c$), hence a *renormalisation* procedure must be applied. Issues of this kind are better discussed within the linearised, Gaussian model first: this will be the topic of section 4.2. Perturbative corrections will be considered again in section 4.3, where renormalisation is discussed and performed.

[2] Actually the coefficient of hh vanishes too, by construction of the JD functional.

4.2 Mean field theory

This section is entirely devoted to the model defined by the harmonic action of Eq. (4.27), recalled below for clarity:

$$\begin{aligned}\mathcal{A}_0[h,\tilde{h},\phi,\tilde{\phi}] = \int d^dx dt\ [\tilde{h}\left(\partial_t - \nu_h\nabla^2\right)h - a_h\tilde{h}\phi - D_h\tilde{h}^2 \\ +\tilde{\phi}\left(\partial_t - \nu_\phi\nabla^2\right)\phi - a_\phi\tilde{\phi}\nabla^2 h + D_\phi\tilde{\phi}\nabla^2\tilde{\phi}\,]\,.\end{aligned} \tag{4.43}$$

For all Gaussian models, the outcomes of renormalisation can be inferred with simple scaling analysis—the 'naive' dimensional analysis of subsection 4.2.1. Scaling analysis is aimed at inferring a scale transformation for the fields such that the harmonic action (or equivalently the linearised equations) is invariant for scale transformations of space and time. In momentum space, this procedure begins with the integration of high-wavenumber (and high-frequency) modes in the action. If Λ denotes the upper limit of Fourier integrals [3], the integration produces only a reduction of the Λ by some factor b. This is because, in the Gaussian model, modes with different momenta are not coupled with each other. Restoring the original limits requires an upscaling of momenta, $\mathbb{k} \to b\mathbb{k}$, which introduces a series of b factors in the action. These factors can be removed by choosing an appropriate transformation law for fields an parameters such as

$$\psi \to b^{y_\psi}\psi, \tag{4.44}$$

y_ψ denoting the *scaling dimension* of the generic 'operator' ψ. The scaling dimension determines the fate of the corresponding term under scale transformation, whether it will grow, vanish, or remain unchanged. For critical fields, the scaling dimension governs the power-law decay of correlations.

Generally, the scaling dimensions of the Gaussian model cannot be considered a faithful approximation of the actual scaling dimensions of the full, nonlinear model. Scaling arguments based on the Gaussian model can nonetheless be used to *a)* infer the critical dimension of nonlinear couplings; *b)* determine which vertex functions will contain diverging integrals and how these integral diverge; *c)* check the consistency of the expansion of the action in low-order powers of the fields and derivatives. The scaling dimensions of the Gaussian model, also referred to as *engineering* or *canonical* dimensions, can be obtained with dimensional

[3] The cut-off can be thought as coming from the shortest possible time- and lengthscales of the model, such as a lattice spacing or the highest hopping rate.

arguments as well—this is the subject of subsection 4.2.1.

In addition to being a useful starting point for renormalisation, the computation of engineering dimension allows to have a first look at the model's phase diagram (subsection 4.2.3). In addition, above the critical dimension of nonlinear couplings, the scaling exponents provided by the Gaussian approximation become exact. As the Gaussian approximation implies factorisation of higher-order correlations into a product of two-point correlations, it yields the same results as mean-field theory, whence the name of the section. It can even be the case, as in subsection 4.2.2, that all nonlinear couplings have negative critical dimension, so that mean-field theory provides exact exponents in all dimensions.

4.2.1 Naive dimensional analysis

As anticipated a few paragraphs ago, engineering dimensions can be computed by using dimensional arguments only. First one defines an arbitrary momentum scale μ such that

$$[k] = \mu, \quad [\omega] = \mu^z \quad \Rightarrow \quad [x] = \mu^{-1}, \quad [t] = \mu^{-z}. \tag{4.45}$$

By keeping in mind that the large-scale features of the model are obtained in the $\mu \to 0$ limit, the *dynamic exponent* z prescribes the relation between time- and length-scales in the thermodynamic limit ($[t] = [x]^z$). Dimensions of fields and parameters are then obtained by the requirement of adimensionality of the action, $[\mathcal{A}_0] = \mu^0$. For instance, adimensionality of $\int \tilde{h}\partial_t h$ and $\int \tilde{\phi}\partial_t \phi$ (integral measures omitted) requires

$$y_{\tilde{h}} + y_h = d, \quad y_{\tilde{\phi}} + y_\phi = d. \tag{4.46}$$

Let us now turn to the terms with the squared response fields, corresponding to noise in the Langevin equations, $\int D_h \tilde{h}^2$ and $\int D_\phi (\nabla\phi)^2$. The coefficients D_h and D_ϕ can be removed from the action by rescaling response fields, or, equivalently, assumed adimensional, i.e. $[D_h] = [D_\phi] = \mu^0$. In both cases, adimensionality of the height noise requires $[x]^d [t] \left[\tilde{h}\right]^2 = \mu^0$, that is

$$y_{\tilde{h}} = \frac{d+z}{2} \Rightarrow y_h = \frac{d-z}{2}, \tag{4.47}$$

where Eq. (4.46) has been used to obtain y_h. In complete analogy, adimensionality of the density noise requires $[x]^{d-2}\,[t]\left[\tilde{\phi}\right]^2 = \mu^0$, so that

$$y_{\tilde{\phi}} = \frac{d+z-2}{2} \Rightarrow y_\phi = \frac{d-z+2}{2}, \tag{4.48}$$

obtained again by using Eq. (4.46). A common choice for the dynamic exponent is $z = 2$, i.e. *diffusive scaling*. With such a choice, the coefficients of the Laplacian terms in the Langevin equations, ν_h and ν_ϕ, are automatically dimensionless, and the engineering dimensions of the fields become

$$y_{\tilde{h}} = \frac{d+2}{2}, \quad y_h = \frac{d-2}{2}, \quad y_{\tilde{\phi}} = y_\phi = \frac{d}{2}. \tag{4.49}$$

However, the requirement of adimensionality of the two remaining terms in the action Eq. (4.43) causes the two coupling coefficients a_h—active-growth—and a_ϕ—slope-advection—to acquire a positive scaling dimension,

$$[a_h] = [a_\phi] = \mu. \tag{4.50}$$

The above result implies that both a_h and a_ϕ are *relevant operators*, which means they grow under a scale transformation. In the context of equilibrium statistical mechanics, this situation is typically encountered for parameters such as the distance from the critical temperature of a phase transition. In general, parameters with positive engineering dimension are symptoms of a model being away from a critical point. This last aspect is better understood by computing two-point correlation functions which, for the Gaussian model, are simply given by the elements of the inverse of the coupling matrix appearing in the Fourier representation of the action Eq. (4.43) (see Eq. (4.35)).

In terms of the Fourier components of the fields, the action Eq. (4.43) can be written compactly as

$$\mathcal{A}_0[h,\tilde{h},\phi,\tilde{\phi}] = \frac{1}{2}\int d\mathbb{k} \begin{pmatrix} \tilde{h} & h & \tilde{\phi} & \phi \end{pmatrix} (-\mathbb{k})\boldsymbol{A}_0(\mathbb{k}) \begin{pmatrix} \tilde{h} \\ h \\ \tilde{\phi} \\ \phi \end{pmatrix} (\mathbb{k}). \tag{4.51}$$

If $L_h = -i\omega + \nu_h k^2$ and $L_\phi = -i\omega + \nu_\phi k^2$, with † denoting complex conjugation,

$$\boldsymbol{A}_0 = \begin{pmatrix} -2D_h & L_h & 0 & -a_h \\ L_h^\dagger & 0 & +k^2 a_\phi & 0 \\ 0 & +k^2 a_\phi & -2D_\phi k^2 & L_\phi \\ -a_h & 0 & L_\phi^\dagger & 0 \end{pmatrix}. \tag{4.52}$$

In practice, the coupling matrix represents the Fourier-space dynamical equations for h and ρ. The h equation, for instance, is found on the row corresponding to the $\tilde{h}$ component, i.e. the first row. Within the row, the first element is the (negative) coefficient of the height noise ($-2D_h$), the second is the operator acting on h (L_h), the third the coefficient of the density noise (0 in the height equation) and the fourth the operator acting on ϕ ($-a_h$). The resulting equation is $L_h h - a_h \phi - \sqrt{2D_h}\eta = 0$, the Fourier transform of the linearised height equation (cf. Eq. (4.59a)). The ϕ equation is found analogously on the third row.

The inverse of the coupling matrix can be conveniently split into 4 smaller matrices,

$$\boldsymbol{A}_0^{-1}(\mathbb{k}) = \begin{pmatrix} \boldsymbol{C}_0^{hh}(\mathbb{k}) & \boldsymbol{C}_0^{h\phi}(\mathbb{k}) \\ \boldsymbol{C}_0^{\phi h}(\mathbb{k}) & \boldsymbol{C}_0^{\phi\phi}(\mathbb{k}) \end{pmatrix}, \tag{4.53}$$

each collecting 4 of the 16 two-point correlations between the fields $h, \tilde{h}, \phi$ and $\tilde{\phi}$. $\boldsymbol{C}_0^{hh}(\mathbb{k})$, for instance, is given by (in the notation of subsection 4.1.1),

$$\boldsymbol{C}_0^{hh}(\mathbb{k}) = \begin{pmatrix} C_0^{\tilde{h}\tilde{h}}(\mathbb{k}) & \chi_0^{hh}(-\mathbb{k}) \\ \chi_0^{hh}(\mathbb{k}) & C_0^{hh}(\mathbb{k}) \end{pmatrix}, \tag{4.54}$$

with

$$\chi_0^{hh}(\mathbb{k}) = \frac{1}{L_h + (L_\phi)^{-1} a_h a_\phi k^2}, \tag{4.55}$$

and

$$C_0^{hh}(\mathbb{k}) = 2D_h \left[\chi_0^{hh}(\mathbb{k})\chi_0^{hh}(-\mathbb{k})\right] + \frac{a_h^2 2D_\phi k^2}{|L_h L_\phi + a_h a_\phi k^2|^2}. \tag{4.56}$$

$C_0^{\tilde{h}\tilde{h}}(\mathbb{k})$, as every two-point functions involving response fields only, vanishes by construction of the JD functional. Consider now the static limit $\omega = 0$ of the height response function χ^{hh}, that is the *integral* response. As $L_{h/\phi}(\omega = 0) = \nu_{h/\phi} k^2$,

$$\chi_0^{hh}(\boldsymbol{k}, \omega = 0) = \frac{1}{\nu_h} \frac{1}{k^2 + a_h a_\phi / \nu_h \nu_\phi}, \tag{4.57}$$

which displays the typical Ornstein-Zernicke form $(k^2 + a)^{-1}$.

The integral response coincides with the static susceptibility, i.e. the variation of the steady-state average $\langle h(\boldsymbol{x}, t \to \infty)\rangle_0$ of the field $h(\boldsymbol{x}, t)$ due to a constant perturbation $v(\boldsymbol{x}')$ switched on in the far past:

$$\langle h(\boldsymbol{x}, \infty)\rangle_0 = \int d^d x' \left[\int \frac{d^d k}{(2\pi)^d}\, \chi_0^{hh}(\boldsymbol{k}, 0)\right] v(\boldsymbol{x}'). \tag{4.58}$$

In real space, the term $a_h a_\phi/\nu_h\nu_\phi$ in the denominator of Eq. (4.57) causes the exponential decay of the effects of the perturbation with $|\boldsymbol{x}-\boldsymbol{x}'|$: the decay length is $\sqrt{\nu_h\nu_\phi/a_h a_\phi}$. All the non-vanishing two-point functions of the problem display a similar phenomenology, with $\sqrt{\nu_h\nu_\phi/a_h a_\phi}$ playing the role of a finite *correlation length*. For the system to display critical behaviour, the correlation length must diverge: this is the case, for instance, when $a_\phi = a_h = 0$, as in section 4.3. Furthermore, the correlation length can be made to diverge by a suitable rescaling of time in the Langevin equations, or by setting only one between a_ϕ and a_h to 0. By indicating the portions of the parameter space where to expect critical behaviour, these two possibilities hint at the structure of the phase diagram: they will be explored in subsection 4.2.2 and subsection 4.2.3, respectively.

4.2.2 Oscillating dynamics at the Euler scale

According to Eq. (4.50), the active-growth and slope-advection coefficients a_ϕ and a_h increase under scale transformation. However, a closer look at the model's equations,

$$\partial_t h = a_h\phi + \nu_h\nabla^2 h + \sqrt{2D_h}\eta, \tag{4.59a}$$
$$\partial_t \phi = a_\phi\nabla^2 h + \nu_\phi\nabla^2\phi + \sqrt{2D_\phi}\boldsymbol{\nabla}\cdot\boldsymbol{\xi}, \tag{4.59b}$$

suggests that the divergence of the parameters a_ϕ, a_h in the large-scale limit can be fixed by rescaling time-derivatives. Precisely, as $\left[a_{h/\phi}\right] = \mu$, the required rescaling is $t \to t' = \mu t$. Such rescaling is tantamount to a reduction of the dynamic exponent z by one unit.

As a matter of fact, the positive scaling dimension of a_h and a_ϕ is related to the peculiar thermodynamic limit considered in subsection 4.2.1, where $t \to \infty$ as a squared length. Setting $z = 1$, so that $t \to \infty$ as a length, modifies engineering dimensions: they will now describe the scaling of the Gaussian model at the *Euler*

scale rather than the diffusive scale. From Eq. (4.47), with $z = 1$,

$$y_{\tilde{h}} = \frac{d+1}{2} \Rightarrow y_h = \frac{d-1}{2}, \tag{4.60}$$

whereas

$$y_{\tilde{\phi}} = \frac{d-1}{2} \Rightarrow y_\phi = \frac{d+1}{2}, \tag{4.61}$$

from Eq. (4.48). Using the above engineering dimensions, one finds $[a_h] = [a_\phi] = \mu^0$, $[\nu_h] = [\nu_\phi] = \mu^{-1}$, which means ν_h and ν_ϕ are *irrelevant* parameters. As irrelevant parameters, ν_ϕ and ν_h decrease under scale transformation and do not affect the scale-invariant properties of the system. In this respect, the results of this section provide a scaling perspective on the inviscid limit of section 3.2. $z = 1$, in particular, represents both the ballistic motion of activator clusters and interface ripples (subsection 3.3.1 and subsection 2.3.2, Fig. 2.18), and the oscillatory pattern found in observing the roughening of flat interfaces (subsection 2.3.1, Fig. 2.15).

Let us now derive the engineering dimension of the coefficient λ which multiplies the nonlinear contributions to the JD action in Eq. (4.28). Because of $y_{\tilde{h}} + y_h = d = y_{\tilde{\phi}} + y_\phi$, adimensionality of $\lambda\tilde{h}(\nabla h)^2$ and $\lambda\tilde{\phi}\boldsymbol{\nabla}\cdot(\phi\boldsymbol{\nabla}h)$ implies

$$[\lambda] = \mu^{z-2-y_h} = \mu^{-\frac{d+1}{2}} \equiv \mu^{y_\lambda}. \tag{4.62}$$

The engineering dimension y_λ is negative for each positive d, so that the nonlinear terms in the action have no effect on critical properties at the Euler scale. In general, the vanishing of y_λ defines the *critical dimension* d_c of the corresponding nonlinear term (both $\tilde{h}(\nabla h)^2$ and $\tilde{\phi}\boldsymbol{\nabla}\cdot(\phi\boldsymbol{\nabla}h)$, in the present case). As explained in [79], chapter 7, engineering dimensions coincide with true scaling dimensions above d_c—it is said that mean field theory holds for $d > d_c$. The reason is that the perturbative corrections introduced in subsection 4.1.3 contain Fourier integrals with ultraviolet divergences. In the context of statistical mechanics, these divergences are usually not interesting and can be removed by introducing a small length-scale such as the lattice spacing or the interatomic distance. Therefore, ultraviolet divergences cannot alter the large-scale properties of the system, as given by the engineering dimensions.

All higher-order nonlinearities have engineering dimensions smaller than y_λ, thus are irrelevant for the scaling. This statement can be proved by noticing that *i)* the addition of another gradient (time-derivative) lowers the engineering dimension

by 1 (z); *ii)* the insertion of ϕ reduces the dimension by y_ϕ, which is positive $\forall d > 0$; *iii)* the insertion of $\boldsymbol{\nabla} h$ (a single h with no gradient is forbidden by translational invariance) reduces the dimension by $y_h + 1 = y_\phi$. In addition, because of the positivity of y_ϕ, the coefficient of the nonlinear term $\phi(\nabla\tilde{\phi})^2$, which correspond to a multiplicative noise $\boldsymbol{\nabla} \cdot (\sqrt{2\phi}\boldsymbol{\xi})$ in the Langevin equation, is also irrelevant. Having established that the mean-field exponents of Eq. (4.60) and Eq. (4.61) are exact in all dimension—at least at the Euler scale—we can now comment on the implications of such exponents. As mentioned a few paragraphs ago, $z = 1$, reflects the propagation of waves of excess density ϕ and interface height h along the system. The corresponding scaling agrees with the numerics of chapter 2 and the analytics of chapter 3. In fact, $z = 1$ is the most reasonable choice for the description of a system whose dynamics is dominated by waves, such as the travelling nanoclusters of membrane activators and lateral membrane ripples observed at the cell membrane [45].

The scaling dimensions of the fields, instead, reflects the static steady-state properties of the system. Their meaning is better understood by recalling that, by definition of the scaling dimension of an operator ψ, $\psi \to b^{y_\psi}\psi$ when $k \to bk$, where k could be any relevant momentum scale. By considering the momentum modulus, $k = \sqrt{\boldsymbol{k} \cdot \boldsymbol{k}}$, the definition fixes the form of ψ as a function of k:

$$\psi(k) \sim k^{y_\psi}. \tag{4.63}$$

The scaling dimension of the equal-time height-height correlation $\langle h(\boldsymbol{k}, t)h(\boldsymbol{q}, t)\rangle$, for instance, is $2y_h - 2d$ ($2y_h$ from the two h fields, $-2d$ because each Fourier transform entails a $d^d x$ integral which reduces the scaling dimension by d). Upon removing the dimension μ^{-d} of $\delta(\boldsymbol{k} + \boldsymbol{q})$, the scaling dimension of the height structure factor follows (cf. Eq. (A.12)).

$$\left[S^h(k)\right] = \mu^{2y_h - d} \Rightarrow S(k) \sim k^{2y_h - d}. \tag{4.64}$$

As explained in Appendix A, the width of an interface having linear size L can be written as [14]

$$w^2(L, t) = \frac{1}{L^d} \sum_{\boldsymbol{k} \neq 0} S(k, t) \xrightarrow{L,t\to\infty} C \int_{2\pi/L}^{\infty} k^{d-1} dk\, S(k). \tag{4.65}$$

Integration w.r.t. k of $k^{d-1}S(k) \sim k^{2y_h - 1}$ yields the scaling of the saturation width with the system size, $w^2_\infty(L) \sim L^{-2y_h} \equiv L^{2\alpha}$, allowing for the identification

of the scaling dimension y_h with the negative roughness exponent α. According to Eq. (4.47), $\alpha = (1-d)/2$, meaning $\alpha \leq 0 \; \forall \; d$, i.e. a flat interface at the Euler scale. This result is unfortunately not supported by the numerics of chapter 2, except for the surfing regime of the test-particle problem (Fig. 2.12). The reason is that, for a finite interface, there will always be a small surface tension ν_h which eventually causes the decay of correlations in steady-state, resulting in $\alpha = 1/2$.

Similar arguments can be applied to the excess density ϕ. The integral of the real-space ϕ-ϕ correlation over a portion of space of linear size L, for instance, is a measure of density fluctuations:

$$\delta N^2(L) = \int_{[0,L]^d} d^d x \int_{[0,L]^d} d^d y \; \langle \phi(\boldsymbol{x},t)\phi(\boldsymbol{y},t)\rangle \; , \left[\delta N^2(L)\right] = \mu^{2(y_\phi - d)}. \qquad (4.66)$$

From Eq. (4.61), $\delta N^2(L) \sim L^{d-1}$, which is the signature scaling of *hyperuniform* states [90]. A point-pattern or density distribution is termed hyperuniform when its large-scale fluctuations are strongly suppressed—as in the density distribution of a crystal. The hyperuniformity of our activator density results from the activators gathering in finite-size clusters which are (statistically) homogeneously distributed over the system, as discussed in subsection 2.3.2.

4.2.3 Two novel critical lines

Returning now to the diffusive scale $z = 2$, the active interface can still exhibit critical behaviour in some restricted regions of the parameter (sub)space (a_h, a_ϕ). There is, for instance, a standard Gaussian fixed point at $a_h = a_\phi = 0$, where h and ϕ obey the stochastic and conserved stochastic diffusion equation, respectively. Corrections due to the nonlinear coupling terms of Eq. (4.28) will be considered in the next section. According to Eq. (4.57), the finite correlation length which drives the active interface away from criticality is proportional to $\sqrt{a_h a_\phi}$: critical behaviour can also be achieved by setting only one between a_h and a_ϕ to 0, as discussed in what follows. It is worthwhile stressing that, in order to obtain different results from subsection 4.2.1 the assumption of adimensionality of the noise coefficients D_ϕ and D_h shall be relaxed.

In examining the $a_h = 0$ line of the (a_h, a_ϕ) plane, which is reached by suppressing active growth, it is meaningful to assume a_ϕ to be adimensional. In fact, another assumption would lead again to the cases already discussed. As for $[D_h] = [D_\phi] =$

μ^0, also the condition $[a_\phi] = \mu^0$ can be met by a suitable rescaling of the response field $\tilde{\phi}$ in the action, aimed at removing the parameter a_ϕ. Then, adimensionality of the action requires $\int \tilde{\phi}\nabla^2 h$ to be adimensional, i.e. $[x]^{d-2}\,[t]\left[\tilde{\phi}\right][h] = \mu^0$, verified for (recall now $z = 2$)

$$y_{\tilde{\phi}} + y_h = d. \tag{4.67}$$

Combining the above condition with Eq. (4.46) results in $y_\phi = y_h$. The parameter D_h can be removed again by rescaling $\tilde{h}$, so as to obtain $y_h = (d-2)/2$ as in Eq. (4.49). Thus,

$$y_\phi = y_h = \frac{d-2}{2}. \tag{4.68}$$

Interestingly, with these engineering dimensions $[a_h] = \mu^2$, as if all the dimension of a_ϕ and a_h has been transferred to a_h, and $[D_\phi] = \mu^{-1}$.

In simple terms, scaling analysis suggests a critical line at $a_h = 0$, where the noise on the excess density is irrelevant—the field ϕ can still be perturbed indirectly via perturbations on h. There is an additional action term $c_h \int \tilde{h}\nabla^2\phi$ which is compatible with all the model symmetries. As $y_{\tilde{h}} = 1 + d/2$,

$$[x]^{d-2}\,[t]\left[\tilde{h}\right][\phi] = \mu^0 \Rightarrow [c_h] = \mu^0. \tag{4.69}$$

Having vanishing engineering dimension, the parameter c_h is *marginal* with respect to scale transformations, hence it can be generated by the latter even if absent from the original model. Including c_h is equivalent to the addition of a term $c_h\nabla^2\phi$ in the height Langevin equation Eq. (4.17a). Such a term causes the interface to acquire curvature in response to an excess of activator density ϕ. Whether the acquired curvature is positive or negative, it depends on the sign of c_h. Remarkably, the coupling between activator density and interface curvature is meaningful in the context of active membranes and it has been considered before [31], as mentioned in the final part of chapter 1. We have neglected such a coupling in the presence of the "more relevant" active growth process, but it can re-emerge as a result of scale transformations after active growth, represented here by the parameter a_h, has been made to vanish.

Critical behaviour can also be found on the $a_\phi = 0$ line of the (a_h, a_ϕ) plane, where slope advection does not occur. Here non-trivial results can be obtained by assuming a_h to be adimensional, then shift all the dimension of $a_h a_\phi$ to a_ϕ. In detail, $[a_h] = \mu^0$ means that $\int \tilde{h}\phi$ is adimensional too, i.e. $[x]^d\,[t]\left[\tilde{h}\right][\phi] = \mu^0$, which is verified for

$$y_{\tilde{h}} + y_\phi = d + 2. \tag{4.70}$$

y_ϕ is obtained after removing the parameter D_ϕ from the action, resulting in $y_\phi = d/2$ as in Eq. (4.49). Inserting $y_\phi = d/2$ into Eq. (4.70) yields $y_{\tilde{h}}$, then y_h via Eq. (4.46) as

$$y_h = y_\phi - 2 = \frac{d-4}{2}. \tag{4.71}$$

Upon recalling the equivalence between y_h and the negative roughness exponent, Eq. (4.68) indicates that, when the slope-advection coefficient vanishes, the active interface is much rougher than the passive counterparts ($(4-d)/2 > (2-d)/2$, the EW and KPZ mean-field roughness), at least in the mean-field approximation. As on the $a_h = 0$ line, there is a new term of the action which emerges, for $a_\phi = 0$, under scale transformation. This term reads $c_\phi \int \tilde{\phi} \nabla^4 h$ and the dimension of the corresponding coefficient is

$$[c_\phi] = \left([x]^{d-4} [t] \left[\tilde{\phi}\right] [h] \right)^{-1} = \mu^0. \tag{4.72}$$

The introduction of this new marginal parameter is equivalent to adding a term proportional to $\nabla^4 h$ in the density equation Eq. (4.17b), which causes the excess activator density to interact with the interface curvature. Specifically, c_ϕ can be perceived as the negative activator spontaneous curvature, so that activators become attracted by interface regions with their same curvature [31]. This is another example where the curvature-coupling, neglected in the original formulation of our model, emerges again when the slope-coupling is suppressed.

We are finally in the position to sum up the (mean-field) phase diagram of the active interface equations, goal of this section. As shown in Fig. 4.3, the phase diagram consists of two critical lines which cross at a bicritical point $a_h = a_\phi = 0$. At the Euler scale $z = 1$ (subsection 4.2.2), the mean-field exponents are exact in all dimensions, resulting in a flat interface with hyperuniform fluctuations in the activator density. This is not the case for the diffusive scale $z = 2$, where the two critical lines emerge. For both the critical lines the nonlinear coupling constant λ has a finite critical dimension d_c. The latter, obtained by setting $z = 2$ in Eq. (4.62), equals 4 on the $a_\phi = 0$ critical line; 2 on the $a_h = 0$ line. Below such critical dimensions, the mean-field exponents presented in this section might acquire non-trivial corrections whose determination is beyond the scope of this thesis: it will be left as a future perspective. The remainder of the chapter discusses renormalisation at the bicritical point $a_h = a_\phi = 0$.

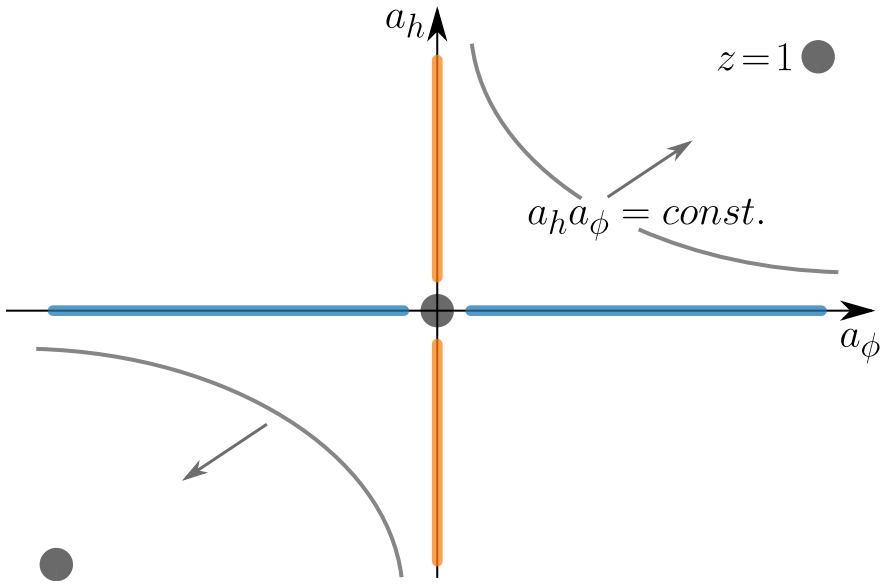

Figure 4.3 *Mean-field phase diagram of the active interface equations. For any non-zero a_h and a_ϕ, such that $a_h a_\phi > 0$, scale transformations push the model towards the $z = 1$ fixed points, located at the top-right and bottom-left corners of the figure. The same is actually true for $a_h a_\phi < 0$, but the Gaussian model is unstable in this region. The 'unstable' and 'stable' phases, coinciding with the quadrants of the (a_h, a_ϕ) plane, are separated by two critical lines $a_h = 0$ and $a_\phi = 0$, with a bicritical point lying at their intersection.*

4.3 One-loop corrections at the KPZ fixed point

This last section deals with renormalisation of the active interface equations at the "KPZ" fixed point $a_h = a_\phi = 0$. Here the height obeys the KPZ equation while the excess density ϕ follows an advection-diffusion equation. In redefining fields $h \to \sqrt{D_h/\nu_h}h$ and $\phi \to \sqrt{D_\phi/\nu_\phi}\phi$, with $g = \lambda\sqrt{D_h/\nu_h^3}$ and $r = \nu_\phi/\nu_h$,

$$\partial_t h = \frac{\nu_h g}{2}(\nabla h)^2 + \nu_h \nabla^2 h + \sqrt{2D_h}\eta, \tag{4.73a}$$

$$\partial_t \phi = \nu_h g \boldsymbol{\nabla}\cdot(\phi\boldsymbol{\nabla}h) + r\nu_h\nabla^2\phi + \boldsymbol{\nabla}\cdot\left(\sqrt{2r\nu_h}\boldsymbol{\xi}\right). \tag{4.73b}$$

The relevant vertex functions are introduced in the following paragraphs, and computed at order g^2 of the perturbation theory. Renormalisation is performed in subsection 4.3.1 and the resulting flow equations are studied in subsection 4.3.2. As for the single KPZ equation [83], perturbation theory will be proven incapable of reaching other fixed points than the Gaussian one. The calculation which follows is nonetheless instructive and useful for a future studies of the full phase diagram. Subsection 4.3.3 provides a short summary of the whole chapter.

Coming back to the KPZ fixed point, as $a_h = a_\phi = 0$, the inverse coupling matrix of the Gaussian theory Eq. (4.52) becomes block-diagonal. The first diagonal block $\boldsymbol{A}_0^h(\mathbb{k})$ coincides with the coupling matrix of the EW equation, Eq. (4.42) (with $D_h = \nu_h$), while the second block is the coupling matrix of a stochastic diffusion equation,

$$\delta(\mathbb{k}+\mathbb{k}')\begin{pmatrix} -2r\nu_h k^2 & -i\omega + r\nu_h k^2 \\ +i\omega + r\nu_h k^2 & 0 \end{pmatrix} = \begin{pmatrix} \Gamma_0^{\tilde\phi\tilde\phi}(\mathbb{k},\mathbb{k}') & \Gamma_0^{\tilde\phi\phi}(\mathbb{k},\mathbb{k}') \\ \Gamma_0^{\phi\tilde\phi}(\mathbb{k},\mathbb{k}') & \Gamma_0^{\phi\phi}(\mathbb{k},\mathbb{k}') \end{pmatrix}. \quad (4.74)$$

As each two-point vertex function is proportional to $\delta(\mathbb{k}+\mathbb{k}')$, it is convenient to set $\Gamma_0(\mathbb{k},\mathbb{k}') = \delta(\mathbb{k}+\mathbb{k}')\Gamma_0(\mathbb{k})$ and work with functions of one momentum only.

Perturbative corrections to the vertex function $\Gamma^{\tilde h h}$ are obtained by exploiting the relation between vertex and correlation functions, which are, in turn, obtained from Eq. (4.40) by differentiation (see Appendix C for details). Perturbative corrections to correlations are conveniently organised with Feynman diagrams. First, lines are assigned to all the independent two-point functions of the Gaussian theory: $\chi_0^{hh}(\mathbb{k})$ ($\left\langle h\tilde h\right\rangle$), $C_0^{hh}(\mathbb{k})$ ($\langle hh\rangle$), $\chi_0^{\phi\phi}(\mathbb{k})$ ($\left\langle \phi\tilde\phi\right\rangle$) and $C_0^{\phi\phi}(\mathbb{k})$ ($\langle\phi\phi\rangle$),

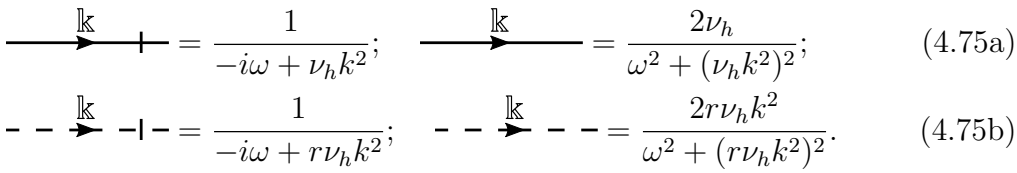

(4.75a)

(4.75b)

The convention is that solid lines represent height fields, while dashed lines are used for density fields, and an orthogonal tick distinguishes normal fields (h,ϕ) from response fields $(\tilde h,\tilde\phi)$. Secondly, vertices are assigned to the coefficients of nonlinear terms in Fourier space,

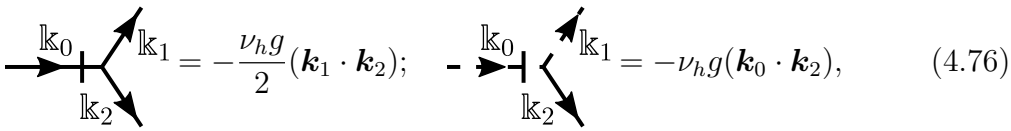

(4.76)

plus delta functions which ensure the balance of incoming and outgoing momenta and an integral over all momenta. The m-th order (in g) correction to a generic N-point correlation function is obtained by drawing all possible topologically distinct diagrams with N loose ends and n_V nonlinear vertices, compatible with conservation of momentum along the diagram. Diagrams consisting of two separate diagrams are removed by considering connected correlations only.

When switching to vertex functions (cf. Eq. (C.11) and (C.16)), also diagrams

that separate upon severing an internal line can be dropped—only *one-particle irreducible* graphs contribute. In addition, the N lines constituting the loose ends of the diagram do not contribute to its numerical value. At second order in g, the height vertex functions are [83] (or [81], 11.4.1)

$$\Gamma^{\tilde{h}h}(\mathbb{k}) = -i\omega + \nu_h k^2 - \quad (4.77)$$

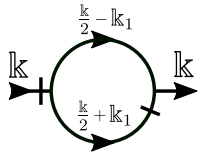

$$= i\omega + \nu_h k^2 + \nu_h \frac{g^2}{2} \int_{k_1} \frac{\frac{k^2}{2} - \boldsymbol{k}_1 \cdot \boldsymbol{k}}{\left(\frac{\boldsymbol{k}}{2} - \boldsymbol{k}_1\right)^2} \frac{\frac{k^2}{4} - k_1^2}{\frac{k^2}{4} + k_1^2 - \frac{i\omega}{2\nu_h}};$$

$$\Gamma^{\tilde{h}\tilde{h}}(\mathbb{k}) = -2\nu_h - \quad (4.78)$$

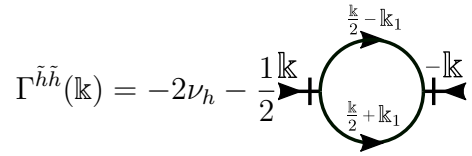

$$= -2\nu_h - 2\nu_h \frac{g^2}{4} \int_{k_1} \frac{\left(\frac{k^2}{4} - k_1^2\right)^2}{\left(\frac{\boldsymbol{k}}{2} + \boldsymbol{k}_1\right)^2 \left(\frac{\boldsymbol{k}}{2} - \boldsymbol{k}_1\right)^2} \mathrm{Re}\left[\frac{1}{\frac{k^2}{4} + k_1^2 - \frac{i\omega}{2\nu_h}}\right];$$

where $\int_k$ is a shorthand for $\int d^d k/(2\pi)^d$. Corrections to the density vertex functions are given by

$$\Gamma^{\tilde{\phi}\phi}(\mathbb{k}) = -i\omega + r\nu_h k^2 - \quad (4.79)$$

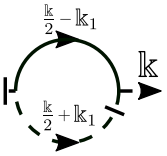

$$= i\omega + r\nu_h k^2 + \nu_h \frac{g^2}{2} \int_{k_1} \frac{\frac{k^2}{2} - \boldsymbol{k}_1 \cdot \boldsymbol{k}}{\left(\frac{\boldsymbol{k}}{2} - \boldsymbol{k}_1\right)^2} \frac{\frac{k^2}{4} - k_1^2}{\frac{r\left(\frac{\boldsymbol{k}}{2}+\boldsymbol{k}_1\right)^2 + \left(\frac{\boldsymbol{k}}{2}-\boldsymbol{k}_1\right)^2}{2} - \frac{i\omega}{2\nu_h}};$$

$$\Gamma^{\tilde{\phi}\tilde{\phi}}(\mathbb{k}) = -2r\nu_h k^2 - \quad (4.80)$$

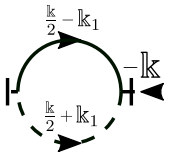

$$= -2r\nu_h k^2 - 2\nu_h \frac{g^2}{2} \int_{k_1} \frac{\left(\frac{k^2}{2} - \boldsymbol{k} \cdot \boldsymbol{k}_1\right)^2}{\left(\frac{\boldsymbol{k}}{2} - \boldsymbol{k}_1\right)^2} \mathrm{Re}\left[\frac{1}{\frac{r\left(\frac{\boldsymbol{k}}{2}+\boldsymbol{k}_1\right)^2 + \left(\frac{\boldsymbol{k}}{2}-\boldsymbol{k}_1\right)^2}{2} - \frac{i\omega}{2\nu_h}}\right];$$

as shown in Appendix D and Appendix E, respectively. These results will be used in the next subsection to renormalise the parameters ν_h, r and g and the fields.

4.3.1 Renormalisation

As anticipated in section 4.2, dimensional analysis can be used to determine which vertex functions gain diverging contributions from perturbative corrections. Let us then recall the engineering dimensions of the model, given by Eq. (4.73),

$$y_{\tilde{h}} = \frac{d+2}{2}, \quad y_h = \frac{d-2}{2}, \quad y_{\tilde{\phi}} = y_\phi = \frac{d}{2}, \quad [g] = \mu^{z-2-y_h} = \mu^{-\frac{d-2}{2}}. \tag{4.81}$$

A combination of the fields dimensions yields the engineering dimension of a vertex function $\Gamma^{\psi_1,\dots,\psi_n}$, where each ψ_i is one between $h, \tilde{h}, \phi, \tilde{\phi}$. The starting point is the definition of the vertex generating function, Eq. (4.41). The generating function, like the action, is adimensional,

$$\left[\Gamma^{\psi_1,\dots,\psi_n}(\mathbb{k}_1,\dots\mathbb{k}_n)\right]\prod_{i=1}^{n}\left[\int d\mathbb{k}_i\psi_i(-\mathbb{k}_i)\right] = \mu^0, \tag{4.82}$$

so that the dimension of an n-point vertex function is the negative sum of the dimensions of all its fields ψ_i. Considering also that $\Gamma(\mathbb{k}_1,\dots\mathbb{k}_n) = \Gamma(\mathbb{k}_1,\dots\mathbb{k}_{n-1})\delta(\mathbb{k}_1+\dots+\mathbb{k}_n)$ (see, e.g., Eq. (4.42) or Eq. (4.74)), the overall engineering dimension of $\Gamma^{\psi_1,\dots,\psi_n}$ increases by $d+2$ [4]. Let us denote this engineering dimension with $y(\{n_\psi\})$, n_ψ being the number of ψ fields in the vertex function. The sum of the field dimensions can be written as a sum over fields of the number of fields of a given kind times the dimension of this kind of field, i.e.

$$y(\{n_\psi\}) = d + 2 - \sum_\psi n_\psi y_\psi. \tag{4.83}$$

Each perturbative correction $\mathcal{I}$ must have the same dimension as the vertex function itself. However, every additional vertex in the Feynman diagram of $\mathcal{I}$ carries a factor of g, with dimension $(2-d)/2$. This added dimensionality must be compensated by the momenta appearing in the k-integrals in $\mathcal{I}$: the difference between momentum powers at the numerator (including d from d^dk) and those of the denominator defines the *primitive degree of divergence* $\delta(\mathcal{I})$ of $\mathcal{I}$. With $n_V(\mathcal{I})$ denoting the number of nonlinear vertices in the diagram of $\mathcal{I}$,

$$\delta(\mathcal{I}) = d + 2 - \sum_\psi y_\psi - n_V(\mathcal{I})\frac{2-d}{2}. \tag{4.84}$$

[4] Recall the dimension of a delta-function is that of the inverse of its argument.

$\delta(\mathcal{I})$ describes the ultraviolet divergence of $\mathcal{I}$: if all $\boldsymbol{k}$-integrals are restricted to $[-\Lambda,\Lambda]^d$, then $\mathcal{I}\sim\Lambda^{\delta(\mathcal{I})}$ by simple power counting. According to Eq. (4.84), at the critical dimension $d_c=2$, where the coupling constant g is dimensionless, the primitive degree of divergence of a diagram does not depend on the number of vertices, i.e. on the order of perturbation. Thus, $d=d_c$ is a necessary condition for keeping the number of diverging perturbative corrections finite. At the critical dimension $d_c=2$, using Eq. (4.81) for $y_h, y_{\tilde{h}}, \ldots$,

$$\delta_{d_c}(\mathcal{I}) = 4 - 2n_{\tilde{h}} - n_\psi - n_{\tilde{\psi}}. \tag{4.85}$$

The above equations yields $\delta=2$ for $\Gamma^{\tilde{h}h}$. Actually, one of the two powers comes from the fact that, due to the symmetry for h translations, h always appears with a gradient. Rotational invariance, then, requires another vector contracted to that gradient—it can only be another gradient in the $\tilde{h}h$ term of the action, whence the other power. One might say that, after this subtraction, the effective value of δ_{d_c} is 0. Indeed, a small $\boldsymbol{k}$ expansion of the k_1-integral of Eq. (4.77) yields ([81], 11.4.1),

$$\Gamma^{\tilde{h}h}(\omega,\boldsymbol{k}) \simeq -i\omega + \nu_h k^2 \left[1 - \frac{g^2}{4}\frac{d-2}{d}\int_{k_1}\frac{1}{k_1^2 - \frac{i\omega}{2\nu_h}}\right]. \tag{4.86}$$

In the long-time limit, $\omega\to 0$, the k_1-integral is only logarithmically divergent at $d=2$, i.e. $\delta=0$. Actually, this particular perturbative correction vanishes at $d=2$ because of the $d-2$ factor. However, the role of logarithmic divergences is critical in the general case, in that they couple large and short scales: one can then isolate the relevant infrared singularities by renormalising the ultraviolet behaviour of the theory.

An actual logarithmic divergence comes from $\Gamma^{\tilde{h}\tilde{h}}$, having $\delta=0$. For this vertex function, the external momentum k can be set to 0, so that (from Eq. (4.78))

$$\Gamma^{\tilde{h}\tilde{h}}(\boldsymbol{k}=0,\omega) = -2\nu_h\left[1 + \frac{g^2}{4}\int_{k_1}\mathrm{Re}\left(\frac{1}{k_1^2 - \frac{i\omega}{2\nu_h}}\right)\right]. \tag{4.87}$$

$\Gamma^{\tilde{\phi}\phi}$ and $\Gamma^{\tilde{\phi}\tilde{\phi}}$ are both quadratically divergent, with $\delta=2$. For $\Gamma^{\tilde{\phi}\tilde{\phi}}$, both powers come from density conservation, which imposes $\tilde{\phi}$ to always appear coupled to a gradient. For $\Gamma^{\tilde{\phi}\phi}$, instead, one power comes from the gradient coupled with $\tilde{\phi}$, the other from an additional gradient required, as for $\Gamma^{\tilde{h}h}$, by rotational invariance. The logarithmically divergent corrections can be extracted, as in Eq. (4.86), from

a small-$\boldsymbol{k}$ expansion (details in Appendix D and Appendix E):

$$\Gamma^{\tilde{\phi}\phi}(\omega,\boldsymbol{k}) \simeq -i\omega + r\nu_h k^2 \left[1 - \frac{g^2}{2r}\left(\frac{d-2}{d(1+r)}\int_{k_1}\frac{1}{k_1^2 - \frac{i\omega}{2\nu_h}\frac{2}{1+r}}\right) - \frac{g^2}{2r}\left(\frac{2(r-1)}{d(1+r)^2}\int_{k_1}\left(\frac{k_1}{k_1^2 - \frac{i\omega}{2\nu_h}\frac{2}{1+r}}\right)^2\right)\right]; \tag{4.88}$$

$$\Gamma^{\tilde{\phi}\tilde{\phi}}(\boldsymbol{k},\omega) \simeq -2r\nu_h k^2 \left[1 + \frac{g^2}{dr(1+r)}\int_{k_1}\mathrm{Re}\left(\frac{1}{k_1^2 - \frac{i\omega}{2\nu_h}\frac{2}{1+r}}\right)\right]. \tag{4.89}$$

The question to be answered next is whether other logarithmically divergent corrections exist. It is worthwhile, in this respect, reformulating the results of the past two paragraphs in terms of the JD action (Eq. (4.27) and (4.28)),

$$\mathcal{A}[h,\tilde{h},\phi,\tilde{\phi}] = \int d^dx dt\ [\tilde{h}\left(\partial_t - \nu_h\nabla^2\right)h - \nu_h\tilde{h}^2 + \frac{\nu_h g}{2}\tilde{h}(\nabla h)^2 + \tilde{\phi}\left(\partial_t - r\nu_h\nabla^2\right)\phi - r\nu_h(\nabla\tilde{\phi})^2 + \nu_h g(\boldsymbol{\nabla}\tilde{\phi})\cdot(\phi\boldsymbol{\nabla}h)\ ]. \tag{4.90}$$

Corrections to $\Gamma^{\tilde{h}h}$ and $\Gamma^{\tilde{\phi}\phi}$ are quadratically divergent. However, because the interaction terms $\tilde{h}hh$ and $\tilde{\phi}\phi h$ are proportional to one of the outgoing momenta and the incoming momentum, respectively (see Eq. (4.76)), both vertex functions vanish with the external momentum $\boldsymbol{k}$ at all orders of perturbation theory. As a result, the terms $\tilde{h}\partial_t h$,$\tilde{\phi}\partial_t\phi$ are not renormalised. The only terms proportional to $\tilde{h}h$,$\tilde{\phi}\phi$ left include Laplacians, so that the quadratically divergent corrections to the vertex functions become logarithmically divergent corrections to the Laplacian coefficients ν_h and $r\nu_h$. The quadratic divergence of corrections to $\Gamma^{\tilde{\phi}\tilde{\phi}}$, analogously, translates into the logarithmic divergence of corrections to the coefficient of $(\nabla\tilde{\phi})^2$. According to Eq. (4.85), the addition of extra fields $\tilde{h}$, ϕ or $\tilde{\phi}$ reduces the primitive degree of divergence, meaning that higher-order vertex functions do not gain divergent perturbative corrections. Also adding another h field reduces δ, because h always comes with a gradient. The only exceptions are the interaction terms $\tilde{h}(\nabla h)^2$, which can be obtained by adding a gradient-less h field to $\tilde{h}\nabla^2 h$, and $(\boldsymbol{\nabla}\phi)\cdot(\phi\boldsymbol{\nabla}h)$, similarly obtained from $\tilde{\phi}\nabla^2\phi$. However, such terms are related to the time-derivative terms by the tilt symmetry, hence they will not renormalise if time derivatives do not [5].

Now that all the diverging factors at $d = d_c = 2$ have been identified, they should

[5] See [83], IIC, for a discussion of this point in terms of Ward-Takahashi identities.

be *regularised*—assigned a meaningful finite value such that divergence can be recovered in the proper limit. One of the possible prescriptions, called *dimensional regularisation* [91], is based on the following formula [81]:

$$\int_0^\infty dk\, \frac{k^{d-1+2\sigma}}{(k^2+\tau)^s} = \frac{\Gamma(\sigma+d/2)\Gamma(s-\sigma-d/2)}{2\Gamma(s)}\tau^{\sigma-s+d/2}, \tag{4.91}$$

where Γ denotes the Euler Gamma function. Close to an equilibrium critical point, τ would be a relevant parameter such as the distance from the critical temperature. Introducing again the relevant parameters a_h, a_ϕ would lead to unrequired complications due to additional couplings between height and density fields—it is much easier to evaluate diverging corrections at a finite external frequency ω, such that $-i\omega/2\nu_h = \mu^2$. The two diverging integrals in Eq. (4.86) and Eq. (4.87) are then performed by following the formula above:

$$\int \frac{d^dk_1}{(2\pi)^d}\frac{1}{k_1^2+\mu^2} = \frac{1}{2^{d-1}\pi^{d/2}\Gamma(d/2)}\int dk\, \frac{k^{d-1}}{k^2+\mu^2} \equiv \frac{B_d}{2-d}\mu^{(d-2)}, \tag{4.92}$$

where the factor $(2-d)^{-1}$ has been extracted using $\Gamma(1+n) = n\Gamma(n)$ and $B_d = \Gamma(2-d/2)/(2^{d-1}\pi^{d/2})$. For the integrals in Eq. (4.88) and Eq. (4.89), instead, it is more convenient to set $-i\omega/\nu_h(1+r) = \mu^2$. As a result, the k_1-integral in Eq. (4.89) becomes that of Eq. (4.92), while

$$\int \frac{d^dk_1}{(2\pi^2)}\frac{k_1^2}{(k_1^2+\mu^2)^2} = \frac{d}{2}\frac{B_d}{2-d}\mu^{(d-2)}. \tag{4.93}$$

Once sorted and regularised, the diverging corrections can be finally absorbed in the renormalised action. This is done by setting $\psi = \psi_R/Z_\psi$, for parameters ν_h, r and fields, and $B_d\mu^{d-2}g^2 = g_R^2/Z_g$ (in order to render g_R dimensionless). The Z_ψ's are then chosen so as to absorb perturbative corrections:

$$Z_hZ_{\tilde{h}} = Z_\phi Z_{\tilde{\phi}} = 1, \qquad Z_{\nu_h}Z_h(Z_g)^{1/2} = 1, \tag{4.94a}$$

$$Z_{\nu_h} = \left[1+\frac{g^2}{4d}B_d\mu^{d-2}\right], \quad Z_{\nu_h}Z_{\tilde{h}}^2 = \left[1+\frac{g^2}{4}\frac{B_d\mu^{d-2}}{2-d}\right], \tag{4.94b}$$

$$Z_rZ_{\nu_h} = \left[1+\frac{g^2}{2r}\left(\frac{2-d}{d(1+r)}+\frac{1-r}{(1+r)^2}\right)\frac{B_d\mu^{d-2}}{2-d}\right], \tag{4.94c}$$

$$Z_rZ_{\nu_h}Z_{\tilde{\phi}}^2 = \left[1+\frac{g^2}{dr(1+r)}\frac{B_d\mu^{d-2}}{2-d}\right], \tag{4.94d}$$

where the first line comes from the condition of non-normalisation on time derivatives and nonlinear terms.

4.3.2 Renormalisation Group flow

The *renormalisation group equation* is obtained by simply recalling that the original model—with all its vertex functions—cannot depend on the arbitrary scale μ introduced in the previous subsection. The *beta function* β_g describes how the renormalised non-linear coupling g_R^2 changes with the scale. From $g_R^2 = B_d \mu^{d-2} g^2 Z_g$,

$$\beta_g = \mu \frac{\partial g_R^2}{\partial \mu} = g_R^2 \left(d - 2 + \mu \frac{\partial}{\partial \mu} \ln Z_g \right). \tag{4.95}$$

Z_g can be easily obtained, at order g_R^2, from Eq. (4.94). First, all the factors $B_d \mu^{d-2} g^2$ inside the renormalisation constants can be replaced with g_R^2 without changing the order of perturbation theory. Then, from Eq. (4.94b) and $Z_h = Z_{\tilde{h}}^{-1}$,

$$Z_h^2 = Z_{\nu_h} \left(1 - \frac{g_R^2}{4(2-d)} \right) = 1 + \frac{g_R^2}{2d} \frac{1-d}{2-d}. \tag{4.96}$$

From Eq. (4.94a), instead,

$$Z_g = (Z_{\nu_h} Z_h)^{-2} = 1 - \frac{g_R^2}{2d} \frac{3-2d}{2-d}. \tag{4.97}$$

In order to compute the logarithmic derivative w.r.t. μ, it is convenient to make the μ dependence in g_R^2 explicit, i.e. replace again g_R^2 with $B_d \mu^{d-2} g^2$. Furthermore, $\ln(1 + \alpha g_R^2) \simeq \alpha g_R^2$, yielding the know KPZ one-loop result [83]

$$\mu \frac{\partial}{\partial \mu} \ln Z_g = \frac{3-2d}{2d} B_d \mu^{d-2} g^2 \Rightarrow \beta_g = g_R^2 \left(d - 2 - g_R^2 \frac{2d-3}{2d} \right). \tag{4.98}$$

The condition $\beta_g = 0$ determines the fixed points of the scale transformation—one is $(g_R^2)^* = 0$, corresponding to the Gaussian fixed point, the other $(g_R^2)^* \sim d - 2$. Actually, $d = 2$ is the critical dimension, where, in the language of the previous subsection, perturbative corrections can be renormalised. In fact, all these calculations should be performed around $d = 2$, i.e. performing another Taylor expansion in $\epsilon = d - 2$. Ideally, one would be interested in setting $\epsilon > 0$, because corrections to mean-field behaviour emerge in $d < d_c = 2$. However, given that $(g_R^2)^* = 4\epsilon$, there is no other (perturbative) fixed point than the Gaussian one below d_c, where ϵ is negative. Above d_c, by computing the derivative of β_g, the non-trivial fixed point $(g_R^2)^* = 4\epsilon$ is found to be unstable [83]. In simple terms,

interfaces with $(g_R^2) < 4\epsilon$ display mean-field scaling, while those with $(g_R^2) > 4\epsilon$ converge on a large-g_R fixed point inaccessible by perturbation theory. As the mean-field interface is flat in (and above) $d = 2$, while KPZ interfaces have a positive roughness exponent in $d \geq 2$ [92], $(g_R^2)^*$ is said to correspond to a *roughening* transition.

As anticipated at the beginning of the section, the absence of stable perturbative fixed points hinders the computation of corrections to the mean-field exponents, thus concluding our calculations. However, it is still allowed to compute the flow of the parameter r_R around the unstable fixed point and study the timescale ratio between interface and density fluctuations at the roughening transition. β_r can be defined similarly to the beta function of g^2. However, r being dimensionless, there will be no explicit dimensional factor. By subtracting Z_{ν_h} from Eq. (4.94c),

$$Z_r = 1 + \frac{1-r}{2r(1+r)^2}\frac{g_R^2}{2-d} + \frac{2-r-r^2}{4dr(1+r)}g_R^2, \tag{4.99}$$

so that r_R's beta function reads (in $d = 2 + \epsilon$)

$$\beta_r = r\mu\frac{\partial}{\partial_\mu}\ln Z_r = \frac{r-1}{2(1+r)^2}g_R^2 + \frac{2-r-r^2}{8(1+r)}\epsilon g_R^2. \tag{4.100}$$

At the Gaussian fixed point, $\beta_r = 0$ irrespective of r. At $g_R^2 = 4\epsilon$, another fixed point with $r = 1$ emerges at first order in ϵ. The derivative of β_r is positive at $r = 1$, implying that $r = 1$, $g_R^2 = 4\epsilon$ is stable in the r-direction.

As another interesting remark, notice that the corrections in Eq. (4.94b) coincide in $d = 1$. In general, the coincidence of 'response' vertex function $\Gamma^{\tilde{h}h}$ and 'noise' vertex function $\Gamma^{\tilde{h}\tilde{h}}$ is an hallmark of the fluctuation theorem. This is natural, as $\Gamma^{\tilde{h}h}$ is related to the response function (cf. Eq. (C.11)) while $\Gamma^{\tilde{h}\tilde{h}}$ is proportional to the correlation function (cf. Eq. (C.16)). The KPZ equation does satisfy the FDT in $d = 1$ and the theorem, together with tilt invariance, fixes the scaling exponents uniquely. Namely, $z = 3/2$ and $y_h = -1/2$, the mean-field value. In asking coincidence of the corrections in Eq. (4.94c) and (4.94d), one finds, for $d = 1$,

$$1 = \frac{1}{2}\left(1 + \frac{1-r}{1+r}\right) \Leftrightarrow r = 0. \tag{4.101}$$

Unfortunately, knowing that the model satisfies the FDT at the KPZ fixed point for $r = 0$ does not fix any other exponent: for $r = 0$, the $\tilde{\phi}^2$ term disappears from the action in Eq. (4.90) and y_ϕ remains undetermined.

4.3.3 Concluding remarks

This chapter provided a field-theoretic perspective on the active interface equations: stochastic PDEs which describe the large-scale properties of the model of chapter 2 and possibly of active interfaces such as the leading edge of motile cells. The equations considered in this chapter have been derived from physical considerations independent of the lattice model, thus are different from those derived in chapter 3. Nevertheless, the two sets of equations display analogous terms, sign of the eligibility of the lattice active interface model as a representative of the scaling properties of real active interfaces.

The most significative results of this chapter are those presented in section 4.2. The dynamics of the active interface equations, as it turns out, can be described with different scaling hypotheses, i.e. different scaling exponents, depending of the specific thermodynamic limit considered. If the observation time and the system size are increased simultaneously ($t \sim L$) the scaling is dominated by ballistic phenomena, such as the waves and oscillations described in the previous chapters. It is interesting to notice that, in such regime, the results of mean-field theory are exact. The most intriguing predictions are the scaling exponents of interface and density fluctuations. For a one-dimensional system, in particular, the exponents indicate a flat interface with a hyperuniform distribution of activators—as this is the case relevant for the leading edge dynamics, it will be discussed further in chapter 5.

If the observation time is increased as the square of the system size ($t \sim L^2$) the scaling is dominated by diffusive phenomena. In this regime the system is not critical for general values of the parameters, in agreement with the only exact result available for the steady-state properties of the lattice model, i.e. the steady-state measure of chapter 3. The latter measure implies the absence of spatial correlations in the system, a symptom of non-critical behaviour. Other scale-invariant theories can be obtained by tuning some of the parameters to zero, as in Fig. 4.3. The mean-field scaling of such theories was also presented in section 4.2, whereas one-loop renormalisation was performed on a specific point of the phase diagram only. A full renormalisation-group study of the complete phase diagram is left as a future perspective.

Chapter 5

Conclusions

In this thesis I have proposed a statistical description of active interfaces, with the leading edge of motile cells as a model system. The leading edge, recalling section 1.2, is the portion of membrane which advances during cell locomotion: in the lattice model of chapter 2 (shown here in Fig. 5.1), the membrane is represented as a collection of unitary slopes on the ring lattice. The motion of the leading edge, as mentioned in section 1.2, is regulated by activators of actin polymerisation: in our idealised description, the activators are point particles occupying the sites of the ring lattice. Thermal fluctuations of the membrane are encoded in a random slope-exchange dynamics for the interface and hops between neighbouring sites for activators. In addition, each activator biases the slope-exchange process so as to push negative slopes on right and positive slopes on the left. The resulting effect, as indicated in Fig. 5.1, is vertical displacement of the interface.

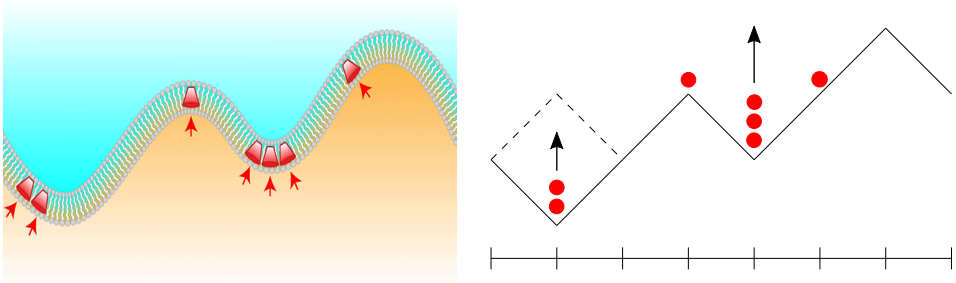

Figure 5.1 *Comparison of a sketch of the leading edge (left, credits to* APS/Alan Stonebraker*) with the lattice active interface (right). Slope exchange causes vertical fluctuations of the interface.*

Actually, the displacement of the interface is aligned to the local normal to the interface itself, rather than the vertical direction of an external reference frame. As a result, the motion of the interface generates an advective force on the activators, proportional to the interface slope. This important ingredient is introduced in subsection 2.1.2 as a bias in the activator hops towards sites with lower height. In general, the possibility of an effective coupling between interface slope and the spatial distribution of activators was considered in an earlier model of active membranes [31], although the deeper consequences of such coupling had not been explored before. Notably, slope-coupling and active-growth conspire to the generation of a negative feedback loop, whereby activators create peaks on the interface and the peaks push the activators away. The feedback is the essential feature of the model discussed here: it causes the peculiar regimes of the test-particle problem, described in section 2.2, and the special spatiotemporal structure of the model's steady state, described in section 2.3. The steady state, in particular, consists of finite-size aggregates of activators which travel the system by riding interfacial ripples, thus it matches *qualitatively* the typical dynamics of the leading edge [45]. In addition, features of the steady state such as the size of the clusters and the speed of the waves can be related to the parameters representing the aforementioned couplings.

This is done, in chapter 3, by deriving hydrodynamic equations for the conserved variables of the lattice model: activator density and interface slope. The resulting equations, as shown in section 3.2, can be solved in the inviscid limit, i.e. neglecting diffusive contributions. The solution, which can be thought of as a coarse-grained description of the model's steady state, relates wave speed and cluster size to the parameters of the equations, which are in turn related to the biases of the lattice model. Therefore, the results of section 3.3 can be used to test the model against the dynamics of real membranes and possibly promote the qualitative match to a *quantitative* one. The speed of the lateral waves, in particular, is found to scale with the square root of the product of the active-growth and slope-coupling parameters. Both these parameters are proportional to the vertical interface speed, implying a proportionality between the velocity of the vertical motion of the interface and the speed of the waves which travel laterally along the interface. This is the principal contribution of this thesis to leading edge physics and also a distinctive feature of the mechanism proposed by this model: it can be tested experimentally by comparing the propagation of lateral waves on the leading edge of cells which travel at different speed.

Beyond the reproduction of the key features of the leading edge and the introduction of a measurable prediction, the lattice model of chapter 2 is a step towards the extension of the theory of kinetic roughening to active phenomena and, in particular, active membranes. Some remarks on the lexicon are due here. The phrase "kinetic roughening" is used whenever the interface is set into motion by local and stochastic events, such as the deposition of atoms on an aggregate. It is also intended that such kind of interfaces display some degree of roughness, which generally depends on the scale of observation. In fact, the measure of how the interface width changes with the scale, i.e. the *roughness exponent*, is one of the protagonists in the theory of kinetic roughening. Due the limited size, fluid membranes such as the cell's might seem unsuited for such a framework, yet their fluctuations can also be characterised with an exponent—the power of momentum in the structure factor's asymptotics for small momenta. The relationship between interface width and structure factor (Appendix A, [14]) links the two approaches: even if the cell membrane does not undergo any kinetic roughening, we can still prepare our membrane model in an flat initial condition; then let it roughen under a model stochastic dynamics and measure the scaling of steady-state interface width with its size. The ensuing roughness exponent will also determine the structure factor divergence at small momenta, which, in turn, can be compared against the results of scattering experiments on real membranes.

Active interface scaling

The analogy with kinetic roughening, as well as the introduction of exponents to characterise the system's large-scale behaviour, calls for some scaling analysis, to which the whole of chapter 4 has been devoted. In the first part of the chapter, as a consistency check, the partial differential equations of chapter 3 have been compared to those obtained by symmetry arguments: the fact that the two sets of equations display the same kind of terms supports the idea that the lattice model of chapter 2, from which the equations of chapter 3 are derived, comprises all the relevant ingredients for the description of an active interface. Loosely speaking, this comparison is a positive answer to the question asked at the beginning of the introduction: "All these problems can, when looked at from sufficiently far away, be described with surprisingly similar equations. Is there an analogous description for plasma membranes?". The next, ensuing question is whether the active interface equations succeed in capturing the *universal* properties of the dynamics of active interfaces.

An answer can be given within the context of the mean-field theory discussed in section 4.2. In particular, in the physical region of the parameter space where $a_h \propto a_\phi$ (upper-right and lower-left quadrants of Fig. 4.3), all the nonlinearities of the model are irrelevant and the results of mean-field theory are exact in all dimensions. In this region, the large-scale properties of the active interface are summarised by the exponents (Eq. (4.60), Eq. (4.61))

$$z = 1; \qquad y_h = \frac{d-1}{2}; \qquad y_\phi = \frac{d+1}{2}. \tag{5.1}$$

The first, z, relates time- and length-scales in the thermodynamic limit. $z = 1$, specifically, is synonymous with waves and ballistic transport. The second, y_h, relating lengths and heights, implies the active interface to be flat in $d \geq 1$. Returning to the example of the leading edge, with $d = 1$, a statistically flat advancing front helps the cell to keep its shape unaltered during locomotion. In addition, a flat advancing front is believed to be the result of the lateral ballistic propagation of interface ripples. The third exponent, y_ϕ, relates lengths and the amplitude of fluctuations in the activator density. In particular, the calculations of subsection 4.2.2 show that the observed value of y_ϕ is representative of a *hyperuniform* spreading of activators over the interface. This is a feature which, to the best of my knowledge, has never been discussed before, but it is compatible with the idea that clusters of activators are (statistically) evenly spread across the membrane, so as to maximise the displacement of the cell.

There is plenty of numerical evidence, from the lattice model in $d = 1$, supporting $z = 1$; less so for the exponents y_ϕ and y_h. The reason is that the inviscid limit is never formally achieved on a system of finite size L: after a time of order L^2, the diffusive decay dominates, and the steady-state is controlled by the Gaussian exponents of Eq. (4.49),

$$y_h = \frac{d-2}{2}; \qquad y_\phi = \frac{d}{2}. \tag{5.2}$$

These exponents mirror a disordered steady state, where there is no spatial correlation between fluctuations. In fact, the $d = 1$ values of the above exponents can be predicted from the product steady-state measure of subsection 3.1.1. Although the steady-state scaling of a finite active interface is controlled by the Gaussian exponents, the 'inviscid' scaling should not be misunderstood for a finite-time effect. This is a crucial aspect of the active interface dynamics, which is worthwhile clarifying by resorting to the example of a persistent random walk.

A persistent random walk moves ballistically for a certain length, called the persistence length, then it changes direction, so that its motion looks diffusive on larger scales. Below the persistence length, $z=1$ due to ballistic motion. Above the persistence length, $z=2$ as in standard diffusion. If the persistence length is finite, then the long-time scaling is the diffusive one: the short persistence length becomes an irrelevant detail. However, there are cases such as the surfing regime of the test-particle problem (see subsection 2.2.3), where the persistence length of the walk is proportional to the system size. As, in such cases, the persistence length cannot be considered as finite, the long-time scaling depends on the thermodynamic limit. Both observation time and size of the system are to be let to grow to infinity: if time grows as the square of the size, the relevant scaling will be the diffusive one; or the inviscid scaling if the observation time is proportional to the system size. Consider, for concreteness, the oscillating width of Fig. 2.14 and Fig. 2.15, from subsection 2.3.1: the period of oscillation scales as the system size L, but the width saturates after time $\sim L^2$. Therefore, any interface of finite size has constant width in steady state, while, if the $L\to\infty$ limit is taken first, oscillations are the only observable phenomenon.

The phase diagram: implications and outlook

According to the symmetry arguments of subsection 4.1.1, the active interface equations can be extended beyond the $a_h \propto a_\phi$ sector of the parameter space, which is relevant for the dynamics of the leading edge. In doing so, one finds two phase transitions (see the phase diagram in Fig. 4.3): one in changing the sign of a_ϕ at fixed a_h, another in changing the sign of a_h at fixed a_ϕ. A similar phase transition can be found in a model of a sedimenting colloidal crystal, known as the Lahiri-Ramaswamy (LR) model [93, 94]. This model can be obtained from the lattice model of chapter 2 by assuming that each lattice site hosts at most one activator, or, equivalently, implementing an exclusion interaction among activators (plus other minor modifications). The two phases are termed *stable* (for $a_h a_\phi > 0$) and *unstable* (for $a_h a_\phi < 0$) because of the linear stability of the field equations with respect to large-scale perturbations of height and density profiles [95]. From the lattice model perspective, the stable phase corresponds to a disordered phase, whereas the unstable phase looks like an ordered phase.

The ordered phase of the lattice model has been studied in detail for the LR model and generalisations [96–98]. For the lattice active interface, the ordered

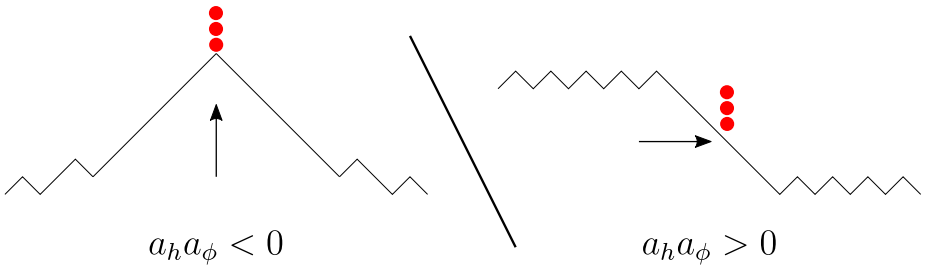

Figure 5.2 *Pictorial representation of he two phases of the active interface model: for $a_h a_\phi < 0$, all the activators in the system are gathered on a single, macroscopic peak; for $a_h a_\phi < 0$ aggregates of finite size roam the interface by riding interface ripples.*

phase is a tent-like shape similar to the steady-state interface of the test-particle problem, attained when the interface dynamics is much faster that the particle one (subsubsection 2.2.3.1, inset of Fig. 2.13). Consider, for instance, the realisation of $a_h a_\phi < 0$ with positive a_h and negative a_ϕ, so that the negative feedback loop discussed earlier becomes a positive feedback loop: activators generate a peak and the peak attracts more activators. All the activators will ultimately gather on a single peak (as in the left of Fig. 5.2), so that the growth rate of the peak becomes as large as the total number of activators in the system. As a result, the peak expands until it covers the whole interface. The macroscopic peak can be viewed as a phase separation of the slopes: negative slopes are on the right of the activator cluster, positive slopes on the left. Far away from the activator cluster, negative and positive slopes are mixed due to finite size effects.

It is interesting to notice that the total displacement of the interface is minimal in this ordered phase. Specifically, in order to increase the height of the peak, one positive slope must cross the macroscopic negative slope on the peak's right, while a negative slope must cross the macroscopic positive slope on the peak's left. As all the activators are on the peak, the slope dynamics is purely diffusive and, as the size of the macroscopic slopes is a fraction of the system length, it takes a time proportional to L^2 to increase the height of the peak by one unit. In the disordered phase, conversely, the motion of the interface is much more efficient. First of all, the hyperuniform spreading of activator nanoclusters ensures that the protrusive force is evenly distributed. In addition, as the nanoclusters surf the interface no large peaks are formed and the interface advances as a whole (as in the right of Fig. 5.2). It is tempting to speculate on how the cell could choose, by tuning the coupling between activators and membrane shape, one of the two

phases, depending on the task to perform and available resources. The extension of slow and large structures in the ordered phase, for instance, could be useful for exploratory purposes, while the uniform displacement afforded by the disordered phase seems better suited for fast locomotion.

Wild speculations aside, the complete characterisation of the phase diagram is interesting *per se* and for the field of phase transitions in out-of-equilibrium systems. The mean-field theory for both the critical lines is provided in subsection 4.2.3. On the $a_h = 0$ critical line, where active growth is suppressed, arguments based on the engineering dimensions show the nonlinearities of the model to be relevant below $d = 2$: the application of the apparatus described in section 4.3 might yield corrections to the mean-field scaling, as a Taylor series in $d - 2$, and a clearer picture on the structure of the phase transition. Similarly, the same apparatus can be applied to the $a_\phi = 0$ critical line, where the slope-advection is suppressed—here the nonlinearities alter mean-field scaling below $d = 4$. Unfortunately, the complete renormalisation-group study of the active interface equations constitutes a whole new project, thus it is left as a future perspective.

In this respect, section 4.3 can be considered as an attempt to scratch the surface of the problem, by studying the $a_h = a_\phi = 0$ point of the phase diagram. The model, on this point, reduces to a KPZ equation for the interface height, coupled to an advection-diffusion equation for the density, where advection is caused by the slopes of the interface. This is the old problem of passive scalar advection by the Burger's flow [56], which is a simplified version of the problem of passive scalar advection by a turbulent flow. The issue with this problem is that perturbative renormalisation techniques are known to fail for the single KPZ equation already, due to the presence of a strong coupling fixed point. Besides, section 4.3 adds two new results to the existing literature. First, when expanding the density (ρ) as average (ρ_0) plus fluctuations (ϕ), the linear advective term $\propto \rho_0 \nabla^2 h$ becomes a relevant term, hence it must be set to zero when searching for critical behaviour. Secondly, the incidental fluctuation-dissipation theorem of the KPZ equation in $d = 1$ extends to the excess density equation only if diffusion and noise are removed from the latter equation.

Appendix A

Fourier transform conventions

The Fourier transform of a function f of the spatial coordinate $\boldsymbol{x}$ is defined as

$$\hat{f}(\boldsymbol{k}) = \int d^d x\, f(\boldsymbol{x}) e^{-i\boldsymbol{k}\cdot\boldsymbol{x}}, \quad f(\boldsymbol{x}) = \int \frac{d^d k}{(2\pi)^d}\, \hat{f}(\boldsymbol{k}) e^{i\boldsymbol{k}\cdot\boldsymbol{x}}, \tag{A.1}$$

where d is the dimension of the space. For a finite system of linear size L the inverse transform reads

$$\frac{1}{L^d} \sum_{\boldsymbol{n}\in\mathbb{Z}^d}^{\boldsymbol{k}=2\pi\boldsymbol{n}/L} \hat{f}(\boldsymbol{k}) e^{i\boldsymbol{k}\cdot\boldsymbol{x}}. \tag{A.2}$$

The consistency between transform and inverse transform implies the following representation of the identity

$$(2\pi)^d\, \delta(\boldsymbol{k} - \boldsymbol{k}') = \int d^d x\, e^{i(\boldsymbol{k}-\boldsymbol{k}')\cdot\boldsymbol{x}}, \tag{A.3}$$

or, for the finite-size case,

$$\delta_{\boldsymbol{k},\boldsymbol{k}'} = \frac{1}{L^d} \int_{[0,L]^d} d^d x\, e^{i(\boldsymbol{k}-\boldsymbol{k}')\cdot\boldsymbol{x}}, \quad \delta(\boldsymbol{x}-\boldsymbol{y}) = \frac{1}{L^d} \sum_{\boldsymbol{n}\in\mathbb{Z}^d}^{\boldsymbol{k}=2\pi\boldsymbol{n}/L} e^{i\boldsymbol{k}\cdot(\boldsymbol{x}-\boldsymbol{y})}. \tag{A.4}$$

Consider, as an example, the Edwards-Wilkinson equation with viscosity ν,

$$\partial_t h(\boldsymbol{x}, t) = \nu \nabla^2 h(\boldsymbol{x}, t) + \eta(\boldsymbol{x}, t), \tag{A.5}$$

with the stochastic force η being a Gaussian white noise, i.e. an independent, zero-mean Gaussian variable for each point in time and space. By calling the

variance $2D$, one writes

$$\langle \eta(\boldsymbol{x},t)\eta(\boldsymbol{x}',t')\rangle = 2D\delta(\boldsymbol{x}-\boldsymbol{x}')\delta(t-t'). \tag{A.6}$$

Applying the Fourier transform to the partial differential equation Eq. (A.5) yields a set of independent ordinary differential equations with parameter $\boldsymbol{k}$,

$$\partial_t h(\boldsymbol{k},t) = -\nu k^2 h(\boldsymbol{k},t) + \eta(\boldsymbol{k},t). \tag{A.7}$$

Notice that the hat symbol $\hat{}$ has been dropped so as to ease the notation—whether the function is considered in the real-space or Fourier-space representation will be unambiguously denoted by its argument. As a weighted sum of Gaussian variables, $\eta(\boldsymbol{k})$ is also a Gaussian noise. The variance is obtained by Fourier-transforming η's variance,

$$\begin{aligned}\langle \eta(\boldsymbol{k},t)\eta(\boldsymbol{k}',t')\rangle &= 2D\delta(t-t')\int d^dx \int d^dx'\, e^{-i\boldsymbol{k}\cdot\boldsymbol{x}} e^{-i\boldsymbol{k}'\cdot\boldsymbol{x}'}\delta(\boldsymbol{x}-\boldsymbol{x}') = \\ &= (2\pi)^d\, 2D\delta(\boldsymbol{k}+\boldsymbol{k}')\delta(t-t'),\end{aligned} \tag{A.8}$$

where, in the last equality, the representation of the identity Eq. (A.3) has been used.

As a consequence of the $\delta(\boldsymbol{k}+\boldsymbol{k}')$ factor in the noise correlations, the $\boldsymbol{k}$-th height mode $h(\boldsymbol{k},t)$ is independent from all the other modes but $h(-\boldsymbol{k},t)$. Precisely,

$$h(\boldsymbol{k},t) = e^{-\nu k^2 t} h(\boldsymbol{k},0) + \int_0^t ds\, e^{-\nu k^2 (t-s)} \eta(\boldsymbol{k},s), \tag{A.9}$$

so that

$$\begin{aligned}\langle h(\boldsymbol{k},t)h(\boldsymbol{q},t)\rangle &= e^{-2\nu k^2 t} h(\boldsymbol{k},0)h(\boldsymbol{q},0) \\ &\quad + 2D(2\pi)^d\delta(\boldsymbol{k}+\boldsymbol{q})\int_0^t ds\, e^{-2\nu k^2(t-s)} \\ &\simeq (2\pi)^d\delta(\boldsymbol{k}+\boldsymbol{q})D\frac{1-e^{-2\nu k^2 t}}{\nu k^2},\end{aligned} \tag{A.10}$$

where the term coming from the initial condition $h(\boldsymbol{k},0)$ has been dropped in the third line. The finite-size version of the above is obtained under the replacement

$$(2\pi)^d\delta(\boldsymbol{k}+\boldsymbol{q}) \to L^d\delta_{\boldsymbol{k},-\boldsymbol{q}}. \tag{A.11}$$

As h is a real function, $h(-\boldsymbol{k},t) = h^*(\boldsymbol{k},t)$, where the star denotes complex conjugation. Because of this and the correlation between modes of opposite

wavevector, it is natural to consider the average square modulus $\langle |h(\boldsymbol{k},t)|^2 \rangle$ as a measure of the interface mode fluctuations.

In particular, the static structure factor $S(\boldsymbol{k})$ is defined as

$$\lim_{t\to\infty} \left\langle \hat{h}(\boldsymbol{q},t)\hat{h}(\boldsymbol{k},t) \right\rangle = (2\pi)^d \delta(\boldsymbol{k}+\boldsymbol{q}) S(\boldsymbol{k}). \tag{A.12}$$

The structure factor of an Edwards-Wilkinson interface, for instance, coincides with

$$S_{EW}(\boldsymbol{k}) = \frac{D}{\nu k^2}. \tag{A.13}$$

Notice S_{EW} depends only on the square modulus of $\boldsymbol{k}$, due to the rotational symmetry of EW interfaces. The structure factor of thermal undulation shown in section 1.2 can be obtained similarly by adding to the EW equation a bending rigidity term $\kappa\nabla^4 h$, thus setting $D = K_B T$ as required by the Einstein-Smoluchowski relation with unitary mobility.

In complete analogy, by defining Fourier transform of a function of time as

$$f(\omega) = \int dt\, f(t) e^{+i\omega t}, \quad f(t) = \int \frac{d\omega}{(2\pi)}\, f(\omega) e^{-i\omega t}, \tag{A.14}$$

with corresponding representation of the identity

$$\delta(\omega - \omega') = \int \frac{dt}{(2\pi)}\, e^{-i(\omega-\omega')t}, \tag{A.15}$$

one can define structure factors in the frequency domain. The dynamic structure factor $S(\boldsymbol{k},\omega)$, for instance, is obtained by a Fourier transformation in time of the intermediate scattering function $G(\boldsymbol{k},t)$,

$$S(\boldsymbol{k},\omega) = \int dt\, G(\boldsymbol{k},t) e^{+i\omega t}, \quad \lim_{s\to\infty} \langle h(\boldsymbol{k},s+t) h(\boldsymbol{q},s) \rangle = (2\pi)^d \delta(\boldsymbol{k}+\boldsymbol{q}) G(\boldsymbol{k},t). \tag{A.16}$$

From Eq. (A.9),

$$G(\boldsymbol{k},t) = \frac{D}{\nu k^2} e^{-\nu k^2 |t|}, \tag{A.17}$$

so that

$$S(\boldsymbol{k},\omega) = \frac{2D}{\omega^2 + (\nu k^2)^2}. \tag{A.18}$$

In roughening experiments, where one considers a finite interface of linear size L with flat initial condition, $h(\boldsymbol{k},0)$ can be set to zero with a global shift of the

height. Another time-dependent structure factor can be defined as

$$\langle h(\boldsymbol{k},t)h(\boldsymbol{q},t)\rangle = L^d \delta_{\boldsymbol{k},-\boldsymbol{q}} S(\boldsymbol{k},t). \tag{A.19}$$

As $\int d^d x\, h(\boldsymbol{x},t) = h(\boldsymbol{k}=0,t)$, the squared width can be written as

$$\begin{aligned} w^2(L,t) &= \frac{1}{L^d}\int d^d x \left\langle \left(h(\boldsymbol{x},t) - \frac{1}{L^d}\int d^d y\, h(\boldsymbol{y},t)\right)^2 \right\rangle \\ &= \frac{1}{L^d}\int d^d x \left\langle h(\boldsymbol{x},t)^2\right\rangle - \left(\frac{1}{L^d}\int d^d x \left\langle h(\boldsymbol{x},t)\right\rangle\right)^2 \\ &= \frac{1}{L^{2d}}\sum_{\boldsymbol{k}\neq 0} \left\langle h(\boldsymbol{k},t)h(-\boldsymbol{k},t)\right\rangle , \end{aligned} \tag{A.20}$$

where the finite-space identity representations of Eq. (A.4) have been used. Upon substituting the right-hand side with Eq. (A.19), one gets

$$w^2(L,t) = \frac{1}{L^d}\sum_{\boldsymbol{k}\neq 0} S(\boldsymbol{k},t). \tag{A.21}$$

For a rotationally invariant interface, where $S(\boldsymbol{k},t) = S(k,t)$, the asymptotics of $w^2(L,t)$ for large L can be computed as follows, first by replacing the sum with an integral

$$\frac{1}{L^d}\sum_{\boldsymbol{k}} \to \int \frac{d^d k}{(2\pi)^d} = \frac{S_d}{(2\pi)^d}\int_0^\infty dk\, k^{d-1}, \tag{A.22}$$

with S_d the surface of a d-dimensional sphere of unit radius [1], then noticing that the constraint $\boldsymbol{k}\neq 0$ on the sum implies that $2\pi/L$ is the smallest possible value of $k = \sqrt{\boldsymbol{k}\cdot\boldsymbol{k}}$. Therefore,

$$w^2(L,t) \xrightarrow{L\to\infty} \frac{S_d}{(2\pi)^d}\int_{2\pi/L}^\infty k^{d-1} dk\, S(k,t), \tag{A.23}$$

as in Eq. (4.65).

[1] $S_d = 2\pi^{d/2}/\Gamma(d/2)$, with Γ the Euler Gamma function.

Appendix B

Method of characteristics for conservation laws

This appendix is a concise solver's guide for the application of the method of characteristics to conservation laws. It is largely based on Evans' book on partial differential equations [74] (PDE) and some lecture notes from a PDE course at Stanford university [99].

Conservation laws are abundant in Physics. Many problems, in fact, are easily solved once one defines the system boundaries carefully and identifies those quantities that do not change over time. Under the suitable assumption that the conserved quantities does not disappear somewhere to instantaneously reappear somewhere else, conservation laws admit a local differential form. It takes, for instance, a popular undergraduate-level calculation to show that the local density $\rho(x,t)$ of a system whose global density $\int_V \rho\, dx$ is conserved obeys a partial differential equation of the form

$$\partial_t \rho + \nabla \cdot \mathbf{J} = 0, \tag{B.1}$$

where $\mathbf{J}$ is the density current. The closure of the problem requires a relation $\mathbf{J}(\rho)$, given by physical intuition as in traffic flow problems, phenomenological laws as the Fick's law of diffusion $\mathbf{J} = -D\nabla\rho$ or even a microscopic theory. What is special about conservation laws is that they have the structure of quasi-linear equations, which are easier to solve than their fully nonlinear companions.

In order to understand the implications of quasi-linearity, it is useful to consider

a *scalar* conservation law in one dimension. By applying the chain rule,

$$\partial_t \rho + J' \partial_x \rho = 0, \tag{B.2}$$

where the $'$ denotes derivative w.r.t. ρ. The equation above is called quasi-linear as it is linear in its higher-order derivatives, namely $\partial_t \rho$ and $\partial_x \rho$. The method of characteristics is aimed at transforming the PDE into an ordinary differential equation (ODE), by considering some special lines in the (x, t) plane—or simply the $t \geq 0$ half-plane, if the initial datum is a function of x at time $t = 0$. To find such lines, imagine one of the two variables in $\rho(x, t)$ to be a function of the other one, say $x = x(t)$[1]. The unknown function total time derivative, denoted here with a dot, is given by $\dot{\rho} = (\partial_x \rho)\dot{x} + \partial_t \rho$. By extracting $\partial_t \rho$ from the latter equation and substituting it into the conservation law, one finds

$$\dot{\rho} + [J' - \dot{x}(t)]\, \partial_x \rho = 0. \tag{B.3}$$

It is clear, from Eq. (B.3), that along the straight lines defined by $\dot{x}(t) = J'(\rho)$, Eq. (B.2) becomes the ODE $\dot{\rho} = 0$. Such lines are called *characteristics*.

This relatively innocent property provides a simple, geometrical route to build a solution $\rho(x, t)$ of Eq. (B.2) by propagating the initial condition into the whole $t \geq 0$ sector of the (x, t) plane. The recipe is the following: first, for each point $\bar{x}$ on the x-axis, find the characteristic intersecting the axis at $\bar{x}$. Then, take the initial datum $\rho_0(\bar{x})$ and propagate it along the characteristics towards positive t's. If, for instance, $\rho_0(\bar{x}) = \bar{\rho}$, set $\rho(x(t), t) = \bar{\rho}$ on the whole characteristic line passing through $\bar{x}$. It can be easily checked that, in the linear case $J' = v$, this scheme yields the usual travelling solution

$$\rho(x, t) = \rho_0(x - vt). \tag{B.4}$$

In general, the ρ dependence of J' causes distinct characteristic lines to have different slopes. The obvious yet catastrophic consequence is that characteristic lines can cross: once it happens the PDE solution ceases to be defined, as it is not clear which value to assign to it at the crossing point. The conservation law structure of the PDE, however, allows for enough insight that the solution can be determined uniquely even after some characteristic lines have crossed.

[1] This choice is useful as the coefficient of the time derivative is usually one in a conservation law. Furthermore, it corresponds to moving from the Eulerian to the Lagrangian frame of reference in fluid-related problems.

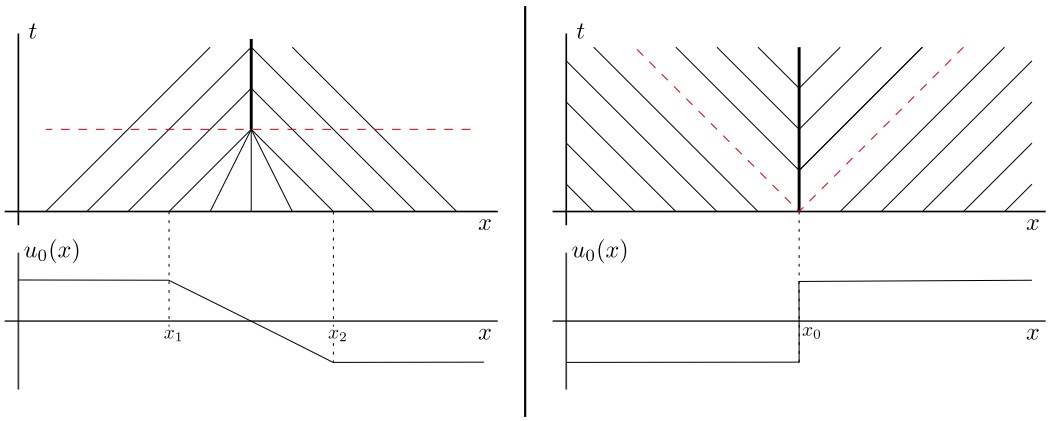

Figure B.1 *Two examples of shock wave in the Burgers' equation. The initial profile is shown on the bottom as a function of x, while characteristic lines in the $x-t$ plane are displayed on the top of the figure. In the left panel, a decreasing velocity profile evolves into a shock which is physical, as it satisfies the Lax entropy condition (see discussion in the text). The right panel depicts an unphysical shock: it satisfies the Rankine-Hugoniot equation but not Lax condition.*

Let us consider, for the sake of concreteness, the inviscid Burgers' equation as a working example,

$$\partial_t u + u\partial_x u = 0, \tag{B.5}$$

which is a conservation law with current $J = u^2/2$. The important thing to notice here is that the current derivative J, which also sets the characteristics' slopes, is an increasing function of the variable u. In fact, the current derivative coincides with u for this specific problem. This allows us to nicely illustrate the phenomenon of characteristics crossing by taking a decreasing initial condition. Take, for instance, the piecewise linear function depicted in the lower part of Fig. B.1, left panel. The initial profile, together with the current derivative, is positive on the left but negative on the right, hence characteristic lines will meet somewhere in the middle—in the inviscid fluid picture, it is like the channel was prepared so that the fluid on the right has negative speed and that on the left has positive speed. Once characteristics have met, physical intuition suggests that the fluid on the right will keep pushing left while the fluid on the left will keep pushing right. In mathematical terms, such a situation corresponds to admitting a discontinuous $u(x,t)$. Specifically, after the characteristics cross $u(x,t)$ develops a moving discontinuity which separates the initial speeds of the left and right portions and travels at fixed speed σ—such a discontinuity is called a *shock wave* and σ is the shock speed.

Even though a discontinuous solution would not, in principle, make sense, one

can check it still satisfies Eq. (B.5) in the *weak* sense. In general, the weak formulation of a conservation law reads

$$\int_0^\infty \mathrm{d}t \int_{-\infty}^\infty \mathrm{d}x\, \varphi \left[\partial_t \rho + \partial_x J(\rho)\right] = 0. \tag{B.6}$$

A (possibly discontinuous) function ρ which satisfies Eq. (B.6) for any smooth test function $\varphi(x,t)$ is called a weak solution of Eq. (B.2). If $\rho(x,t)$ is assumed to be a piecewise-constant function such that

$$\rho(x,t) = \begin{cases} \rho_l, & x < \sigma t, \\ \rho_r, & x > \sigma t, \end{cases} \tag{B.7}$$

then the weak equation Eq. (B.6) translates into a constraint for the discontinuity speed σ, or the *shock* speed, called the *Rankine-Hugoniot condition*. The Rankine-Hugoniot condition reads

$$J(\rho_r) - J(\rho_l) = \sigma(\rho_r - \rho_l), \tag{B.8}$$

where ρ_r and ρ_l denote the solution values on the right and left of the shock, respectively. For the Burgers' equation $\rho = u$ and $J = u^2/2$, so that the speed of the shock is the average between those on its sides, as common sense would suggest in the inviscid fluid picture. Common sense plays indeed an important role when dealing with weak solutions: the relaxation of the differentiability requirement needed to move from the standard to the weak formulation may cause a proliferation of unphysical solutions.

One of the possible systematic ways of dealing with the issue consists in regarding shock waves as highly dissipative and irreversible phenomena. Characteristics crossing represents in fact a loss of information, in that it does not afford further propagation of the initial condition. If the shock formation is irreversible, it cannot be observed by running time backwards. Rephrasing, characteristics are allowed to impinge on a shock as in the left panel of Fig. B.1, but not to depart from it as in the right panel. Mathematically, this is yet another constraint on the shock speed σ called *Lax entropy condition*

$$J'(\rho_l) > \sigma > J'(\rho_r). \tag{B.9}$$

Lax entropy condition can be seen at work in the right panel of Fig. B.1 and in Fig. B.2. The propagation of the initial, discontinuous profile $-\mathrm{sign}(x)$ leaves the

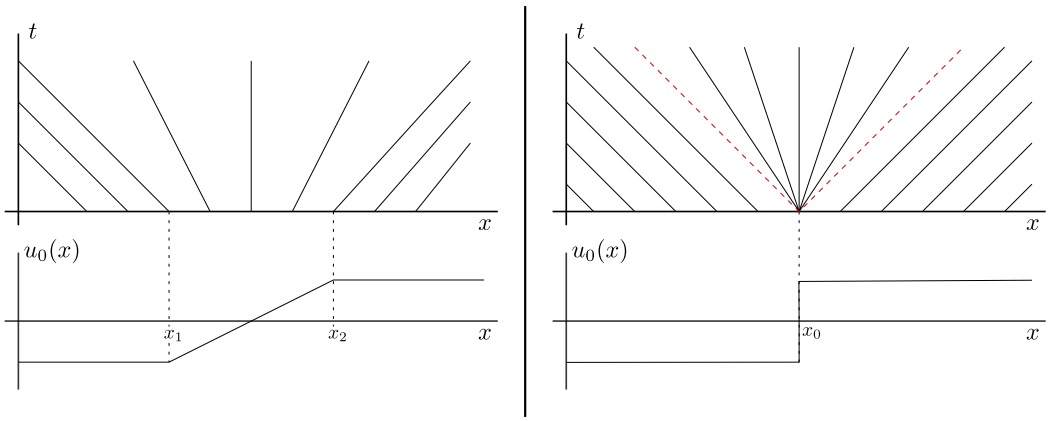

Figure B.2 *A limiting procedure shows how to fill the cone within the red dashed lines in the right panel with a rarefaction fan. Start with a piecewise linear function consisting of the $u = -1$ line up to x_1, a slope-1 segment from x_1 to x_2 and the $u = 1$ line from x_2 on (left panel, bottom). The solution of this problem is obtained with the standard method of characteristics (left panel, top). The solution for the original initial datum (right panel) emerges in the limit where x_1 and x_2 tend simultaneously to x_0.*

solution unspecified in the cone originating from x_0 (marked by dashed red lines in the left panels of both figures). The cone can be filled with *a)* a discontinuity corresponding to a vanishing-speed shock wave, as in the right panel of Fig. B.1; *b)* a *rarefaction fan* $u(x,t) = (x-x_0)/t$ for $(x-x_0) \in [-t, +t]$, as in the right panel of Fig. B.2. Both are admissible weak solutions of Eq. (B.5))—the vanishing-speed shock wave satisfying Eq. (B.8) too. The latter, however, does not satisfy the entropy condition Eq. (B.9) ($J(u_l) = -1 < +1 = J(u_r)$). The correct filling for the empty cone is indeed the rarefaction fan, as can be checked with a limiting procedure sketched in Fig. B.2. Once again, the correct solution corresponds to the one suggested by common sense: two portions of a fluid which are moving away from each other are connected continuously through a portion at rest rather than a source pushing new material in both the directions.

To sum up, solving a first-order PDE along the characteristic lines transforms the problem into a—simpler—ODE, at least in some regions of the (x,t) plane. When the PDE is a conservation law, the aforementioned ODE does not even need to be solved: the solution is constant along characteristics. Furthermore, the physics of the conservation law can be directly exploited to propagate the solution out of the boundaries set by the method of characteristics, and to understand the emergence of shock waves and rarefaction fans. The last sentence finds its mathematical translation in the Rankine-Hugoniot and Lax entropy conditions, which generalise also to systems of conservation laws such as the coupled equation studied in section 3.2.

Appendix C

Connected correlation and Vertex functions

The vertex generating function, introduced in subsection 4.1.3 as

$$\begin{aligned}\Gamma[h,\tilde{h}] = \sum_{n_h,n_{\tilde{h}}=0}^{\infty} \int d\mathbb{k}_1 \dots d\mathbb{k}_{n_h+n_{\tilde{h}}} \Gamma^{n_h,n_{\tilde{h}}}(\mathbb{k}_1,\dots,\mathbb{k}_{n_h+n_{\tilde{h}}}) \\ \times \frac{h(-\mathbb{k}_1)\dots h(-\mathbb{k}_{n_h})}{n_h!} \frac{\tilde{h}(-\mathbb{k}_{n_h+1})\dots \tilde{h}(-\mathbb{k}_{n_h+n_{\tilde{h}}})}{n_{\tilde{h}}!}.\end{aligned} \tag{C.1}$$

and the connected correlation generating function

$$\begin{aligned}F[v,\tilde{v}] = \sum_{n_h,n_{\tilde{h}}=0}^{\infty} \int d\mathbb{k}_1 \dots d\mathbb{k}_{n_v+n_{\tilde{v}}} C_c^{n_v,n_{\tilde{v}}}(\mathbb{k}_1,\dots,\mathbb{k}_{n_v+n_{\tilde{v}}}) \\ \times \frac{v(-\mathbb{k}_1)\dots v(-\mathbb{k}_{n_v})}{n_v!} \frac{\tilde{v}(-\mathbb{k}_{n_v+1})\dots \tilde{v}(-\mathbb{k}_{n_v+n_{\tilde{v}}})}{n_{\tilde{v}}!}.\end{aligned} \tag{C.2}$$

are related by Legendre-Fenchel transform,

$$\Gamma[h,\tilde{h}] = \sup_{v,\tilde{v}} \left\{ \int d\mathbb{k} \, \left[\tilde{v}(\mathbb{k})\tilde{h}(-\mathbb{k}) + v(\mathbb{k})h(-\mathbb{k})\right] - F[v,\tilde{v}] \right\}. \tag{C.3}$$

By duality of the Legendre-Fenchel transform, F is the transform of Γ. In general, the following identity holds

$$\Gamma[h,\tilde{h}] + F[v,\tilde{v}] = \int d\mathbb{k} \, \left[\tilde{v}(\mathbb{k})\tilde{h}(-\mathbb{k}) + v(\mathbb{k})h(-\mathbb{k})\right], \tag{C.4}$$

as a function or $\tilde{v}, v$ or $\tilde{h}, h$. The change of variable from the v's to the h's and vice versa is performed via the relations

$$h(\mathbb{k}) = \frac{\delta F}{\delta v(-\mathbb{k})}, \quad v(\mathbb{k}) = \frac{\delta \Gamma}{\delta h(-\mathbb{k})}, \tag{C.5}$$

valid also for the response fields $\tilde{h}$ and $\tilde{v}$. Legendre-Fenchel duality leads to some relations between the derivatives of $\Gamma[h, \tilde{h}]$, i.e. the vertex functions, and those of $F[\tilde{v}, v]$, i.e. connected correlation functions, which can be used to derive perturbative corrections to vertex functions from the perturbative corrections to correlations.

Consider, e.g., the double derivative,

$$\frac{\delta}{\delta \tilde{v}(\mathbb{k}')} \frac{\delta \Gamma}{\delta \tilde{h}(-\mathbb{k})} = \frac{\delta \tilde{v}(\mathbb{k})}{\delta \tilde{v}(\mathbb{k}')} = \delta(\mathbb{k} - \mathbb{k}'). \tag{C.6}$$

Also, from the chain rule,

$$\frac{\delta^2 \Gamma}{\delta \tilde{v}(\mathbb{k}') \delta \tilde{h}(-\mathbb{k})} = \int d\mathbb{k}_1 \left[\frac{\delta^2 \Gamma}{\delta \tilde{h}(-\mathbb{k}) \delta \tilde{h}(-\mathbb{k}_1)} \frac{\delta \tilde{h}(-\mathbb{k}_1)}{\delta \tilde{v}(\mathbb{k}')} + \frac{\delta^2 \Gamma}{\delta \tilde{h}(-\mathbb{k}) \delta h(-\mathbb{k}_1)} \frac{\delta h(-\mathbb{k}_1)}{\delta \tilde{v}(\mathbb{k}')} \right]. \tag{C.7}$$

According to Eq. (C.5), $h(-\mathbb{k}_1)$ can be replaced with $\delta F / \delta v(\mathbb{k}_1)$, so that

$$\frac{\delta h(-\mathbb{k}_1)}{\delta \tilde{v}(\mathbb{k}')} = \frac{\delta^2 F}{\delta \tilde{v}(\mathbb{k}') \delta v(\mathbb{k}_1)}. \tag{C.8}$$

Analogously,

$$\frac{\delta \tilde{h}(-\mathbb{k}_1)}{\delta \tilde{v}(\mathbb{k}')} = \frac{\delta^2 F}{\delta \tilde{v}(\mathbb{k}') \delta \tilde{v}(\mathbb{k}_1)}. \tag{C.9}$$

Upon taking the limit $\tilde{v}, v \to 0$, the right-hand side of Eq. (C.9) becomes the connected correlation function $C_c^{\tilde{h}\tilde{h}}(-\mathbb{k}', -\mathbb{k}_1)$, which vanishes, as all the correlations containing response fields only, by construction of the JD action. The right-hand side of Eq. (C.8), instead, becomes the connected correlation function $C_c^{\tilde{h}h}(-\mathbb{k}', -\mathbb{k}_1) = \left\langle \tilde{h}(-\mathbb{k}') h(-\mathbb{k}_1) \right\rangle_c$, where the subscript c on $\langle . \rangle$ indicates that the product of averages is subtracted. Taking also the $\tilde{h}, h \to 0$ limit, the left-hand side of Eq. (C.7) remains unaltered, while the double derivative of Γ w.r.t. $\tilde{h}(-\mathbb{k})$ and $h(-\mathbb{k}_1)$ tends to the vertex function $\Gamma^{\tilde{h}h}(\mathbb{k}, \mathbb{k}_1)$. Substituting the left-hand side with the right-hand side of Eq. (C.6) yields

$$\delta(\mathbb{k} - \mathbb{k}') = \int d\mathbb{k}_1 \, \Gamma^{\tilde{h}h}(\mathbb{k}, \mathbb{k}_1) \left\langle \tilde{h}(-\mathbb{k}') h(-\mathbb{k}_1) \right\rangle_c. \tag{C.10}$$

Finally, by setting $\Gamma^{\tilde{h}h}(\mathbb{k},\mathbb{k}_1) = \delta(\mathbb{k}+\mathbb{k}_1)\Gamma^{\tilde{h}h}(\mathbb{k})$ and $\left\langle \tilde{h}(-\mathbb{k}')h(-\mathbb{k}_1)\right\rangle_c$ with $\chi^{hh}(\mathbb{k}')\delta(\mathbb{k}_1+\mathbb{k}')$ (see Eq. (4.36)), and performing the $\mathbb{k}_1$ integral, we get

$$\delta(\mathbb{k}-\mathbb{k}') = \delta(\mathbb{k}-\mathbb{k}')\Gamma^{\tilde{h}h}(\mathbb{k})\chi^{hh}(\mathbb{k}') \Rightarrow \Gamma^{\tilde{h}h}(\mathbb{k}) = \left[\chi^{hh}(\mathbb{k})\right]^{-1}. \tag{C.11}$$

For an Edwards-Wilkinson interface, for example, whose JD action is specified by the coupling matrix of Eq. (4.34), $\Gamma^{\tilde{h}h}$ is given by $-i\omega+\nu_h k^2$ (from Eq. (4.42)) while $\chi^{hh} = (-i\omega+\nu_h k^2)^{-1}$ (from Eq. (4.8)), so that Eq. (C.11) is satisfied.

Another relevant double derivative is

$$\frac{\delta^2\Gamma}{\delta v(\mathbb{k}')\delta\tilde{h}(-\mathbb{k})} = \int d\mathbb{k}_1 \left[\frac{\delta^2\Gamma}{\delta\tilde{h}(-\mathbb{k})\delta\tilde{h}(-\mathbb{k}_1)}\frac{\delta\tilde{h}(-\mathbb{k}_1)}{\delta v(\mathbb{k}')} + \frac{\delta^2\Gamma}{\delta\tilde{h}(-\mathbb{k})\delta h(-\mathbb{k}_1)}\frac{\delta h(-\mathbb{k}_1)}{\delta v(\mathbb{k}')}\right]. \tag{C.12}$$

The left-hand side of Eq. (C.12) vanishes because $\delta\Gamma/\delta\tilde{h} = \tilde{v}$. On the right-hand side,

$$\frac{\delta h(-\mathbb{k}_1)}{\delta v(\mathbb{k}')} = \frac{\delta^2 F}{\delta v(\mathbb{k}')\delta v(\mathbb{k}_1)} \xrightarrow{\tilde{v},v\to 0} C_c^{hh}(-\mathbb{k}',-\mathbb{k}_1) \tag{C.13}$$

and

$$\frac{\delta\tilde{h}(-\mathbb{k}_1)}{\delta v(\mathbb{k}')} = \frac{\delta^2 F}{\delta v(\mathbb{k}')\delta\tilde{v}(\mathbb{k}_1)} \xrightarrow{\tilde{v},v\to 0} C_c^{h\tilde{h}}(-\mathbb{k}',-\mathbb{k}_1). \tag{C.14}$$

In the $h,\tilde{h}\to 0$ limit the derivatives of Γ become vertex functions and Eq. (C.12) becomes

$$\begin{aligned} 0 &= \int d\mathbb{k}_1 \left[\Gamma^{\tilde{h}\tilde{h}}(\mathbb{k},\mathbb{k}_1)C_c^{h\tilde{h}}(-\mathbb{k}',-\mathbb{k}_1) + \Gamma^{\tilde{h}h}(\mathbb{k},\mathbb{k}_1)C_c^{hh}(-\mathbb{k}',-\mathbb{k}_1)\right] \\ \Rightarrow 0 &= \delta(\mathbb{k}-\mathbb{k}')\left[\Gamma^{\tilde{h}\tilde{h}}(\mathbb{k})\chi^{hh}(-\mathbb{k}') + \Gamma^{\tilde{h}h}(\mathbb{k})C_c^{hh}(\mathbb{k}')\right], \end{aligned} \tag{C.15}$$

where the definitions $\langle\tilde{h}(-\mathbb{k}')h(-\mathbb{k}_1)\rangle_c = \chi^{hh}(\mathbb{k}')\delta(\mathbb{k}'+\mathbb{k}_1)$ and $\langle h(-\mathbb{k}')h(-\mathbb{k}_1)\rangle_c = \chi^{hh}(-\mathbb{k}_1)\delta(\mathbb{k}'+\mathbb{k}_1)$ have been used. The substitution of $\Gamma^{\tilde{h}h}$ with the inverse response function (Eq. (C.11)) yields another relation between vertex and correlation functions:

$$\Gamma^{\tilde{h}\tilde{h}}(\mathbb{k}) = -\frac{C_c^{hh}(\mathbb{k})}{\chi^{hh}(-\mathbb{k})\chi^{hh}(\mathbb{k})}. \tag{C.16}$$

The derivations of Eq. (C.11) and Eq. (C.16) are easily extended to the theory with more than one dynamic variable and higher-order vertex and correlation functions.

Appendix D

One-loop corrections to $\Gamma^{\tilde{\phi}\phi}$

This appendix is a detailed proof of Eq. (4.79), recalled below.

$$\begin{aligned}\Gamma^{\tilde{\phi}\phi}(\mathbb{k}) &= -i\omega + r\nu_h k^2 - \\ &= i\omega + r\nu_h k^2 + \nu_h \frac{g^2}{2}\int_{k_1} \frac{\frac{k^2}{2} - \boldsymbol{k}_1\cdot\boldsymbol{k}}{\left(\frac{\boldsymbol{k}}{2}-\boldsymbol{k}_1\right)^2} \frac{\frac{k^2}{4}-k_1^2}{\frac{r\left(\frac{\boldsymbol{k}}{2}+\boldsymbol{k}_1\right)^2+\left(\frac{\boldsymbol{k}}{2}-\boldsymbol{k}_1\right)^2}{2} - \frac{i\omega}{2\nu_h}}.\end{aligned} \tag{D.1}$$

As mentioned in section 4.3, the easier path towards the perturbative corrections of a given vertex functions passes through connected correlation functions, specifically

$$\left\langle \phi(\mathbb{k})\tilde{\phi}(\mathbb{k}')\right\rangle = \chi^{\phi\phi}(\mathbb{k})(2\pi)^d\delta(\mathbb{k}+\mathbb{k}'). \tag{D.2}$$

At order 0 in g, $\chi^{\phi\phi}$ is given (graphically and symbolically) by Eq. (4.75b). As the nonlinear terms of the action contain 3 fields, corrections at order 1 in g are proportional to five-point Gaussian averages. The latter averages, under Wick's theorem, become a product of 2 two-point averages and a single-field average, which vanishes. Therefore, the first non-trivial contribution is of order g^2 and contains two nonlinear vertices. Let us draw the corresponding diagrammatic

representation:

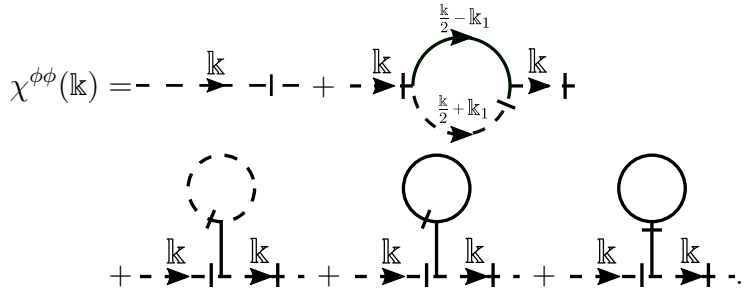

(D.3)

Notice the absence of arrows and momenta on the vertical "tadpole" graphs of the last three diagrams in Eq. (D.3). In fact, due to conservation of momentum, the vertical line carries none. In addition, from Eq. (4.76), the $\tilde{\phi}\phi h$ vertex carries a factor $\nu_h g(\boldsymbol{k}\cdot\boldsymbol{k}_1)$, where $\boldsymbol{k}_1$ is the momentum on the h-line. As a result, the three diagrams in the second line of Eq. (D.3) right-hand side represent vanishing contributions. Upon removal of the external legs and inversion, required when switching from connected correlations to vertex functions (cf. Eq. (C.11)), we are left with the first line of Eq. (D.1), i.e.

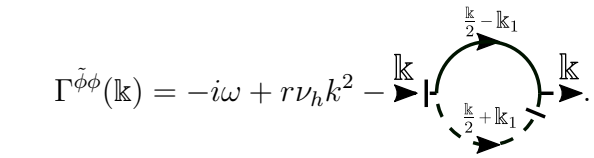

(D.4)

All is left to do is computing the contribution of the only diagram left. By substituting lines and vertices according to Eq. (4.75) and (4.76) and integrating over the internal momentum,

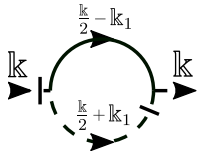

$$= (\nu_h g)^2 \int_{\mathbb{k}_1} \left[\boldsymbol{k}\cdot\left(\frac{\boldsymbol{k}}{2}-\boldsymbol{k}_1\right)\right]\left[\left(\boldsymbol{k}_1+\frac{\boldsymbol{k}}{2}\right)\cdot\left(\boldsymbol{k}_1-\frac{\boldsymbol{k}}{2}\right)\right] \times\frac{1}{\left[-i\left(\frac{\omega}{2}+\omega_1\right)+r\nu_h\left(\frac{\boldsymbol{k}}{2}+\boldsymbol{k}_1\right)^2\right]} \times\frac{2\nu_h}{\left[\left(\frac{\omega}{2}-\omega_1\right)^2+\nu_h^2\left(\frac{\boldsymbol{k}}{2}+\boldsymbol{k}_1\right)^4\right]}. \tag{D.5}$$

There should be an additional symmetry factor of 2, taking into account the permutation of the 2 nonlinear vertices in the diagram. However, the factor cancels the 1/2 from the Taylor expansion of the exponential of the nonlinear action to order g^2.

Let us now perform the ω_1 integral, $(2\pi)^{-1}\int d\omega_1$. It is useful, in this respect, to define

$$I_1(\mathbb{k},\boldsymbol{k}_1)=\int\frac{d\omega_1}{(2\pi)}\frac{1}{\left[-i\left(\frac{\omega}{2}+\omega_1\right)+r\nu_h\left(\frac{\boldsymbol{k}}{2}+\boldsymbol{k}_1\right)^2\right]\left[\left(\frac{\omega}{2}-\omega_1\right)^2+\nu_h^2\left(\frac{\boldsymbol{k}}{2}-\boldsymbol{k}_1\right)^4\right]}, \tag{D.6}$$

so that

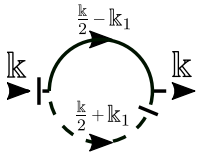

$$=2\nu_h(\nu_h g)^2\int\frac{d^dk}{(2\pi)^d}\left(k^2/2-\boldsymbol{k}\cdot\boldsymbol{k}_1\right)\left(k_1^2-k^2/4\right)I_1(\mathbb{k},\boldsymbol{k}_1). \tag{D.7}$$

The integrand of $I_1(\mathbb{k},\boldsymbol{k}_1)$ decays as ω_1^{-3} for ω_1 large. Thus, the ω_1-integral, originally over $(-\infty,\infty)$, can be extended to a semicircular contour in the complex plane having infinite diameter: the integral over the diameter coincides with $I_1(\mathbb{k},\boldsymbol{k}_1)$, while the integral over the arc vanishes together with the integrand. Having expressed $I_1(\mathbb{k},\boldsymbol{k}_1)$ as a complex integral over a closed contour, its value can be determined with the residue theorem as $2\pi i\times$(sum of the residues inside the contour). The integrand of $I_1(\mathbb{k},\boldsymbol{k}_1)$ has 3 poles in ω_1,

$$\omega_{1,1}=-\frac{\omega}{2}-ir\nu_h\left(\frac{\boldsymbol{k}}{2}+\boldsymbol{k}_1\right)^2; \tag{D.8a}$$

$$\omega_{1,2}=\frac{\omega}{2}-i\nu_h\left(\frac{\boldsymbol{k}}{2}-\boldsymbol{k}_1\right)^2; \tag{D.8b}$$

$$\omega_{1,3}=\frac{\omega}{2}+i\nu_h\left(\frac{\boldsymbol{k}}{2}-\boldsymbol{k}_1\right)^2. \tag{D.8c}$$

Upon choosing the semicircular contour in the upper half of the complex plane, only the pole with positive imaginary part contributes, i.e.

$$\begin{aligned}I_1(\mathbb{k},\boldsymbol{k}_1)&=2\pi i\mathrm{Res}(\omega_{1,3})\\&=\frac{1}{2\nu_h\left(\frac{\boldsymbol{k}}{2}-\boldsymbol{k}_1\right)^2\left[-i\omega+\nu_h\left(\frac{\boldsymbol{k}}{2}-\boldsymbol{k}_1\right)^2+r\nu_h\left(\frac{\boldsymbol{k}}{2}+\boldsymbol{k}_1\right)^2\right]}.\end{aligned} \tag{D.9}$$

By extracting another $2\nu_h$ factor out of the square bracket in Eq. (D.9), then substituting in the $I_1(\mathbb{k},\boldsymbol{k}_1)$ factor in Eq. (D.7) right-hand side, one gets

$-$ 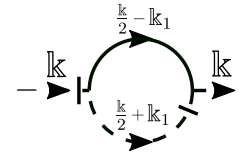

$$=\nu_h\frac{g^2}{2}\int_{k_1}\frac{\frac{k^2}{2}-\boldsymbol{k}_1\cdot\boldsymbol{k}}{\left(\frac{\boldsymbol{k}}{2}-\boldsymbol{k}_1\right)^2}\frac{\frac{k^2}{4}-k_1^2}{\frac{r\left(\frac{\boldsymbol{k}}{2}+\boldsymbol{k}_1\right)^2+\left(\frac{\boldsymbol{k}}{2}-\boldsymbol{k}_1\right)^2}{2}-\frac{i\omega}{2\nu_h}}. \tag{D.10}$$

Substituting again the value of the diagram in Eq. (D.4) yields the one-loop correction shown in Eq. (D.1) and used in the calculations of section 4.3. Let us conclude by deriving the small-$\boldsymbol{k}$ expansion of Eq. (4.88). It is convenient, in this respect, to set $-i\omega/2\nu_h = \mu^2$ and to manipulate the right-hand side of Eq. (D.10) as

$$\nu_h \frac{g^2}{2} \int_{k_1} \frac{\left(\frac{k^2}{2} - \boldsymbol{k}_1 \cdot \boldsymbol{k}\right)\left(\frac{k^2}{4} - k_1^2\right)}{k_1^2 \left(1 - \boldsymbol{k}_1 \cdot \boldsymbol{k} + \frac{k^2}{4k_1^2}\right)} \frac{1}{\mu^2 + \frac{r+1}{2} k_1^2 + \frac{r-1}{2} \boldsymbol{k}_1 \cdot \boldsymbol{k} + \frac{r+1}{8} k^2}. \tag{D.11}$$

All the factors at the denominator can be Taylor-expanded in $\boldsymbol{k}$ by using $(1 + ax)^{-1} = 1 - ax + \mathcal{O}(x^2)$, yielding

$$\begin{aligned} \nu_h \frac{g^2}{2} \int_{k_1} \frac{\boldsymbol{k}_1 \cdot \boldsymbol{k} - k^2/2 + \mathcal{O}(k^3)}{\mu^2 + \frac{r+1}{2} k_1^2} \left[1 + \frac{\boldsymbol{k}_1 \cdot \boldsymbol{k}}{k_1^2} + \mathcal{O}(k^2)\right] \\ \left[1 - \frac{r-1}{2} \frac{\boldsymbol{k}_1 \cdot \boldsymbol{k}}{\mu^2 + \frac{r+1}{2} k_1^2} + \mathcal{O}(k^2)\right]. \end{aligned} \tag{D.12}$$

By symmetry of the $\boldsymbol{k}_1$-integral, the contributions which are linear in $\boldsymbol{k}_1$ all vanish, whereas each factor $(\boldsymbol{k}_1 \cdot \boldsymbol{k})^2$ can be replaced with $k_1^2 k^2/d$. The result is

$$\nu_h \frac{g^2}{2} \int_{k_1} \frac{1}{k_1^2 + \frac{2\mu^2}{1+r}} \frac{2}{r+1} \left[\frac{2-d}{2d} - \frac{(r-1)}{d(r+1)} \frac{k_1^2}{k_1^2 + \frac{2\mu^2}{1+r}}\right] k^2 + \mathcal{O}(k^4). \tag{D.13}$$

Upon recalling that $-i\omega/2\nu_h = \mu^2$ and adding the 0-th order contribution,

$$\begin{aligned} \Gamma^{\tilde{\phi}\phi}(\omega, \boldsymbol{k}) \simeq -i\omega + r\nu_h k^2 \left[1 - \frac{g}{2r}\left(\frac{d-2}{d(1+r)} \int_{k_1} \frac{1}{k_1^2 - \frac{i\omega}{2\nu_h}\frac{2}{1+r}}\right)\right. \\ \left. - \frac{g}{2r}\left(\frac{2(r-1)}{d(1+r)^2} \int_{k_1} \left(\frac{k_1}{k_1^2 - \frac{i\omega}{2\nu_h}\frac{2}{1+r}}\right)^2\right)\right], \end{aligned} \tag{D.14}$$

as in Eq. (4.88).

Appendix E

One-loop corrections to $\Gamma^{\tilde{\phi}\tilde{\phi}}$

This appendix is a detailed proof of Eq. (4.80), recalled below.

$$\begin{aligned}\Gamma^{\tilde{\phi}\tilde{\phi}}(\mathbb{k}) &= -2r\nu_h k^2 - \\ &= -2r\nu_h k^2 - 2\nu_h \frac{g^2}{2}\int_{k_1} \frac{\left(\frac{k^2}{2} - \boldsymbol{k}\cdot\boldsymbol{k}_1\right)^2}{\left(\frac{\boldsymbol{k}}{2} - \boldsymbol{k}_1\right)^2} \mathrm{Re}\left[\frac{1}{\frac{r\left(\frac{\boldsymbol{k}}{2}+\boldsymbol{k}_1\right)^2+\left(\frac{\boldsymbol{k}}{2}-\boldsymbol{k}_1\right)^2}{2} - \frac{i\omega}{2\nu_h}}\right];\end{aligned} \tag{E.1}$$

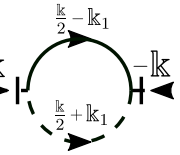

As in Appendix D, this is done by considering the corresponding connected correlation function first,

$$\langle\phi(\mathbb{k})\phi(\mathbb{k}')\rangle = C^{\phi\phi}(\mathbb{k})(2\pi)^d\delta(\mathbb{k}+\mathbb{k}'). \tag{E.2}$$

At order 0 in g, $C^{\phi\phi}$ is given by Eq. (4.75b). The first non-trivial correction is found at order g^2. Omitting all the tadpole diagrams, which vanish for the same argument presented in Appendix D,

$C^{\phi\phi}(\mathbb{k}) =$ 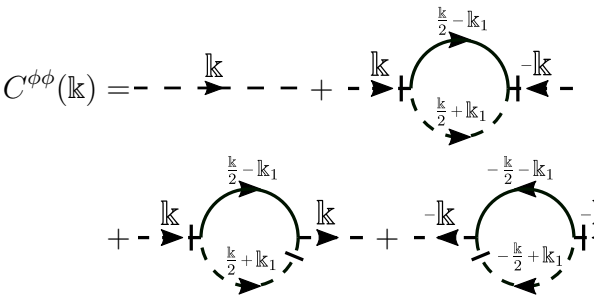

(E.3)

External legs removed (cf. Eq. (C.16)), the two diagrams in the second line of Eq. (E.3) are easily recognised as the corrections to $\Gamma^{\tilde{\phi}\phi}(\mathbb{k})$ and its complex conjugate $\Gamma^{\tilde{\phi}\phi}(-\mathbb{k})$, which coincides with $\Gamma^{\phi\tilde{\phi}}(\mathbb{k})$. Such corrections have been already discussed in Appendix D. What is left is the first line of Eq. (E.1), i.e.

$$\Gamma^{\tilde{\phi}\tilde{\phi}}(\mathbb{k}) = -2r\nu_h k^2 -$$

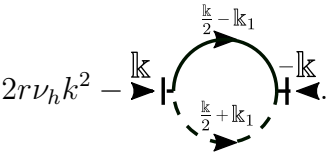

. (E.4)

By substituting lines and vertices according to Eq. (4.75) and (4.76) and integrating over the internal momentum,

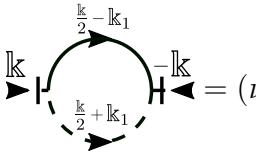

$$= (\nu_h g)^2 \int_{\mathbb{k}_1} \left[\boldsymbol{k}\cdot\left(\frac{\boldsymbol{k}}{2}-\boldsymbol{k}_1\right)\right]\left[\boldsymbol{k}\cdot\left(\frac{\boldsymbol{k}}{2}-\boldsymbol{k}_1\right)\right] \times \frac{2r\nu_h\left(\frac{\boldsymbol{k}}{2}+\boldsymbol{k}_1\right)^2}{\left[\left(\frac{\omega}{2}+\omega_1\right)^2 + r^2\nu_h^2\left(\frac{\boldsymbol{k}}{2}+\boldsymbol{k}_1\right)^4\right]} \times \frac{2\nu_h}{\left[\left(\frac{\omega}{2}-\omega_1\right)^2 + \nu_h^2\left(\frac{\boldsymbol{k}}{2}+\boldsymbol{k}_1\right)^4\right]}. \quad \text{(E.5)}$$

There should be again an additional symmetry factor of 2 due to permutations of the 2 nonlinear vertices in the diagram, but it cancels the 1/2 from the Taylor expansion of the exponential of the nonlinear action to order g^2.

Let us define, before performing the ω_1 integral $(2\pi)^{-1}\int d\omega_1$,

$$I_2(\mathbb{k},\boldsymbol{k}_1) = \int \frac{d\omega_1}{(2\pi)} \frac{1}{\left[\left(\frac{\omega}{2}+\omega_1\right)^2 + r^2\nu_h^2\left(\frac{\boldsymbol{k}}{2}+\boldsymbol{k}_1\right)^4\right]\left[\left(\frac{\omega}{2}-\omega_1\right)^2 + \nu_h^2\left(\frac{\boldsymbol{k}}{2}+\boldsymbol{k}_1\right)^4\right]}, \quad \text{(E.6)}$$

so that

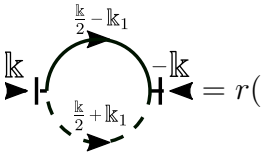

$$= r(2\nu_h)^2(\nu_h g)^2 \int_{k_1} \left(\frac{k^2}{2}-\boldsymbol{k}\cdot\boldsymbol{k}_1\right)^2 \left(\frac{\boldsymbol{k}}{2}+\boldsymbol{k}_1\right)^2 I_2(\mathbb{k},\boldsymbol{k}_1). \quad \text{(E.7)}$$

The integrand of $I_2(\mathbb{k},\boldsymbol{k}_1)$ decays as ω_1^{-4} for ω_1 large. Thus, the ω_1-integral, originally over $(-\infty,\infty)$, can be extended to a semicircular contour in the complex plane having infinite diameter: the integral over the diameter coincides with $I_2(\mathbb{k},\boldsymbol{k}_1)$, while the integral over the arc vanishes together with the integrand.

Having expressed $I_2(\mathbb{k}, \boldsymbol{k}_1)$ as a complex integral over a closed contour, its value can be determined with the residue theorem as $2\pi i\times$(sum of the residues inside the contour). The integrand of $I_2(\mathbb{k}, \boldsymbol{k}_1)$ has 4 poles in ω_1,

$$\omega_{1,1} = -\frac{\omega}{2} + ir\nu_h \left(\frac{\boldsymbol{k}}{2} + \boldsymbol{k}_1\right)^2; \tag{E.8a}$$

$$\omega_{1,2} = -\frac{\omega}{2} - ir\nu_h \left(\frac{\boldsymbol{k}}{2} + \boldsymbol{k}_1\right)^2; \tag{E.8b}$$

$$\omega_{1,3} = \frac{\omega}{2} + i\nu_h \left(\frac{\boldsymbol{k}}{2} - \boldsymbol{k}_1\right)^2; \tag{E.8c}$$

$$\omega_{1,4} = \frac{\omega}{2} - i\nu_h \left(\frac{\boldsymbol{k}}{2} - \boldsymbol{k}_1\right)^2, \tag{E.8d}$$

so that Eq. (E.6) can be written as

$$I_2(\mathbb{k}, \boldsymbol{k}_1) = \int \frac{d\omega_1}{(2\pi)} \frac{1}{(\omega_1 - \omega_{1,1})(\omega_1 - \omega_{1,2})(\omega_1 - \omega_{1,3})(\omega_1 - \omega_{1,4})}. \tag{E.9}$$

If the semicircular contour lies in the upper half of the complex plane, only the poles with positive imaginary part ($\omega_{1,1}$ and $\omega_{1,3}$) contribute, i.e.

$$\begin{aligned} I_2(\mathbb{k}, \boldsymbol{k}_1) &= 2\pi i \mathrm{Res}(\omega_{1,1}) + 2\pi i \mathrm{Res}(\omega_{1,3}) \\ &= \frac{i}{(\omega_{1,1} - \omega_{1,2})(\omega_{1,1} - \omega_{1,3})(\omega_{1,1} - \omega_{1,4})} \\ &+ \frac{i}{(\omega_{1,3} - \omega_{1,1})(\omega_{1,3} - \omega_{1,2})(\omega_{1,3} - \omega_{1,4})} \\ &= \frac{i}{(\omega_{1,1} - \omega_{1,3})} \left[\frac{1}{(\omega_{1,1} - \omega_{1,2})(\omega_{1,1} - \omega_{1,4})} - \frac{1}{(\omega_{1,3} - \omega_{1,2})(\omega_{1,3} - \omega_{1,4})}\right]. \end{aligned} \tag{E.10}$$

As

$$\omega_{1,1} - \omega_{1,2} = 2ir\nu_h \left(\frac{\boldsymbol{k}}{2} + \boldsymbol{k}_1\right)^2, \quad \omega_{1,3} - \omega_{1,4} = 2i\nu_h \left(\frac{\boldsymbol{k}}{2} - \boldsymbol{k}_1\right)^2, \tag{E.11}$$

the factor in square brackets on the right-hand side of Eq. (E.10) can be written as

$$\frac{1}{2ir\nu_h \left(\frac{\boldsymbol{k}}{2} + \boldsymbol{k}_1\right)^2 \left(\frac{\boldsymbol{k}}{2} - \boldsymbol{k}_1\right)^2} \left[\frac{\left(\frac{\boldsymbol{k}}{2} - \boldsymbol{k}_1\right)^2}{(\omega_{1,1} - \omega_{1,4})} - \frac{r\left(\frac{\boldsymbol{k}}{2} + \boldsymbol{k}_1\right)^2}{(\omega_{1,3} - \omega_{1,2})}\right]. \tag{E.12}$$

Furthermore,

$$
\begin{aligned}
(\omega_{1,1}-\omega_{1,4})^{-1} &= \left(-\omega + i\nu_h\left[\left(\frac{\boldsymbol{k}}{2}-\boldsymbol{k}_1\right)^2 + r\left(\frac{\boldsymbol{k}}{2}+\boldsymbol{k}_1\right)^2\right]\right)^{-1} \\
&= -\frac{\omega + i\nu_h\left[\left(\frac{\boldsymbol{k}}{2}-\boldsymbol{k}_1\right)^2 + r\left(\frac{\boldsymbol{k}}{2}+\boldsymbol{k}_1\right)^2\right]}{\omega^2+\nu_h^2\left[\left(\frac{\boldsymbol{k}}{2}-\boldsymbol{k}_1\right)^2 + r\left(\frac{\boldsymbol{k}}{2}+\boldsymbol{k}_1\right)^2\right]^2},
\end{aligned}
\tag{E.13}
$$

and

$$
\begin{aligned}
(\omega_{1,3}-\omega_{1,2})^{-1} &= \left(\omega + i\nu_h\left[\left(\frac{\boldsymbol{k}}{2}-\boldsymbol{k}_1\right)^2 + r\left(\frac{\boldsymbol{k}}{2}+\boldsymbol{k}_1\right)^2\right]\right)^{-1} \\
&= \frac{\omega - i\nu_h\left[\left(\frac{\boldsymbol{k}}{2}-\boldsymbol{k}_1\right)^2 + r\left(\frac{\boldsymbol{k}}{2}+\boldsymbol{k}_1\right)^2\right]}{\omega^2+\nu_h^2\left[\left(\frac{\boldsymbol{k}}{2}-\boldsymbol{k}_1\right)^2 + r\left(\frac{\boldsymbol{k}}{2}+\boldsymbol{k}_1\right)^2\right]^2},
\end{aligned}
\tag{E.14}
$$

so that

$$
\begin{aligned}
&\left[\frac{\left(\frac{\boldsymbol{k}}{2}-\boldsymbol{k}_1\right)^2}{(\omega_{1,1}-\omega_{1,4})} - \frac{r\left(\frac{\boldsymbol{k}}{2}+\boldsymbol{k}_1\right)^2}{(\omega_{1,3}-\omega_{1,2})}\right] = \\
&-\frac{\omega\left[\left(\frac{\boldsymbol{k}}{2}-\boldsymbol{k}_1\right)^2 + r\left(\frac{\boldsymbol{k}}{2}+\boldsymbol{k}_1\right)^2\right]}{\omega^2+\nu_h^2\left[\left(\frac{\boldsymbol{k}}{2}-\boldsymbol{k}_1\right)^2 + r\left(\frac{\boldsymbol{k}}{2}+\boldsymbol{k}_1\right)^2\right]^2} \\
&+\frac{i\nu_h\left[\left(\frac{\boldsymbol{k}}{2}-\boldsymbol{k}_1\right)^2 + r\left(\frac{\boldsymbol{k}}{2}+\boldsymbol{k}_1\right)^2\right]\left[r\left(\frac{\boldsymbol{k}}{2}+\boldsymbol{k}_1\right)^2 - \left(\frac{\boldsymbol{k}}{2}-\boldsymbol{k}_1\right)^2\right]}{\omega^2+\nu_h^2\left[\left(\frac{\boldsymbol{k}}{2}-\boldsymbol{k}_1\right)^2 + r\left(\frac{\boldsymbol{k}}{2}+\boldsymbol{k}_1\right)^2\right]^2} \\
&= \left[\left(\frac{\boldsymbol{k}}{2}-\boldsymbol{k}_1\right)^2 + r\left(\frac{\boldsymbol{k}}{2}+\boldsymbol{k}_1\right)^2\right]\frac{-\omega + i\nu_h\left[r\left(\frac{\boldsymbol{k}}{2}+\boldsymbol{k}_1\right)^2 - \left(\frac{\boldsymbol{k}}{2}-\boldsymbol{k}_1\right)^2\right]}{\omega^2+\nu_h^2\left[r\left(\frac{\boldsymbol{k}}{2}+\boldsymbol{k}_1\right)^2 + \left(\frac{\boldsymbol{k}}{2}-\boldsymbol{k}_1\right)^2\right]^2}.
\end{aligned}
\tag{E.15}
$$

The numerator $-\omega + i\nu_h\left[r\left(\frac{\boldsymbol{k}}{2}+\boldsymbol{k}_1\right)^2 - \left(\frac{\boldsymbol{k}}{2}-\boldsymbol{k}_1\right)^2\right]$ cancels with the factor $(\omega_{1,1}-\omega_{1,3})^{-1}$ in $I_2(\mathbb{k},\boldsymbol{k}_1)$, from Eq. (E.10) (fourth line). Therefore, by substituting the factor in square brackets of Eq. (E.12) with Eq. (E.15), then plugging the result in Eq. (E.10),

$$
\begin{aligned}
I_2(\mathbb{k},\boldsymbol{k}_1) =& \frac{\left[\left(\frac{\boldsymbol{k}}{2}-\boldsymbol{k}_1\right)^2 + r\left(\frac{\boldsymbol{k}}{2}+\boldsymbol{k}_1\right)^2\right]}{2r\nu_h\left(\frac{\boldsymbol{k}}{2}+\boldsymbol{k}_1\right)^2\left(\frac{\boldsymbol{k}}{2}-\boldsymbol{k}_1\right)^2} \\
&\times\frac{1}{\omega^2+\nu_h^2\left[r\left(\frac{\boldsymbol{k}}{2}+\boldsymbol{k}_1\right)^2 + \left(\frac{\boldsymbol{k}}{2}-\boldsymbol{k}_1\right)^2\right]^2}.
\end{aligned}
\tag{E.16}
$$

By multiplying and dividing the right-hand side with ν_h, Eq. (E.16) becomes

$$\begin{aligned} I_2(\mathbb{k}, \boldsymbol{k}_1) =& \frac{1}{2r\nu_h^2 \left(\frac{\boldsymbol{k}}{2} + \boldsymbol{k}_1\right)^2 \left(\frac{\boldsymbol{k}}{2} - \boldsymbol{k}_1\right)^2} \\ & \times \mathrm{Re}\left[\frac{1}{i\omega + \nu_h \left[\left(\frac{\boldsymbol{k}}{2} - \boldsymbol{k}_1\right)^2 + r\left(\frac{\boldsymbol{k}}{2} + \boldsymbol{k}_1\right)^2\right]}\right]. \end{aligned} \tag{E.17}$$

Finally, by substituting the function $I_2(\mathbb{k}, \boldsymbol{k}_1)$ in Eq. (E.7) with the right-hand side of Eq. (E.17),

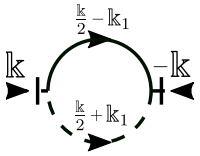

$$= 2\nu_h \frac{g^2}{2} \int_{k_1} \frac{\left(\frac{k^2}{2} - \boldsymbol{k}\cdot\boldsymbol{k}_1\right)^2}{\left(\frac{\boldsymbol{k}}{2} - \boldsymbol{k}_1\right)^2} \mathrm{Re}\left[\frac{1}{\frac{r\left(\frac{\boldsymbol{k}}{2}+\boldsymbol{k}_1\right)^2 + \left(\frac{\boldsymbol{k}}{2}-\boldsymbol{k}_1\right)^2}{2} - \frac{i\omega}{2\nu_h}}\right], \tag{E.18}$$

which proves Eq. (E.1).

The small-$\boldsymbol{k}$ expansion of the diagram above is straightforward, as the factor in brackets at the numerator of the integrand, $(k^2/2 - \boldsymbol{k}\cdot\boldsymbol{k}_1)^2$ is of order $\mathcal{O}(k^2)$. Therefore, the expansion required is obtained by setting all the $\boldsymbol{k}$'s in the k_1-integral to zero, apart from the one in $\boldsymbol{k}\cdot\boldsymbol{k}_1$, i.e.

$$\begin{aligned} & 2\nu_h \frac{g^2}{2} \int_{k_1} \frac{\left(\frac{k^2}{2} - \boldsymbol{k}\cdot\boldsymbol{k}_1\right)^2}{\left(\frac{\boldsymbol{k}}{2} - \boldsymbol{k}_1\right)^2} \mathrm{Re}\left[\frac{1}{\frac{r\left(\frac{\boldsymbol{k}}{2}+\boldsymbol{k}_1\right)^2 + \left(\frac{\boldsymbol{k}}{2}-\boldsymbol{k}_1\right)^2}{2} - \frac{i\omega}{2\nu_h}}\right] = \\ & 2\nu_h \frac{g^2}{2} \int_{k_1} \frac{\left(\boldsymbol{k}\cdot\boldsymbol{k}_1\right)^2}{\left(\boldsymbol{k}_1\right)^2} \mathrm{Re}\left(\frac{1}{\frac{r+1}{2}k_1^2 - \frac{i\omega}{2\nu_h}}\right) + \mathcal{O}(k^4) = \\ & 2\nu_h k^2 \frac{g^2}{d(r+1)} \int_{k_1} \mathrm{Re}\left(\frac{1}{k_1^2 - \frac{i\omega}{2\nu_h}\frac{2}{1+r}}\right) + \mathcal{O}(k^4), \end{aligned} \tag{E.19}$$

where, in the last equality, $(\boldsymbol{k}\cdot\boldsymbol{k}_1)^2$ has been replaced with $k^2k_1^2/d$ because of the $\boldsymbol{k}_1$-integral symmetry. The addition of the 0-th order contribution yields

$$\Gamma^{\tilde{\phi}\tilde{\phi}}(\boldsymbol{k}, \omega) \simeq -2r\nu_h k^2 \left[1 + \frac{g^2}{dr(1+r)} \int_{k_1} \mathrm{Re}\left(\frac{1}{k_1^2 - \frac{i\omega}{2\nu_h}\frac{2}{1+r}}\right)\right], \tag{E.20}$$

as in Eq. (4.89).

Bibliography

[1] F. Cagnetta, M. R. Evans, and D. Marenduzzo. Active growth and pattern formation in membrane-protein systems. *Phys. Rev. Lett.*, 120:258001, 2018.

[2] F. Cagnetta, M. R. Evans, and D. Marenduzzo. Statistical mechanics of a single active slider on a fluctuating interface. *Phys. Rev. E*, 99:042124, 2019.

[3] F. Cagnetta and M. R. Evans. Inviscid limit of the active interface equations. *J. Stat. Mech.: Theory Exp.*, (11):113206, 2019.

[4] F. Cagnetta, M. R. Evans, and D. Marenduzzo. Kinetic roughening in active interfaces. *EPJ Web Conf.*, 230:00001, 2020.

[5] F. Cagnetta, D. Michieletto, and D. Marenduzzo. Epiphoresis: a nonequilibrium mechanism for fast search on dna. *arXiv:1908.06671*, 2019.

[6] F. Cagnetta and E. Mallmin. Efficiency of one-dimensional active transport conditioned on motility. *Phys. Rev. E*, 101:022130, 2020.

[7] T. D. Pollard and G. G. Borisy. Cellular motility driven by assembly and disassembly of actin filaments. *Cell*, 112(4):453–465, 2003.

[8] E. Hannezo. A toy model for active interfaces. *Physics*, 11:61, 2018.

[9] M. Eden. A two-dimensional growth process. In *Proceedings of the Fourth Berkeley Symposium on Mathematical Statistics and Probability*, volume 4: Contributions to Biology and Problems of Medicine, pages 223–239. University of California Press, 1961.

[10] F. Family and D. P. Landau. *Kinetics of aggregation and gelation*. Elsevier, 2012.

[11] A.-L. Barabási and H. E. Stanley. *Fractal concepts in surface growth*. Cambridge university press, 1995.

[12] T. Halpin-Healy and Y.-C. Zhang. Kinetic roughening phenomena, stochastic growth, directed polymers and all that. aspects of multidisciplinary statistical mechanics. *Phys. Rep.*, 254(4-6):215–414, 1995.

[13] B. B. Mandelbrot. on the aggregative fractals called "squigs", which include recursive models of polymers and of percolation clusters. In *Kinetics of Aggregation and Gelation*, pages 5–7. Elsevier, 1984.

[14] J. Krug. Origins of scale invariance in growth processes. *Adv. Phys.*, 46(2):139–282, 1997.

[15] H. E. Stanley. Fractal concepts in aggregation and gelation: an introduction. In *Kinetics of Aggregation and Gelation*, pages 1–4. Elsevier, 1984.

[16] F. Family and T. Vicsek. Scaling of the active zone in the eden process on percolation networks and the ballistic deposition model. *J. Phys. A*, 18(2):L75, 1985.

[17] S. F. Edwards and D. R. Wilkinson. The surface statistics of a granular aggregate. *Proc. R. Soc. Lond. A*, 381(1780):17–31, 1982.

[18] M. Kardar, G. Parisi, and Y.-C. Zhang. Dynamic scaling of growing interfaces. *Phys. Rev. Lett.*, 56(9):889, 1986.

[19] T. Kriecherbauer and J. Krug. A pedestrian's view on interacting particle systems, kpz universality and random matrices. *J. Phys. A*, 43(40):403001, 2010.

[20] T. Halpin-Healy and K. A. Takeuchi. A kpz cocktail-shaken, not stirred... *J. Stat. Phys.*, 160(4):794–814, 2015.

[21] T. Browicz. Further observation of motion phenomena on red blood cells in pathological states. *Zbl. med. Wissen*, 28(1):625–627, 1890.

[22] F. Brochard and J. F. Lennon. Frequency spectrum of the flicker phenomenon in erythrocytes. *J. Phys.*, 36(11):1035–1047, 1975.

[23] S. Levin and R. Korenstein. Membrane fluctuations in erythrocytes are linked to mgatp-dependent dynamic assembly of the membrane skeleton. *Biophys. J.*, 60(3):733–737, 1991.

[24] J. Prost and R. Bruinsma. Shape fluctuations of active membranes. *EPL*, 33(4):321, 1996.

[25] J.-B. Manneville, P. Bassereau, D. Lévy, and J. Prost. Activity of transmembrane proteins induces magnification of shape fluctuations of lipid membranes. *Phys. Rev. Lett.*, 82:4356–4359, 1999.

[26] H. Turlier, D. A. Fedosov, B. Audoly, T. Auth, N. S. Gov, C. Sykes, J.-F. Joanny, G. Gompper, and T. Betz. Equilibrium physics breakdown reveals the active nature of red blood cell flickering. *Nat. Phys.*, 12(5):513, 2016.

[27] C. S. Peskin, G. M. Odell, and G. F. Oster. Cellular motions and thermal fluctuations: the brownian ratchet. *Biophys. J.*, 65(1):316–324, 1993.

[28] A. Mogilner and G. Oster. Cell motility driven by actin polymerization. *Biophys. J.*, 71(6):3030–3045, 1996.

[29] A. Mogilner and G. Oster. Force generation by actin polymerization ii: the elastic ratchet and tethered filaments. *Biophys. J.*, 84(3):1591–1605, 2003.

[30] R. D. Mullins, J. A. Heuser, and T. D. Pollard. The interaction of arp2/3 complex with actin: Nucleation, high affinity pointed end capping, and formation of branching networks of filaments. *PNAS*, 95(11):6181–6186, 1998.

[31] S. Ramaswamy, J. Toner, and J. Prost. Nonequilibrium fluctuations, traveling waves, and instabilities in active membranes. *Phys. Rev. Lett.*, 84:3494–3497, 2000.

[32] N. S. Gov and A. Gopinathan. Dynamics of membranes driven by actin polymerization. *Biophys. J.*, 90(2):454 – 469, 2006.

[33] A. Maitra, P. Srivastava, M. Rao, and S. Ramaswamy. Activating membranes. *Phys. Rev. Lett.*, 112:258101, Jun 2014.

[34] W. Cai and T. C. Lubensky. Covariant hydrodynamics of fluid membranes. *Phys. Rev. Lett.*, 73:1186–1189, 1994.

[35] W. Cai and T. C. Lubensky. Hydrodynamics and dynamic fluctuations of fluid membranes. *Phys. Rev. E*, 52:4251–4266, 1995.

[36] D. Boal and D. H. Boal. *Mechanics of the Cell*. Cambridge University Press, 2012.

[37] T. D. Pollard. Regulation of actin filament assembly by arp2/3 complex and formins. *Annu. Rev. Biophys.*, 36:451–477, 2007.

[38] R. H. Insall and L. M. Machesky. Actin dynamics at the leading edge: from simple machinery to complex networks. *Dev. Cell*, 17(3):310–322, 2009.

[39] A. J. Ridley. Life at the leading edge. *Cell*, 145(7):1012–1022, 2011.

[40] B. Habermann. The bar-domain family of proteins: a case of bending and binding? *EMBO Rep.*, 5(3):250–255, 2004.

[41] V. Vogel and M. Sheetz. Local force and geometry sensing regulate cell functions. *Nat. Rev. Mol. Cell Biol.*, 7(4):265, 2006.

[42] S. Ramaswamy and M. Rao. The physics of active membranes. *C. R. Acad. Sci.*, 2(6):817–839, 2001.

[43] A. B. Goryachev and A. V. Pokhilko. Dynamics of cdc42 network embodies a turing-type mechanism of yeast cell polarity. *FEBS Lett.*, 582(10):1437–1443, 2008.

[44] K. Gowrishankar, S. Ghosh, S. Saha, C. Rumamol, S. Mayor, and M. Rao. Active remodeling of cortical actin regulates spatiotemporal organization of cell surface molecules. *Cell*, 149(6):1353–1367, 2012.

[45] J. Allard and A. Mogilner. Traveling waves in actin dynamics and cell motility. *Curr. Opin. Cell Biol.*, 25(1):107–115, 2013.

[46] A. Clarke. The thermal limits to life on earth. *Int. J. Astrobiol.*, 13(2):141–154, 2014.

[47] L. P. Kadanoff. More is the same; phase transitions and mean field theories. *J. Stat. Phys.*, 137(5):777, 2009.

[48] S. Chen and G. D. Doolen. Lattice boltzmann method for fluid flows. *Annu. Rev. Fluid Mech.*, 30(1):329–364, 1998.

[49] P. Meakin, P. Ramanlal, L. M. Sander, and R. C. Ball. Ballistic deposition on surfaces. *Phys. Rev. A*, 34(6):5091, 1986.

[50] M. Plischke, Z. Rácz, and D. Liu. Time-reversal invariance and universality of two-dimensional growth models. *Phys. Rev. B*, 35(7):3485, 1987.

[51] L. Bertini and G. Giacomin. Stochastic burgers and kpz equations from particle systems. *Commun. Math. Phys.*, 183(3):571–607, 1997.

[52] V. Démery and D. Lacoste. Mechanical factors affecting the mobility of membrane proteins. In *Physics of Biological Membranes*, pages 191–211. Springer, 2018.

[53] R. H. Kraichnan. Anomalous scaling of a randomly advected passive scalar. *Phys. Rev. Lett.*, 72:1016–1019, 1994.

[54] D. Das and M. Barma. Particles sliding on a fluctuating surface: Phase separation and power laws. *Phys. Rev. Lett.*, 85:1602–1605, 2000.

[55] D. Das, M. Barma, and S. N. Majumdar. Fluctuation-dominated phase ordering driven by stochastically evolving surfaces: Depth models and sliding particles. *Phys. Rev. E*, 64:046126, 2001.

[56] B. Drossel and M. Kardar. Passive sliders on growing surfaces and advection in burger's flows. *Phys. Rev. B*, 66:195414, 2002.

[57] B. Derrida and M. R. Evans. Bethe ansatz solution for a defect particle in the asymmetric exclusion process. *J. Phys. A*, 32(26):4833, 1999.

[58] A. Laio and M. Parrinello. Escaping free-energy minima. *PNAS*, 99(20):12562–12566, 2002.

[59] M. Plischke and Z. Rácz. Active zone of growing clusters: Diffusion-limited aggregation and the eden model. *Phys. Rev. Lett.*, 53(5):415, 1984.

[60] C.-S. Chin. Passive random walkers and riverlike networks on growing surfaces. *Phys. Rev. E*, 66(2):021104, 2002.

[61] M. Gopalakrishnan. Dynamics of a passive sliding particle on a randomly fluctuating surface. *Phys. Rev. E*, 69:011105, 2004.

[62] A. Nagar, S. N. Majumdar, and M. Barma. Strong clustering of noninteracting, sliding passive scalars driven by fluctuating surfaces. *Phys. Rev. E*, 74(2):021124, 2006.

[63] J.-P. Bouchaud and A. Georges. Anomalous diffusion in disordered media: statistical mechanisms, models and physical applications. *Phys. Rep.*, 195(4-5):127–293, 1990.

[64] T. Bohr and A. Pikovsky. Anomalous diffusion in the kuramoto-sivashinsky equation. *Phys. Rev. Lett.*, 70(19):2892, 1993.

[65] T. Singha and M. Barma. Clustering, intermittency, and scaling for passive particles on fluctuating surfaces. *Phys. Rev. E*, 98:052148, 2018.

[66] Y. G. Sinai. The limiting behavior of a one-dimensional random walk in a random medium. *Theory Probab. Its Appl.*, 27(2):256–268, 1983.

[67] J. M. Deutsch. Aggregation-disorder transition induced by fluctuating random forces. *J. Phys. A*, 18(9):1449, 1985.

[68] A. J. Bray. Theory of phase-ordering kinetics. *Adv. Phys.*, 43(3):357–459, 1994.

[69] H. Spohn. *Large scale dynamics of interacting particles*. Springer Science & Business Media, 2012.

[70] P. Ehrenfest and T. Ehrenfest. *The conceptual foundations of the statistical approach in mechanics*. Courier Corporation, 1990.

[71] C. Kipnis and C. Landim. *Scaling limits of interacting particle systems*, volume 320. Springer Science & Business Media, 2013.

[72] G. Giacomin, J. L. Lebowitz, and E. Presutti. Deterministic and stochastic hydrodynamic equations arising from simple microscopic model systems. *Mathematical Surveys and Monographs*, 64:107–152, 1998.

[73] M. R. Evans and T. Hanney. Nonequilibrium statistical mechanics of the zero-range process and related models. *J. Phys. A*, 38(19):R195, 2005.

[74] L. C. Evans. *Partial Differential Equations*. Graduate studies in mathematics. American Mathematical Society, 2010.

[75] P. D. Lax. *Hyperbolic systems of conservation laws and the mathematical theory of shock waves*, volume 11. SIAM, 1973.

[76] D. S. Dean. Langevin equation for the density of a system of interacting langevin processes. *J. Phys. A*, 29(24):L613, 1996.

[77] H. Spohn and G. Stoltz. Nonlinear fluctuating hydrodynamics in one dimension: the case of two conserved fields. *J. Stat. Phys.*, 160(4):861–884, 2015.

[78] V. Popkov, J. Schmidt, and G. M. Schütz. Universality classes in two-component driven diffusive systems. *J. Stat. Phys.*, 160(4):835–860, 2015.

[79] D. J. Amit. *Field Theory, the Renormalization Group, and Critical Phenomena*. World Scientific Publishing Company, 1984.

[80] J. Cardy. *Scaling and renormalization in statistical physics*, volume 5. Cambridge university press, 1996.

[81] U. C. Täuber. *Critical dynamics: a field theory approach to equilibrium and non-equilibrium scaling behavior*. Cambridge University Press, 2014.

[82] L. P. Kadanoff. Scaling laws for ising models near t_c. *Phys. Phys. Fiz.*, 2:263–272, Jun 1966.

[83] E. Frey and U. C. Täuber. Two-loop renormalization-group analysis of the burgers–kardar-parisi-zhang equation. *Phys. Rev. E*, 50:1024–1045, Aug 1994.

[84] R. Kubo. The fluctuation-dissipation theorem. *Rep. Prog. Phys.*, 29(1):255, 1966.

[85] F. W. Wiegel. *Introduction to path-integral methods in physics and polymer science*. World Scientific, 1986.

[86] M. Hattori and S. Abe. Path probability of stochastic motion: A functional approach. *Physica A*, 451:198–204, 2016.

[87] J. Honkonen. Ito and stratonovich calculuses in stochastic field theory. *arXiv:1102.1581*, 2011.

[88] C. W. Gardiner. *Handbook of stochastic methods*, volume 3. springer Berlin, 1985.

[89] R. S. Ellis. *Entropy, large deviations, and statistical mechanics*. Springer, 2007.

[90] S. Torquato and F. H. Stillinger. Local density fluctuations, hyperuniformity, and order metrics. *Phys. Rev. E*, 68(4):041113, 2003.

[91] G. 't Hooft and M. Veltman. Regularization and renormalization of gauge fields. *Nucl. Phys. B*, 44(1):189–213, 1972.

[92] E. Marinari, A. Pagnani, and G. Parisi. Critical exponents of the kpz equation via multi-surface coding numerical simulations. *J. Phys. A*, 33(46):8181, 2000.

[93] R. Lahiri and S. Ramaswamy. Are steadily moving crystals unstable? *Phys. Rev. Lett.*, 79:1150–1153, 1997.

[94] R. Lahiri, M. Barma, and S. Ramaswamy. Strong phase separation in a model of sedimenting lattices. *Phys. Rev. E*, 61:1648–1658, 2000.

[95] S. Ramaswamy, M. Barma, D. Das, and A. Basu. Phase diagram of a two-species lattice model with a linear instability. *Phase Transit.*, 75:363–375, 2002.

[96] S. Chakraborty, S. Chatterjee, and M. Barma. Large compact clusters and fast dynamics in coupled nonequilibrium systems. *Phys. Rev. E*, 93:050102, 2016.

[97] S. Chakraborty, S. Chatterjee, and M. Barma. Ordered phases in coupled nonequilibrium systems: Static properties. *Phys. Rev. E*, 96:022127, 2017.

[98] S. Chakraborty, S. Chatterjee, and M. Barma. Ordered phases in coupled nonequilibrium systems: Dynamic properties. *Phys. Rev. E*, 96:022128, 2017.

[99] J. Levandosky. Stanford Math 220A, Lecture Notes: Partial Differential Equations of Applied Mathematics, 2002. URL: `https://web.stanford.edu/class/math220a/lecturenotes.html`. Last visited on 10-02-2020.